

An Investigation of Methane Autoignition Behaviour Under Diesel Engine-Relevant Conditions

by

Jean-Louis Iaconis

B.A.Sc., The University of British Columbia, 2001

A thesis submitted in partial fulfilment of

the requirements for the degree of

Master of Applied Science

in

the Faculty of Graduate Studies

Department of Mechanical Engineering

We accept this thesis as conforming

to the required standard

The University of British Columbia

March 2003

© Jean-Louis Iaconis, 2003

In presenting this thesis in partial fulfilment of the requirements for an advanced degree at the University of British Columbia, I agree that the Library shall make it freely available for reference and study. I further agree that permission for extensive copying of this thesis for scholarly purposes may be granted by the head of my department or by his or her representatives. It is understood that copying or publication of this thesis for financial gain shall not be allowed without my written permission.

Department of Mechanical Engineering

The University of British Columbia
Vancouver, Canada

Date April 20, 2003

Abstract

"An Investigation of Methane Autoignition Behaviour Under Diesel Engine-Relevant Conditions"

by Jean-Louis laconis

As an extension to recent experimental methane ignition delay time measurements conducted at diesel engine-relevant temperatures and pressures, further work has been conducted in an attempt to more closely converge shock tube results with actual engine operating environments. This was performed in three phases that involved reviewing previous homogeneous autoignition delay time data, characterizing a gaseous fuel injector for use in non-premixed ignition studies, and finally conducting non-premixed autoignition delay time measurements in a shock tube.

First, in response to recent homogenous methane autoignition delay results that questioned the applicability of existing induction time correlations at low temperatures/high pressures, a series of homogeneous methane autoignition experiments were conducted to isolate whether pressure or temperature differences between recent results and existing correlations were responsible for observed discrepancies. Shock tube experiments were conducted at pressures between 2-4 bar and temperatures between 1100-2000 K, facilitating direct comparison with existing correlations over high temperatures and with recent results at lower, engine-relevant temperatures. These experiments indicated existing correlations could predict ignition delay times at low pressures, but differences in ignition detection methods caused noticeable scatter between correlations.

Subsequently, the characteristics of a gaseous fuel injector were investigated to determine the influence of injection parameters on the injector's performance and on the jet produced. These experiments investigated the influence of injection duration and pressure on resultant jets, along with exploring the effects of pulsed injection, and the effects of various obstructions and of an enclosure on overall jet development. These experiments yielded correlations for predicting the injector's behaviour under all intended operating conditions.

Finally, the coupling between chemical kinetics and fluid mechanics was explored in a series of non-premixed autoignition delay experiments. These shock tube experiments utilized a standard reflected shock technique, but with fuel injected into the shock-heated air after reflection of the incident shock wave. Chemical kinetic effects were explored by varying air temperatures and pressures, while the effects of fluid mechanic parameters were investigated by varying the fuel injection pressure and duration. These experiments suggested that high-pressure, partially premixed, pulsed direct injection could form an autoignition delay reduction strategy for diesel engines.

Table of Contents

Abstract.....	ii
Table of Contents	iii
List of Tables	v
List of Figures	vii
1 Introduction	1
2 Homogeneous Methane Autoignition Delay Study	3
2.1 Introduction.....	3
2.2 Background	3
2.3 Experimental Investigation	4
2.3.1 Apparatus	4
2.3.2 Instrument Calibration	5
2.3.3 Procedure.....	6
2.3.4 Experimental Results	7
2.3.5 Error Analysis	14
2.4 Numerical Investigation	16
2.4.1 Reduced Mechanism.....	17
2.4.2 Governing Equations.....	17
2.4.3 Ignition Delay Criteria Definition	18
2.4.4 Parameter Tuning Procedure	22
2.4.5 Numerical Results	22
2.5 Conclusions and Recommendations	25
3 Characterization of a Gaseous Fuel Injection System	27
3.1 Introduction.....	27
3.2 Background	27
3.3 Injector Hardware Characterization	28
3.3.1 Experimental Apparatus	29
3.3.2 Injection Delay Measurement.....	31

3.3.3 Mass Flow Rate Measurement.....	35
3.3.4 Pulsed Injection System Validation	40
3.4 Jet Flow Field Characterization	43
3.4.1 Experimental Apparatus	44
3.4.2 Single Injection Mode	45
3.4.3 Pulsed Injection Mode	54
3.4.4 Effects of Jet Impingement.....	60
3.4.5 Effects of an Enclosure	66
3.5 Conclusions and Recommendations	67
4 Non-Premixed Methane Autoignition Delay Study.....	71
4.1 Introduction.....	71
4.2 Background	71
4.3 Experimental Methods.....	73
4.3.1 Apparatus.....	73
4.3.2 Procedure.....	76
4.4 Experimental Results.....	78
4.4.1 Autoignition Sensitivity to Fluid Mechanic Parameters.....	79
4.4.2 Autoignition Sensitivity to Chemical Kinetic Parameters	84
4.4.3 Error Analysis	93
4.4.4 Autoignition Visualization	94
4.5 Conclusions and Recommendations	102
5 Conclusions and Recommendations	104
References	107
Appendix A: Vacuum Sensor Calibration Data	111
Appendix B: Homogeneous Autoignition Delay Data.....	113
Appendix C: Homogeneous Autoignition Delay Error Analysis.....	114
Appendix D: Numerical Combustion Equations Derivation.....	118
Appendix E: Injector Hardware Characterization Data	123
Appendix F: Jet Flow Field Characterization Data.....	129
Appendix G: Non-Premixed Autoignition Delay Data.....	136
Appendix H: Autoignition Visualization Images.....	139
Appendix I: Shock Tube Test Section Design Calculations	140
Appendix J: Shock Tube Optical Test Section Drawings.....	146

List of Tables

2 Homogeneous Methane Autoignition Delay Study	
Table 2.1: Experimental Test Matrix (Homogeneous Autoignition Study)	8
Table 2.2: Autoignition Delay Time Correlations Comparison	12
Table 2.3: Numerical Ignition Criteria Comparison	19
Table 2.4: Activation Energy Comparison	24
3 Characterization of a Gaseous Fuel Injection System	
Table 3.1: Experimental Test Matrix (Injection Delay Study).....	32
Table 3.2: ANOVA Results for Injection Delay Backpressure Dependence	34
Table 3.3: Experimental Test Matrix (Mass Flow Rate Study).....	35
Table 3.4: Mass Flux Model Parameters	39
Table 3.5: Comparison of Experimental Mass Fluxes to Model Results	40
Table 3.6: Experimental Test Matrix (Pulsed Injection System Validation)	41
Table 3.7: Experimental Test Matrix (Single Injection Visualization Study).....	46
Table 3.8: Jet Penetration Number Comparison	54
Table 3.9: Experimental Test Matrix (Pulsed Injection Visualization Study).....	55
Table 3.10: Experimental Test Matrix (Jet Impingement Visualization Study).....	61
Table 3.11: Experimental Test Matrix (Jet Enclosure Visualization Study)	66
4 Non-Premixed Methane Autoignition Delay Study	
Table 4.1: Experimental Test Matrix (Non-Premixed Fluid Mechanic Parameter Study)	79
Table 4.2: Experimental Test Matrix (Non-Premixed Chemical Kinetic Parameter Study)..	86
Table 4.3: Experimental Test Matrix (Autoignition Visualization Study)	95
Appendices	
Table A.1: Vacuum Sensor Calibration.....	111
Table B.1: Homogeneous Autoignition Delay Data	113
Table E.1: Injection Delay Experimental Data	123
Table E.2: Injector Mass Flow Rate Data	125

Table E.3: Pulsed Injection System Validation Experimental Data.....	126
Table F.1: Single Injection Mode Jet Flow Field Data	129
Table F.2: Pulsed Injection Jet Flow Field Data	132
Table F.3: Jet Impingement Flow Field Data (Circular Obstruction).....	134
Table F.4: Jet Impingement Flow Field Data (Rectangular Obstruction).....	134
Table F.5: Jet Enclosure Flow Field Data.....	135
Table G.1: Non-Premixed Autoignition Delay Data	136
Table I.1: Maximum Stress and Deflection for Fully Constrained B.C.....	142
Table I.2: Maximum Stress and Deflection for Free B.C.	142

List of Figures

2 Homogeneous Methane Autoignition Delay Study

Figure 2.1: Experimental Apparatus (Homogeneous Autoignition Study)	5
Figure 2.2: Shock Velocity and Autoignition Delay Measurement From Pressure Signals ...	7
Figure 2.3: Experimentally Measured Homogenous Autoignition Delay Times	8
Figure 2.4: Normalized Homogeneous Autoignition Delay Times	9
Figure 2.5: Characteristic Pressure Signals Over Three Ignition Regimes	10
Figure 2.6: Comparison of Present Experimental Results to Previous Correlations	11
Figure 2.7: Comparison of Threshold and Gradient Ignition Criteria	20
Figure 2.8: Representative Pressure Time History Slope and Curvature Plots	21
Figure 2.9: Modified Gradient Ignition Definition.....	21
Figure 2.10: Comparison of Present Experimental and Numerical Results.....	23
Figure 2.11: Comparison of Present Numerical Results to Previous Correlations	25

3 Characterization of a Gaseous Fuel Injection System

Figure 3.1: J41 Injector with Control System	29
Figure 3.2: Experimental Apparatus (Injection Hardware Characterization Study)	30
Figure 3.3: Injection Delay Definition	32
Figure 3.4: Histogram of Measured Injection Delay Times	33
Figure 3.5: Probability Plots of Measured Injection Delay Times	33
Figure 3.6: Injection Delay Time vs. Backpressure/Pressure Ratio.....	34
Figure 3.7: Mass Flux Measurements (Nitrogen)	36
Figure 3.8: Mass Flux Measurements (Methane).....	36
Figure 3.9: Pulse Delay and Pulse-to-Pulse Pressure Ratio Definitions	41
Figure 3.10: Normalized Pulse-to-Pulse Pressure Ratio vs. Pulse Delay	42
Figure 3.11: Successive Injections with Insufficient Pulse Delays.....	43
Figure 3.12: Experimental Apparatus (Jet Flow Field Characterization Study)	44
Figure 3.13: Schlieren Images of Single Jet Evolution in Time	47
Figure 3.14: Jet Length Evolution During/After Injection (Single Injection).....	48
Figure 3.15: Jet Width Evolution During/After Injection (Single Injection)	49

Figure 3.16: Numerical Jet Model.....	51
Figure 3.17: Normalized Jet Tip Penetration (During Injection).....	52
Figure 3.18: Normalized Jet Tip Penetration (During/After Injection).....	53
Figure 3.19: Schlieren Images of Pulsed Jet Evolution in Time.....	56
Figure 3.20: Jet Length and Width Evolution (Pulsed Injection).....	57
Figure 3.21: Flow Obstructions for Jet Impingement Study.....	60
Figure 3.22: Schlieren Images of Impinging Jet Evolution in Time.....	62
Figure 3.23: Jet Length and Width Evolution (Circular Obstruction).....	63
Figure 3.24: Jet Length, Width, and Deflection Angle Definition.....	64
Figure 3.25: Jet Length and Width Evolution (Rectangular Obstruction).....	65
Figure 3.26: Schlieren Images of Enclosed Jet Evolution in Time.....	67
Figure 3.27: Jet Length and Width Evolution (Enclosure).....	68
4 Non-Premixed Methane Autoignition Delay Study	
Figure 4.1: Experimental Apparatus (Non-Premixed Autoignition Study).....	74
Figure 4.2: Incident Shock Velocity Measurement From Pressure Signals.....	77
Figure 4.3: Ignition Definition From Optical Emissions Signals.....	78
Figure 4.4: Autoignition Injection Duration Sensitivity.....	80
Figure 4.5: Characteristic Optical Ignition Signals Over Two Regimes.....	81
Figure 4.6: Autoignition Injection Pressure Ratio Sensitivity.....	84
Figure 4.7: Autoignition Temperature Sensitivity (31 bar).....	87
Figure 4.8: Autoignition Temperature Sensitivity (17 bar).....	88
Figure 4.9: Differences in Luminosity Threshold with Pressure.....	90
Figure 4.10: Autoignition Pressure Sensitivity.....	91
Figure 4.11: Characteristic Optical Emission Signals Over Three Ignition Regimes.....	93
Figure 4.12: Experimental Apparatus (Autoignition Visualization Study).....	96
Figure 4.13: Compact Schlieren System Schematic.....	97
Figure 4.14: Autoignition Visualization Image Post-Processing Examples.....	98
Figure 4.15: Comparison of Hot and Cold Jets.....	99
Figure 4.16: Reacting Jet Schlieren Images at Various Ignition Stages.....	100
Figure 4.17: Reacting Jet Self-Illuminated Images at Various Ignition Stages.....	101
Appendices	
Figure C.1: Illustration of Pressure Measurement Error.....	115
Figure H.1: Autoignition Visualization Images.....	139

Figure I.1: Maximum Window Deflection Under Dynamic Loading.....	143
Figure J.1: Optical Window.....	147
Figure J.2: Viewing Window.....	148
Figure J.3: Optical Test Section.....	149
Figure J.4: Endplate Flange.....	150
Figure J.5: Adaptor Flange.....	151
Figure J.6: Injector Mounting Plate.....	152
Figure J.7: 3" Slip-On Adaptor Flange.....	153
Figure J.8: 2.5" Slip-On Adaptor Flange.....	154
Figure J.9: Instrumentation Window.....	155
Figure J.10: Clamping Plate.....	156
Figure J.11: Test Section Assembly.....	157
Figure J.12: Adaptor Assembly.....	158
Figure J.13: Complete Assembly.....	159

Introduction **1**

The thrust to develop clean diesel technology being driven by increasingly stringent emissions regulations has led many to consider the use of natural gas to achieve these objectives without adversely affecting performance. Such an attempt has been made by Westport Innovations Inc. with a High Pressure Direct Injection (HPDI) system that utilizes a minute amount of diesel fuel (as little as 2-5% of the total fuel energy) to ignite a natural gas charge. The diesel pilot is used solely for igniting the natural gas, which has a much longer ignition delay time than diesel and would otherwise not be suitable for late-cycle injection. While such a system is able to maintain most of the torque, power, and efficiency benefits inherent to diesel engines and dramatically reduce emissions, the presence of a diesel pilot requires onboard storage of both diesel fuel and natural gas along with the use of a complicated dual-fuel injector. The cost implications of having redundant fuel systems and complex injectors provide motivation to seek out alternative methods of minimizing natural gas' autoignition delay time without the use of a pilot fuel.

Unfortunately, currently accepted techniques for reducing natural gas' prohibitively long ignition delay time are limited to the following:

- Using dual fuels (i.e. diesel pilot);
- Blending natural gas with an appropriate ignition-promoting additive;
- Using a glow plug or spark plug; or
- Increasing compression ratios to achieve higher temperatures.

Among these four options only the first two are suitable for retrofit applications, with the latter two requiring substantial engine modifications. Therefore, if cost reductions beyond the use of dual fuels are to be achieved, fundamental research investigating the autoignition behaviour of methane in diesel environments is required. Such research requires the thorough investigation of the chemical kinetics involved in methane oxidation, the fluid mechanics governing transient gaseous fuel jets, and finally the coupling that occurs between both fluid mechanic and kinetic parameters in an engine. Correspondingly, the present investigation is segregated into three phases.

In the first phase, the autoignition delay times of various methane/air mixtures are measured to validate the existing experimental apparatus (by verifying that previous researchers' results can be adequately reproduced) while also attempting to resolve discrepancies between autoignition delay results obtained at low pressure and high temperature and those obtained under engine-relevant conditions (high pressure and low temperature). Since many previous ignition studies have been conducted, the scope of the first phase of this investigation is simply to validate the existing apparatus and attempt to resolve observed discrepancies between various researchers' results.

In the second phase of the investigation, transient jets produced by a Westport Innovations J41 fuel injector are studied to understand this injector's characteristics and quantify the effects of various injection parameters on the jet produced. As with the first phase of this investigation, an abundance of research is available in the literature describing the development of gaseous jets in addition to many scaling laws developed based on previous experimental studies. Therefore, the purpose of this study is to validate the existing fuel injector for future use in non-premixed autoignition delay time shock tube studies and to facilitate the application of previously deduced scaling laws and empirical relations.

Finally, once the influence of kinetic parameters on the autoignition delay time of methane has been clarified, and the fluid mechanic parameters governing transient gaseous jets produced by a Westport injector have been characterized, both the kinetic and the fluid mechanic parameters are studied together in a series of non-premixed methane ignition experiments. This final phase of this investigation attempts to explore the coupling that occurs between both kinetic and fluid mechanic parameters in a diesel engine with the intent of more closely converging shock tube results with engine operating environments. It is hoped that in so doing, alternative techniques for minimizing methane's autoignition delay time will emerge.

Homogeneous Methane Autoignition Delay Study **2**

2.1 Introduction

Driven by increasingly stringent environmental regulations, rapid developments are occurring in the field of combustion research, especially relating to internal combustion engines with a large part of this effort focussed on the conversion of diesel engines, notorious for their emission of smog-producing nitrogen oxides (NO_x) and carcinogenic soot, to much cleaner burning natural gas. Unfortunately, natural gas, or specifically methane (the main component of natural gas), exhibits poor compression ignitability, requiring either excessive temperatures or prohibitively long residence times, to ignite. While in spark-ignited engines this impediment is overcome by the presence of an external ignition source, diesel engines do not have any such ignition source. Therefore, research has principally focussed on developing an appropriate ignition-promoting additive to blend with natural gas or, as Westport Innovations has done with their HPDI system, using a pilot fuel to ignite the natural gas. While this system has been successfully proven to enable diesel engines to operate on natural gas, such a dual-fuel system ultimately poses cost and emissions limitations. Thus if further emission and cost reductions are desired, the diesel pilot must be eliminated. To achieve this objective, alternative methods of reducing natural gas' ignition delay time must be explored and the first step in doing so requires measurement of the autoignition delay time of methane at various operating conditions.

2.2 Background

While many previous researchers have measured the ignition delay time of methane mixtures, most of these investigations have been performed at relatively high temperatures ($T > 1500 \text{ K}$) and low pressures ($P < 10 \text{ bar}$), which are not directly engine-relevant. For operating conditions that are engine-relevant ($P > 30 \text{ bar}$, $T \ll 1500 \text{ K}$) few experimental investigations have been conducted. To remedy this, Huang¹ recently explored this domain. This recent work involved measuring the ignition delay times of $\text{CH}_4/\text{H}_2/\text{DME}/\text{air}$ mixtures in a shock tube over a range of equivalence ratios between 0.7-1.3, pressures from 16-40 bar, and temperatures between 950-

1400 K. This investigation provided compelling evidence that existing methane induction time correlations developed from high-temperature, low-pressure experimental data failed to predict ignition delay times at engine-relevant conditions. However, since previous investigations were conducted at low pressures/high temperatures, and Huang's recent work was conducted at high pressures/low temperatures, a need exists to confirm if the pressure or temperature difference is responsible for observed discrepancies. The present investigation therefore seeks to explore this issue by measuring the ignition delay time of various $\text{CH}_4/\text{O}_2/\text{Ar}$ mixtures at low pressures (2-4 bar) and over a wide temperature range (1100-2000 K). This will permit direct comparison with previous work at high temperatures ($T > 1500$ K) and demonstrate whether existing ignition delay correlations also correctly predict ignition delay times at low temperatures ($T < 1500$ K). In addition, to complement the experimental research and to further compare the present results with existing correlations, numerical simulations with simplified chemical kinetics are performed using a single-step reaction mechanism fit to the current experimental results.

2.3 Experimental Investigation

To permit direct comparison with previously published methane ignition delay time correlations, the experimental portion of the present investigation involved measuring the ignition delay times of stoichiometric $\text{CH}_4/\text{O}_2/\text{Ar}$ mixtures in a shock tube at various experimental temperatures and pressures using a standard reflected shock technique. Experimental conditions were chosen to coincide with those previously investigated by other researchers while extending to low enough temperatures to be engine-relevant, and thus comparable with recent experiments. Details of the specific apparatus used and the test conditions that were investigated are presented below.

2.3.1 Apparatus

Experimental autoignition delay measurements were conducted in a 7.37 m long shock tube (3.11 m driver section, 4.26 m driven section), 5.9 cm in inner diameter with five PCB Piezotronics 112B11 dynamic pressure transducers mounted at 0.763 m, 2.130 m, 3.958 m, 4.108 m, and 4.260 m from the diaphragm for detecting the passage of incident shock waves (refer to Figure 2.1 schematic). An Auto Tran 600D-117 vacuum sensor was used for preparing driven gas compositions and measuring initial driven gas pressure, while an Eclipse[®] high-pressure sensor was used for measuring the driver gas pressure. Voltage outputs from the driven section vacuum sensor and the driver section pressure transducer were measured with a Circuit-Test DMR-3600 multimeter when recording initial pressures,

while outputs from the dynamic pressure transducers were recorded by a Wavebook/512™ data acquisition system set to a sampling frequency of 167 kHz (6 μs sampling interval).

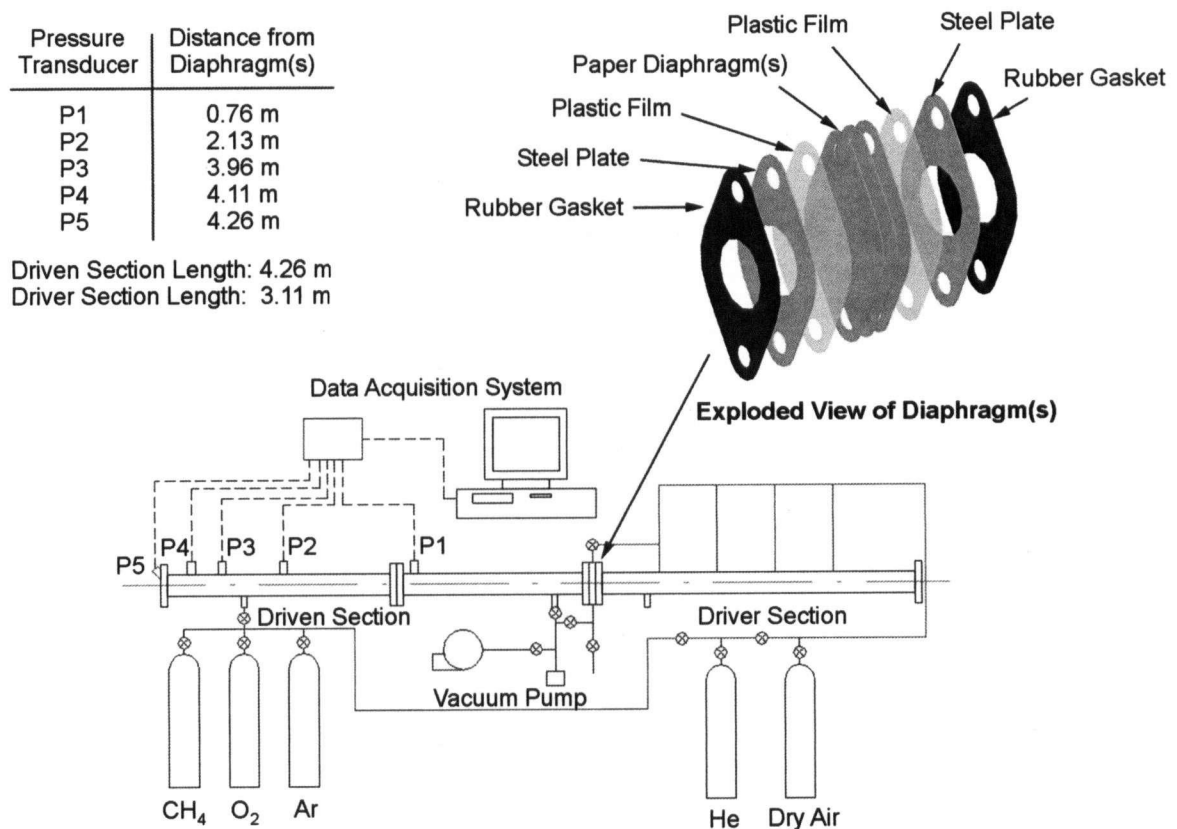


Figure 2.1: Experimental Apparatus (Homogeneous Autoignition Study)

To obtain low test pressures (~ 2-4 bar) paper diaphragms were used consisting of 1-4 layers of coated paper (0.1-0.3 mm thick) with an outer layer of 0.01 mm thick plastic film added to ensure air impermeability (refer to diaphragm illustration in Figure 2.1). Stacking varying numbers of diaphragms controlled their burst pressure, and air impermeability was verified prior to each experiment by evacuating the driven section and ensuring that there was no detectable leakage through the diaphragm for at least 20 minutes.

2.3.2 Instrument Calibration

Since each of the five dynamic pressure transducers along the length of the driven section was used solely for detecting the passage of an incident shock wave, no static calibration was performed (as they were not used for explicitly measuring pressures). Instead, only results of a previous dynamic calibration were used to verify each sensor's response time.

These were previously verified to have a dynamic response time of less than 3 μs and a voltage-to-pressure conversion factor of approximately 930 psi/V^1 .

The vacuum sensor used for measuring the driven section pressure was calibrated using a zero and span calibration corresponding to vacuum and atmospheric pressures prior to each experiment (atmospheric pressure was compared to that recorded from an Oakton[®] Aneroid barometer). Linear regression between these two calibration points was used for calculating all intermediate pressures and was found to agree well with the manufacturer's specifications (refer to Appendix A for calibration data).

The driver section high-pressure transducer was not exhaustively calibrated since it was not used in any ignition measurements. This transducer was used solely for measuring the diaphragm's burst pressure (for estimating the loss coefficient across the diaphragm) and not used in any other calculations. Therefore, the manufacturer's calibration constant was used together with the barometric pressure recorded prior to each test.

2.3.3 Procedure

Prior to each experiment, barometric pressure was recorded and the driven and driver gas pressure transducers calibrated as per the procedure outlined above. Both the driven and driver sections were evacuated using a Cenco Instruments Corp. Hyvac 7 vacuum pump and gas compositions prepared manometrically. Gas mixtures were subsequently allowed to settle for at least 30 minutes, with the driven gas pressure measured immediately after charging the driven section and again prior to conducting the experiment to ensure there was no leakage across the diaphragm. The data acquisition system was then armed (set to be triggered by the rising edge of the incident shock wave as it passed the first dynamic pressure transducer) and driver section gas pressure (Praxair 99.9% He) was increased until the diaphragm(s) ruptured. Throughout all experiments a single diaphragm was used, instead of a double diaphragm, due to the paper diaphragms' inconsistent burst pressure.

Incident shock velocities were calculated from pressure traces obtained from each of the five dynamic pressure transducers along the length of the driven section by measuring the time interval between rising edges as the shock wave passed each successive transducer (see Figure 2.2 (a)). Autoignition delay was defined as the time interval between incident shock reflection from the driven section endplate and the time when maximum curvature in the pressure signal from the endplate transducer was observed (Figure 2.2 (b)). The

experimental pressure and temperature was assumed equal to that immediately behind the reflected shock wave (as calculated from isentropic shock relations and the measured incident shock velocity^{1,2}).

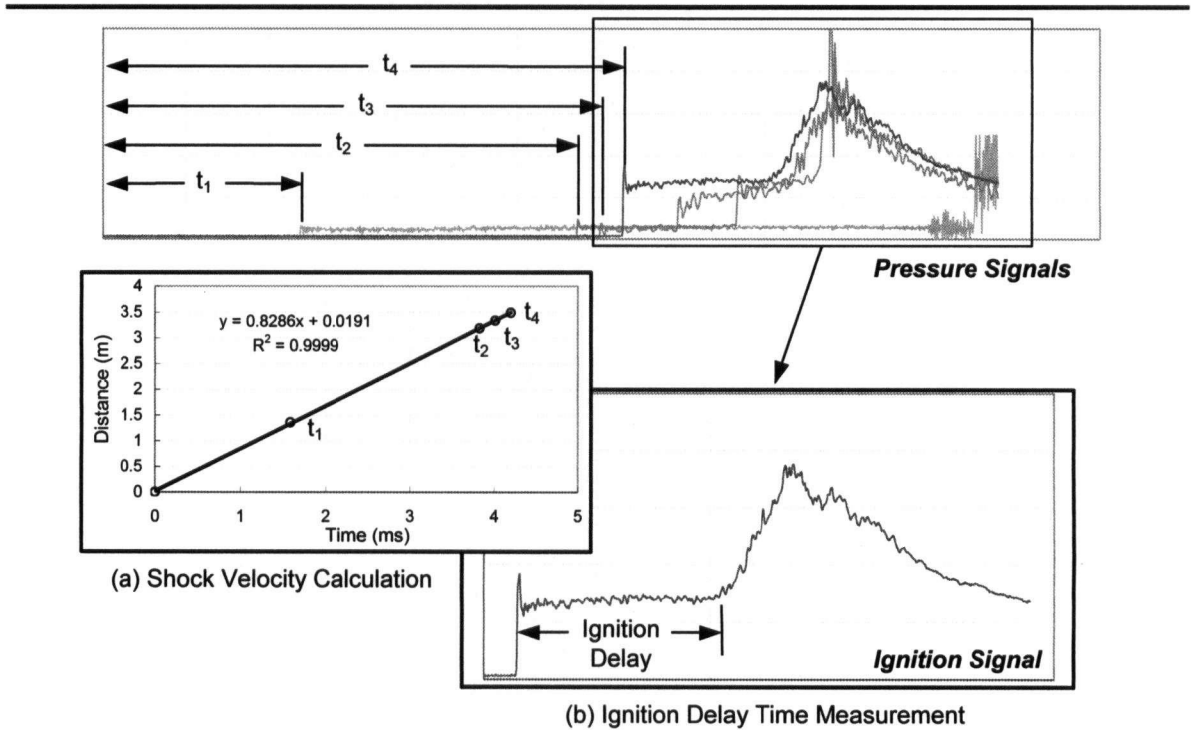


Figure 2.2: Shock Velocity and Autoignition Delay Measurement From Pressure Signals

A summary of all test conditions investigated is presented in Table 2.1 (including several test conditions that did not result in ignition). While ideally experimental pressures ranging from 1-10 bar and temperatures from 1000-2000 K were sought, limitations imposed by the paper diaphragms' rupture behaviour limited the minimum pressure attained to 1.5 bar and the maximum pressure to 7.7 bar, with most experimental pressures between 3-4 bar. Likewise, variability in individual diaphragms' burst pressure resulted in unpredictable test pressures and variability in the resultant test conditions.

2.3.4 Experimental Results

Experimentally measured ignition delay times are presented in Figure 2.3 with tabulated data available in Appendix B. It should be noted that in this figure, five test points in which there was no detectable ignition have been omitted. While these conditions do not appear as test points on the graph they are nevertheless important in establishing ignition limits and have been noted in Table 2.1.

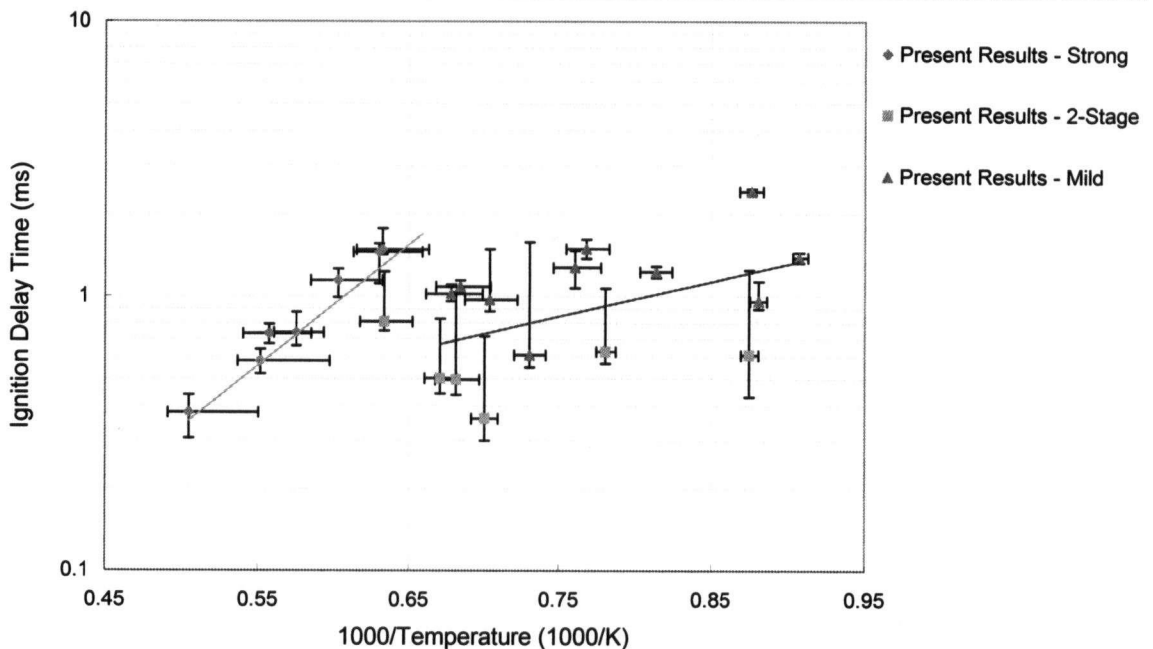
Table 2.1: Experimental Test Matrix (Homogeneous Autoignition Study)

		Temperature (K)												
		900	1100	1200	1300	1400	1500	1600	1700	1800	1900	2000	2400	
Pressure (bar)	1.5	○												
	2.4		○											
	2.6		○ X											
	2.8					X								
	3						X							
	3.2		X		XX	X				○		X		
	3.4			X				X	X	X				
	3.6		X		X			X	X	X				
	3.8						XX	X						
	4					X			X					
	4.2		X	○			X							
	6 - 8										X		X	

*Note: Each X represents a successful test; an O indicates an unsuccessful test (no ignition detected).

Figure 2.3 illustrates two key trends:

- Ignition delay times for temperatures greater than 1550 K ($1000/T < 0.65$) exhibit a much steeper slope than those over the lower temperature range; and
- The point at which the slope sharply changes ($1000/T = 0.65$) corresponds with the strong ignition limit, such that higher temperatures exhibited detonation, and below it deflagration was the primary combustion mode.

**Figure 2.3:** Experimentally Measured Homogenous Autoignition Delay Times

Additionally, a discontinuity exists near the strong ignition limit where ignition delay times seem to exhibit a sudden decrease as temperature decreases. This is partly attributed to differences in test pressures between individual data points, and primarily to differences in initial fuel and oxidant concentrations. In order to achieve the relatively high temperatures in the strong ignition region, high argon mole fractions were used (> 90%), resulting in low initial fuel and oxidant concentrations. Since ignition delay is dependent on temperature, pressure, and initial fuel and oxidant concentrations, reduced initial concentrations yielded increased ignition delay times. To compensate for this diluting effect, experimental data was fit to an empirical correlation of the form:

$$\tau = A \cdot [\text{CH}_4]^a \cdot [\text{O}_2]^b \cdot e^{E/RT} \quad (2.1)$$

and normalized ignition delay times plotted against temperature in Figure 2.4.

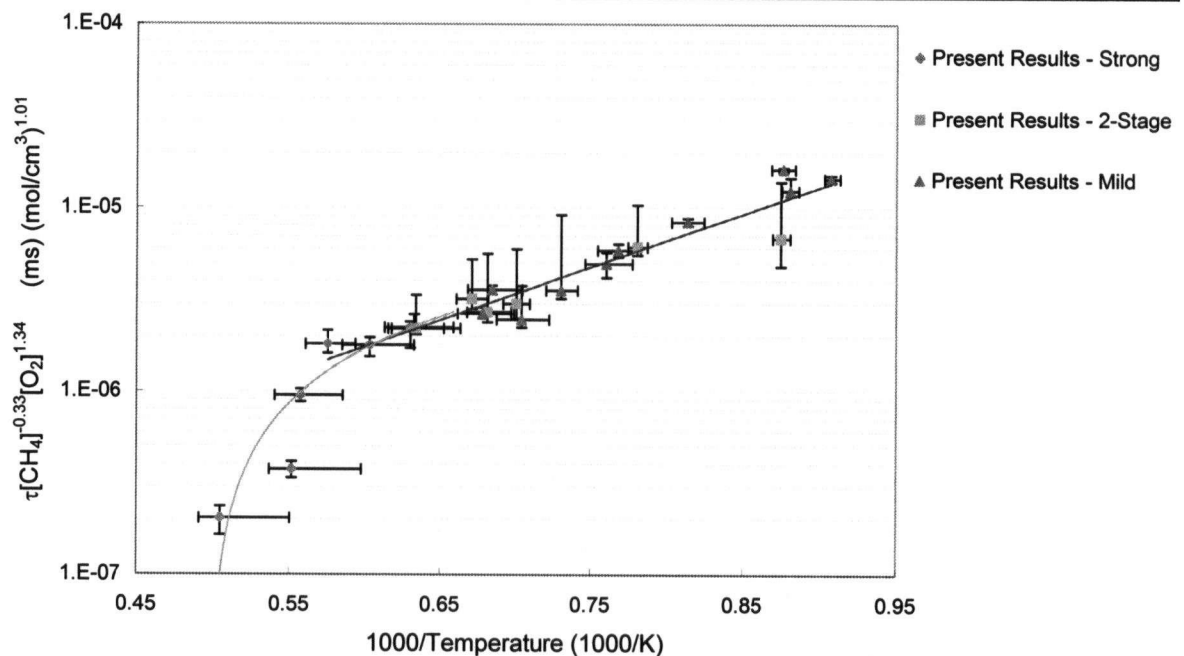


Figure 2.4: Normalized Homogeneous Autoignition Delay Times

**Note:* The methane exponent of 0.33 is very similar to the value found by previous researchers (Table 2.2).

Figure 2.4 demonstrates the importance of normalizing autoignition delay time data by the initial fuel and oxidant concentrations to account for pressure or concentration differences between individual test points. By normalizing the experimental data in this manner, the discontinuity observed in Figure 2.3 was completely eliminated. It is also worth noting that the change in slope originally noted in Figure 2.3 remains after normalization, suggesting that it is a genuine phenomenon and not simply due to pressure/concentration differences

between test points. In particular, the slope change was sufficiently pronounced that over the high-temperature region the best fit was obtained by a linear, rather than exponential, regression while a standard exponential curve fit described the low-temperature data well. Although no obvious physical reason for a linear relationship exists, perhaps at elevated temperatures ignition is more strongly dependent on fuel and oxidant concentrations. If this is true then the temperature terms implicit in the fuel and oxidant concentrations ($[X] = P_x/RT$) which are raised to the power of $a + b$ ($-1.34 + 0.33 = -1.01 \sim -1$) would explain the linear relationship. Alternatively, given the large experimental uncertainties at high temperatures, an exponential relationship may be equally plausible.

Given different ignition behaviour observed over different temperature ranges, the current experimental results are compared with previous researchers' correlations over each of three ignition regimes: strong ignition, observed mostly at high temperatures; two-stage ignition, occurring at intermediate temperatures; and mild ignition, commonly seen at low temperatures (refer to Figure 2.5).

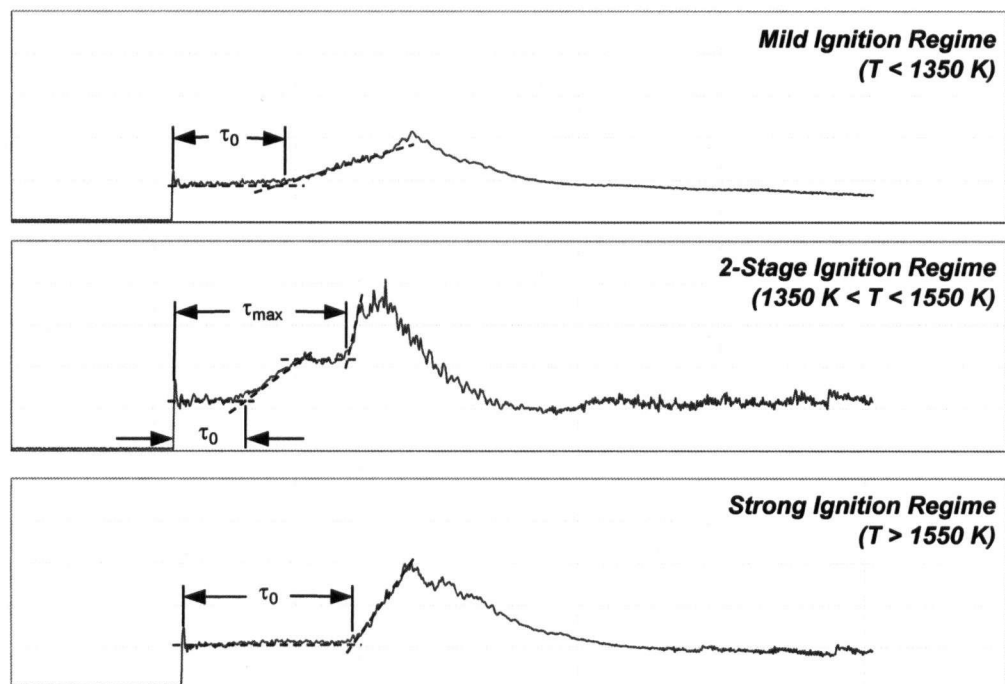


Figure 2.5: Characteristic Pressure Signals Over Three Ignition Regimes

High Temperature/Strong Ignition Regime

When the present experimental results are plotted alongside previous researchers' correlations noticeable discrepancies are observed (see Figure 2.6). In the high

temperature range ($T > 1550$ K, $1000/T < 0.65$) the slope is approximately equal to that of previous correlations (within experimental error), but an offset is present in absolute values. The present results consistently exhibit longer ignition delay times than those calculated from existing correlations. This large discrepancy is attributed mostly to experimental error (as indicated by large error bars over this temperature range), but also to variations in the definition of ignition delay time and the methods used to measure those ignition delay times. Ignition in the present investigation was defined as the time interval between reflection of the incident shock from the driven section endplate and observance of maximum curvature in the pressure signal from the driven section endplate transducer. While this is a common means of defining ignition in shock tube studies, variants on it including detecting maximum curvature from a transducer located some distance from the shock tube endplate³, or defining ignition as the time when sudden changes in temperature, CH₄ concentration, or maximum OH radical emissions are observed have also been previously used by other researchers⁴.

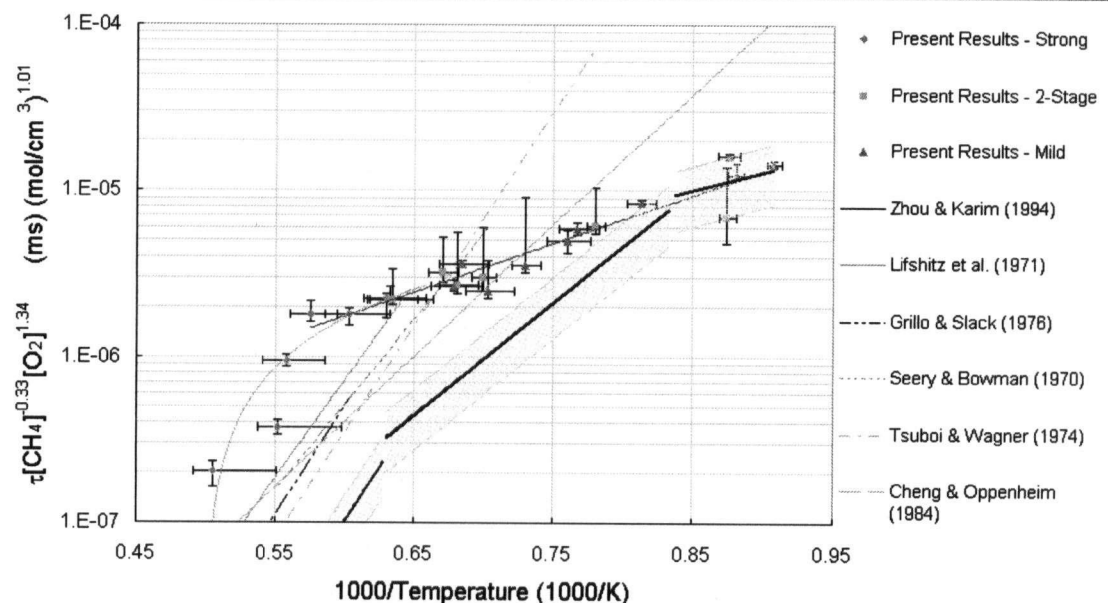


Figure 2.6: Comparison of Present Experimental Results to Previous Correlations

In addition, various researchers also define experimental temperature and pressure differently. In the present study, the pressure and temperature behind the reflected shock wave were defined as the experimental conditions, but others have previously also used a linear average between conditions behind the reflected shock wave and those immediately before ignition to define the experimental conditions³. Variability

in the definition of the ignition delay time and experimental conditions is responsible for some of the observed offsets between various researchers' results.

Among all previous induction time correlations, the results of Zhou and Karim⁴ were the only ones to predict the presence of a slope change experimentally observed in the present results. Zhou and Karim found that detailed numerical simulations using full chemistry suggested a variable activation energy and instead of assigning global values to the parameters A and E in equation (2.1) assigned different values to each parameter over three temperature ranges (650-1200 K, 1200-1600 K, 1600-2400 K). The variable parameters in Zhou and Karim's correlation correctly predicted both the presence and location of the experimentally observed slope change.

Also worth noting is that Zhou and Karim used a variant of the standard correlation equation (2.1), by expressing the concentration terms as mole fractions and adding a second term to explicitly account for temperature and pressure:

$$\tau = A \cdot \left(\frac{T}{P}\right)^c \cdot y_{CH_4}^a \cdot y_{O_2}^b \cdot e^{E/RT} \quad (2.2)$$

where y_{CH_4} and y_{O_2} are the methane and oxygen mole fractions, respectively.

Their choice of parameters specifically weighted the methane mole fraction and the pressure terms more heavily than previous researchers' correlations, while reducing the weighting on temperature (see Table 2.2). This increased dependence on fuel concentration reflects the trend observed in the present study at high temperatures.

Table 2.2: Autoignition Delay Time Correlations Comparison

$$\tau = A \cdot \left(\frac{T}{P}\right)^c \cdot [CH_4]^a \cdot [O_2]^b \cdot e^{E/RT}$$

T (K)	A	a	b	c	E (J/mol)	Researcher(s)
1500-2150	3.62×10^{-14}	0.33	-1.03	-	195000	Lifshitz et al. (1971) ⁵
1640-2150	4.40×10^{-15}	0.33	-1.03	-	219000	Grillo and Slack (1976) ⁶
1350-1900	7.65×10^{-18}	0.40	-1.60	-	215000	Seery and Bowman (1970) ³
1200-2100	2.50×10^{-15}	0.32	-1.02	-	222000	Tsuboi and Wagner (1974) ⁷
800-2400	1.19×10^{-12}	0.48	-1.94	-	194268	Cheng and Oppenheim (1984) ⁸
650-1200	1.929×10^{-6}	0.8	-1.0	0.2	74989	
1200-1600	5.055×10^{-7}	0.8	-1.0	0.2	88124	Zhou and Karim (1994) ⁴
1600-2400	2.337×10^{-9}	0.8	-1.0	0.2	155345	

*Note: In Zhou and Karim's correlation, the concentration terms are replaced with mole fractions.

However, despite some agreement between Zhou and Karim's correlation and the present results, the magnitudes of their correlation's predicted ignition delay times are much shorter than both the present results and all previous correlations. It is unclear whether this is due to incorrectly reported correlation parameters or if their correlation was based on erroneous simulations and thus only capable of predicting trends (variable activation energy) but not absolute autoignition delays. Additionally, Zhou and Karim's correlation was optimized for an initial pressure of 1 bar and they claim that extending their results to a pressure of 3 bar results in errors of $\pm 35\%$ ⁴. Since most experiments in the present study were conducted at pressures between 3-4 bar, errors in excess of 35% are expected. This uncertainty in Zhou and Karim's correlation is illustrated by shaded regions in Figure 2.6, highlighting regions $\pm 40\%$ around their predicted ignition delay times. Despite this adjustment, their correlation still fails to predict measured ignition delay times at high temperatures.

Intermediate Temperature/Two-Stage Ignition Regime

Over the intermediate temperature range (between approximately 1350-1550 K) the effects of differences in the definition and detection of ignition manifest themselves. Within this temperature range, two-stage ignition was common (see Figure 2.5), and the extent to which the current results agreed with particular correlations depended on the ignition definition used. If the initial mild pressure rise was used to define the onset of ignition, experimental autoignition delay times were in close agreement with induction times predicted by Cheng and Oppenheim⁸, but under-predicted values of most other correlations. If the second (detonation) pressure rise was used to signal ignition, the present results agreed well with both Seery and Bowman's³ and Tsuboi and Wagner's⁷ results (the two that extended into this temperature range). Defining ignition based on the second, strong (detonation) ignition signal is believed to agree more closely with some previous researcher's results because they may have used rapid changes in CH₄ concentration or maximum OH radical emissions⁴ to signal the onset of ignition. Such concentration-based criteria would be expected to coincide with strong ignition, rather than mild, since that is the point when most of the mixture is burning and thus the closer agreement when the second pressure rise is used to define ignition. This highlights the importance of utilizing a consistent ignition delay time definition when attempting to compare experimental or numerical results with previous researcher's work.

Low Temperature/Mild Ignition Regime

Over the low temperature range, few correlations exist from previous experimental studies that predicted either the slope or absolute values of measured ignition delay times. Cheng and Oppenheim's⁸ correlation agreed reasonably well with the current results to a temperature of approximately 1250 K and Zhou and Karim's⁴ correlation agreed well with the current results at low temperatures, but Tsuboi and Wagner's⁷ correlation predicted much longer ignition delay times. In general it was observed that at high temperatures the presently measured autoignition delay times exceeded those reported by previous researchers, while at low temperatures the opposite was true. This is partially attributed to the fact that ignition detection from pressure traces is often difficult when ignition is mild (as it is at low temperatures) and this may bias results towards shorter ignition delay times. Over the low temperature range ignition was not detected in several cases, indicating ignition delay times exceeding the total experimental time. Had ignition been detected in each of these cases it would have resulted in several test points with long ignition delays and these would have shifted the present results closer to existing correlations. Instead, since only short ignition delay times were detectable, the data was biased. This bias at low temperatures is one of the main causes for observed discrepancies between the present results and previous researchers' correlations. In the absence of alternative ignition detection methods, it is impossible to decisively state that pressure signals yielded misleading results at low temperatures, but this is believed to be one of the primary causes of the observed discrepancies.

2.3.5 Error Analysis

When analysing experimental results, many errors influenced the experimental data in the present investigation, which must be understood. These errors were introduced mainly by experimental errors in the following measured quantities:

- Ignition delay time;
- Incident shock velocity;
- Driven gas pressure;
- Barometric pressure; and
- Ambient temperature.

The influence of errors in each of these measurements on final calculated experimental

variables of interest is discussed below, with a more thorough error analysis available in Appendix C.

Ignition Delay Time Error

The inherent error in the ignition delay times calculated from the measured pressure signals varied depending on the type of ignition that was observed. Throughout the present investigation, ignition was categorized into three regimes: strong ignition at high temperatures; two-stage ignition at intermediate temperatures; and mild ignition at low temperatures. Characteristic pressure traces from each ignition regime were presented in Figure 2.5 along with illustrations of how ignition delays were defined.

It is important to note that minimal error was associated with strong ignition because the point of ignition was clearly defined, but certain mild ignitions and all two-stage ignitions introduced noticeable ignition delay time errors due to the often-ambiguous nature of their pressure signals. For two-stage ignition, it was often unclear whether the first or second pressure rise should be defined as the point of ignition, while for mild ignition cases the pressure rise was often so gradual that the point of maximum curvature was difficult to discern. Average error over the strong ignition regime was ± 0.135 ms, over the two-stage region was ± 0.241 ms, and in the mild ignition regime was ± 0.135 ms. However, the average error throughout the low-temperature regime is rather misleading because in some cases the pressure rise was very well defined and in other cases ambiguous. When the pressure signal was well defined, average error was ± 0.070 ms, when ambiguous it was ± 0.210 ms.

Additional errors introduced by the dynamic pressure transducers' response time, and the data acquisition system's sampling frequency are negligible relative to those discussed above.

Driven Gas Composition Error

The driven gas composition was calculated from the partial pressure of each gas as the driven section gas mixture was prepared. Thus, errors in the vacuum pressure, barometric pressure, and ambient temperature all contributed to this error.

Errors in the vacuum pressure transducer were due to limitations imposed by the multimeter resolution (± 0.001 V and ± 0.01 V for voltages less than/greater than 4 V,

respectively) and calibration error (± 0.001 bar associated with the barometer used to calibrate the transducer). These cumulatively introduced an error of ± 0.002 bar into individual gas partial pressures, which in conjunction with ambient temperature error of ± 3 K, resulted in average errors of $\pm 0.7\%$ in the argon mole fraction, $\pm 0.8\%$ in the oxygen mole fraction, and $\pm 0.7\%$ in the methane mole fraction.

Experimental Temperature/Pressure Error

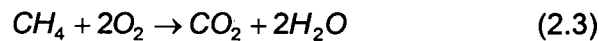
The experimental temperatures and pressures were calculated from the driven gas composition and pressure (errors discussed above) and the incident shock velocity. The incident shock velocity was determined from pressure signals as illustrated in Figure 2.2 (a). Throughout all of the present tests, the radius of convergence of the linear fit used to calculate all velocities always exceeded 0.996 (most > 0.999). The error in the incident shock velocity was therefore minimal and assumed to be ± 5 m/s (due mainly to error in the measured separation distance between dynamic pressure transducers - $\pm 0.2\%$ ¹). These cumulatively resulted in errors ranging from 5-164 K (0.5 - 8%) and ± 0.2 -0.6 bar (6 - 11%). The large experimental errors calculated at certain conditions were due to the accumulated errors of the many measurements that were used to calculate experimental conditions. In particular, the largest errors (164 K) occurred at the highest temperatures because the high argon mole fractions necessary to achieve such high temperatures resulted in greater uncertainty in the measured initial fuel and oxidant concentrations. Errors in the initial fuel and oxidant concentrations were carried forward into experimental temperature uncertainty.

2.4 Numerical Investigation

Since the preceding experimental study compared measured autoignition delay times with both previous experimental and numerical results, numerical simulations must also be conducted to gain insight into uncertainties associated with such calculations. This includes exploring various methods for defining the ignition delay time numerically, and fitting a single-step global reaction mechanism to the current experimental results. While many reduced mechanisms are available that reasonably approximate full chemistry results, these are usually incapable of autoignition as a consequence of the presence of radical species in each reaction step. Thus, the development of a global mechanism is intended to provide insight into errors introduced by various ignition definitions, and to provide a baseline for future mechanism development work.

2.4.1 Reduced Mechanism

To minimize the computational burden of implementing any reduced mechanism, ideally the simplest mechanism (fewest reactions and/or species) is desired. However, it is also anticipated that increased agreement with full chemistry results and experimental data will require increased mechanism complexity. For this reason, a single-step global mechanism was chosen as it represents the simplest possible mechanism and will provide a baseline for any future mechanism development work. The mechanism investigated consists of the global reaction mechanism with only one reaction and four species, presented below:



2.4.2 Governing Equations

Ignition of the combustible gas mixture behind the reflected shock wave was modelled as a homogenous, constant volume, adiabatic process. These assumptions reduced all the conservation equations to the trivial case where each is constant. Previous studies have found that despite this model's apparent simplicity, it approximates the complex chemical and thermal interactions in the shock tube reasonably well^{2,9,10}. The system's temperature, pressure, and species concentrations may then be derived from the reduced form of the energy equation and the ideal gas law to yield the following system of coupled first-order ordinary differential equations (complete derivation available in Appendix D):

$$\frac{dT}{dt} = \frac{\frac{1}{\rho} \cdot \left(\sum_K 1000 \cdot \frac{d[X_k]}{dt} \cdot W_k \cdot h_k - R \cdot T \cdot \sum_K 1000 \cdot \frac{d[X_k]}{dt} \right)}{\left(\frac{P}{\rho \cdot T} - \sum_K Y_k \cdot C_{P_k} \right)} \quad (2.4)$$

$$\frac{dP}{dt} = R \cdot T \cdot \sum_K 1000 \cdot \frac{d[X_k]}{dt} + \frac{P}{T} \cdot \frac{dT}{dt} \quad (2.5)$$

$$\frac{d[X_k]}{dt} = \dot{\omega}_k = \sum_i (v_k^P - v_k^R)_i \cdot \left(k_f \cdot \prod_j [X_j]^{v_j^R} - k_b \cdot \prod_j [X_j]^{v_j^P} \right)_i \quad (2.6)$$

In the above equations, P is the system pressure (kPa), T is the temperature (K), ρ is the mixture density (kg/m^3), and R is the universal gas constant (J/mol/K). Additionally $[X_k]$, W_k , Y_k , C_{P_k} , and h_k are the concentration (mol/cm^3), molecular mass (g/mol), mass fraction,

constant pressure specific heat capacity (J/g/K), and specific enthalpy (J/g), respectively, of the k^{th} species. The factors of 1000 in both the temperature and pressure expressions are included for dimensional homogeneity between the various terms in those equations. Finally, in the species concentration equation, stoichiometric coefficients for the forward and reverse reactions are denoted by ν^R and ν^P , and the forward reaction rate coefficient, k_f , for each reaction, i , is expressed in the following Arrhenius form:

$$k_{f_i} = A_i \cdot T^{n_i} \cdot e^{-E_i/RT} \quad (2.7)$$

where A_i is the frequency factor, n_i the pre-exponential temperature exponent, and E_i the activation energy of the i^{th} reaction. The reverse reaction rate coefficient, k_b , is calculated from the forward reaction rate coefficient and the equilibrium constant.

The equations developed above were simultaneously solved using a MATLAB program developed for this purpose while species properties were calculated from JANAF tables.

2.4.3 Ignition Delay Criteria Definition

Critical to the use of any numerical simulation for predicting autoignition delay times is the establishment of criteria to define ignition. Since the combustible mixture begins reacting immediately, albeit very slowly initially, and accelerates as the mixture temperature and pressure increase as a result of the combustion reaction's exothermic nature, the ignition delay is physically the time when the global reaction rate exceeds some threshold value. The problem of defining ignition therefore involves determining an appropriate threshold reaction rate to use as an ignition indicator. However, global reaction rates are not readily measurable experimentally and thus researchers have employed numerous techniques for deducing this threshold reaction rate, and thus the onset of ignition, using other readily measurable or calculable quantities.

Zhou and Karim⁴ summarized some of the various ignition criteria that have been used in both experimental and numerical studies and these are reproduced in Table 2.3. Although many ignition criteria exist, most can be broadly categorized as either "threshold" criteria, in which ignition is signalled by the temperature, pressure, or concentration of a particular species exceeding (or falling below) a prescribed threshold value, or "gradient" criteria, in which ignition is signalled by the rate of change of the pressure, temperature, or a species concentration reaching a maximum. Based on these broad classifications, the suitability

of two ignition criteria was investigated; one threshold criterion, and one gradient criterion.

Table 2.3: Numerical Ignition Criteria Comparison

Ignition Definition	Threshold	Gradient
1. Sudden increase in mixture temperature		X
2. Rate of temperature rise reaching its maximum value		X
3. Sudden increase in pressure		X
4. Changes in the density of the mixture		X
5. Sudden change in the energy release rate		X
6. Consumption of a specified fraction of the fuel	X	
7. Onset of a rapid decrease in the CH ₄ concentration		X
8. Onset of a rapid decrease in the O ₂ concentration		X
9. Emission of either CO ₂ or H ₂ O	X	
10. Emission of CO	X	
11. Sudden changes in the distribution of some products		X
12. Concentration of the species O reaching a maximum	X	
13. Emission rate of the species OH reaching a maximum		X
14. Emission of the OH radical	X	
15. Maximum slope change on the absorption profiles of CH ₃		X
16. Appearance of various chemi-luminescent emissions	X	

Concentration-Based (Threshold) Criterion

Concentration-based ignition criteria, namely defining ignition as the time when the concentration of a particular reactant species falls below a certain level, or a product species exceeds a given threshold, is numerically easily implemented, but presents several limitations. In particular, it cannot be easily implemented experimentally and secondly, selecting the threshold value to use as the ignition indicator is arbitrary. A common threshold is to use the time when 5% of the initial fuel has been consumed to define ignition but this qualitatively corresponds to different points on the pressure time history curves for different initial conditions. Several representative pressure histories are plotted in Figure 2.7 to graphically illustrate how such a threshold does not qualitatively correspond to the point of maximum curvature at all temperatures.

Since in shock tube experiments the autoignition delay is most commonly defined by changes in pressure, ideally a numerical ignition indicator should correlate well with the experimental ignition definition. Unfortunately, as shown in Figure 2.7, this is not the case for the simple concentration-based criterion. At low temperatures, the time when 8.4% of the initial fuel is consumed correlates well with the autoignition delay times defined by the point of maximum curvature in the pressure history, but at high

temperatures a larger fraction of the initial fuel concentration is consumed before maximum curvature is observed. For a 5% consumed fuel threshold, the situation is even worse, with predicted ignition delay times corresponding to only 87% of those predicted by maximum curvature in the pressure signal at 1000 K and only 44% at 2000 K. Such qualitative disagreement between a threshold criterion and common experimental ignition definitions based on pressure traces suggests that threshold criteria are only appropriate if ease of implementation outweighs their limitations.

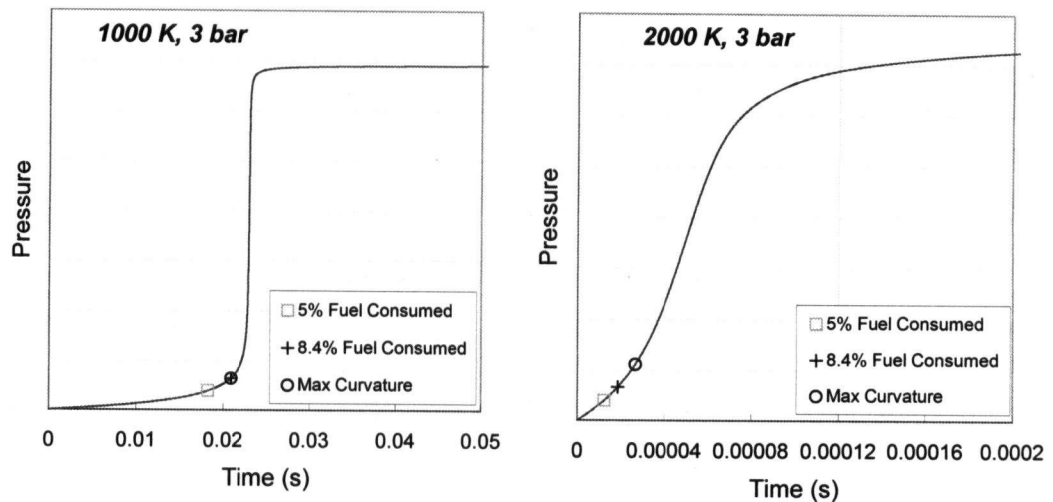


Figure 2.7: Comparison of Threshold and Gradient Ignition Criteria

Pressure-Based (Gradient) Criterion

A second ignition indicator is based directly on the combustible mixture's pressure, defining ignition as the point of maximum curvature in the pressure time history. However, unlike the simplicity of the concentration-based (threshold) criterion, this criterion poses several problems in locating the point of maximum curvature.

Direct calculation of the pressure time history curvature, d^2P/dt^2 , from the numerical pressure and time data using a numerical differencing scheme proved problematic because the resultant curvature is not a smooth function of time. As a result of unevenly distributed time steps and rounding errors in the pressure history solution, the computed curvature frequently exploded to a large number or became negative (see Figure 2.8). Several data smoothing techniques were attempted, including fitting an exponential curve to the pressure data or using a high-order differencing scheme, but regardless, direct computation of the curvature remained difficult.

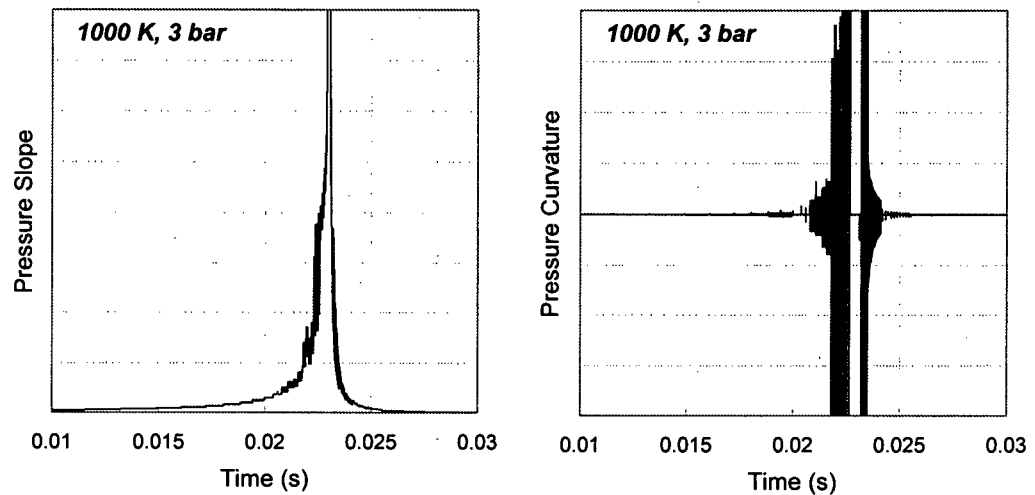


Figure 2.8: Representative Pressure Time History Slope and Curvature Plots

As an alternative to the above criterion, a second technique, defining ignition as the intersection point of a pair of lines drawn tangent to the initial and maximum slope points was explored. Since both the maximum and initial pressure slopes are easily determined, this technique was also easily implemented. However, while it provided an extremely robust method of determining the autoignition delay time, qualitatively it agreed reasonably well with the maximum curvature point at high temperatures but over-predicted the point of maximum curvature at low temperatures. Defining ignition as the point on the pressure time history nearest the intersection of these two tangent lines improved agreement (see Figure 2.9).

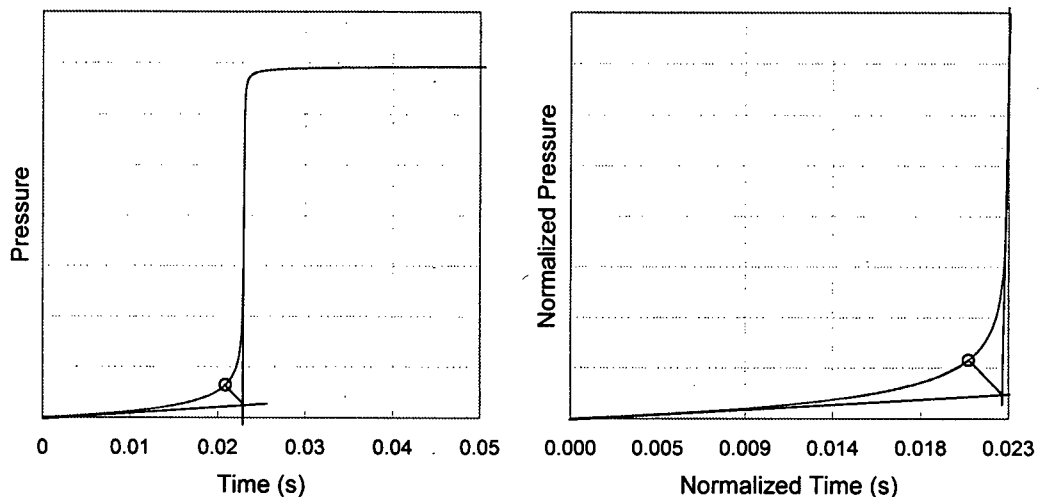


Figure 2.9: Modified Gradient Ignition Definition

Implementing such an ignition definition required determining the intersection of the two tangent lines and then trigonometrically calculating the point on the pressure time history nearest the intersection point. However, as a result of a large difference in scales between the pressure (in kPa) on the ordinate and the time (in ms) on the abscissa, normalization was required before such a calculation could be performed. While many normalization schemes are plausible, it seemed most appropriate to normalize both time and pressure by the time and pressure difference, respectively, between the maximum and initial slope tangent points. This normalization causes the resultant ignition point on the pressure history to correspond with the qualitative maximum curvature point. Although the normalization scheme chosen may seem like a trivial point, it is important because normalizing by different values has the effect of unequally stretching each axis such that the computed ignition point on the pressure trace no longer qualitatively corresponds to the maximum curvature.

2.4.4 Parameter Tuning Procedure

With ignition formally defined, Adaptive Simulated Annealing (ASA) was used to tune the Arrhenius equation parameters to fit experimental ignition delay times. Ingber's ASA code¹¹ was used in conjunction with a MATLAB interface written by Sakata¹². Details of the simulated annealing algorithm used in the present investigation are available from each of these references along with an extensive list of references to various publications discussing simulated annealing methods in general. ASA was used in conjunction with a Nelder-Mead simplex algorithm (commonly referred to as an amoeba algorithm) after use of ASA proved extremely computationally expensive, and exclusive use of the Nelder-Mead algorithm failed to converge on a global minimum. Therefore, ASA was used for finding the vicinity of the global minimum, and the simplex algorithm converged to the final solution.

2.4.5 Numerical Results

Using the procedure described above, the single-step reaction mechanism's Arrhenius equation parameters were fit to the present experimental data, with the following resulting forward reaction rate expression:

$$k_{1-step} = 1.3 \times 10^{10} \cdot T^{2.33} \cdot e^{-129000/RT} \quad (2.8)$$

Results of the numerical simulations using the above simplified reaction mechanism with both a concentration-based definition of ignition (threshold criterion) and a pressure-based ignition criterion (gradient criterion) are presented in Figure 2.10 below.

This figure illustrates that the threshold criterion agrees well with experimental data and the gradient criterion at low temperatures but under-predicts ignition delay times at higher temperatures (as previously illustrated in Figure 2.7). Qualitatively, this difference results in the pressure-based ignition definition yielding a shallower slope and longer delay times than the concentration-based criteria at high temperatures, and subsequently converging at low temperatures. This distinction is important because it further highlights the effect of various ignition definitions. Throughout the experimental portion of this investigation, the differences between various researchers results were often attributed to variations in the ignition definition used by each, and this numerical result reaffirms this. Despite using an identical single-step reaction mechanism, differences in the method used to define ignition had a pronounced effect on the resultant autoignition times.

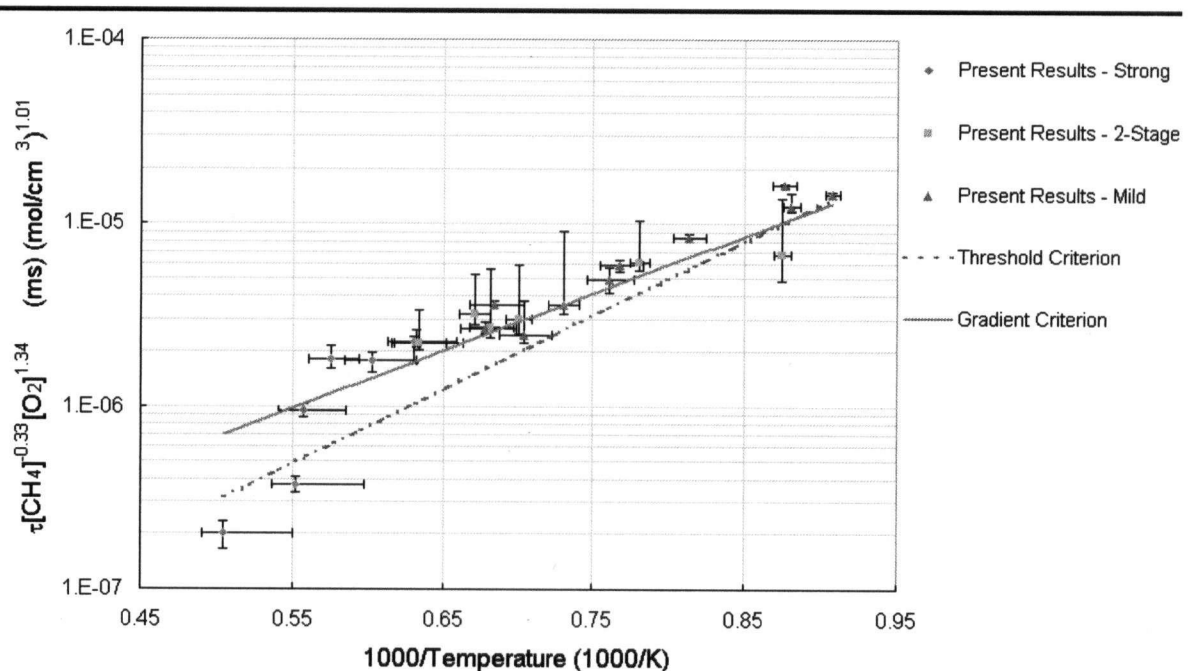


Figure 2.10: Comparison of Present Experimental and Numerical Results

Unfortunately since the Arrhenius equation parameters in the simplified global reaction mechanism were optimized based on the present experimental data, which as discussed previously may have been biased towards short ignition delay times at low temperatures, the optimized activation energy was lower than that reported by other researchers. Table

2.4 lists the activation energy reported by several researchers including those previously presented in Table 2.2.

This table illustrates how the current activation energy was 19-42% lower than that of all previous correlations except Zhou and Karim's results. Although, the accuracy of Zhou and Karim's simulation is uncertain, it is encouraging to see that the present single-step reaction mechanism predicted an activation energy that is approximately equal to the average of their full chemistry results. The disagreement with other correlations is largely attributed to difficulties encountered in the experimental portion of this investigation, which may have biased the data used to optimize the single-step reaction mechanism.

Table 2.4: Activation Energy Comparison

T (K)	P (bar)	E (J/mol)	Researcher
-	-	159000	Vandenabeele et al. (1960) ¹³
1350 - 1900	1.5 - 4	215000	Seery and Bowman (1970) ³
1500 - 2150	2 - 10	195000	Lifshitz et al. (1971) ⁵
1200 - 2100	2 - 300	222000	Tsuboi and Wagner (1974) ⁷
-	-	188000	Cooke and Williams (1975) ¹⁴
1200 - 1800	3 - 20	195000	Dorko et al. (1975) ¹⁵
1640 - 2150	1 - 6	219000	Grillo and Slack (1976) ⁶
800 - 2400	1 - 3	194268	Cheng and Oppenheim (1984) ⁸
650-2400	1	75000 - 155000	Zhou and Karim (1994) ⁴
1100 - 2000	2.6 - 4.2	129000	Present Results (2002)

Figure 2.11 further compares the present numerical simulations with previous correlations and full-chemistry results of Zhou and Karim. These results were obtained using a single-step mechanism to calculate ignition delay times of stoichiometric CH₄/O₂/Ar mixtures at a pressure of 3.5 bar using both the threshold (5% fuel consumed) and gradient (maximum curvature in pressure history) criteria. These conditions were chosen because they correspond with those investigated experimentally and thus Figure 2.11 is the "numerical" equivalent of the "experimental" Figure 2.6. This graph illustrates reasonable agreement between both the threshold and gradient criteria and previous correlations at intermediate temperatures, but divergence at both high and low temperatures. Additionally, over the entire temperature range shown, the slope of the single-step reaction mechanism is much shallower than the slope of all other correlations. These phenomena (the shorter ignition delays at low temperature, longer ignition delays at high temperatures, and the shallower slope) all reflect the trends observed in the experimental portion of the investigation. Thus

the numerical simulation may be used to calculate ignition delay times over a broad range of temperatures, but additional experimental data would be required to further optimize the global mechanism's Arrhenius equation parameters if improved agreement with existing correlations is desired.

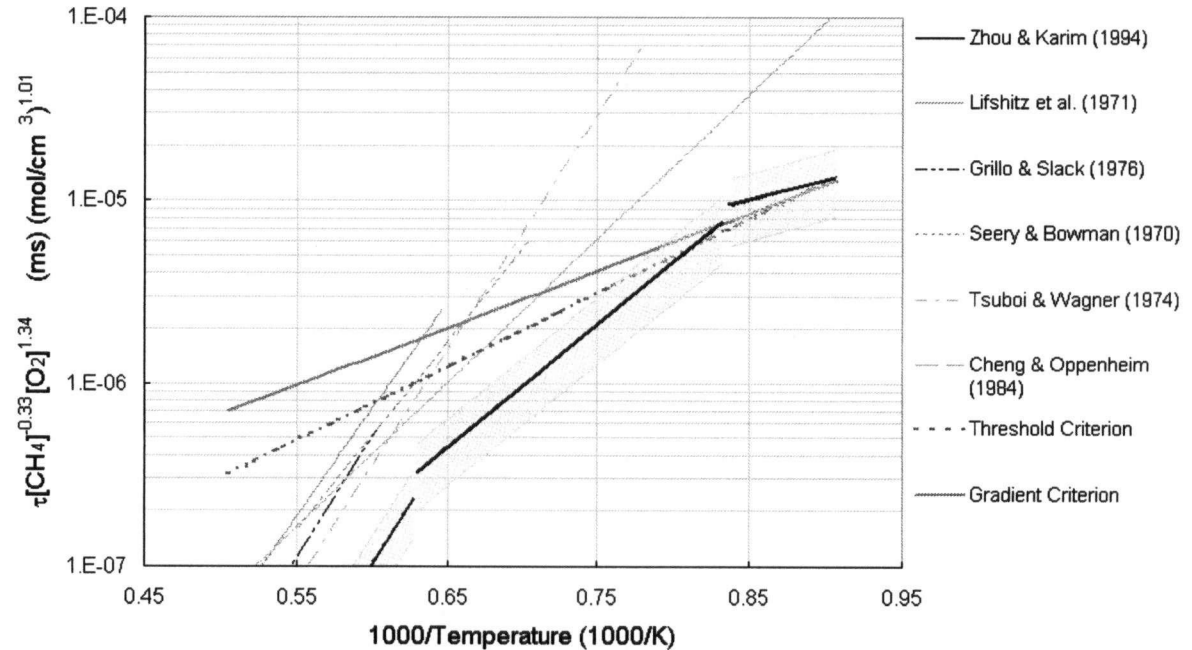


Figure 2.11: Comparison of Present Numerical Results to Previous Correlations

2.5 Conclusions and Recommendations

The present experimental and numerical investigation of the autoignition behaviour of various stoichiometric $\text{CH}_4/\text{O}_2/\text{Ar}$ mixtures illustrated several important trends in autoignition data, while also emphasizing the many sources of uncertainty in such measurements. These observations are summarized below:

1. Experimentally measured autoignition delay times agreed with previous researchers' correlations over small temperature ranges but over-predicted ignition delay times at high temperatures and under-predicted them at low temperatures. These differences were attributed to experimental error, inability to detect mild ignitions using pressure traces alone, and differences in the definition of ignition. Since such differences in the definition of experimental conditions, the definition of ignition delay, and the method of detecting ignition may all result in different induction time correlations, care must be taken when using such correlations.

2. A discontinuity in measured ignition delay times was initially observed but attributed to differences in initial fuel and oxidant concentrations. This emphasized the importance of normalizing experimental results by initial fuel/oxidant concentrations as a failure to do so could misleadingly suggest the presence of trends that are not genuinely there.
3. The activation energy change experimentally observed at approximately 1550 K (and confirmed by Zhou and Karim's simulations) is not reflected in standard induction time correlations, but clearly should be since failure to recognize the change in activation energy can result in severe over-prediction of ignition delay times at low temperatures.
4. Numerical simulations qualitatively illustrated the effects of various ignition criteria on the resultant ignition delay times but were unable to duplicate previous researchers' work since the Arrhenius parameters in the simulation were based on experimental results that were not in agreement with previous results at low temperatures.
5. The importance of a consistent ignition definition illustrated by both the experimental and numerical portions of this investigation suggests that multiple ignition detection methods should be used simultaneously when conducting autoignition delay studies. Differences in the ability of various techniques to detect ignition over given operating ranges may distort the measured results and subsequently adversely influence any numerical simulations based on those results.

Characterization of a Gaseous Fuel Injection System

3

3.1 Introduction

Increasing environmental and political pressures on both the automotive and power generation industries are encouraging the exploration of alternative fuels, moving towards decarbonisation. Along these lines, natural gas and eventually hydrogen are being rigorously explored as future fuel replacements for conventional gasoline- and diesel-powered engines. However, among the many challenges presented by the transition to such fuels includes the need to characterize and precisely control the injection and ignition of gaseous fuels to optimize engine performance and minimize emissions. In this study a J41 gaseous fuel injector provided by Westport Innovations Inc. is characterized for such operation, with particular emphasis on the requirements of non-premixed autoignition delay studies. This requires validation of the injector hardware to ensure it is capable of performing adequately under intended operating conditions and characterizing the jet produced. Hardware characterization includes verifying the injection system can respond sufficiently rapidly to issued control signals and perform multiple injections in rapid succession, along with measuring mass flow rates under various operating conditions. Jet characterization involves observing the jet plume issued from the injector under the aforementioned operating conditions and studying the influences of impingement and of an enclosure on the transient jet's development.

3.2 Background

Numerous previous experimental and numerical studies have been conducted on axisymmetric jets leading to a thorough understanding of the development and behaviour of such jets under a variety of operating conditions. Such studies have included elementary measurements of mass entrainment in axisymmetric jets like the well-known work of Ricou and Spalding¹⁶, to studies of velocity and species profiles in jets such as those of Abdel-Rahman et al.¹⁷, Malmström et al.¹⁸, and many others. However, of most direct relevance to the current investigation is the work of Hill and Ouellette¹⁹ who reviewed a variety of previous jet studies, especially those pertaining to

transient gaseous jets, deduced scaling laws from existing results, and summarized the present understanding of the development of transient turbulent gaseous jets. Their recent work made extensive use of a transient jet model proposed by Turner²⁰ and Abramovich and Solan²¹, which models a transient jet as a spherical vortex fed by a self-similar steady-state jet. This particular model has been used successfully in various applications from atmospheric flows to gaseous fuel jets. Additionally, Hill and Ouellette's scaling laws and Turner's jet model have been used jointly by subsequent researchers such as Boyan and Furuyama²², who used their results to successfully predict the behaviour of a natural gas jet.

In addition to the extensive research conducted on the fundamental study of axisymmetric jets, several researchers have also studied the interactions between multiple jet plumes (Jenkins et al.²³), pulsed injection behaviour (Murase et al.²⁴, Ishii et al.²⁵), and jet impingement onto objects of various geometries and at various orientations (Donaldson and Snedeker²⁶, Donaldson et al.²⁷, Looney and Walsh²⁸, Krothapalli et al.²⁹, etc.). However, these studies aimed at addressing a specific application such as studying the early development of injection pulses, or mass, heat, and momentum transferred by impinging jets. Therefore, although they provide insight into the behaviour of gaseous jets, they are not directly applicable to the present problem. In addition, almost all studies (except for those studying the initial development of a pulsed jet) utilized fully developed steady-state jets rather than transient jets. Little work has been performed to study the development of transient gaseous jets other than the works cited by Hill and Ouellette in their investigation.

In addition to the stated differences between previously studied jets and the transient gaseous jets of interest in the present application, even the well understood behaviour of axisymmetric jets requires basic knowledge of the particular injector's characteristics before any correlations may be successfully applied. Hence, before any of the results of previous researcher's work can be applied to predict or manipulate the behaviour of the given jet, that jet's properties, and specifically the injector's characteristics must be quantified. Thus the aim of this investigation is to quantify the flow characteristics unique to the J41 fuel injector such that existing correlations and scaling laws may be used in future to accurately model the injector's behaviour.

3.3 Injector Hardware Characterization

The J41 injector is a magneto-restrictive, mono-fuel injector used to facilitate natural gas injection into spark-ignited engines for light duty vehicles. This injector operates in conjunction

with Westport's WCut software, which is used to specify the fuel injection duration and delay, an injector control module, which generates the required square wave at the appropriate times and duration based on parameters specified by the control software, and a driver that amplifies the controller's signal to produce the large current required to actuate the fuel injector (see Figure 3.1). These components are shown below:

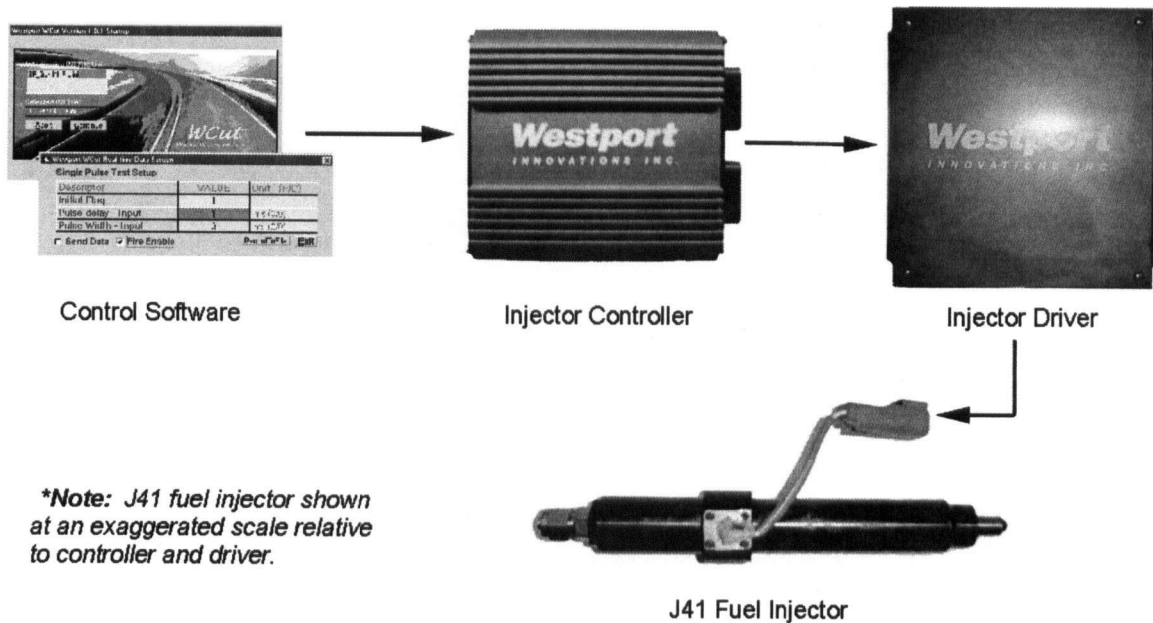


Figure 3.1: J41 Injector with Control System

Given the complexity of this injection system, there are inherent delays in the system requiring measurement to ensure accurate injection timing. Additionally, since the system was designed to perform only a single injection, modifications were made to facilitate pulsed injection and the system's response to such unconventional operation also requires validation.

3.3.1 Experimental Apparatus

To quantify the intrinsic properties of the fuel injection system hardware a J41 injector was mounted to inject into a small test chamber created by two 2.5 in ANSI B16.5 blind flanges bolted together (as illustrated in Figure 3.2) and repeatedly fired under various operating conditions while recording the injector control signal and the test chamber pressure. Both the control signal and test chamber pressure were recorded using a Wavebook/512™ data acquisition system at a 140 kHz sampling frequency (corresponding to a 7.1 μs sampling

interval). The control signal was sampled directly from the signal line between the injector controller and driver using a voltage divider circuit to reduce the 0-20 V signal to a 0-10 V signal suitable for connection to the data acquisition system. Test chamber pressure was monitored with two PCB Piezotronics 112B11 dynamic pressure transducers. These had been previously calibrated¹ and have a manufacturer-stated response time of 3 μs , which is sufficiently rapid to be negligible relative to the injection time scales of interest.

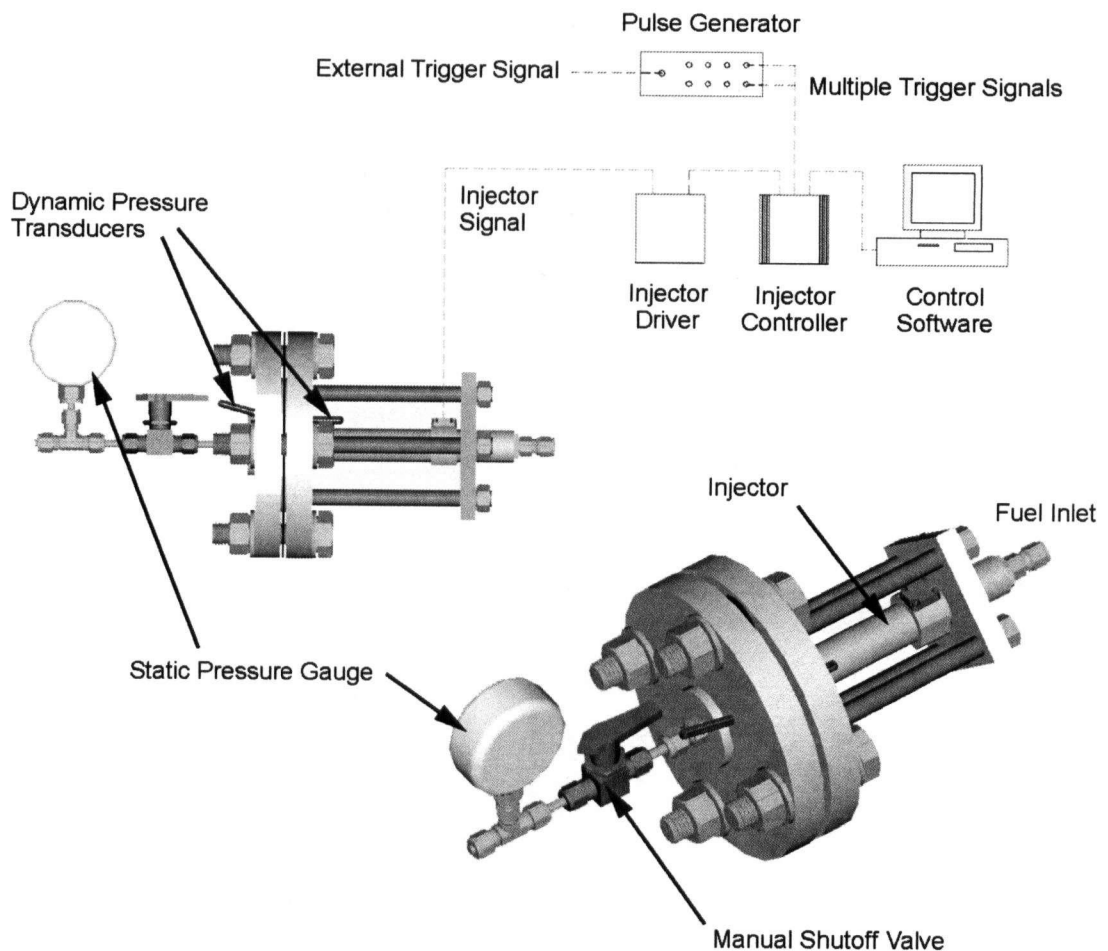


Figure 3.2: Experimental Apparatus (Injection Hardware Characterization Study)

Initial test chamber pressure (backpressure) was recorded using a Matheson bourdon c-tube pressure gauge mounted as shown in Figure 3.2 with a manual shutoff valve placed between the test chamber and the pressure gauge to facilitate separating the two during each experiment, minimizing the test chamber volume. Additionally, to further reduce the total internal test chamber volume, the 0.25 in steel tube connecting the test chamber and manual shutoff valve was filled with small-diameter electrical wires, leaving only capillary

passages for transmitting pressure. Minimizing the test chamber volume in this manner not only minimized the system's response time, but also caused a sufficient test chamber pressure rise during each experiment to allow the backpressure for the subsequent test to be controlled by either not draining at all or only partially draining the test chamber gases between experiments.

The injector control system was a slightly modified version (to facilitate pulsed injection) of a standard J41 control system provided by Westport Innovations Inc. This system was modified to enable pulsed injection through insertion of an 8-channel BNC programmable pulse generator upstream of the injector controller (refer to Figure 3.2 inset). The injector controller and driver remained intact, and Westport's WCut software was used to control injection durations. The only difference between the present and standard control system configuration was that rather than triggering the injector controller directly with an external trigger signal, the pulse generator was used to issue multiple successive trigger signals to the controller. This allowed the fuel injector to operate in either a continuous or pulsed injection mode, with the injection duration controlled by Westport's WCut software and the delay between successive injections independently controlled by the programmable pulse generator.

3.3.2 Injection Delay Measurement

The injection delay, defined as the interval between the time a control signal is issued to the injector driver and when injection begins, is an extremely important parameter in both non-premixed autoignition delay experiments, and in engine operation. In ignition delay experiments the injection delay is used in identifying the start of injection, from which the ignition delay itself is defined, while in engine operation the injection delay is important in ensuring optimal fuel injection timing. Unfortunately, since direct detection of the start of injection is not possible, the voltage or current sent to the injector is monitored instead to record the time when a control signal is issued to the injector, with the understanding that there may be a slight delay before injection actually begins. In the present configuration, the control signals between the injector controller and driver were most easily monitored owing to their low voltage, which facilitated direct connection to a data acquisition system. Therefore, the delay time between this directly measurable signal and the start of injection (attributable to any lag in the injector driver circuitry and any mechanical delay associated with the injector itself) was quantified.

Procedure

The injection delay was easily measured using the above-described apparatus by repeatedly injecting methane into the test chamber while recording both the injector control signal and test chamber pressure. The injection delay time was then defined as the time interval between the rising edge of the control signal and observance of an initial rise in the test chamber pressure (see Figure 3.3).

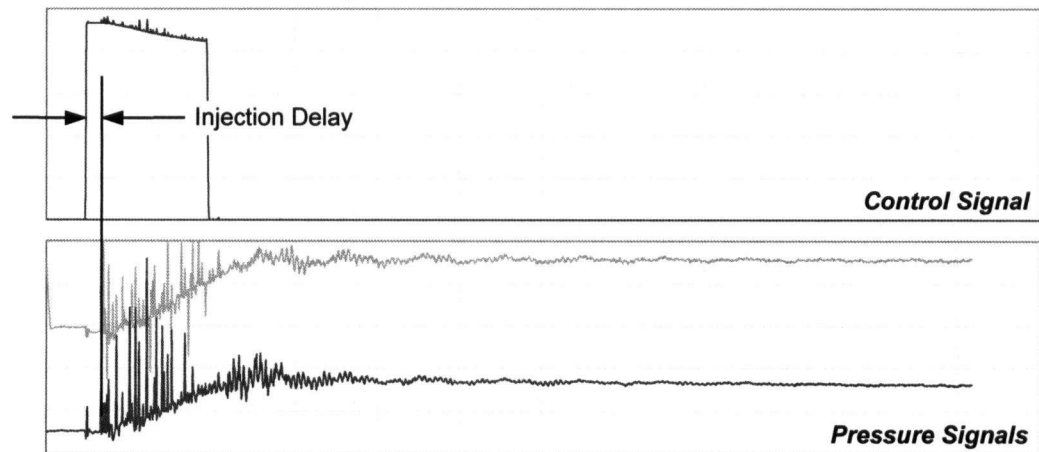


Figure 3.3: Injection Delay Definition

Using the above procedure, an injection delay was measured for a range of injection durations and pressure ratios (by varying the initial chamber pressure) to determine the injection delay's dependence on each parameter. The operating conditions that were investigated are summarized in Table 3.1 with data available in Appendix E.

Table 3.1: Experimental Test Matrix (Injection Delay Study)

Injection Duration:	1.5-3.5 ms
Injection Pressure:	110 bar (1600 psi)
Backpressure:	0-48 bar (0-700 psi)
Pressure Ratio:	2.3-111

**Note: All indicated pressures are gauge pressures.*

Experimental Results

In total 96 experiments were conducted yielding 192 measured injection delay data points (one from each dynamic pressure transducer). The average injection delay was calculated to be 180 μs with a standard deviation of 20 μs . A histogram of all experimental measurements is presented in Figure 3.4, illustrating that most delay times fell between 150 and 200 μs , exhibiting a positive skew. For comparison, both

normal and lognormal distributions have been superimposed upon this histogram. Each distribution fits the data reasonably well, with the lognormal fitting marginally better than the normal distribution upon examination of each probability plot (Figure 3.5). Although it may appear as though neither distribution accurately captures the spike at 200 μs in the present data, it must be taken into consideration that 19 data points exhibited a delay of exactly 200 μs , and thus the unusually low frequency at 190 μs and high frequency at 200 μs may have been exaggerated by the number of points which fell exactly on the boundary between those two bins.

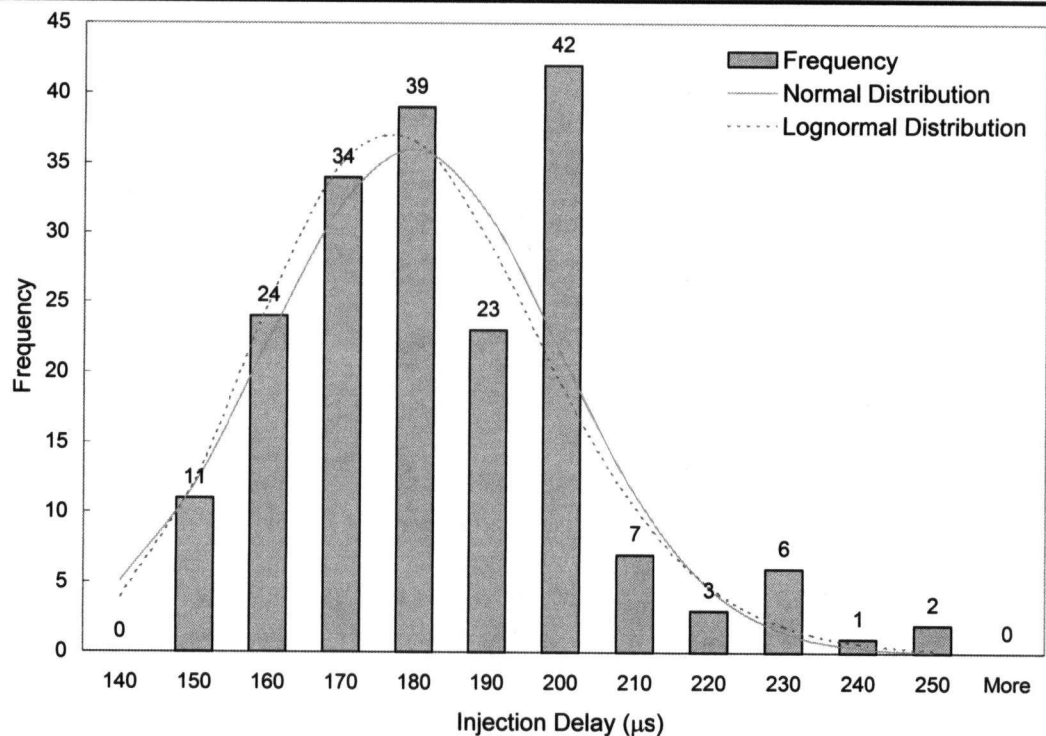


Figure 3.4: Histogram of Measured Injection Delay Times

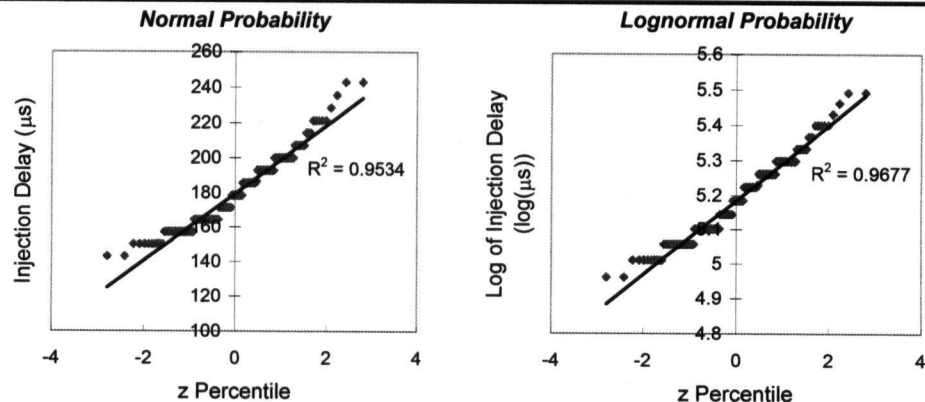


Figure 3.5: Probability Plots of Measured Injection Delay Times

Finally, Figure 3.6 presents measured injection delay times sorted by backpressure (the numbers indicate the number of samples collected at each pressure; error bars represent one standard deviation from the mean). This figure qualitatively illustrates the injection delay time's backpressure *independence*, and an analysis of variance (ANOVA) quantitatively indicates the average injection delay is independent of the backpressure to a significance level of 0.481 (Table 3.2). Such a high significance level (and the F-value of 0.935) further shows the total backpressure independence. Additionally, among all of the tests conducted at three injection durations between 1.5-3.5 ms, no obvious injection duration dependence was observed either. The injection delay of $180 \pm 20 \mu\text{s}$ is therefore independent of both injection duration and backpressure.

Table 3.2: ANOVA Results for Injection Delay Backpressure Dependence

Source of Variation	SS	df	MS	F	P-value
Between Groups:	2614.32	7	373.4737	0.9347	0.4810
Within Groups:	73520.72	184	39.5691		
Total:	76135.04	191			

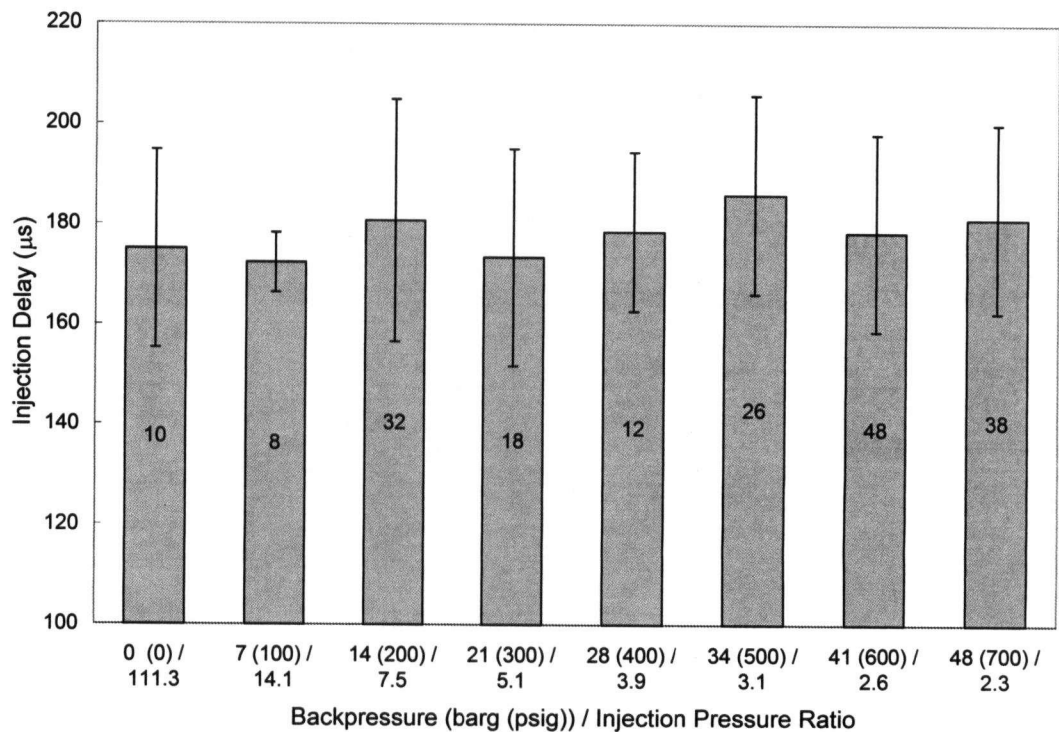


Figure 3.6: Injection Delay Time vs. Backpressure/Pressure Ratio

3.3.3 Mass Flow Rate Measurement

The mass flow rate through the injector is not easily measurable with standard mass flow devices, which are typically designed for steady-state operation, and must therefore be correlated to the injection duration and pressure. Such measurements were conducted at Westport prior to delivery of the J41 injector used in the present investigation and further validated after delivery, with results from both measurements presented below.

Procedure

Mass flow rates measured using nitrogen gas as the injected gas were supplied with the J41 injector and also validated after receiving the injector using an experimental apparatus similar to that depicted in Figure 3.2. These tests also included additional measurements using methane as the injected gas to observe the effects of using different gases on the measured mass flow rate. A range of injection pressures that were sufficiently high to yield measurable mass flow rates were investigated using several injection durations. The total mass injected was measured manometrically and converted to a mass flow rate assuming ideal gas behaviour. Test conditions investigated are summarized in Table 3.3 with data available in Appendix E.

Table 3.3: Experimental Test Matrix (Mass Flow Rate Study)

Injection Duration:	0.3-1.75 ms
Injection Pressure:	62-172 bar (1000-2500 psi)
Injection Temperature:	295 K
Injected Gas:	Nitrogen/Methane

**Note: All indicated pressures are gauge pressures.*

Experimental Results

Experimental nitrogen mass flow measurements injected at four injection pressures are plotted as mass fluxes in Figure 3.7. At each pressure the mass flux remains nearly constant regardless of injection duration indicating mass flux is independent of the injection period. While the mass fluxes for injection durations below 0.8 ms exhibit slight fluctuations, these do not exceed 10% of the average mass flux value and are mainly attributable to transient effects associated with the start and end of injection occupying a larger fraction of the total injection duration for short injections.

Measured mass fluxes with methane gas exhibited similarly constant values across a range of injection durations and are plotted in Figure 3.8. Additionally worth noting

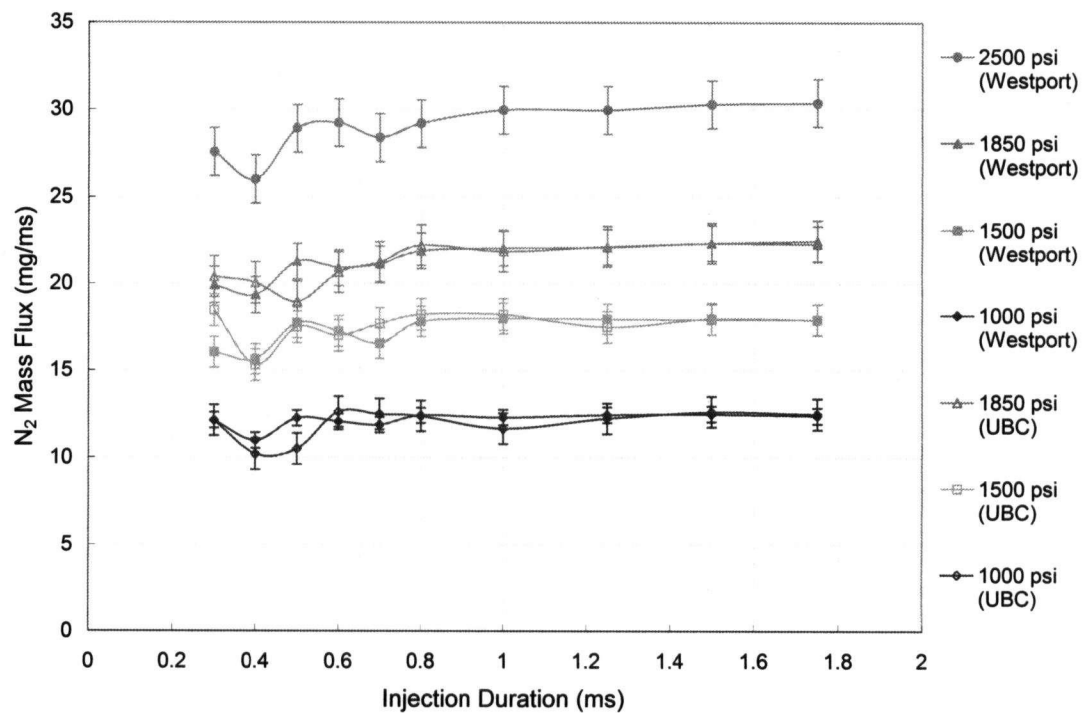


Figure 3.7: Mass Flux Measurements (Nitrogen)

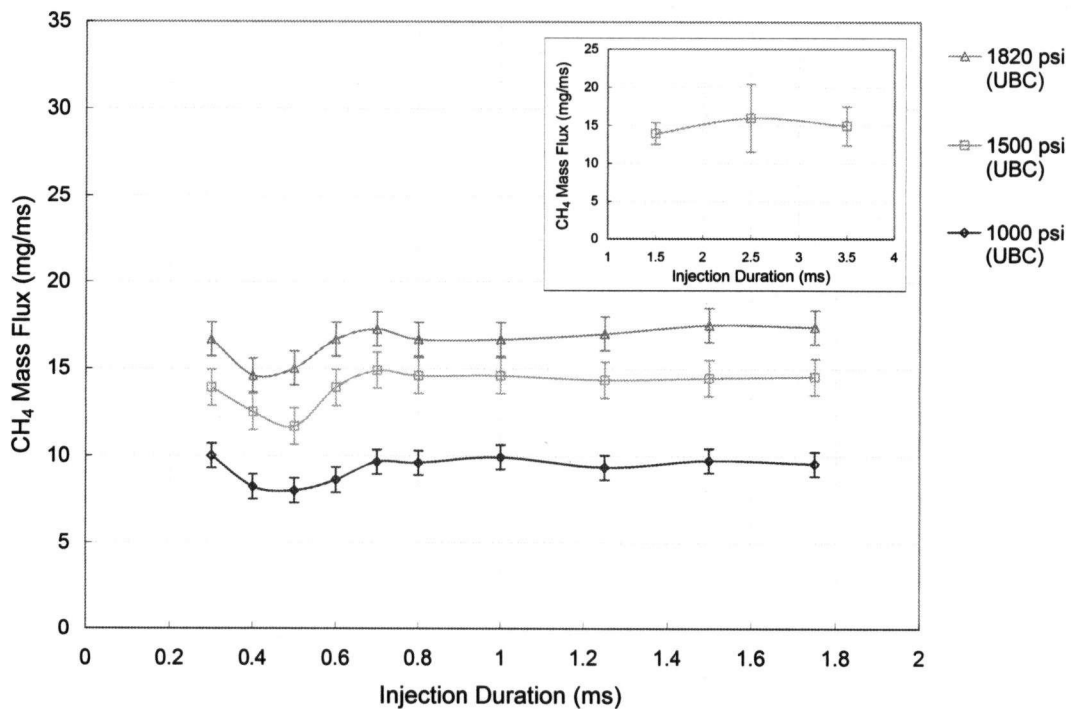


Figure 3.8: Mass Flux Measurements (Methane)

***Note:** Experimental data labelled "Westport" collected at Westport Innovations Inc., experimental data labelled "UBC" collected at the University of British Columbia by J. Huang, Research Engineer, Dept. of Mechanical Engineering (Combustion Laboratory).

is that while this data only extends to injection durations of 1.75 ms, data collected during the injection delay time study (extending from 1.5-3.5 ms injection durations) indicated that the rate of change of the test chamber pressure (which is proportional to the mass flow rate) remained constant within experimental uncertainty (Figure 3.8 inset). The measured mass flow rates may therefore be assumed constant up to an injection duration of 1.75 ms and possibly up to 3.5 ms or greater.

Numerical Results

To predict the mass flow through the injector for any conditions, a model assuming an adiabatic, isentropic expansion from the fuel reservoir (stagnation state) to the injector nozzle, where choked flow was assumed ($Ma=1$), was found to agree well with actual measured mass fluxes for both nitrogen and methane. The governing equations for calculating the mass flux (\dot{m}) from the given stagnation temperature (T_0), pressure (P_0), gas properties (γ, R), and nozzle diameter (d_n) are:

$$T_n = \frac{2}{\gamma + 1} \cdot T_0 \quad (3.1)$$

$$V_n = a_n = \sqrt{\gamma \cdot R \cdot T_n} \quad (3.2)$$

$$P_n = \left(\frac{T_n}{T_0} \right)^{\frac{\gamma}{\gamma-1}} \cdot P_0 \quad (3.3)$$

$$\rho_n = \frac{P_n}{R \cdot T_n} \quad (3.4)$$

$$\dot{m} = \rho_n \cdot V_n \cdot \left(\frac{\pi \cdot d_n^2}{4} \right) \quad (3.5)$$

where subscript 0 represents stagnation properties, n represents nozzle conditions.

Although the assumption of isentropic flow initially yielded mass fluxes that were 22-32% greater than those experimentally measured, several proposed modifications to this simple model reproduced the experimental data extremely well. These models each improved the original results by attempting to predict the losses in the injector. The assumptions made by each of four variants on the above model are described below along with the equation from the five listed above that each model replaces:

1. *Equivalent Diameter*: This model assumes adiabatic, isentropic flow, but with an equivalent diameter instead of the actual nozzle diameter to compute the mass flow rate. The equivalent diameter, d_e , models the frictional losses in the injector as having the net effect of reducing the exit area, and is tuned to experimental mass flux data. In this model the mass flow rate is calculated using the following equation:

$$\dot{m} = \rho_n \cdot V_n \cdot \left(\frac{\pi \cdot d_e^2}{4} \right) \quad (3.6)$$

2. *Discharge Coefficient*: This model assumes adiabatic, isentropic flow, just as the equivalent diameter model, but an empirical discharge coefficient, C_d , is used to reduce the mass flow rate to fit experimental data. In this model the mass flow rate is calculated using the following equation:

$$\dot{m} = C_d \cdot \rho_n \cdot V_n \cdot \left(\frac{\pi \cdot d_n^2}{4} \right) \quad (3.7)$$

3. *Pressure Loss Coefficient*: This model also assumes adiabatic, isentropic flow, but with a pressure loss to reduce the nozzle exit pressure slightly. The pressure loss is non-dimensionalized by modelling it as a loss coefficient, K_p , and is fit to experimental mass flux data. In this model the following equation is used for computing the nozzle exit pressure and must be solved iteratively due to the dependence of the nozzle density on pressure:

$$P_n = \left(\frac{T_n}{T_0} \right)^{\frac{\gamma}{\gamma-1}} \cdot P_0 - K_p \cdot \frac{1}{2} \cdot \rho_n \cdot V_n^2 \quad (3.8)$$

4. *Non-Isentropic (Polytropic) Expansion*: This models the flow in the injector as an adiabatic, but *non-isentropic* flow. Therefore, instead of using the specific heat ratio, γ , in the polytropic expansion equation, an experimentally tuned polytropic expansion coefficient, k , is used. In this model the pressure at the nozzle is calculated as follows:

$$P_n = \left(\frac{T_n}{T_0} \right)^{\frac{k}{k-1}} \cdot P_0 \quad (3.9)$$

Of the models considered, the pressure loss coefficient and discharge coefficient models reproduced experimental data best. However, each model has its distinct

advantages and may be suitable for certain applications. The equivalent diameter and discharge coefficient are advantageous for their simplicity as they only involve applying a correction factor to the final mass flow rate, which is otherwise calculated using the isentropic expansion equations. The pressure loss coefficient is favoured simply because it fits the present experimental data best, but it is the most difficult to implement since it requires an iterative calculation procedure. Finally, the polytropic expansion model is practical because unlike the equivalent diameter and discharge coefficient models, which rely purely on empirical mass flow rate corrections, this model has some physical significance. A summary of each model's coefficient that most closely reproduced experimental data is presented in Table 3.4.

Table 3.4: Mass Flux Model Parameters

	Optimal Model Parameters		
	Mean	Std. Deviation	Mass Flux Error
Equivalent Diameter, d_e (mm)	0.970	0.016	3.03 %
Discharge Coefficient, C_d	0.778	0.025	3.00 %
Pressure Loss Coefficient, K_p	0.417	0.050	2.53 %
Polytropic Coefficient, k	1.242	0.015	4.20 %

Interestingly, the tuned model parameters that most closely reproduce experimental results correspond to a stagnation pressure loss between 11-24%, which is greater than a 10% stagnation pressure loss suggested by Hill and Ouellette¹⁹ for gaseous injections. This difference is believed to be caused by the different injector used in their investigation, which exhibited a smaller internal pressure loss partially due to internal flow passage differences and partially as a result of operating at a different Reynolds number.

Modelling the flow between the fuel reservoir and the injector nozzle using each of the models described above (using the optimal parameters tabulated in Table 3.4) mass fluxes for both methane and nitrogen injected at various pressures are listed alongside their experimental measurements in Table 3.5. This illustrates the close agreement between the pressure loss coefficient model and experimental results at all injection pressures investigated for both gases. The model developed herein is therefore a valid predictive tool for estimating the mass flow rate from the present injector given only the fuel reservoir conditions.

Table 3.5: Comparison of Experimental Mass Fluxes to Model Results

		Injection Pressure (psi)			
		1000	1500	1820/1850	2500
CH ₄ Mass Flux (mg/ms)	Experimentally Measured	9.27±0.71	13.95±1.04	16.56±0.98	
	Equivalent Diameter, d_e	8.87	13.24	16.04	
	Discharge Coefficient, C_d	8.88	13.25	16.05	
	Pressure Loss Coefficient, K_p	8.95	13.36	16.17	
	Polytropic Coefficient, k	9.83	14.67	17.77	
N ₂ Mass Flux (mg/ms)	Experimentally Measured	12.03±0.69	17.42±0.88	21.27±1.09	28.99±1.37
	Equivalent Diameter, d_e	11.96	17.85	21.98	29.64
	Discharge Coefficient, C_d	11.97	17.86	21.99	29.65
	Pressure Loss Coefficient, K_p	11.91	17.77	21.88	29.51
	Polytropic Coefficient, k	11.42	17.05	20.99	28.31

**Note: All indicated pressures are gauge pressures.*

3.3.4 Pulsed Injection System Validation

While the J41 injector, controller, and driver were designed and tested for use in single injection operation, the modifications performed to enable pulsed injection were unproven. Although these control system modifications were relatively minor, consisting only of the additional programmable pulse generator inserted upstream of the controller to repeatedly trigger the injector, it remained uncertain whether the injector, driver, and controller could respond sufficiently rapidly to successive trigger signals. The purpose of the present tests was therefore to validate the system's response to pulsed injection operation.

Procedure

To validate the injector's ability to respond to multiple successive trigger signals the experimental apparatus previously described was used. The injector's response to pulsed injection operation was investigated by rapidly issuing multiple trigger signals to the injector controller while monitoring signals from both the controller and test chamber pressure. The J41 injector *controller's* response was verified by observing if multiple control signals were issued in response to each trigger, while the injector *driver* was verified to be responding to the multiple control signals by observing if distinct test chamber pressure rises were observed corresponding to each issued control signal. Additionally, in order to estimate if equal amounts of fuel were being injected during each injection pulse, the magnitude of each pressure rise was also

measured. Figure 3.9 presents typical control and pressure signals obtained in the current study illustrating how the pulse delay and pressure ratio were defined.

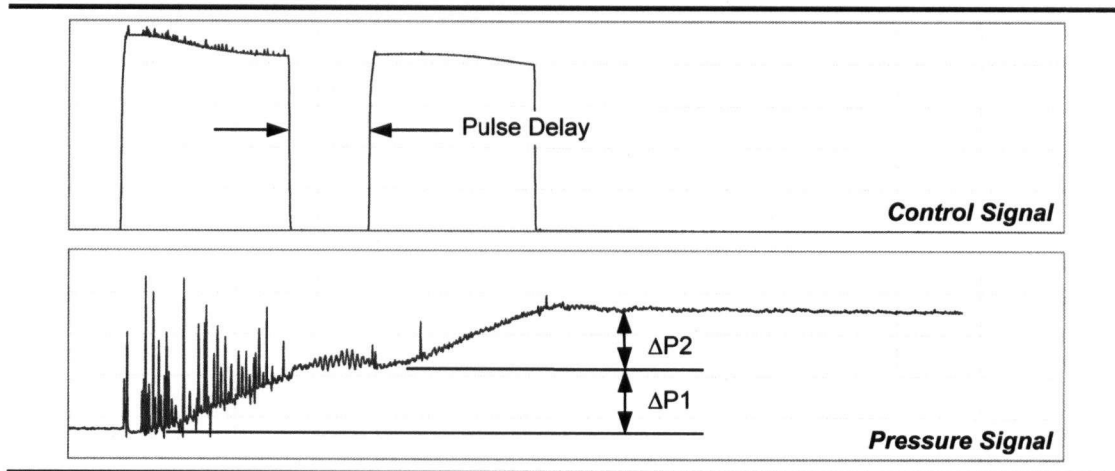


Figure 3.9: Pulse Delay and Pulse-to-Pulse Pressure Ratio Definitions

This procedure was used to validate the pulsed injection system at several realistic injection durations with variable delays between successive injections to determine the minimum delay between successive pulses that the system could respond to. In all cases two successive injections were investigated to minimize the size of the test matrix, although up to eight successive injection pulses are possible with the current configuration. These operating conditions are summarized in Table 3.6, with the experimental data available in Appendix E.

Table 3.6: Experimental Test Matrix (Pulsed Injection System Validation)

Injection Duration:	1-3 ms (each injection pulse)
Number of Injection Pulses:	2
Injection Delay (Between Pulses):	0.5-50 ms
Injection Pressure:	95 bar (1400 psi)

**Note: All indicated pressures are gauge pressures.*

Experimental Results

Figure 3.10 presents the normalized pressure ratio ($\Delta P2/\Delta P1$) plotted against pulse delay (see Figure 3.9 for definition of pulse delay, $\Delta P1$, and $\Delta P2$). It was observed that even when a very long delay separated two injection pulses, the pressure rise associated with the second injection ($\Delta P2$) was consistently smaller than the first ($\Delta P1$). This may have been caused by changing test chamber pressure or mixture composition. Since the volume of the test chamber was so small, the pressure and

density within it increased dramatically after the first injection. Therefore, while the first injection fired into a low-pressure, air-filled chamber, the second injection fired into a high-pressure methane/air mixture, resulting in a reduced mass flow and thus yielding a smaller pressure rise. To compensate for this effect, all values plotted in Figure 3.10 have been normalized by the $\Delta P_2/\Delta P_1$ ratio observed when long pulse delays separated the two injections.

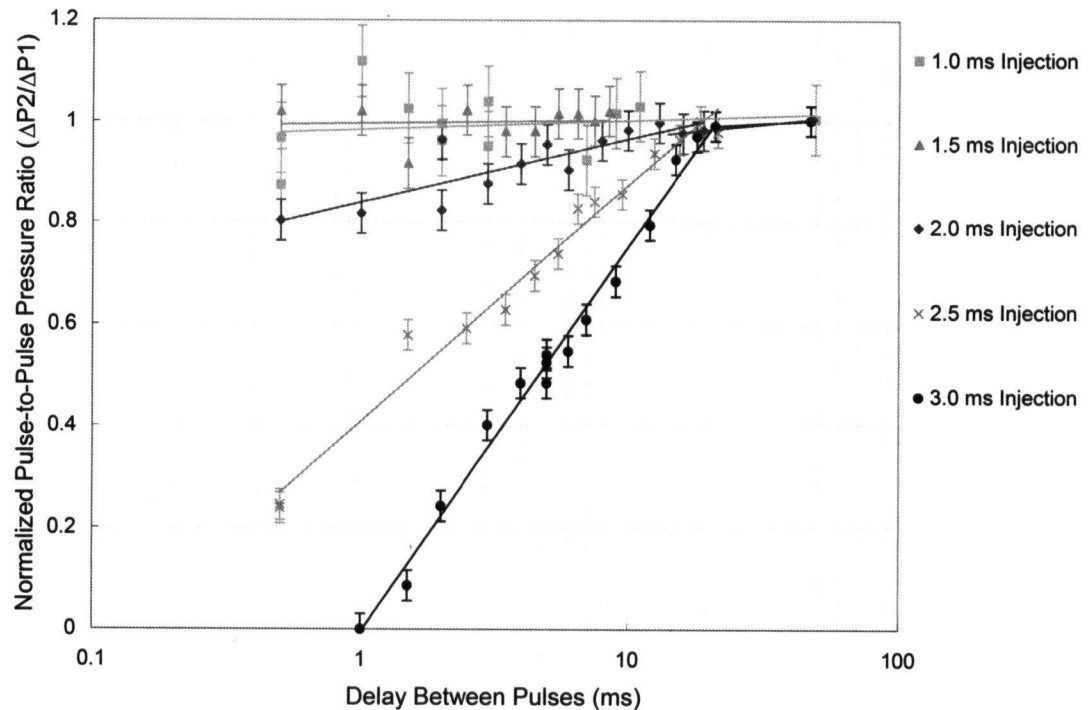


Figure 3.10: Normalized Pulse-to-Pulse Pressure Ratio vs. Pulse Delay

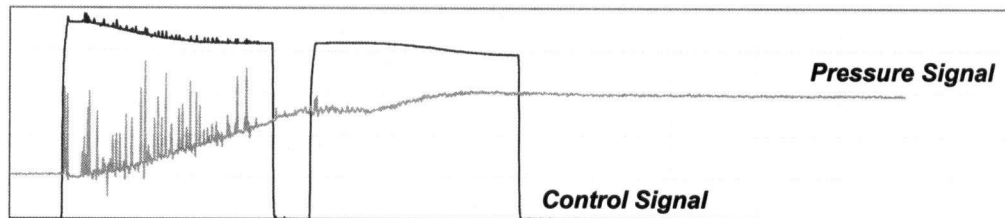
Figure 3.10 illustrates that for short injection durations (< 1.8 ms), the injector is fully capable of two successive injections even if pulses are separated by as little as 0.5 ms (this was the shortest delay tested, shorter delays may also be possible), but for long injection durations (> 1.8 ms), the pulse delay must exceed 20 ms if unequal injection pulses are to be avoided. Sample pressure traces are presented in Figure 3.11 to illustrate the effects of injection pulses with insufficient pulse delays.

The required minimum separation time between injection pulses is attributable to the injector driver's internal capacitance requiring time to accumulate a sufficient charge after each injection and is therefore unavoidable. To predict its effects in the region where the two pressure rises are not equal (i.e. pulse widths > 1.8 ms, pulse delays < 20 ms), the following empirical correlation may be used:

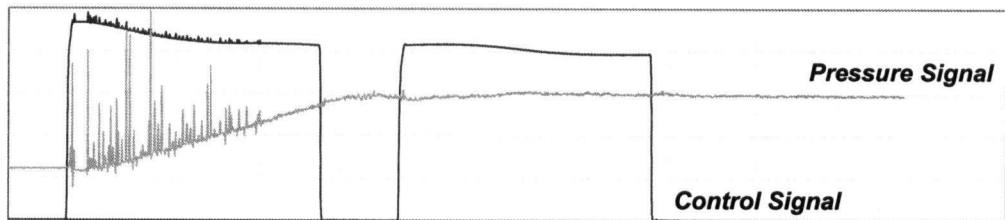
$$\frac{\Delta P_2}{\Delta P_1} = \begin{cases} A \cdot \ln\left(\frac{PD}{20}\right) + 1 & \text{if } PW > 1.8 \text{ ms and } PD < 20 \text{ ms} \\ 1 & \text{otherwise} \end{cases}$$

where PW is the pulse width (injection duration - ms), PD is the pulse delay (ms), and A is given by the following relation:

$$A = 0.2744 \cdot PW - 0.4908$$



(a) 2.5 ms Injection Duration, 0.5 ms Pulse Delay ($\Delta P_2/\Delta P_1 = 0.24$)



(b) 3.0 ms Injection Duration, 1.0 ms Pulse Delay ($\Delta P_2/\Delta P_1 = 0$)

Figure 3.11: Successive Injections with Insufficient Pulse Delays

3.4 Jet Flow Field Characterization

The jet flow field characteristics of the J41 injector were the second set of properties requiring characterization after the hardware itself had been validated. The injector's jet characteristics are of relevance to the present investigation because it is desirable to understand whether the transient jet that develops during and after injection develops similarly under different injection conditions. Additionally, in cases where multiple successive injection pulses are produced, the interactions between each injection and the net effect they have on the overall jet length scales (penetration length and jet width) must be investigated. Finally, to gain insight into how the jet may respond during in-cylinder injection the effects of impingement and of an enclosure on the resultant jet's development require investigation.

3.4.1 Experimental Apparatus

The impulsively started transient jet that develops during injection was investigated with a CCD camera-based Schlieren imaging system. This apparatus (illustrated in Figure 3.12) comprised of two 0.3048 m (12 in) diameter concave mirrors each with a 2.4384 m (8 ft) focal length aligned to produce a parallel light beam between them. A 200 W mercury arc lamp was focussed onto a 0.5 mm diameter pinhole to produce a point source of light and placed at the focal point of one of the concave mirrors, slightly off-axis to avoid interfering with any part of the parallel light beam. At the focal point of the other concave mirror, also slightly off-axis, a circular aperture filtered the focused image, yielding a Schlieren image (rather than a shadowgraph) before projecting it onto a camera.

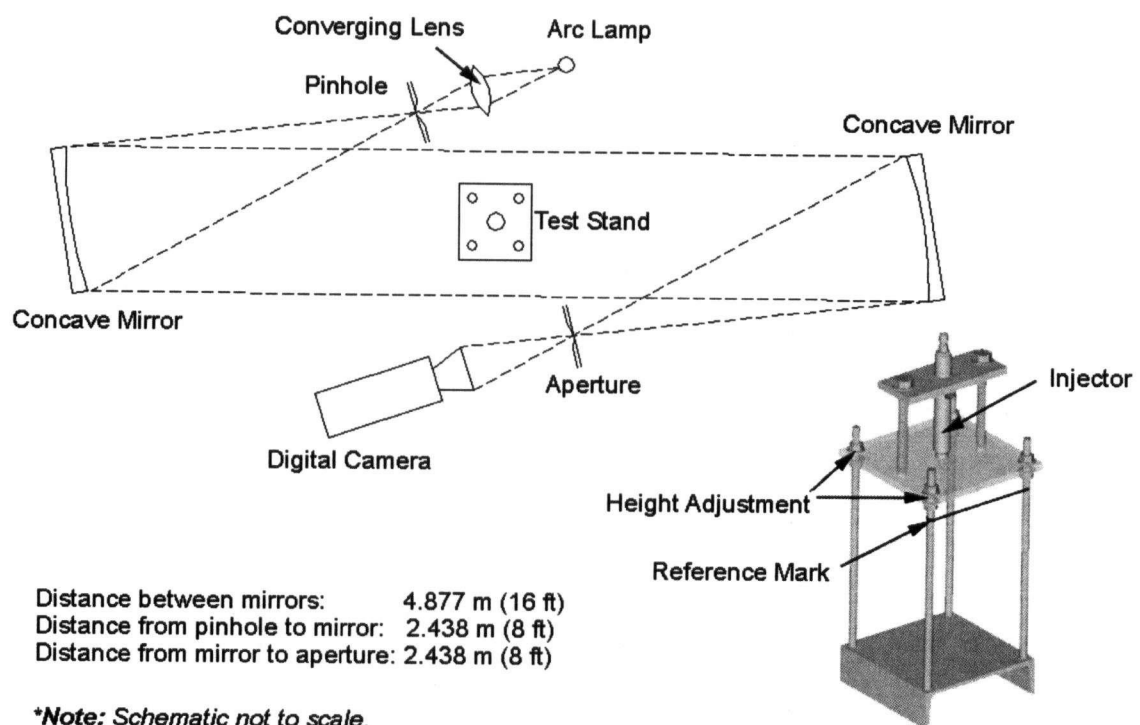


Figure 3.12: Experimental Apparatus (Jet Flow Field Characterization Study)

A circular aperture was used to filter the images, as opposed to a conventional Schlieren system using a knife edge, because the aperture allows resolving spatial density gradients in all planar directions rather than only visualizing those gradients that are perpendicular to the knife edge. Alternatively, a graded filter consisting of concentric rings would have also resolved spatial density gradients in all directions simultaneously and may have been

particularly useful if images were captured in colour. However, since the camera used in the present tests was only capable of capturing greyscale images, a graded filter was not deemed to provide any noticeable advantage over use of a circular aperture, and so the latter was used (since it was readily available).

Images were captured with a Kodak Megaplug ES 1.0 digital camera, which has a spatial resolution of 1008 (H) by 1018 (V) pixels. This camera is capable of capturing two images in a triggered double-exposure mode, with the first image exposure duration variable from 127 μs to 33 ms, while the second image has a fixed exposure of 33 ms. Unfortunately, the second image's exposure duration was too long to be of practical use in the present investigation, therefore the camera was used in the single exposure mode with exposure duration set to its shortest value; 127 μs . Although this exposure duration was sufficiently short to capture large-scale details of the flow, noticeable blurring of the small turbulent length scales was inevitable with the existing equipment.

The injector was mounted vertically (injecting downward) on a simple test stand that firmly secured the injector to a mounting plate during all experiments and provided the ability to adjust the injector's height for alignment with the focussing mirrors (see Figure 3.12 inset). This ensured that the largest possible area was visible to capture the entire jet plume and provided some flexibility in adjusting the location of the jet relative to the light source to compensate for any irregularities in the illumination level. Finally, a string was tied taught 30 mm below the face of the injector mounting plate to provide a reference scale for use during subsequent image processing.

Injector and camera timing and synchronization were accomplished by triggering both with a BNC programmable pulse generator. Two separate channels were used such that the relative delay time (the interval between the start of injection and the image capture) could be varied to capture the transient jet at various stages in its evolution. Additionally, use of the pulse generator allowed the investigation of the flow field that develops during pulsed injection operation by configuring the pulse generator to trigger the injector multiple times, as was previously done when validating the pulsed injection system.

3.4.2 Single Injection Mode

The single injection mode is the operating mode for which the J41 injector was specifically designed, in which the injector is triggered only intermittently, with delays on the order of

20 ms (corresponding to a four stroke engine operating at 6000 rpm) or greater separating injections. The jet characteristics in this operating mode are therefore of great practical interest in optimizing internal combustion engine operation. Additionally, data collected in this operating mode provides a baseline for comparison to experimental and numerical jet studies.

Procedure

Jet characteristics, namely the jet tip penetration length and maximum width, were measured from a series of images (17-35 at each operating condition, depending on the injection duration) captured using the apparatus described above. Methane was repeatedly injected at various injection pressures into atmospheric air while images were captured at 200 μ s intervals throughout the injection duration and at intervals ranging between 200 μ s and 1.2 ms once injection ceased. Throughout, the jet tip penetration length and width were measured (in pixels) from the digital images and subsequently converted to millimetres by way of the reference scale on the injector mounting apparatus (Figure 3.12 inset).

Five injection durations between 0.5-5.0 ms were explored at each of two injection pressure ratios of 3 and 5, representative of those typical in engine operation. The test conditions are summarized in Table 3.7 with data available in Appendix F.

Table 3.7: Experimental Test Matrix (Single Injection Visualization Study)

Injection Duration:	0.5-5 ms
Injection Pressure:	2-4 bar (30-60 psi)
Pressure Ratio:	3-5

**Note: All indicated pressures are gauge pressures.*

Experimental Results

Figure 3.13 below contains representative images typical of those captured at each of 10 distinct injection conditions (combination of injection duration and pressure) presently investigated. These images illustrate how the jet tip length and width were relatively easily defined from the sequence of images as a consequence of the large density gradients between the methane jet and surrounding still air.

From many series of images such as those in Figure 3.13, the length and width of the methane jet was measured at several injection conditions with results presented

in Figure 3.14 and Figure 3.15. These figures illustrate that despite collecting data over many successive injections (distinct realizations of the jet), the resultant length and width measurements are relatively smooth. This indicates that the jet produced for any given injection is very consistent and repeatable. Although fluctuations and deviations from the dominant trends are present for all injection durations these are relatively small, typically falling within 5-10% of the trend line. Width measurements (Figure 3.15) exhibit greater fluctuations than the lengths due to the high turbulence levels along the edges of the jet where vortices interact to stretch the jet in various directions, causing greater variability between jet realizations. Additionally, density gradients are not as pronounced along the edges of the jet as they are at the tip, making width measurements from Schlieren images much more difficult than length measurements.

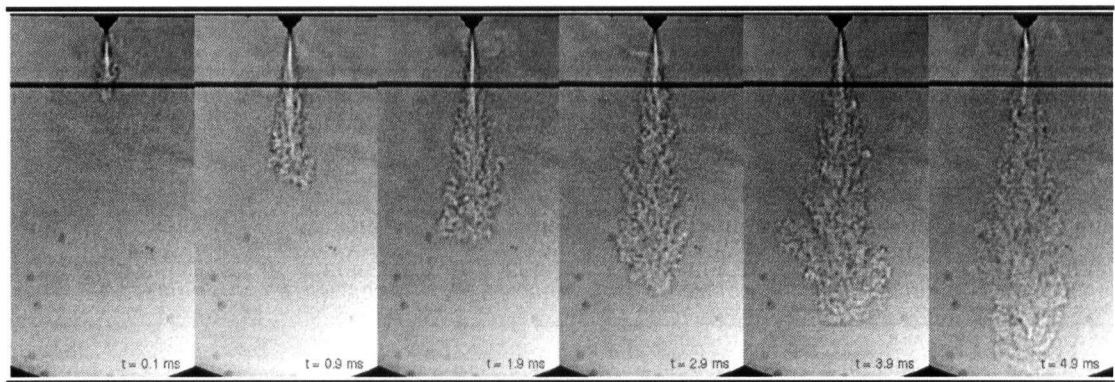
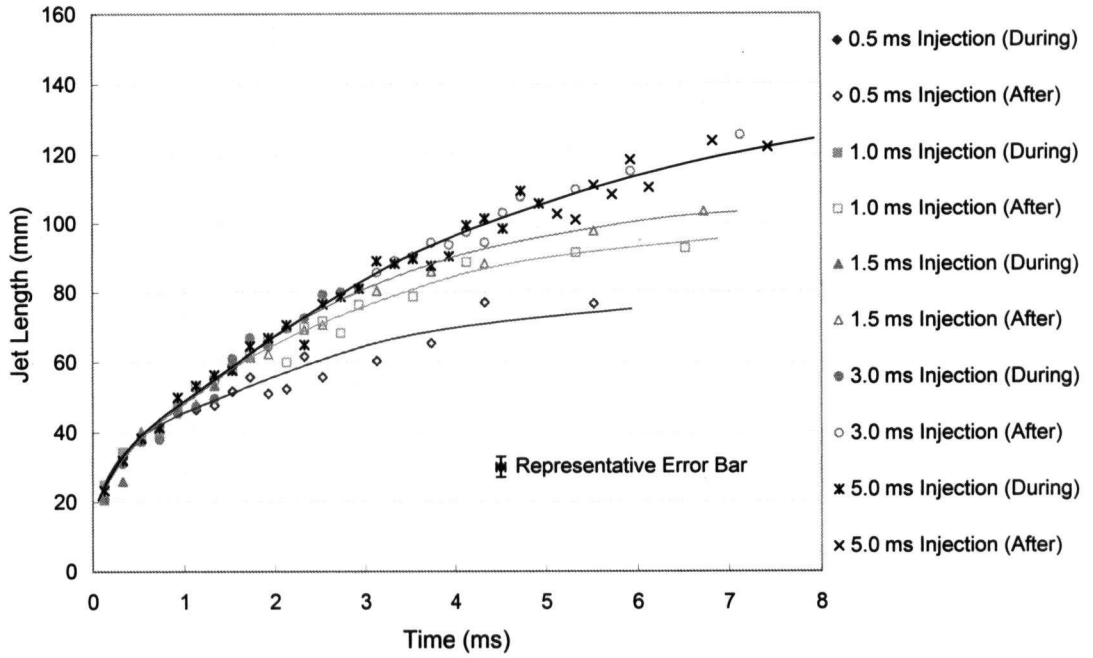
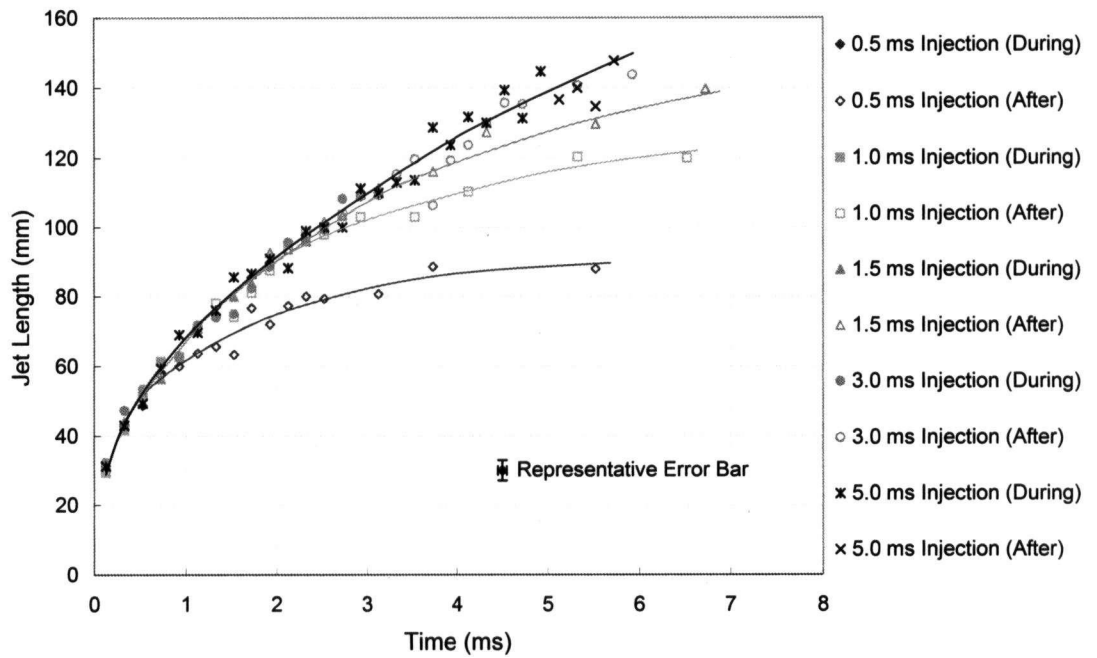


Figure 3.13: Schlieren Images of Single Jet Evolution in Time

A second noteworthy point from Figure 3.14 is the self-similarity exhibited by the jet throughout the full range of injection durations investigated. During injection, all jets regardless of their total injection duration collapse well onto a common curve. This further illustrates the consistent, repeatable nature of the jet and is not unexpected since all previous mass flow rate measurements illustrated similar injection duration independence (Figure 3.8). However, after the end of injection, the length ceases to increase as rapidly as during injection (illustrated by a deviation from the main trend line) since a lack of any further momentum injection causes the viscous drag forces on the jet to dominate, slowing the jet's penetration rate. While this effect is most pronounced in the penetration length curves, a similar effect is also observed on the jet width, but is partially masked by the larger fluctuations inherently present in those measurements.

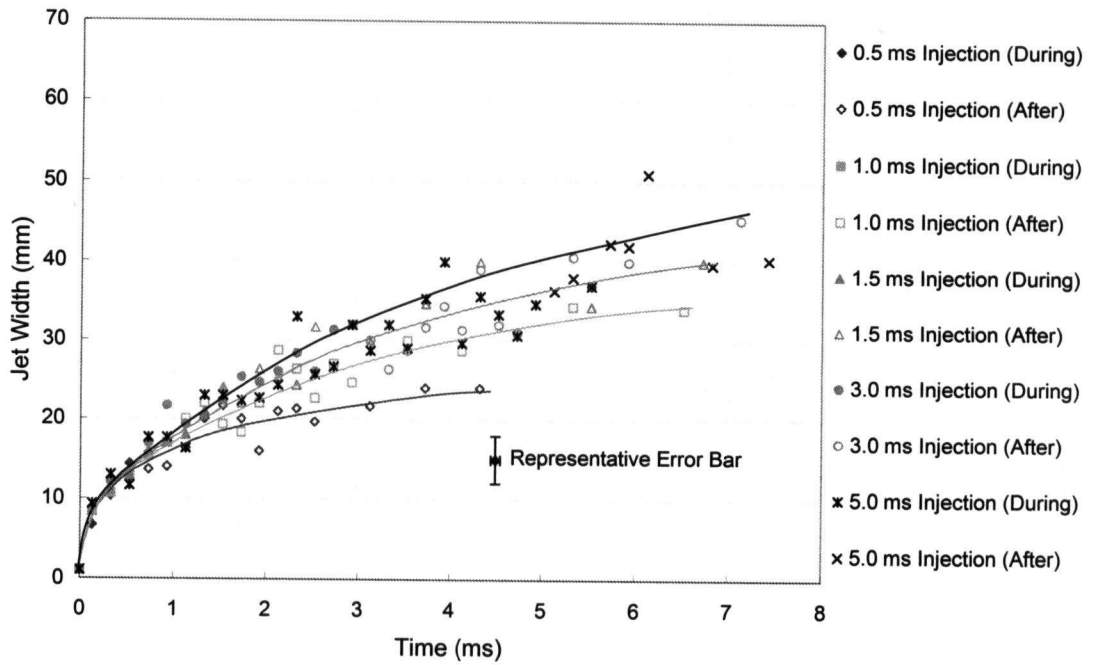


(a) Injection Pressure Ratio = 3

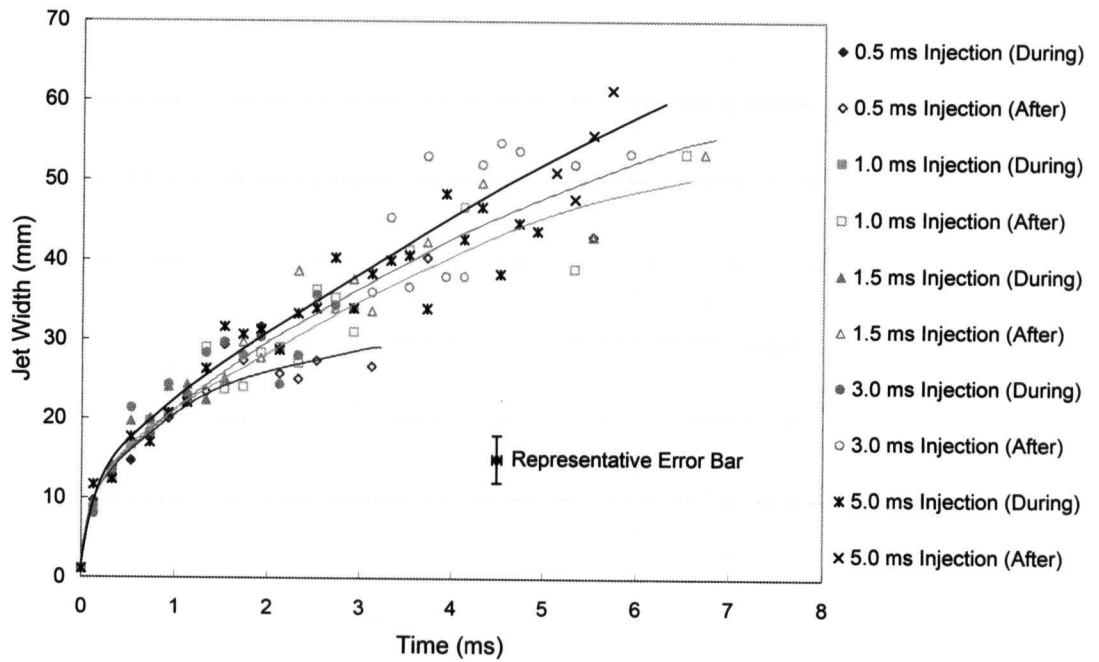


(b) Injection Pressure Ratio = 5

Figure 3.14: Jet Length Evolution During/After Injection (Single Injection)



(a) Injection Pressure Ratio = 3



(b) Injection Pressure Ratio = 5

Figure 3.15: Jet Width Evolution During/After Injection (Single Injection)

Finally, increasing the pressure ratio from 3 to 5 increased the jet length (measured at fixed time intervals after injection) by a factor of approximately 1.4, and the width by a factor of 1.3, indicating both increased axial and radial jet velocities. Although these increased velocities are not predicted by the previously developed mass flow model, which assumes choked flow, implying the nozzle exit velocity is independent of the pressure ratio, that model does suggest a linear momentum flux dependence on the pressure ratio. Therefore, although the choked nozzle limits the mass flow rate, higher pressure at the sonic throat arising from a higher pressure ratio yields a higher exit momentum flux. This greater momentum flux yields a higher jet velocity *after* the gas exits the nozzle and expands to ambient pressure.

Numerical Results

Among the many previous researchers that have modelled transient axisymmetric jet development, the most relevant is the work of Hill and Ouellette¹⁹, who reviewed an array of previous studies and proposed scaling laws for transient axisymmetric gaseous jets. This development was based on dimensional analysis of the jet tip penetration length (Z_t) as a function of the exit momentum flux (\dot{M}), jet density at the nozzle exit (ρ_n), ambient density (ρ_a), exit velocity (U_0), and nozzle diameter (d).

Two relations were derived depending on whether the jet and ambient gas densities were equal or not, and both made use of a dimensionless constant: the penetration number, Γ . The derived relations for equal and different densities, respectively, are reproduced below:

$$Z_t = \Gamma \cdot \left(\frac{\dot{M}}{\rho} \right)^{1/4} \cdot t^{1/2} \quad (3.10)$$

$$\frac{Z_t}{d \sqrt{\frac{\rho_n}{\rho_a}}} = \Gamma \cdot \sqrt{\frac{\pi}{4}} \cdot \left(\frac{U_0}{d \sqrt{\frac{\rho_n}{\rho_a}}} \right)^{1/2} \cdot t^{1/2} \quad (3.11)$$

These results, which are based on dimensional analysis, may be solved analytically if one assumes a transient jet of the Turner²⁰ variety. This model treats the transient jet as a transient vortex ball in front of a steady-state jet (refer to illustration in Figure 3.16), and in conjunction with the well-known mass entrainment results of Ricou and Spalding¹⁶ can be used to derive analytical equations for the vortex ball's and jet's

momentum. Substituting the penetration number equations into these momentum equations yields an analytical penetration number solution (Hill and Ouellette¹⁹). Additionally, since the jet momentum, density, and penetration length in time are experimentally measurable, the penetration number may also be calculated from experimental data.

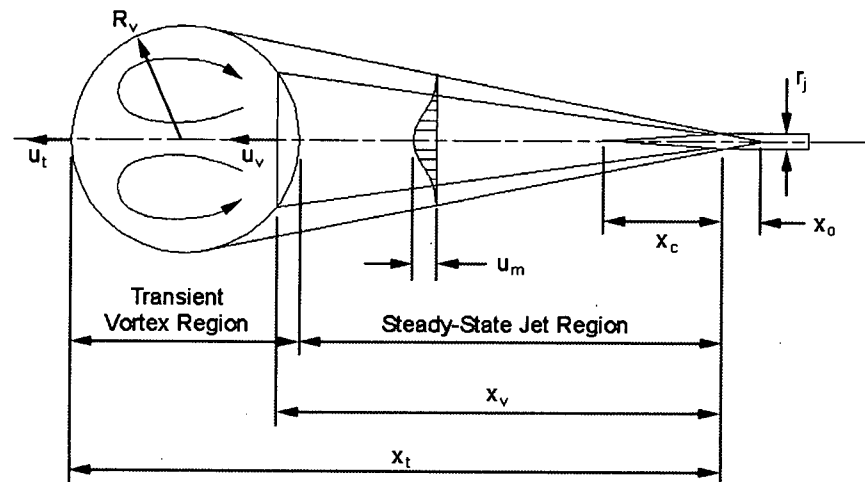
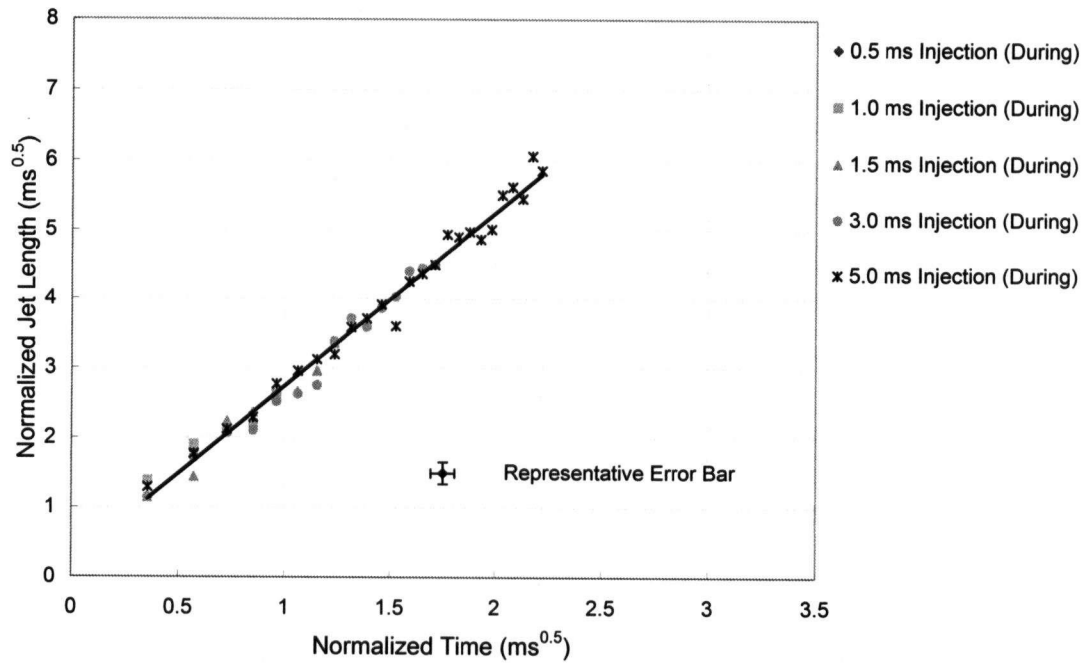


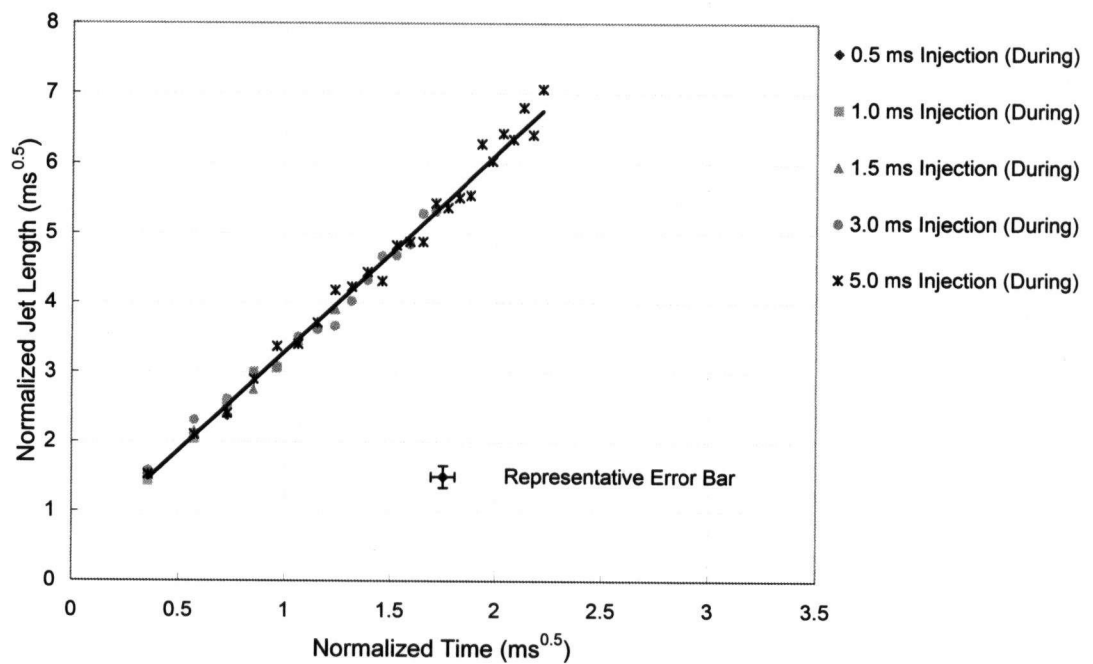
Figure 3.16: Numerical Jet Model

To examine the validity of the scaling laws presented above, the jet length data from Figure 3.14 is replotted in Figure 3.17 in non-dimensionalized form, whereby the jet penetration is normalized such that when plotted against the square root of time, the slope of the curve is the penetration number. In Figure 3.17 only those data points collected during injection are plotted to illustrate how well the data collapses onto a straight line when normalized. Figure 3.18 includes all the data collected to illustrate how the penetration number decreases at the end of injection as the jet slows and tends towards puff jet behaviour.

Quantitatively, the value of the slope in Figure 3.17 depends upon the normalization that is performed on the jet tip penetration length. Of the two penetration numbers presented earlier, clearly the latter (different jet and ambient densities) is relevant in the present investigation, but the momentum flux, exit velocity, and jet density are all required, none of which are directly measured. Using the various mass flow models developed earlier, in which expansion from the fuel reservoir to the nozzle is treated as an adiabatic, isentropic process with corrections to compensate for any losses,

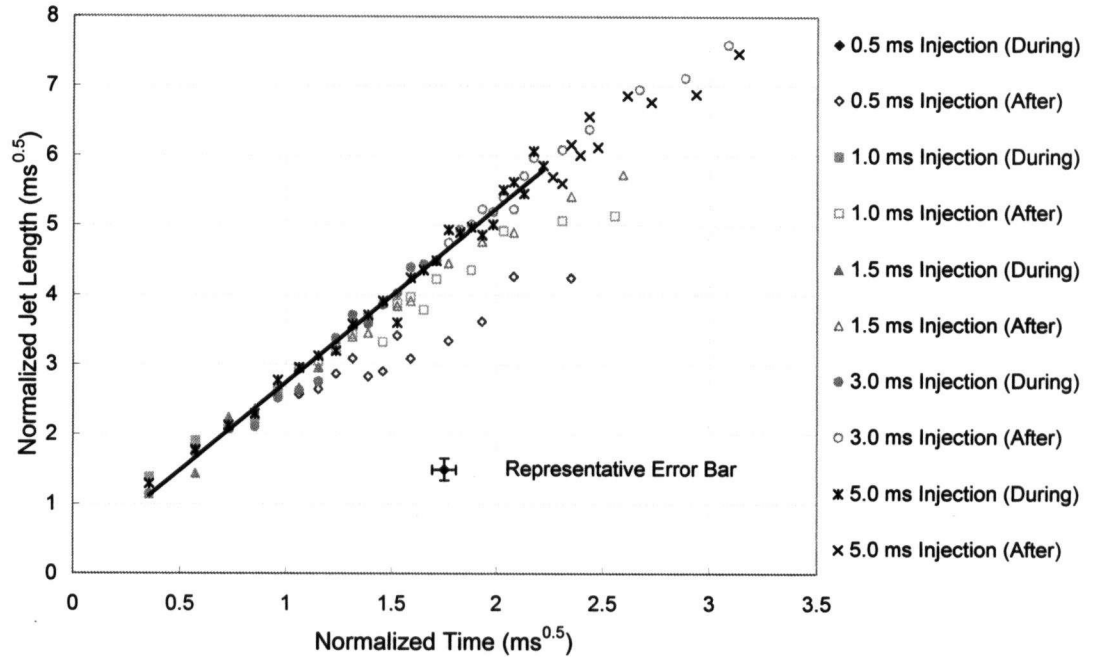


(a) Injection Pressure Ratio = 3

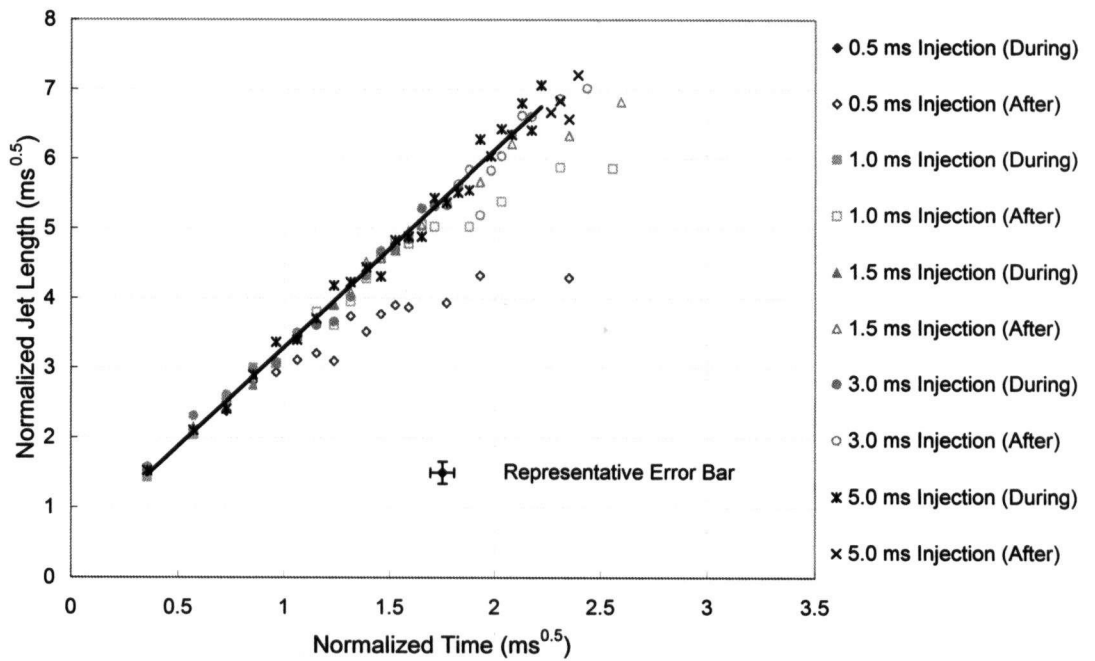


(b) Injection Pressure Ratio = 5

Figure 3.17: Normalized Jet Tip Penetration (During Injection)



(a) Injection Pressure Ratio = 3



(b) Injection Pressure Ratio = 5

Figure 3.18: Normalized Jet Tip Penetration (During/After Injection)

uncertainty in the tuned model parameters and differences between various models result in uncertainties in the penetration number. For comparison, Table 3.8 lists the penetration number (the slope in Figure 3.17) calculated using various assumptions for determining the mass flow, momentum, and nozzle density.

Table 3.8: Jet Penetration Number Comparison

		PR = 3	PR = 5	Theoretical
Width Ratio, D/Z_t , at Various Injection Stages	During	0.37±0.05	0.33±0.04	0.25±0.05
	After	0.37±0.05	0.36±0.05	0.5-0.6 (puff jet)
Penetration Number, Γ , Assuming Various Stagnation Pressure Losses	10% loss	2.42±0.04	2.74±0.04	-
	20% loss	2.50±0.04	2.83±0.04	-
	30% loss	2.58±0.04	2.92±0.04	-
Uniform Density Solution, Γ		2.25±0.04	2.89±0.04	-
Analytical Solution, Γ		2.71±0.13	2.82±0.10	2.99±0.10

It is seen, regardless of what stagnation pressure loss is assumed within the injector or even if the differential density equation is used at all, that the penetration number for a pressure ratio of 3 is markedly lower than that predicted. Improved penetration number agreement with predicted results is observed at a higher pressure ratio of 5. The discrepancies between the low pressure ratio jet and the analytical solution is attributed mostly to the low Reynolds number. This effect is somewhat expected since the correlations developed by Hill and Ouellette assumed fully turbulent jets ($Re > 500,000$) while the current pressure ratios corresponded to nozzle Reynolds numbers between 33,000-43,000 and 56,000-72,000 for pressure ratios of 3 and 5, respectively, depending upon the stagnation pressure loss assumption. The closer agreement between experimental and analytical results at the higher pressure ratio is believed due to closer Reynolds number agreement.

Nevertheless, despite minor differences in the numerical values for the penetration number, overall the experimental data is seen to collapse well using the scaling laws derived by Hill and Ouellette. Additionally, as the jet Reynolds number is increased, even the quantitative agreement converges with previously stated analytical results.

3.4.3 Pulsed Injection Mode

Pulsed injection mode is the operating mode in which each individual injection is split into multiple successive shorter fuel injections, such that the total fuel injected equals that that

would have been injected in one continuous injection pulse. The motivation behind such pulsed injection operation is speculation that pulsing injection can increase jet turbulence levels thereby increasing mixing rates and accelerating the autoignition process.

Procedure

To investigate the effects of pulsed injection operation, a series of Schlieren images were captured of two successive injections of various injection durations, separated by several injection pulse delays. Methane was injected at a constant pressure into atmospheric air while 17-20 sequential images were captured at intervals between 200 μ s to 1.2 ms. Jet tip penetration length and width were subsequently measured from captured digital images. While two distinct injection pulses were identifiable in several images, the jet tip and jet width of the second injection was not consistently measurable and therefore only the penetration length and width of the large scale flow (not individual injection pulses) was measured.

Three injection durations between 0.5-1.5 ms were investigated at each of three pulse delays between 0.5-2.0 ms. These particular conditions result in injection of an equivalent quantity of fuel as single injection durations ranging between 1.0-3.0 ms, previously chosen for their engine relevance. The pulse delay was defined as the time interval between the *end* of the first injection and the *beginning* of the next injection (see Figure 3.9). Throughout all tests, a constant pressure ratio of 3 was maintained to limit the size of the test matrix. Experimental conditions investigated are summarized in Table 3.9 and experimental data is available in Appendix F.

Table 3.9: Experimental Test Matrix (Pulsed Injection Visualization Study)

Number of Injection Pulses:	2
Injection Duration:	0.5-1.5 ms (per injection pulse)
Injection Delay:	0.5-2.0 ms
Injection Pressure:	2 bar (30 psi)
Pressure Ratio:	3

**Note: All indicated pressures are gauge pressures.*

Experimental Results

Representative images of those captured in the present investigation are included in Figure 3.19. These images highlight the difficulty of distinguishing each individual injection pulse. Although in several images the jet tip of the second injection pulse

is discernible, in others it is not, and the overall flow field appears no different than that observed when operating the injector in single injection mode (Figure 3.13).

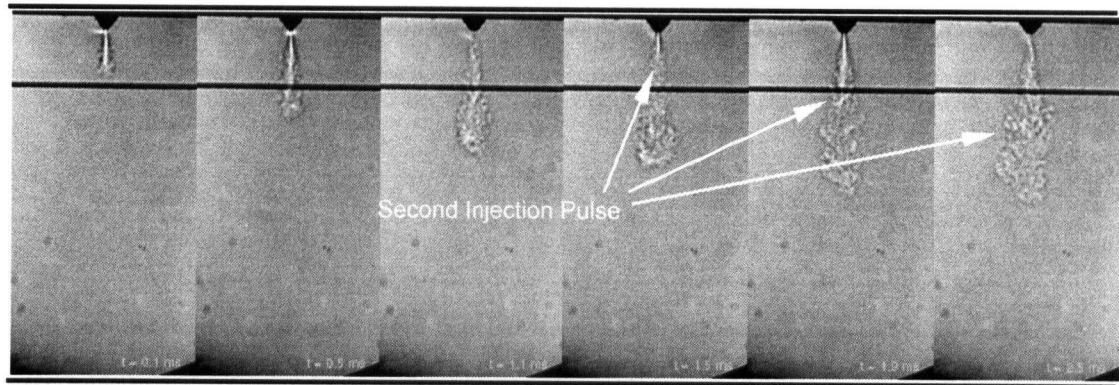
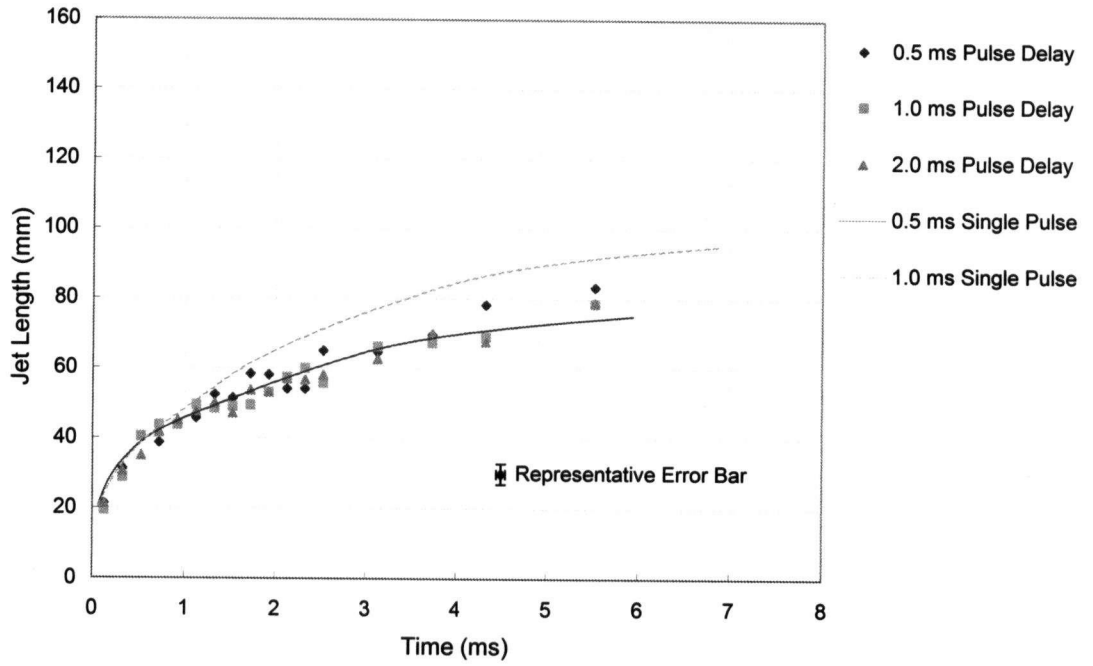


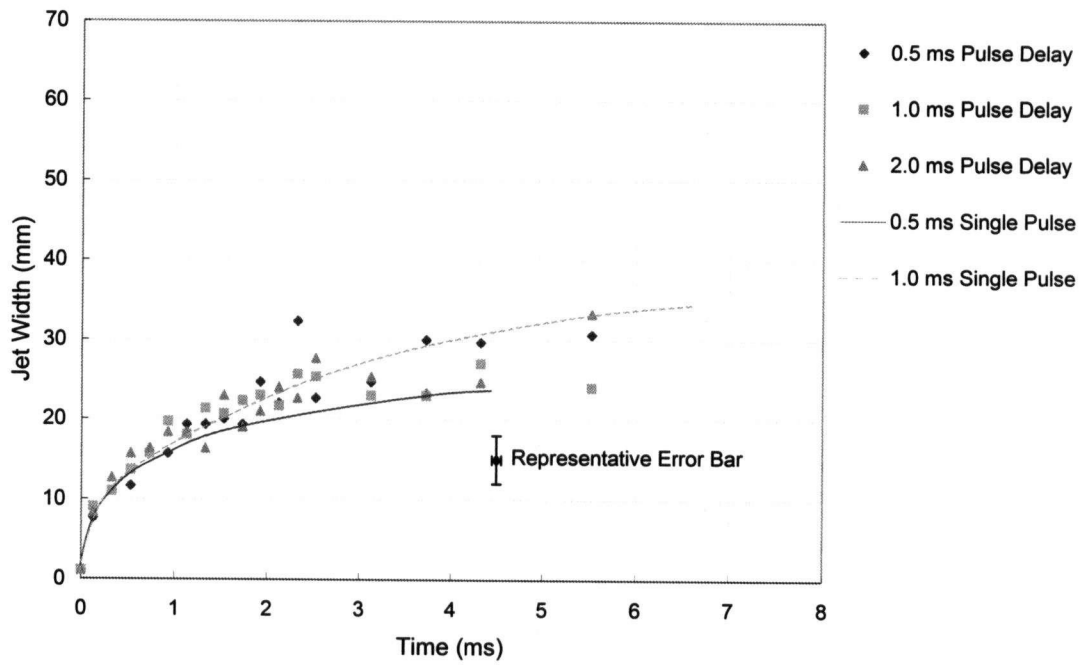
Figure 3.19: Schlieren Images of Pulsed Jet Evolution in Time

The jet tip penetration and jet width evolution in time are presented in Figure 3.20. In addition to plotting results from pulsed injection experiments, each of the graphs in Figure 3.20 also includes the jet length and width corresponding to a comparable single injection pulse to illustrate the similarities between the jet that develops during single and pulsed injection. This figure highlights the irrelevance of the pulse delay. For all injection durations, varying the delay between 0.5-2.0 ms had no noticeable effect on the ensuing jet, with each data point falling within experimental error of all others at any given time after the start of injection. Although increasing pulse delays much further (by orders of magnitude) would produce an observable effect on the jet flow field, such long pulse delays are of no interest since then the jet is considered two distinct injections rather than one pulsed injection.

Furthermore, similarities observed between the jet development for the case of two successive injections and one long, continuous injection (which may be considered two successive pulses with no pulse delay) implies that the jet development is solely dependent on the total momentum injected, regardless of whether it is continuous or pulsed. This is especially demonstrated by comparing the pulsed injection case at an injection duration of 1.5 ms with a single injection with an injection duration of 3.0 ms (Figure 3.20 (e)). The jet tip penetration length for these two cases is nearly identical, and this is due to the momentum injection being equal in each case (two 1.5 ms duration pulses inject an equivalent momentum as a single 3.0 ms injection). Similar trends are illustrated by the injection durations of 0.5 ms and 1.0 ms, with all pulsed injection data points lying between those of the single injection curves.

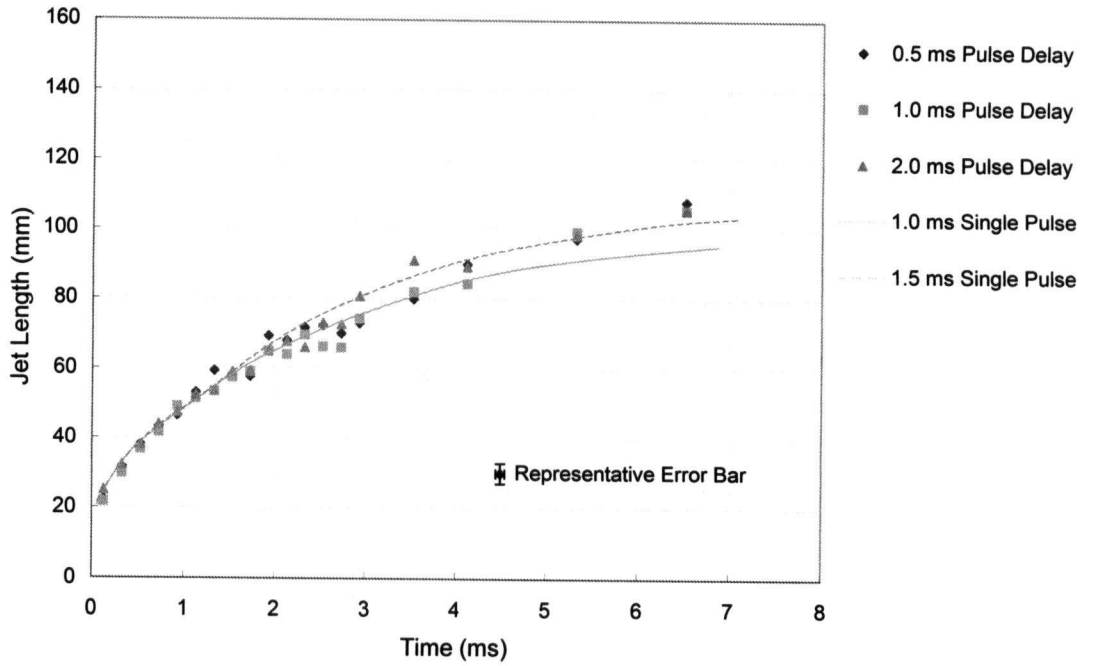


(a) Jet Length (0.5 ms Injection Duration Per Pulse)

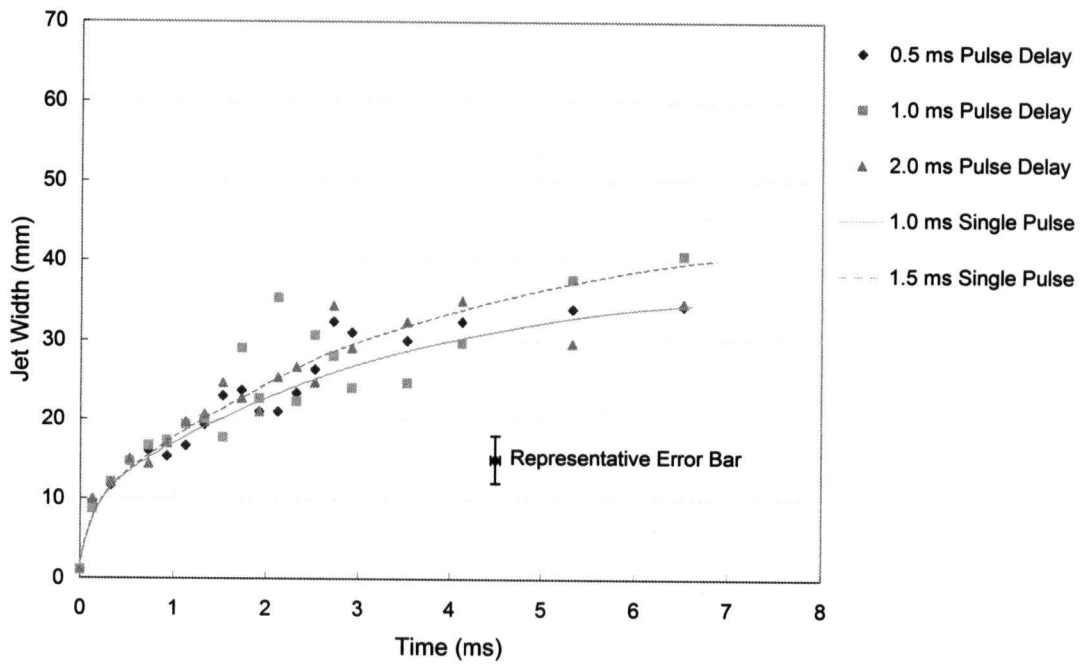


(b) Jet Width (0.5 ms Injection Duration Per Pulse)

Figure 3.20: Jet Length and Width Evolution (Pulsed Injection)

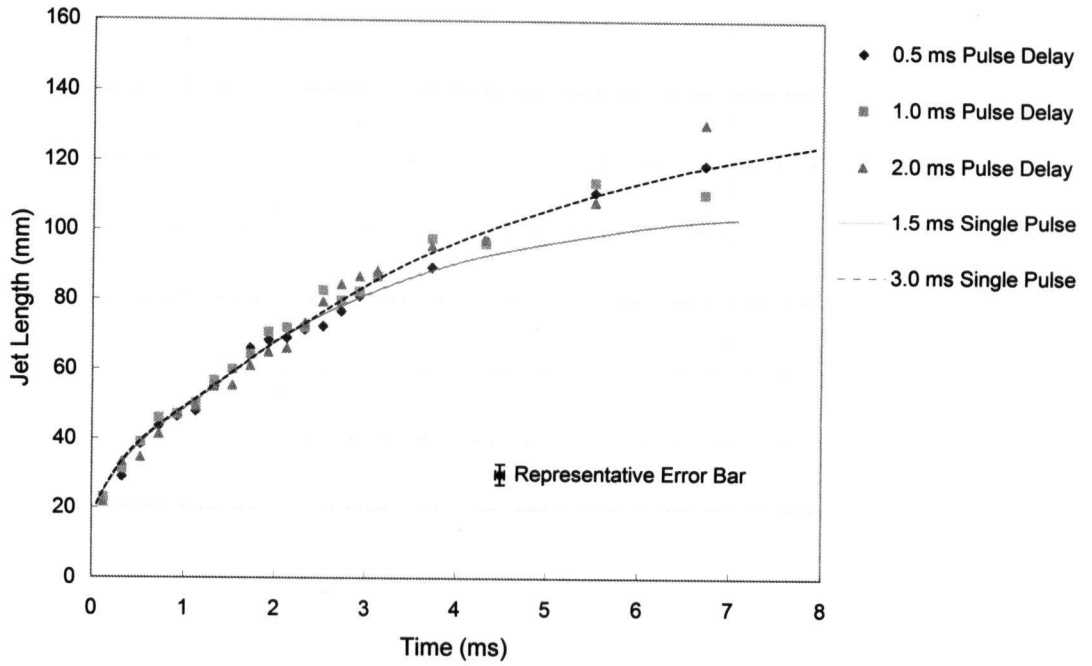


(c) Jet Length (1.0 ms Injection Duration Per Pulse)

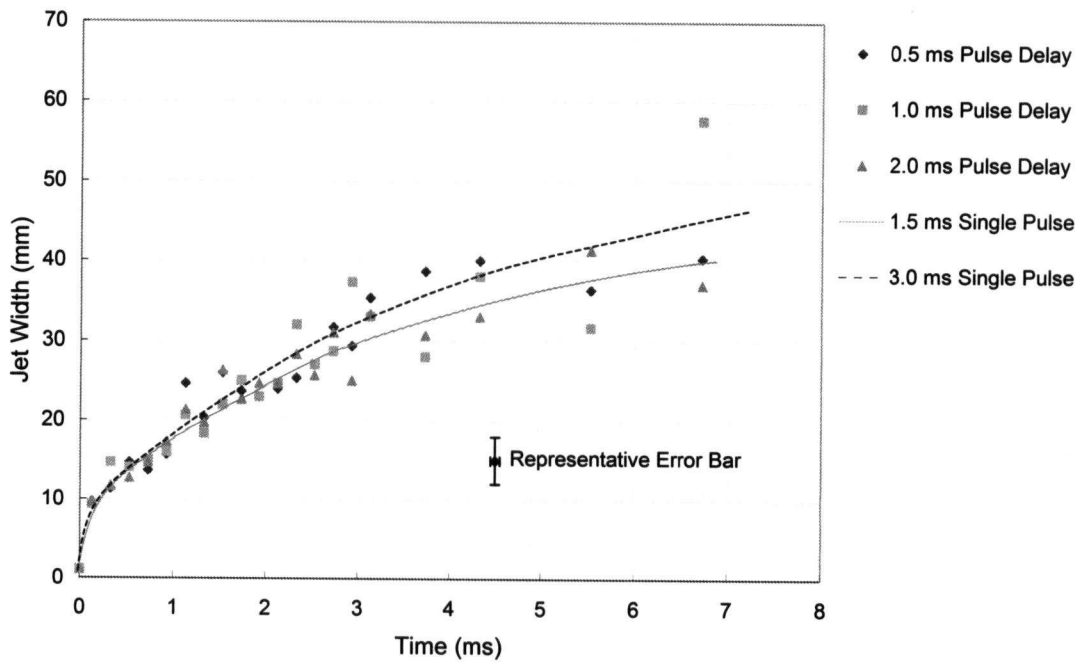


(d) Jet Width (1.0 ms Injection Duration Per Pulse)

Figure 3.20: Jet Length and Width Evolution (Pulsed Injection) cont'd.



(e) Jet Length (1.5 ms Injection Duration Per Pulse)



(f) Jet Width (1.5 ms Injection Duration Per Pulse)

Figure 3.20: Jet Length and Width Evolution (Pulsed Injection) cont'd.

The effect of pulsing the jet therefore exclusively seems to affect internal strain rates within the jet, which unfortunately could not be quantitatively resolved in the present study. If pulsing the jet has any effect in combustion applications it must arise from the effects it has on the strain intensity and/or distribution within the jet, not from any large-scale effects on the transient jet's development. Additionally, since the large-scale flow field properties of a pulsed injection seem identical to those of continuous injections of equal momentum flux, all scaling laws developed for the single injection mode are applicable to pulsed injection operation.

3.4.4 Effects of Jet Impingement

Studying the effects of jet impingement on ensuing transient jet development is of interest because such a scenario may arise in the presence of a protruding spark or glow plug, or an obstruction intended to enhance mixing or, if coated with a catalyst, accelerate ignition. While many configurations for such impingements are possible, and in some cases have been previously investigated, only two simple geometries were investigated in the current study to gain insight into the jet's behaviour.

Procedure

To investigate the effects of jet impingement, two blunt bodies were chosen as flow obstructions (see Figure 3.21). These consisted of a circular cross-section, 1.575 mm diameter wire placed perpendicular to the jet's axis, and a rectangular cross-section body 2.896 mm wide and 1.067 mm thick, mounted so that the jet impinged

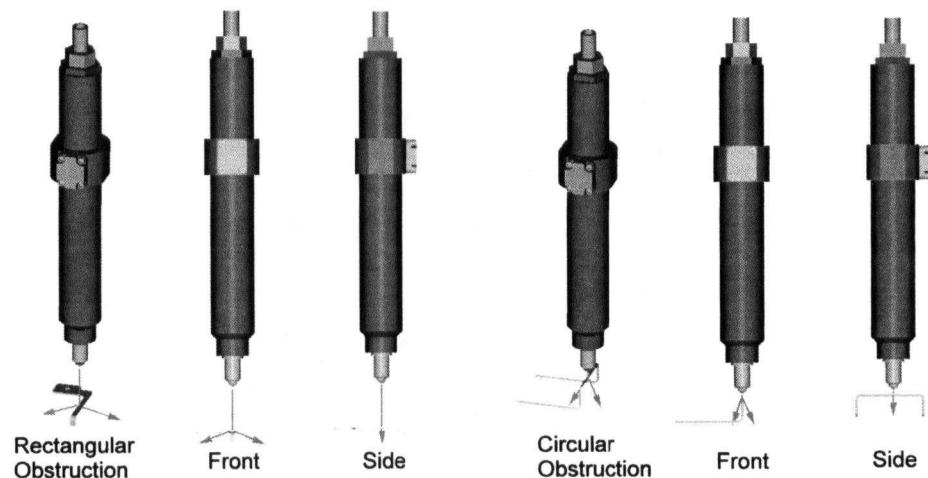


Figure 3.21: Flow Obstructions for Jet Impingement Study

on its widest side. Each obstruction was located a distance from the injector nozzle such that 80-100% of the jet's width impinged on the obstruction. Methane was then injected at a constant pressure into atmospheric air while a sequence of 19 images captured the jet impinging on the flow obstructions with both the jet length and width measured along with qualitative observations of the jet's behaviour.

Each of the flow obstructions was tested at several axial distances from the injector nozzle. All other parameters, including injection duration and pressure, ratio were held constant throughout the experiments. The test conditions are summarized in Table 3.10 and data is available in Appendix F.

Table 3.10: Experimental Test Matrix (Jet Impingement Visualization Study)

Obstruction Distance from Injector:	Circular Rectangular	0.5-2.0 mm 10.0-15.0 mm
Injection Duration:		1.0 ms
Injection Pressure:		2 bar (30 psi)
Pressure Ratio:		3

**Note: All indicated pressures are gauge pressures.*

Experimental Results

Several sample images captured in this study are shown in Figure 3.22 to illustrate the markedly different jet behaviour with the circular and rectangular obstructions. The circular obstruction had the net effect of decreasing the length and increasing the width of the jet while also noticeably increasing the turbulence and unsteadiness of the jet. Throughout the injection, the jet was observed to meander from one side to the other of the obstruction, occasionally even splitting into two jets. Additionally, little, if any, effect from moving the obstruction closer or farther from the nozzle was observed. Contrarily, the rectangular obstruction was observed to create a very stable, repeatable flow pattern. The jet consistently split into two distinct jets upon impinging on the flat obstruction, with few instabilities, and the effect of moving the obstruction closer or farther from the injector nozzle was to change the angle of the two deflected jets relative to the initial impinging jet.

Quantitatively, since the cylindrical obstruction only occasionally caused the jet to split in two, the same measures used to analyse the original undisturbed jet, namely the tip penetration length and width, were used. These are presented in Figure 3.23 alongside length and width measurements for undisturbed jets at the same injection

pressure and duration. As discussed above, these graphs illustrate how the effect of the circular obstruction was to reduce the jet penetration length by approximately 39% and increase the jet's width by 43%. Additionally, they illustrate that varying the obstruction's distance from the nozzle had no identifiable effect, within experimental uncertainty. This may be caused by the fact that the circular obstruction was placed very near the nozzle (separation distance to nozzle diameter ratio, L/d , of 0.45-1.81) to ensure the entire jet width impinged on the obstruction. Perhaps if the obstruction were located much farther (4-8 mm from nozzle) a stronger relationship between the separation distance and the jet's development would have been observed. Lastly, the jet width plot demonstrates the unsteady nature of the deflected jet, as the width is observed to fluctuate wildly as the jet would drift from one side to the other of the obstruction and occasionally even split into two jets.

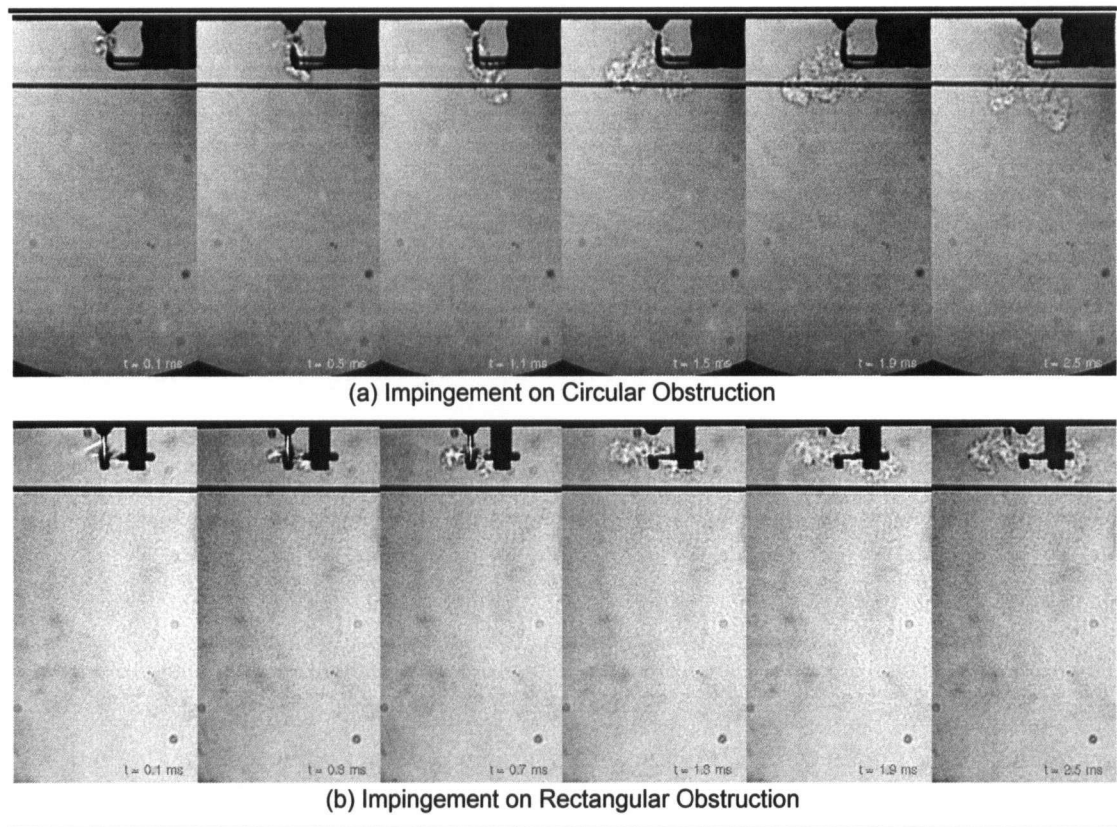
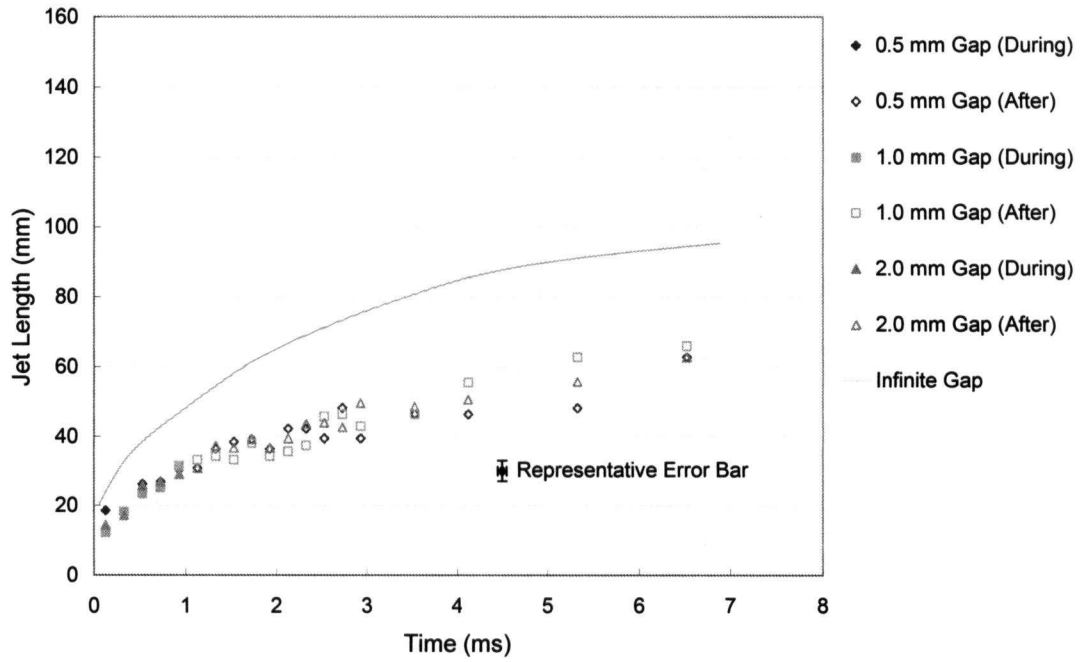
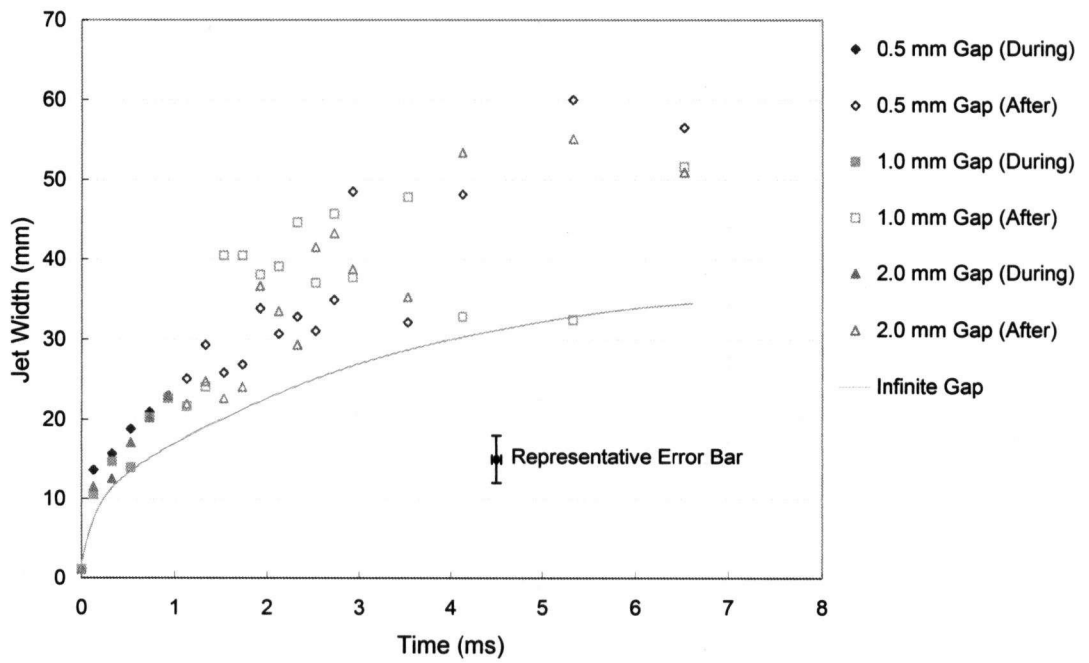


Figure 3.22: Schlieren Images of Impinging Jet Evolution in Time

Since the rectangular obstruction consistently caused the jet to split into two distinct jets, it was inappropriate to solely rely on the tip penetration length and width of the jet as quantitative measures of its response. Instead, the jet length and width were defined as shown in Figure 3.24 along with the deflection angle. Since the jet split



(a) Jet Length (Circular Obstruction)



(b) Jet Width (Circular Obstruction)

Figure 3.23: Jet Length and Width Evolution (Circular Obstruction)

into two jets, the “length” measure is no longer representative of the tip penetration length, but rather the maximum axial distance travelled and the “width” is a measure of the maximum radial distance travelled.

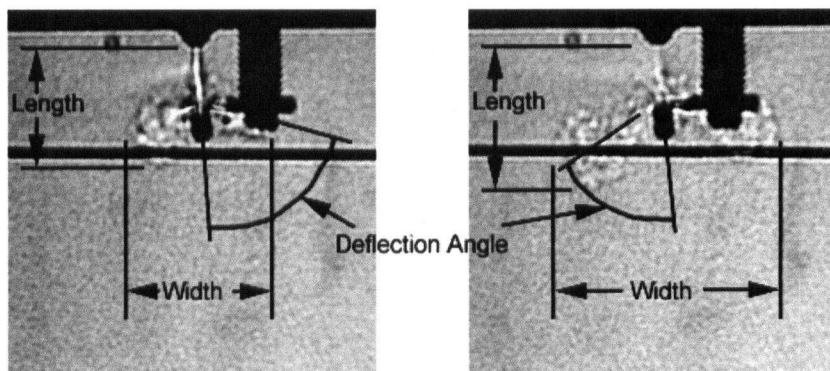
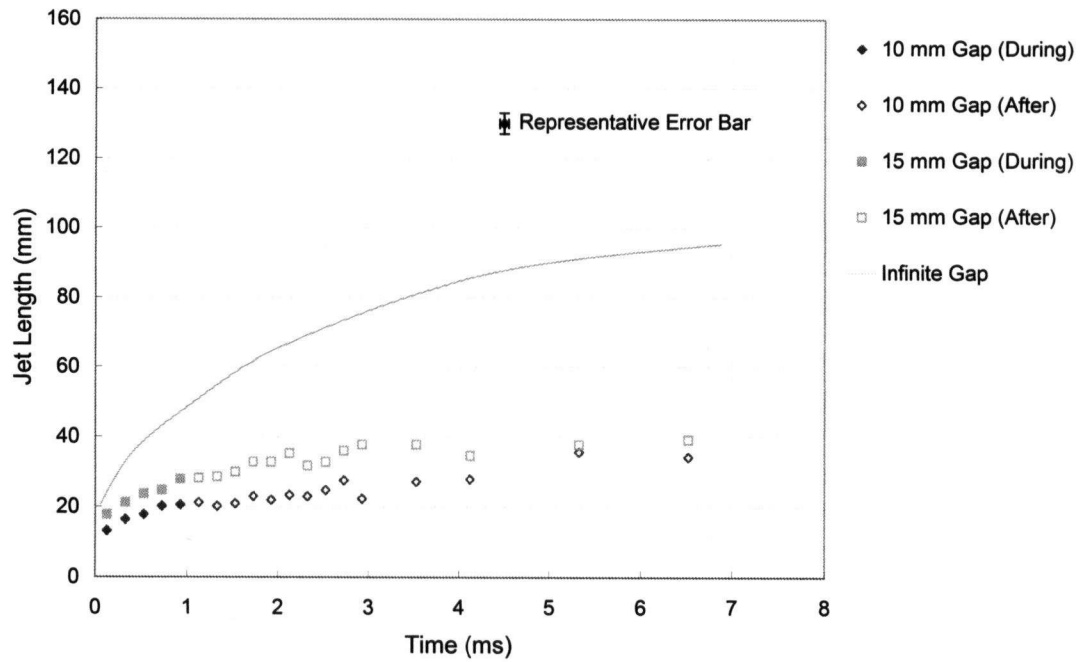
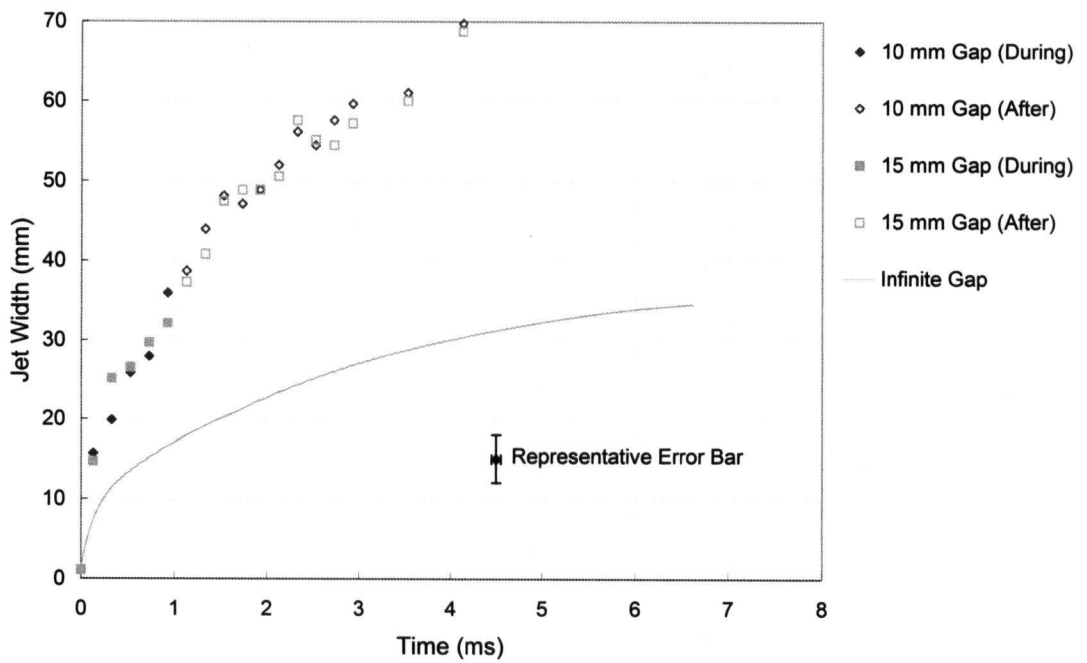


Figure 3.24: Jet Length, Width, and Deflection Angle Definition

Using the above definitions of the jet length and width, Figure 3.25 presents both the measured values of each using the rectangular obstruction, and for comparison also plots the penetration length and width of an unobstructed jet. As one would expect, length and width differ greatly from those of an unobstructed jet since impingement on the rectangular obstruction caused such a large deflection of the jet. Depending on the distance the obstruction was placed from the nozzle, either 10 mm or 15 mm ($L/d = 9.09-13.64$), the jet was deflected by 86° and 69° , respectively. Such a strong relationship between the obstruction’s distance from the nozzle and the deflection angle is expected since locating the obstruction close to the nozzle causes a greater portion of the jet to impinge on the obstruction, whereas as the obstruction is moved farther from the injector, a smaller fraction of the jet impacts the obstruction. This relationship is also responsible for differences between the jet length’s and width’s response to the obstruction’s location, with the penetration length seemingly more sensitive than the width. However, this effect is due mostly to the deflection angle change that occurs, which trigonometrically results in a larger increase in the length than the width for the particular deflection angles observed in this study. The effects of an obstruction are thus to increase the surface area and turbulence by splitting a jet into multiple jets, with the degree of turbulence augmentation and/or the angle through which the jets are deflected controlled by the distance from the nozzle to the obstruction.



(a) Jet Length (Rectangular Obstruction)



(b) Jet Width (Rectangular Obstruction)

Figure 3.25: Jet Length and Width Evolution (Rectangular Obstruction)

3.4.5 Effects of an Enclosure

Finally, the effects of an enclosure on a transient jet are of interest to understand how the combustion chamber walls and piston affect the jet's development. As with impingement, many combinations are possible to study such effects so only one special case, with three variants, was investigated. This involved studying the behaviour of a jet confined between parallel plates of various separation distances, such as would be the case for a jet injected parallel to the surface of a flat piston approaching top dead centre in an engine.

Procedure

To investigate the effects of an enclosure, two moveable parallel plates were installed on the apparatus previously described and methane injected between the plates. Methane was injected into atmospheric air at a constant injection pressure and duration while 19 sequential images were captured of the jet at various stages in its evolution. Subsequently both the jet's length and width were measured from the captured images. Three sets of experiments were conducted at three distinct wall separation distances with all injection parameters held constant. A summary of the experimental conditions is presented in Table 3.11 with data in Appendix F.

Table 3.11: Experimental Test Matrix (Jet Enclosure Visualization Study)

Wall Separation Distance:	12-50 mm
Injection Duration:	1.0 ms
Injection Pressure:	2 bar (30 psi)
Pressure Ratio:	3

**Note: All indicated pressures are gauge pressures.*

Experimental Results

Representative images of those captured in the present study are presented below in Figure 3.26. Qualitatively, the images illustrate how confining the jet had minimal influence on the jet length. Although inevitably the jet width was compressed once it filled the gap between the plates, no apparent difference in jet length between each case was present. This is attributed to the fact that the boundary layer that forms along the edges of the plates is very narrow and despite decelerating the flow near the periphery of the jet, it has little influence along the jet centreline. Additionally, since the jet was free to expand parallel to the plates, any constraint posed by the presence of the walls was compensated for by increased jet spread out of plane.

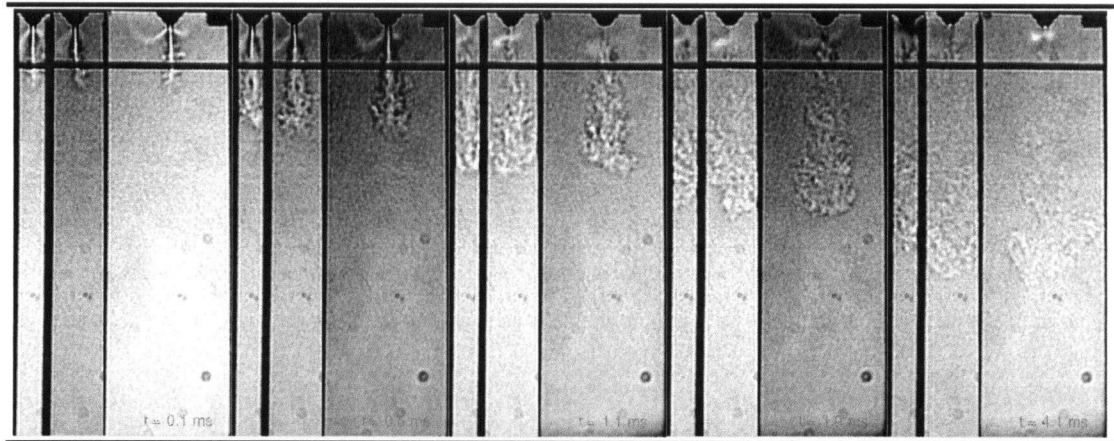
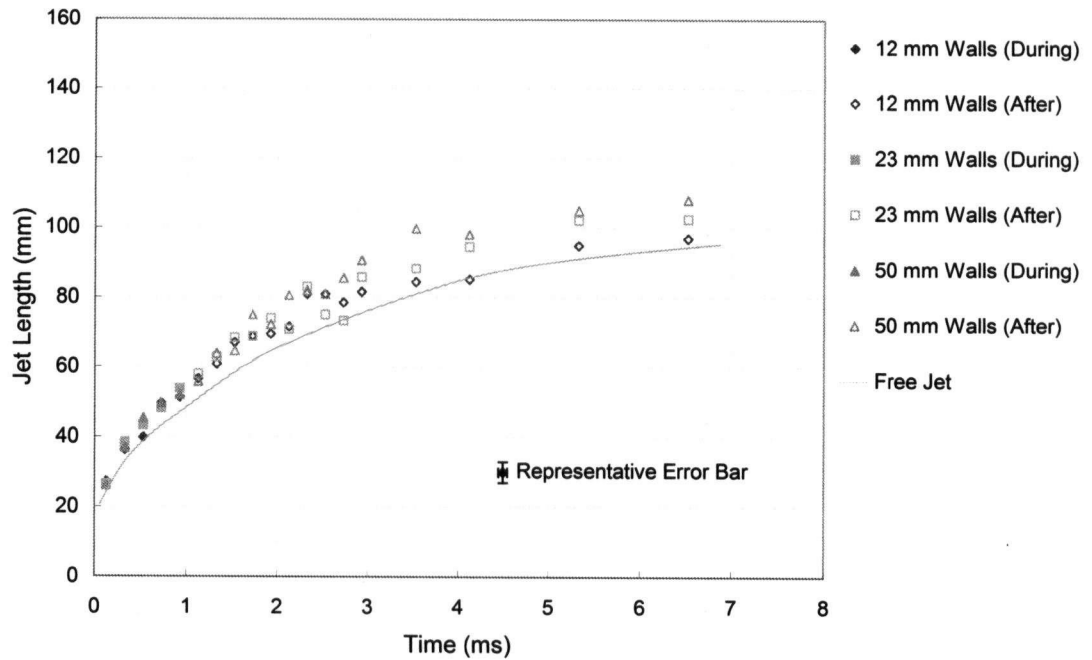


Figure 3.26: Schlieren Images of Enclosed Jet Evolution in Time

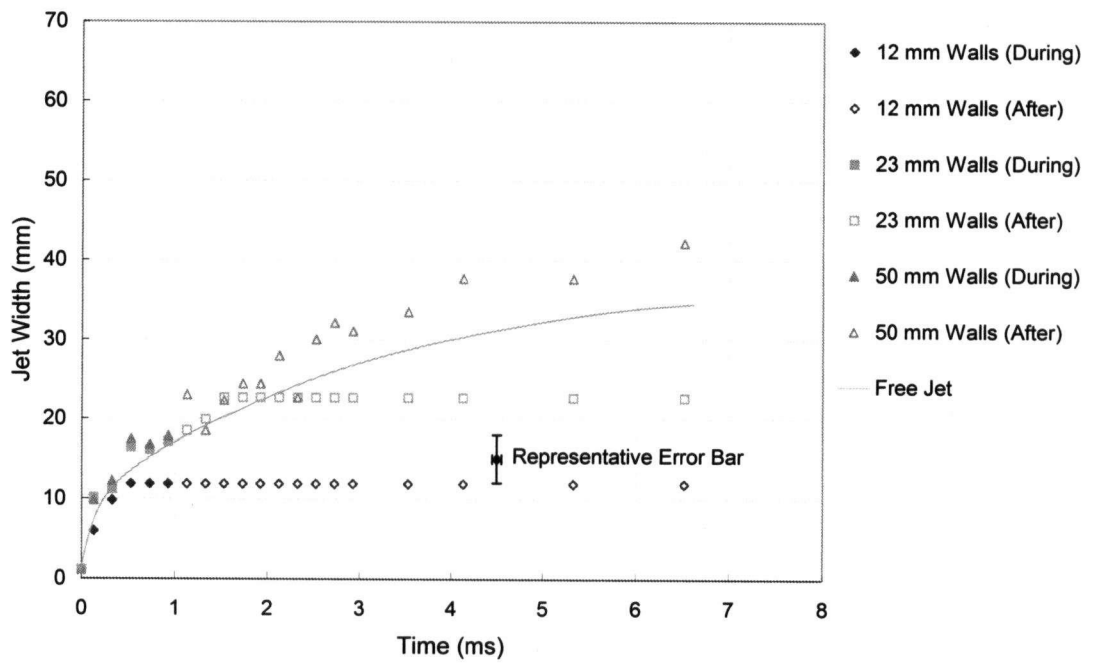
The qualitative observations discussed above are further reaffirmed in Figure 3.27 where the jet length and width are plotted alongside length and width measurements from an unconfined jet at the same injection pressure ratio and duration. This figure illustrates that the presence of parallel plates had a minimal effect on the jet length, as it was just slightly longer than the length of the unconfined jet regardless of the wall separation. Expectedly the width of the confined jet was reduced relative to the unconfined jet, but even this effect is only observed once the jet width fills the entire gap. Prior to filling the space between the walls, the jet width evolves at a similar rate as an unconfined jet. Unfortunately, no comments can be made with regards to any recirculation that occurs between the plates since no such observable flow was resolved in any of the images. However, from limited observations and quantitative measurements that were made, one may conclude that the influence of the viscous boundary layer introduced by the presence of confining parallel plates fails to extend far enough into the jet to have any influence on the transient jet's development and thus the effects of confining walls are only of concern for their potential quenching effects in a reacting flow, and not for any effects on the transient jet's development.

3.5 Conclusions and Recommendations

The present characterization of a Westport Innovations J41 fuel injection system involving both validation of the fuel injector hardware and the jet produced under various operating conditions led to several quantitative measures that can be used in future to predict, control, and optimize the injection system's performance. These have included the following observations of both the hardware's response and the jet's flow field characteristics:



(a) Jet Length (Enclosure)



(b) Jet Width (Enclosure)

Figure 3.27: Jet Length and Width Evolution (Enclosure)

1. A physical delay time of $180 \pm 20 \mu\text{s}$ was found to exist in the injector driver that must be accounted for if using the control signal between the injector controller and driver to monitor injection. Failure to do so will lead to the introduction of a systematic error in non-premixed ignition delay experiments, or inaccurate injection timing during engine operation.
2. Mass flux measurements performed with both methane and nitrogen gas at several injection pressures between 62-172 bar(g) (1000-2500 psi(g)) were very well predicted by a simple model assuming choked, underexpanded flow at the nozzle. This model can be used to predict the mass flow through the injector by modelling the expansion from the stagnation state (reservoir) to the nozzle exit as an adiabatic, isentropic flow and then applying a correction using one of several proposed models.
3. The present injection system was successfully modified to facilitate pulsed injection, but caution must be used in selecting appropriate combinations of injection durations and injection pulse delays to fall within a specified operational envelope. For injection durations less than 1.8 ms, each injection pulse was found to inject equal amounts of fuel, but if operation at longer injection durations is required, an empirical correlation must be used to predict the differential mass injection rates between injection pulses.
4. Schlieren visualization of the jet produced by the injector at several injection durations was found to be extremely repeatable and consistent, with the jet's development being identical regardless of injection duration. Additionally, both the temporal evolution of the jet and the effects of pressure ratio were predicted by a dimensionless penetration number, especially at higher pressures where closer agreement with analytical results was observed.
5. Pulsed injection operation was found to have minimal influence on the jet's large scale flow field development and the effects of pulsed versus continuous injection were thus speculated to only influence internal flow structures, possibly increasing the turbulence intensity. This effect requires further investigation when optical instruments capable of resolving shorter time/length scales become available.
6. Impingement on a circular body resulted in an extremely unstable jet that drifted from side to side and split into multiple jets unpredictably, while decreasing the penetration length and increasing the jet width. Contrarily, impingement on a flat body produced a

very stable jet that split into two upon impingement, with the angle at which each jet propagated relative to the undisturbed jet controlled by varying the separation distance between the obstruction and the injector nozzle. Use of such a device is suggested for turbulence augmentation or jet splitting if such properties are desired. Additionally, such a device coated with a catalyst may potentially be used to accelerate the ignition process and thus warrants future investigation.

7. Confining the jet between parallel plates was found to have no noticeable influence of the transient jet's development regardless of the separation distance between the plates. It was concluded that the effects of viscosity that act at the interface between the jet and wall are confined to such a thin boundary region that they have a negligible influence on the bulk centreline flow.

Non-Premixed Methane Autoignition Delay Study **4**

4.1 Introduction

In the continued evolution of alternative fuel powered diesel engines, such as the HPDI system developed by Westport Innovations Inc., natural gas' prohibitively long autoignition delay time impedes further progress in both emissions and cost reductions and therefore remains critically important. While homogeneous methane autoignition delay time studies have provided insight into methane's behaviour under engine-relevant temperatures and pressures, diesel engines do not operate with homogenous air/fuel mixtures. Thus a need still exists to study the autoignition behaviour of methane under conditions that more closely reflect diesel operating environments. This includes investigating the coupling between the kinetic parameters studied in homogenous autoignition experiments and the fluid mechanic parameters associated with transient gaseous fuel jets. Unfortunately, thus far the kinetic parameters governing methane autoignition and the fluid mechanic parameters governing gaseous jets have been studied independently. Therefore, in an effort to better converge shock tube results with actual diesel engine operating conditions, non-premixed autoignition experiments are conducted in the present investigation to understand the influence of both kinetic and fluid mechanic parameters on methane autoignition.

4.2 Background

The ignition behaviour of non-premixed methane injected into shock-heated air at diesel engine relevant conditions differs from the autoignition behaviour of homogeneous mixtures due to the presence of a diffusion flame and thus the interaction that occurs between chemistry and fluid mechanics. Consequently, ignition delay times depend not only on experimental temperatures and pressures, which affect chemical reaction rates, but also parameters affecting the turbulent jet, including the injection duration and pressure ratio. While many ignition delay studies have been conducted investigating homogenous methane/air mixtures in shock tubes, and likewise a great deal of research has been conducted over many decades studying the flow characteristics of gaseous jets, studying the autoignition behaviour of gaseous jets in diesel environments has

thus far been limited to numerical simulations. While some experimental autoignition work has been conducted with coflow and counterflow diffusion flames to better understand reaction zone properties and ignition characteristics, these are not representative of the autoignition process in a diesel engine.

Recent experimental autoignition research includes that of Fotache et al.^{30,31} who studied the effects of strain rate, fuel concentration, and pressure on the ignition temperature of counterflow cold methane, butane, propane, and ethane against heated air. Additional experiments by such researchers as Stårner and Bilger³² investigated mixture fraction distributions in methane jets, Everest et al.³³ studied field and temperature gradients in non-premixed reacting jets, Rolon et al.³⁴ studied the interactions between a vortex and a diffusion flame, and Phillips³⁵ investigated the ignition location in turbulent jets. These are only a few of many similar experimental studies that investigated various phenomena in either counterflow diffusion flames or steady reacting jets. While these all provide great insight into the general ignition and combustion behaviour of methane diffusion flames, no studies directly investigating the autoignition delay behaviour of methane in diesel environments were discovered.

Numerically, the situation is much the same, with many studies investigating the fundamental behaviour of diffusion flames, but few closely related to the current study. Peters³⁶ and Pitsch and Peters³⁷ work is the most commonly used when describing diffusion flames using a laminar flamelet formulation, with many subsequent researchers using their laminar flamelet formulation to study diffusion flames. These have included studies of the methane-air flame structure and extinction behaviour by researchers such as Chan et al.^{38,39}, Yoshida et al.⁴⁰, and Seshadri and Peters⁴¹, as well as many additional studies investigating the diffusion flame's response to many scenarios such as Im and Chen's⁴² investigation of a methane/air diffusion flame's response to unsteady strain rate, for example. These represent a small sampling of the many studies that have been conducted and are included to highlight the fact that while diffusion flame behaviour is relatively well understood, none of these studies may be directly applied to understanding the ignition behaviour of non-premixed methane in diesel environments.

Two numerical studies that are of close relevance to the current problem include the work of Mastorakos et al.⁴³, who studied autoignition in turbulent mixing flows, and Bi and Agrawal⁴⁴, who studied autoignition of natural gas in diesel environments. The work of Mastorakos et al. involved conducting numerical simulations of various mixing flows of cold (300 K) fuel and hot (1000-1100 K) air to identify conditions favouring early ignition and subsequently compared their

results with previous experimental results and laminar flame theory. Likewise Bi and Agrawal modelled natural gas combustion in diesel environments to compare their findings with existing experimental results.

The purpose of the present investigation is to measure the autoignition delay times of methane injected into shock-heated air under engine relevant temperatures and pressures to facilitate comparison with both previously measured homogeneous autoignition delay times and previous numerical simulation results. Additionally, imaging techniques were used to photograph the autoignition event at various stages in its evolution so that comparisons can be made between reacting and inert gaseous jets, with the aim of better understanding the autoignition behaviour under diesel engine-relevant conditions.

4.3 Experimental Methods

The current investigation involved conducting a series of shock tube experiments measuring the autoignition delay time of gaseous methane fuel injected into shock-heated air under various engine-relevant experimental temperatures and pressures using a standard reflected shock technique. Details of both the specific apparatus used and the test conditions investigated are presented below.

4.3.1 Apparatus

Experimental ignition delay measurements were conducted in a 7.37 m long shock tube (3.11 m driver section, 4.26 m driven section), 5.9 cm in inner diameter previously used for homogeneous methane/air autoignition delay time studies (see Chapter 2 for details). The sole modifications performed to the experimental apparatus included replacement of the Auto Tran 600D-117 vacuum sensor (previously used for measuring initial driven gas pressures) with an Auto Tran 860, and the use of a double diaphragm, rather than a single diaphragm, system for controlling the pressure ratio between the driven and driver section (see Figure 4.1).

The double diaphragm system used for controlling the pressure ratio between driven and driver sections consists of two diaphragms in series separated by a small chamber (~66 cm³, 0.8% of the total driver section volume) that is charged to an intermediate pressure between that of the driven and driver sections. The use of two diaphragms separated by a small chamber at an intermediate pressure ensures that the pressure difference across

each diaphragm does not exceed its burst strength until the pressure in the intermediate chamber is released (by a solenoid valve venting to atmospheric pressure). Each of the diaphragms consists of a 0.635 mm (0.025 in) aluminum or steel sheet, with five radial grooves (each 2.95 cm in length) machined to depths between 0.279-0.381 mm (0.011-0.015 in), depending on the desired rupture strength. Such a system provides control of the pressure ratio between driven and driver sections, as the pressure difference across each diaphragm can be maintained safely below its burst strength until the intermediate chamber pressure is released. This makes the system insensitive to variability between individual diaphragm's burst pressure caused by material property or machining defects.

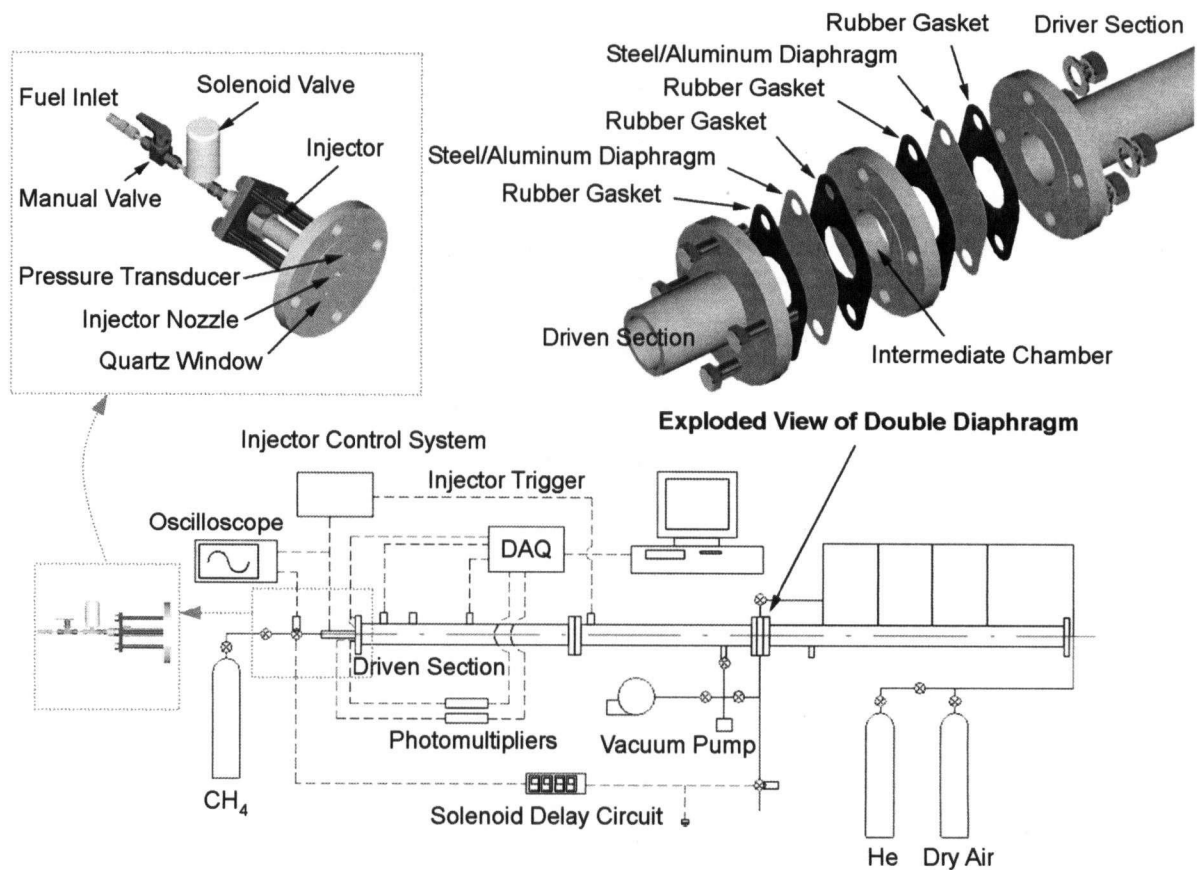


Figure 4.1: Experimental Apparatus (Non-Premixed Autoignition Study)

Fuel injection was performed by a Westport Innovations J41 gaseous fuel injector located on the shock tube endplate as illustrated in Figure 4.1, facilitating the injection of methane fuel axially into the shock tube. This injector, which was previously tested to investigate its jet characteristics (refer to Chapter 3 for details), is a magneto-restrictive unit (allowing rapid opening and closing times) with a 1.1 mm diameter nozzle. Westport's WCut control

software was used for controlling the injection duration and the delay between detection of a trigger signal and the start of injection. The trigger signal was generated by the passage of an incident shock by one of the five dynamic pressure transducers along the length of the shock tube. Throughout the present tests, the delay between arrival of a trigger signal and the start of injection was adjusted to ensure injection began 100-800 μ s after incident shock reflection from the endplate.

Finally, to minimize any fuel leakage into the shock tube before injection, a manual shutoff valve and an Advanced Fuel Components solenoid valve were installed upstream of the injector (see Figure 4.1 inset). Although the fuel injector should have sealed unassisted, this was not found to be the case. Therefore, a manual shutoff valve was used for sealing the injector from fuel lines between experiments, while a solenoid was used to charge the injector immediately prior to injection; thereby minimizing the time it remained in a charged state, potentially leaking fuel into the shock tube.

The injector-charging solenoid valve was controlled by the same signal used for opening the valve that vented the intermediate chamber pressure in the double diaphragm system. This was necessary since it could not be triggered by the shock wave itself because of its excessively long opening time, which exceeded the time available before the arrival of the incident shock. To compensate for the time necessary to drain the intermediate chamber (and thus generate a shock wave), an electronic delay circuit was introduced between the two solenoid valves' control signals such that the injector-charging valve could be opened 0-9999 ms after the solenoid used for venting the intermediate chamber was opened, with typical delays between 0-400 ms throughout the present investigation. This arrangement ensured the injector was pressurized for only a few hundred milliseconds prior to injection to minimize any fuel leakage into the shock tube. The delay between opening the injector-charging solenoid valve and the start of injection was monitored by a Nicolet Instrument Corporation (NIC) 2090-I oscilloscope to measure how long the injector was in a charged state before injection to estimate total fuel leakage.

Ignition itself was detected by light emission signals observed through a 10 mm diameter fused quartz window located on the shock tube endplate adjacent to the fuel injector such that any light emitted along the length of the shock tube was detectable. While ignition is commonly detected by pressure measurements in homogeneous shock tube experiments, such a technique is impractical for non-premixed ignition delay experiments because the

quantity of fuel injected is too small to produce any detectable pressure rise upon ignition. Hence two photomultipliers, an Electron Tubes P30A and a TSI 9162, monitored CH (with a bandpass filter of 470 ± 15 nm) and broadband light emissions, respectively, from a pair of fibreoptic cables placed up against the endplate quartz window for detecting the onset of combustion.

Signals from the photomultipliers, the injector control signal, and three of the five dynamic pressure transducers (due to limited available sampling channels) were acquired using a Wavebook/512™ data acquisition system sampling at a rate of 140 kHz (corresponding to a 7.1 μ s sampling interval).

4.3.2 Procedure

Prior to each experiment, barometric pressure was recorded and the driven section gas pressure transducer was calibrated using a zero and span calibration corresponding to vacuum and atmospheric pressure (similar to the procedure used throughout all previous homogenous autoignition experiments). Both driven and driver sections of the shock tube were subsequently evacuated along with the tubing connecting the fuel injector, injector-charging solenoid, and manual shutoff valve (refer to Figure 4.1). The driven section was filled with air (Praxair medical grade) to the desired initial pressure and the driver section gas composition prepared manometrically with a mixture of helium (Praxair 99.9% purity) and air (Praxair medical grade). The data acquisition system was armed (to be triggered by the rising edge of the incident shock wave as it passed the second of five piezoelectric pressure transducers – the first transducer was used for injector triggering), the injection delay and duration were set through Westport's WCut software and the delay between the solenoid for draining the intermediate chamber pressure in the double diaphragm system and the injector-charging solenoid was set. Finally, the intermediate chamber pressure was vented, initiating the rupture of the diaphragms, and generating the desired incident shock wave.

In order to ensure a quiescent, constant pressure region behind the reflected shock wave (i.e. in the experimental test section), the specific heat ratio of the driver gas was carefully tuned. This was performed by blending air and He to yield a tailored interface between the driven and driver gases upon shock reflection from the endplate. A tailored interface is one where the pressure on either side of the contact surface is equal after the reflected shock passes through the interface (from driven to driver gas), ensuring that the contact

surface remains stationary and maximizing the experimental time. If the shock velocity across the interface is not equal, the driver gas pressure will be greater than the driven gas pressure, or vice versa, after the reflected shock passes through the interface, and the interface is said to be under-tailored or over-tailored, respectively. An under-tailored interface causes the test pressure to rise steadily as the contact surface encroaches into the driven section gas, while an over-tailored interface causes the experimental pressure to decrease due to the contact surface moving away from the experimental section. Both cases are undesirable, and thus by altering the composition (He fraction) of the driver gas, its specific heat ratio is tailored to tune the speed of sound across the contact surface and thus ensure that the pressure difference across the interface is zero. The procedure for calculating required initial conditions to produce a tailored interface was well documented by Huang¹, and a slightly modified version of the numerical code written by Huang was used in the present investigation.

Incident shock velocities were calculated from the pressure traces from each of the three monitored dynamic pressure transducers by measuring the time interval between rising edges as the shock passed each successive transducer location (see Figure 4.2). Using the measured incident shock velocity and initial driven gas properties, the experimental pressure and temperature were calculated by assuming them to be equal to the conditions immediately behind the reflected shock (as calculated using isentropic shock relations^{1,2}).

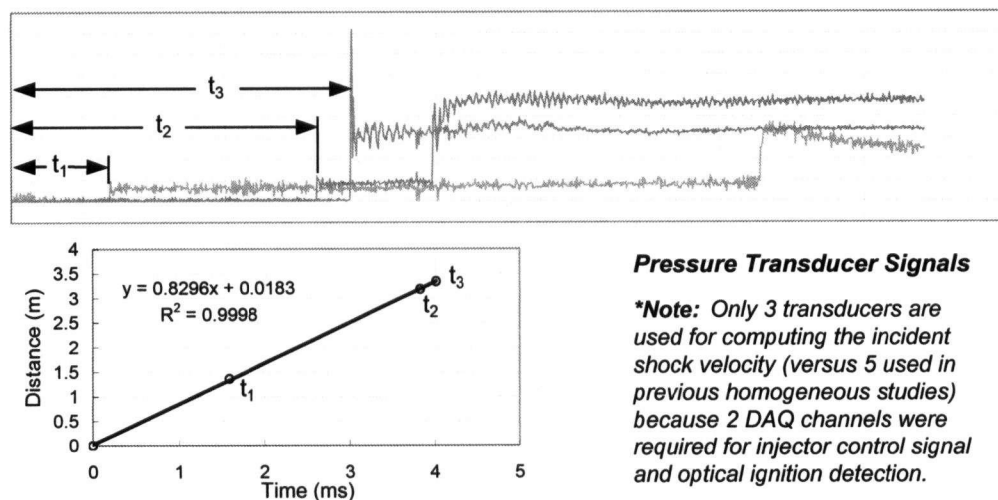


Figure 4.2: Incident Shock Velocity Measurement From Pressure Signals

The ignition delay time was defined as the time interval between the start of injection, as measured by the injector control signal (and corrected to compensate for an inherent 180

μs delay in the injector driver), and the observance of CH and broadband light emissions. In cases where the onset of ignition was not easily identifiable from light emission signals, the intersection of a line tangent to the curve at its inflection point (maximum slope) with its initial baseline was used (see Figure 4.3). Such a definition has been previously used by other researchers in homogeneous autoignition studies⁴ and was employed throughout the current investigation, with ignition measured independently from both broadband and CH band emissions signals.

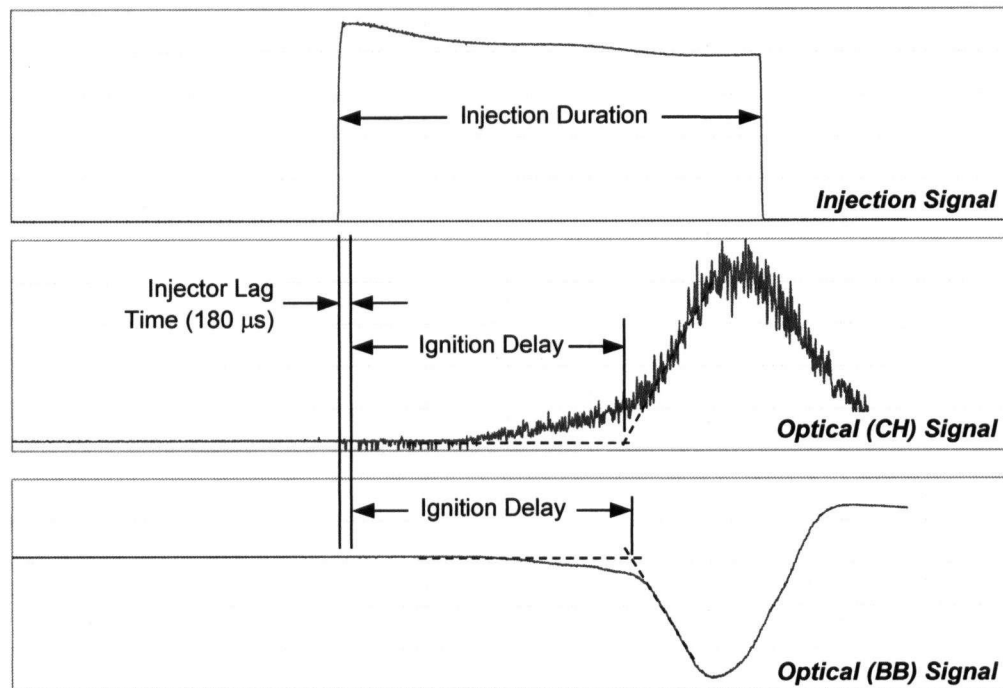


Figure 4.3: Ignition Definition From Optical Emissions Signals

4.4 Experimental Results

The autoignition behaviour of non-premixed methane injected into shock-heated air differs from the behaviour of homogeneous mixtures due to the presence of a diffusion flame and therefore the effects of both chemical kinetics and fluid mechanics on the ignition times were investigated. These included studying the effects of experimental temperature and pressure (directly affecting chemical reaction rates) and also studying parameters influencing the turbulent jet, such as the injection duration and pressure ratio. The results of experimental investigations examining the influences of each of these parameters are presented below.

4.4.1 Autoignition Sensitivity to Fluid Mechanic Parameters

The ignition delay time's fluid mechanic dependence was explored by varying the injection duration and pressure ratio at nominal experimental pressures of 17 and 31 bar. Injection durations between 0.5-5.0 ms and injection pressure ratios between 3-5 were chosen for investigation, as they represent typical diesel engine operating parameters. These test conditions are summarized in Table 4.1 with experimental data available in Appendix G.

Table 4.1: Experimental Test Matrix (Non-Premixed Fluid Mechanic Parameter Study)

Experimental Temperature:	1000-1400 K
Experimental Pressure:	17-31 bar (nominal)
Injection Duration:	0.5-5.0 ms
Injection Pressure Ratio:	3-5 (nominal)

Injection Duration Sensitivity

Injection duration (the time interval during which fuel injection occurs) was the first fluid mechanic parameter governing a transient jet's influence on the establishment of a diffusion flame to be investigated. Injection duration was initially speculated to have a potential influence on methane's autoignition behaviour by virtue of its fuel metering properties, control of overall mixture equivalence ratio, and cooling effects. Additionally, the transient nature of short-duration impulsive jets produces a direct flow field dependence on injection duration, which dictates the temporal evolution of temperature, species, and velocity gradients in the flow, which in turn influence the thermodynamic, kinetic, and transport processes necessary for autoignition. These effects were investigated at a constant experimental pressure of 31.2 ± 0.8 bar and a temperature of 1107 ± 7 K, with the injection pressure ratio maintained at 3.0 ± 0.1 .

Results of all measured autoignition times at each investigated injection duration are presented in Figure 4.4, illustrating the presence of two distinct ignition regimes; one strongly dependent on injection duration, and another independent of the injection duration. Short injection durations ($< \sim 3.0$ ms) exhibited a strong autoignition delay time dependence on injection duration, with decreased injection durations resulting in shorter ignition delay times, but long injection durations yielded autoignition delay times that were approximately independent of the injection duration. Additionally, in the injection duration-dependent regime, autoignition times increased nearly linearly with injection duration, with the shortest autoignition times quantitatively just slightly

longer than the premixed autoignition delay time of 1-1.2 ms measured at similar experimental conditions¹.

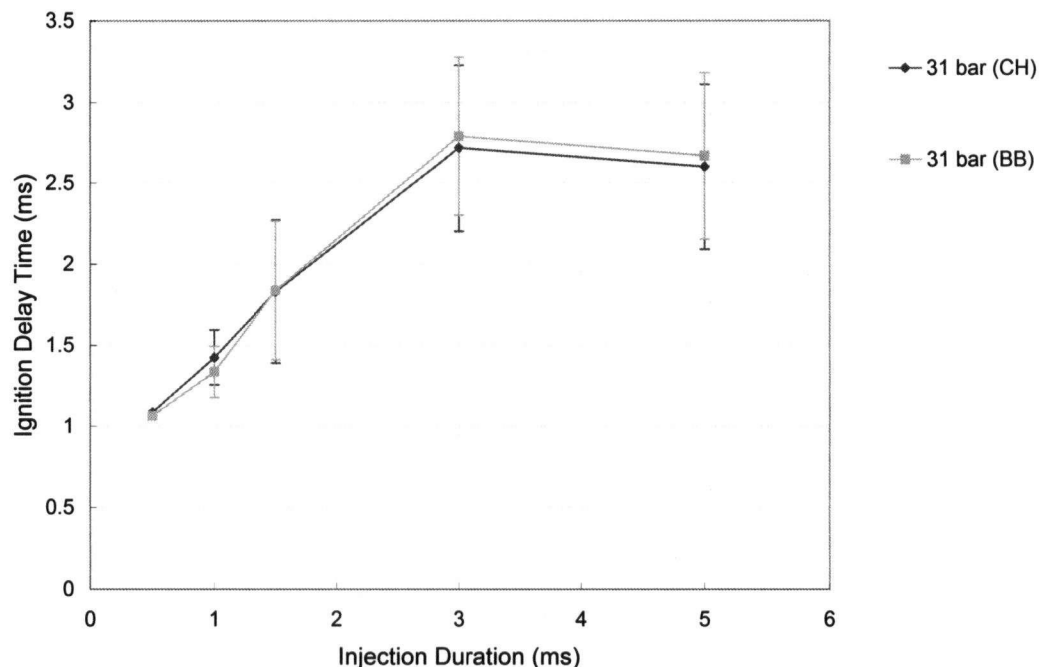
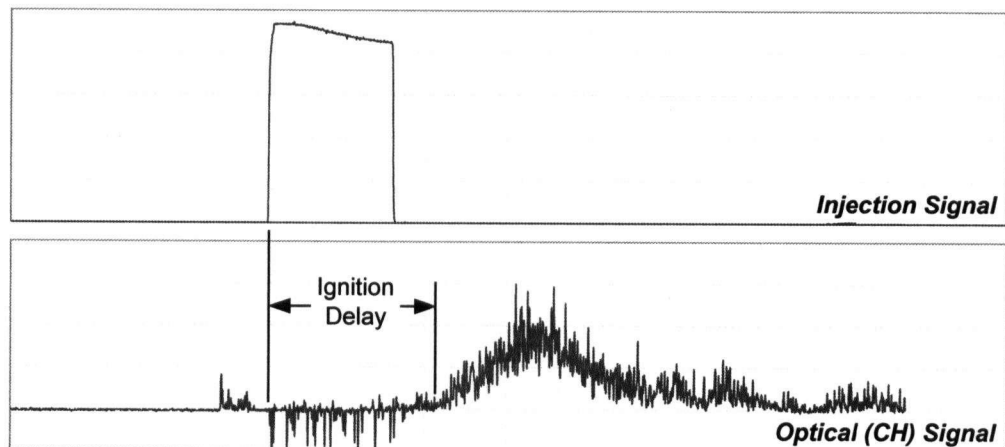


Figure 4.4: Autoignition Injection Duration Sensitivity

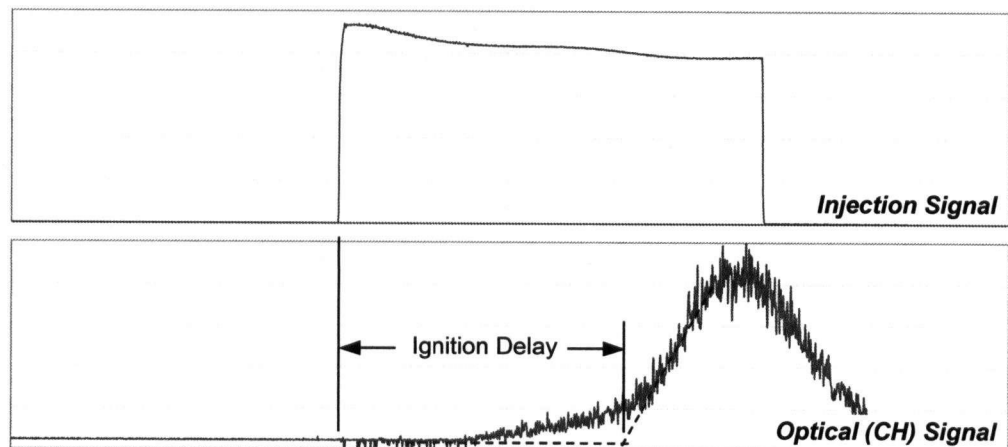
The presence of the threshold below which ignition delay times depend on injection duration and above which are independent of injection duration also coincides with two distinct ignition modes observed in each regime. For injection durations shorter than 3.0 ms, ignition occurred after the end of injection and in most cases produced clear optical emission signals that unambiguously identified ignition (refer to Figure 4.5 (a)). In contrast, for injection durations greater than 3.0 ms, ignition occurred during injection, but optical emissions signals consistently exhibited a gradual rise or a slight initial plateau, indicative of mild reactivity, followed by a sudden increase in combustion intensity near the end of injection or shortly thereafter (Figure 4.5 (b)).

Both the presence of injection duration dependent and independent regimes and the approach to premixed autoignition times for short injection durations are explicable if one adopts the notion of a “kinetic” and “physical” component to ignition delay times as done by Bi and Agrawal⁴⁴. They defined a kinetic delay as the ignition delay time component attributable to the chemical reaction and a physical delay as the portion attributable to the time necessary for the fuel and oxidant to mix and create a locally combustible mixture with a sufficiently favourable strain rate to facilitate autoignition.

Employing such a model, infinitesimally short injection durations would be expected to nearly instantly produce a combustible mixture (negligible mixing time scales) and the autoignition time should approach the kinetically-limited premixed autoignition delay time. At the opposite extreme, long injection durations reach a steady state after a fixed period of time (regardless of total injection duration) and only produce a combustible mixture once the physical delay is exceeded. Between each extreme, injection ceases prior to sufficient time elapsing to overcome the physical delay, but the sudden decrease in strain that occurs immediately at the end of injection rapidly reduces strain rates to levels that allow ignition. Hence, for short injection durations, autoignition occurs shortly after the end of injection and scales linearly with injection duration.



(a) Clearly Defined Autoignition Delay Typical of Short Injection Durations (< 3.0 ms)



(b) Mild Reactivity Preceding Autoignition Typical of Long Injection Durations (> 3.0 ms)

Figure 4.5: Characteristic Optical Ignition Signals Over Two Regimes

Furthermore the observed qualitative differences between optical emissions signals may also be explained by considering the physical and kinetic components of the ignition delay time. The clearly defined optical emissions signals observed for short injection durations are characteristic of those seen in premixed ignition experiments in which an ignition kernel is formed and rapidly spreads. This similarity suggests a shared ignition mode, reinforcing the theory that kinetics dominate ignition for short injection durations. Likewise, the region of mild reactivity preceding ignition for long injection durations is analogous to the "Luminosity Threshold" observed by previous researchers studying steady-state counterflow diffusion flames^{30,31}. In their study of counterflowing cold methane and heated air, they described the luminosity threshold as a state where the mixture glows but does not rigorously burn. In particular they described it as a threshold, because as they gradually increased the temperature of the air jet, the luminosity threshold was defined as the threshold temperature above which luminescence was observed. Observation of a phenomenon analogous to a luminosity threshold in the present study suggests a shared ignition mode between steady-state counterflow jets and the current results for long injection durations.

In addition to qualitative evidence presented herein of the transition from kinetically-limited to mixing-limited combustion, quantitative data also exists supporting such a theory. The recent work by Fotache et al.,³⁰ who investigated the ignition behaviour of counterflow methane-air diffusion flames, affirmed that the flame kernel governing ignition in diffusion flames is essentially a premixed system and behaves similar to homogenous systems, just as qualitatively observed in the present investigation for short injection durations. Additionally, they stated the kernel width was proportional to the square root of the density weighted strain rate and through this relationship all convective-diffusive transport processes influence ignition. Increased strain rates decrease the kernel width and allow heat and many of the stable radicals involved in methane oxidation to convect or diffuse away from the ignition kernel. This explains the observed lack of ignition while injecting, as high strain rates present in the jet convect and diffuse away the heat and radicals necessary for the flame kernel to grow. Additionally, this phenomenon may possibly be responsible for the observed "Luminosity Threshold". As an initial homogenous flame kernel forms, it is inhibited from spreading and further igniting surrounding regions of the jet, giving rise to mild reactivity or multiple ignition/extinction cycles before ignition. Subsequently when injection ends, or sufficient time elapses to convect the flame kernel to a low strain

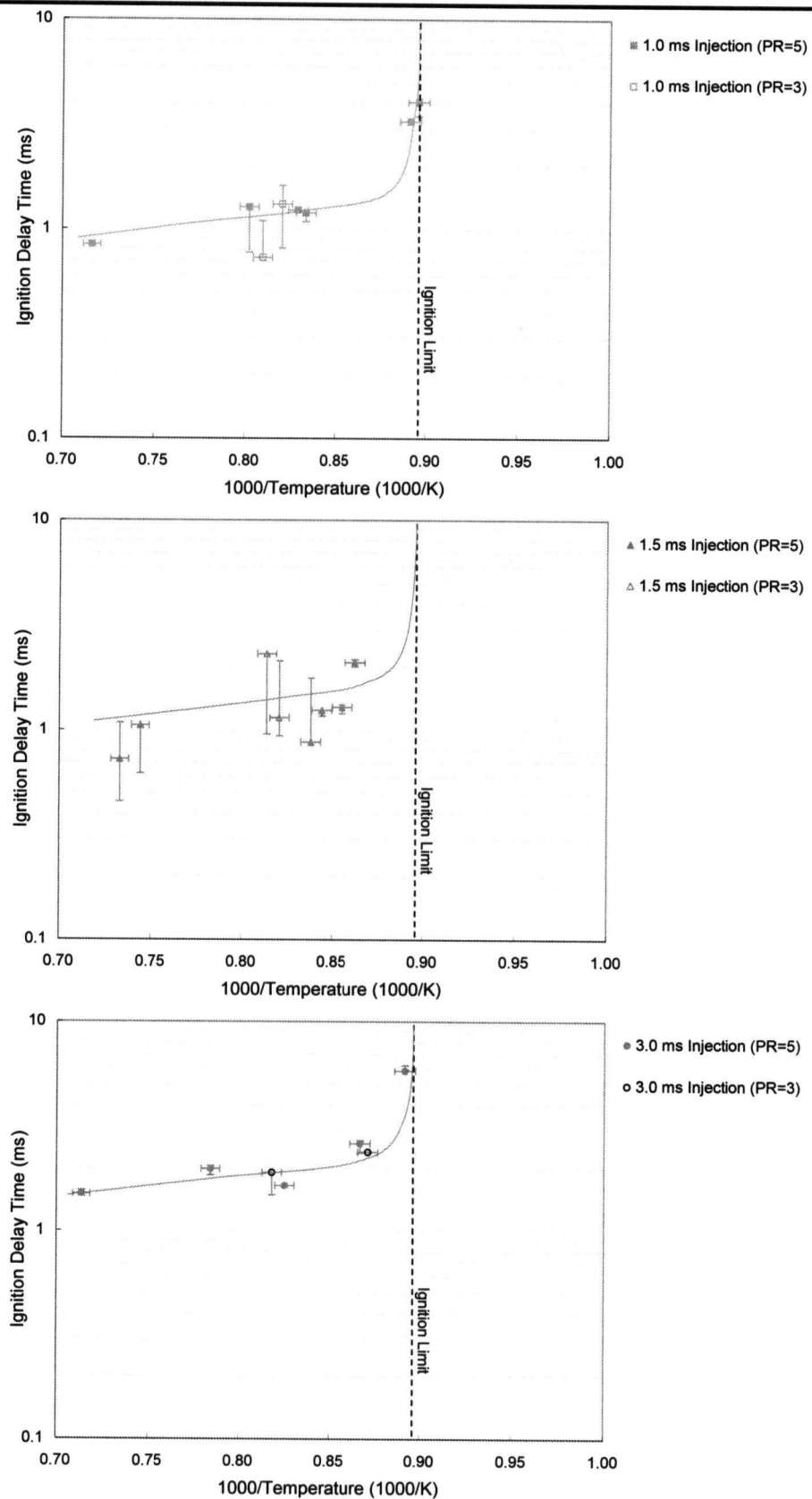
or high temperature region of the flow, the flame kernel is able to spread, and hence the observed abrupt increase in light emission (Figure 4.5 (b)). The counteracting influences of the chemical heat release and the convective and diffusive losses from the ignition kernel identified by Fotache et al. as dominant forces governing ignition in diffusion flames may be used in conjunction with Bi and Agrawal's concept of a kinetic and physical delay to explain the present dependence on injection duration.

Injection Pressure Sensitivity

Having identified the concepts of a kinetic and physical delay as being relevant to the present results and the importance of strain rate in the autoignition process by its promotion or inhibition of flame kernel growth, experiments were conducted to further investigate the effects of strain rate. However, since the strain in a turbulent jet cannot be controlled as it can in counterflow diffusion flame studies, the injection pressure ratio was varied instead. The intention being that increasing the injection pressure would yield a higher Reynolds number and the increased turbulence would produce higher mean strain rates. Several tests were conducted at an experimental pressure of 17.0 ± 0.9 bar and a temperature of 1199 ± 34 K, at each of two injection pressure ratios, 2.7 ± 0.2 and 5.0 ± 0.3 , chosen for their diesel engine relevance.

The result of varying the injection pressure ratio was negligible and no noticeable difference between each pressure ratio at each of several injection durations tested was observed (see Figure 4.6). This was caused by several factors including very large experimental uncertainties inherent in autoignition delay measurements that may mask any differences (note the large error bars on some data points in Figure 4.6), the relatively small difference between each of the pressure ratios tested, and a genuine autoignition delay independence from injection pressure. This latter point is the most noteworthy. Although increasing injection pressure certainly improves mixing between fuel and oxidant and may be beneficial in certain pollutant formation processes, it does not appear to reduce autoignition delays. Support for this finding is provided by the work of Mastorakos et al.⁴³

Mastorakos et al. addressed seemingly contradictory findings whereby experiments had shown that turbulence *decreases* ignition delay times while laminar flame theory suggests that higher strain rates associated with turbulence should prevent ignition and thus *increase* ignition delay times. Their work involved conducting numerical

**Figure 4.6:** Autoignition Injection Pressure Ratio Sensitivity

simulations of various mixing flows of cold (300 K) fuel and hot (1000-1100 K) air to identify the conditions that favoured early ignition. They discovered that ignition was initiated at several locations simultaneously and that these locations were all at the "most reactive" mixture fraction where scalar dissipation rate is lowest. Furthermore the most reactive mixture fraction was found to be in the fuel lean regions, believed to be due to higher temperatures in the lean region compensating for the reduced fuel concentration through the reaction rate's exponential temperature dependence.

However, in addition to mixture fraction requirements, ignition was also conditional upon the lowest possible scalar dissipation. This conditional dependence on scalar dissipation rate offered an explanation as to why (1) partially premixed flows have been found to ignite earlier than non-premixed flows, and (2) turbulent flows ignite earlier than laminar ones. Partially premixing the fuel and air yields smaller mixture fraction gradients and hence lower scalar dissipation rates, while turbulence, with its many length and time scales and its chaotic nature creates regions of both very high and low scalar dissipation rate. The regions of unusually low scalar dissipation rate preferentially ignite and hence result in shorter ignition delay times than in laminar flows despite the higher mean strain. Additionally, since ignition in turbulent flows always occurs in regions of unusually low strain rate, and such regions are present regardless of the turbulence intensity, ignition delay time is independent of turbulent time scales. So their conclusion was that the turbulent length and time scales and partial premixing affect ignition by their effect on the conditional scalar dissipation rate.

Applying the concepts presented above to the current experimental findings, it is not surprising that increasing the injection pressure ratio did not have any effect on the measured ignition delay times. Since the flow is already turbulent at the lower of the injection pressures investigated, increasing injection pressure further only increases the turbulence and has minimal impact on the conditional scalar dissipation rates in the flow. Certainly, if the injection pressure were increased excessively, a negative impact on the ignition delay times would be expected since then the turbulence may inhibit autoignition by dissipating any heat released in the combustion process so rapidly that any small flame kernels that are formed are immediately extinguished. However, for the injection pressure ratios presented here, no autoignition delay time dependence on injection pressure was observed.

4.4.2 Autoignition Sensitivity to Chemical Kinetic Parameters

The ignition delay time's kinetic dependence was investigated by varying the experimental temperature and pressure behind the reflected shock wave. Temperatures between the ignition limit and 1400 K were investigated at two nominal experimental pressures (17 bar and 31 bar) chosen to correspond with conditions previously explored in premixed ignition studies to facilitate direct comparison with existing results. Additionally, given the injection duration dependence discussed above, several injection durations between 0.5-5.0 ms were investigated at each test condition. These experimental conditions are summarized in Table 4.2.

Table 4.2: Experimental Test Matrix (Non-Premixed Chemical Kinetic Parameter Study)

Experimental Temperature:	1000-1400 K
Experimental Pressure:	17-31 bar (nominal)
Injection Duration:	0.5-5.0 ms
Injection Pressure Ratio:	3 (nominal)

Experimental (Air) Temperature Sensitivity

Results of measured autoignition delay times conducted at 31.1 ± 1.4 bar (including data from the previously discussed injection duration sensitivity study) are presented in Figure 4.7. This figure illustrates the expected temperature dependence, namely decreased ignition delay times with increased experimental (air) temperature. Also, in addition to the present experimental results, two additional curves are included in this figure plotting ignition delays measured by Huang¹ in a previous homogeneous ignition delay study conducted at similar experimental conditions. Although at first the ignition delay reduction with increased experimental temperature from 1100 K to 1400 K does not appear to be as large as that observed in premixed ignition delay studies (partly due to the logarithmic scale), the absolute magnitude of the reduction ($\sim 600 \mu\text{s}$) is nearly identical. This is not unexpected since increasing experimental temperatures accelerate chemical reactions and correspondingly reduce the kinetic component of the autoignition delay time. Since both non-premixed and premixed ignition delay times exhibit nearly identical reductions with increasing temperatures, this suggests that *only* the kinetic delay is affected by temperature. The qualitative agreement between the present non-premixed results and previous homogeneous ignition delay times thus reinforces the theory of a kinetic and physical component to non-premixed ignition delay times.

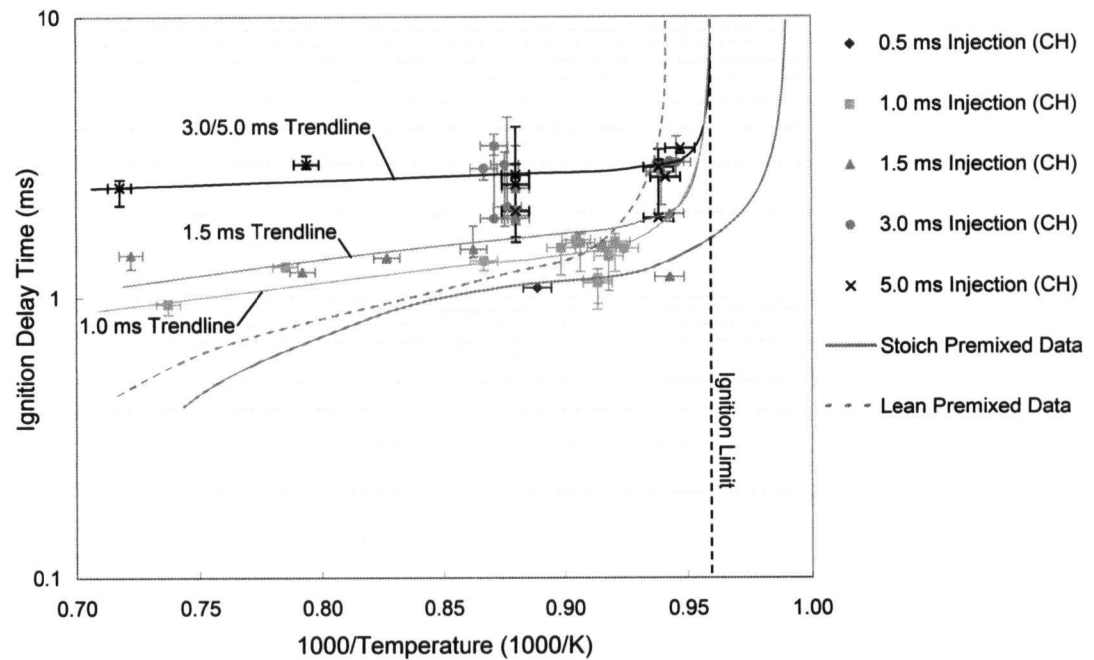


Figure 4.7: Autoignition Temperature Sensitivity (31 bar)

Furthermore, numerical simulations by Bi and Agrawal⁴⁴ similarly concluded that the kinetic delay decreases as temperatures are increased, but in addition they stated that the physical delay also exhibited a reduction at increased temperatures. While in the present study, the magnitude of the ignition delay reduction was found to be approximately equal to only the kinetic reduction (no additional reduction attributable to the physical delay was observed), any physical delay reduction may have simply been too small to detect given large experimental uncertainties. While the ignition delay time's kinetic component is greatly reduced by increased temperatures (due to the chemical reaction rate's exponential temperature dependence), no such reason exists suggesting that the physical delay should exhibit a similar dependence. If the physical component of the ignition delay time is reduced at elevated temperatures it must be attributable to the increased thermal gradients between the heated air and relatively cold fuel, which enhance heat and mass transfer. However, kinetics are far more strongly dependent on temperature than mixing rates are, and therefore the physical delay remains approximately constant.

Experimental (Air) Pressure Sensitivity

To further explore the ignition delay time's kinetic dependence, the tests presented above were repeated at a lower pressure of 16.8 ± 1.0 bar to observe the influence of

the reduced pressure on ignition delay times and explore whether the temperature dependence observed at higher pressures was preserved at a lower test pressure. These results are presented in Figure 4.8 illustrating that the reduced experimental pressure had a minimal impact on the magnitude of the ignition delay times relative to the high-pressure results, but the pressure reduction greatly affected the ignition limit (the temperature below which ignition was no longer observed).

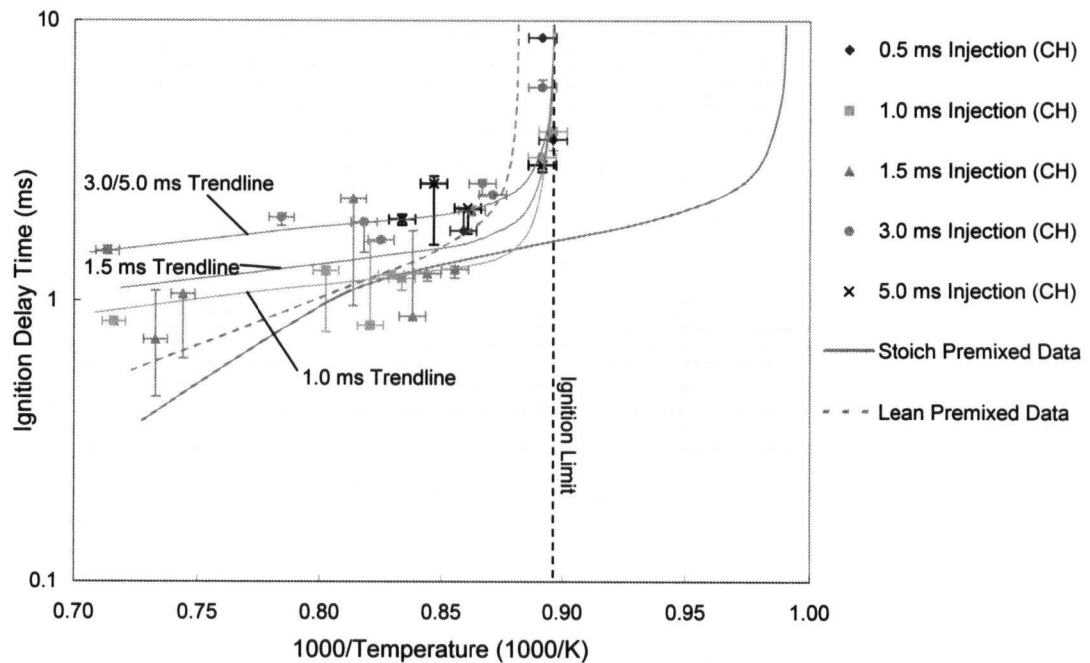


Figure 4.8: Autoignition Temperature Sensitivity (17 bar)

At similar temperatures, ignition delay times at each injection pressure were equal (within experimental uncertainty). This was not unexpected since minimal pressure dependence was observed in a previous homogenous ignition study¹, and Fotache et al.³⁰ indicate that the flame kernel governing diffusion flame's ignition behaves like homogenous systems. However, previous homogeneous autoignition studies found that the ignition delay times *increased* slightly at lower pressure (due to the reduced reactant concentrations) while the present results do not exhibit any increase at all. In fact, a slight *reduction* is seen for some injection durations. While this apparent reduction is not fully understood, it is believed to be partially a manifestation of the luminosity threshold phenomenon observed at higher pressures.

Fotache et al. in their investigation of counterflow diffusion flames indicated that the luminosity threshold approached the ignition temperature at elevated pressures, and

eventually vanished altogether. Therefore, while at higher pressures, the luminosity threshold was easily identifiable because its magnitude was small (vanishing with increased pressure) relative to the ignition signal, at the reduced pressure of 17 bar, the magnitude of this luminosity was comparable to that of ignition signals, and may have been mistakenly interpreted as ignition. This theory is supported by noting that short injection durations exhibited equal autoignition delay times at both pressures, suggesting pressure has a negligible effect on ignition delay, while longer injection durations coincide with the lower error bounds of the data presented in Figure 4.7. These lower error bounds identify the luminosity threshold and interestingly, even at 31 bar several data points from the long injection durations exhibited ignition delay times as short as those seen at 17 bar. This further suggests that at low pressures, and occasionally at higher pressures, the luminosity can be of comparable intensity to the ignition signal and hence cause the observed apparent reduction in ignition times. Figure 4.9 below illustrates this phenomena by plotting several realizations of the "luminosity threshold" to illustrate how the magnitude of the light emission can vary widely. Bearing in mind that the slight apparent ignition delay time reduction for long injection durations may thus not be genuine but simply due to luminescence, then ignition in non-premixed combustion is essentially independent (or extremely weakly dependent) on experimental pressure. It should be expected that the kinetic component of the ignition delay would be slightly reduced with elevated pressures based on previous homogeneous ignition delay results, but the physical delay would not experience any such reduction if the injection pressure ratio were preserved.

To further clarify the negligible change, or perhaps even slight reduction, in ignition delay times at low pressure, ignition delay times measured at each of four injection durations are plotted in Figure 4.10. At each injection pressure, measured ignition delay times fall within experimental error of each other. For short injection durations (1.0 ms and 1.5 ms) the data points collected at 17 bar are scattered equally above and below the trend line plotted based on 31 bar data. At longer injection durations of 3.0 ms and 5.0 ms, the 17 bar data remains within experimental error of the 31 bar data's trendline, but is slightly biased towards shorter ignition delay times. This bias is attributed to the luminosity threshold effects discussed above.

Aside from the negligible impact on ignition delay times, experimental pressure did exhibit a very strong effect on the ignition limit and quantitatively, the magnitude of

the ignition limit shift agreed well with that observed in lean premixed experiments. In the present tests, the ignition limit shifted approximately 70 K (from 1050 K at 31 bar to 1120 K at 17 bar), while a similar pressure reduction yielded a 70 K increase in the ignition limit in lean homogeneous autoignition experiments. In addition to the remarkable agreement between these two cases it is also significant to note that this behaviour is markedly different from the response of stoichiometric mixtures at the same pressures. Unlike the lean data, stoichiometric mixtures failed to demonstrate any ignition limit pressure dependence. This close agreement with lean premixed results lends further support to the belief that autoignition in non-premixed mixtures occurs in fuel-lean regions. Such dependence has also been expressed by Bi and Agrawal and Mastorakos et al. in previous simulations who all suggested ignition preferentially occurs in fuel-lean regions due to higher temperatures in these areas.

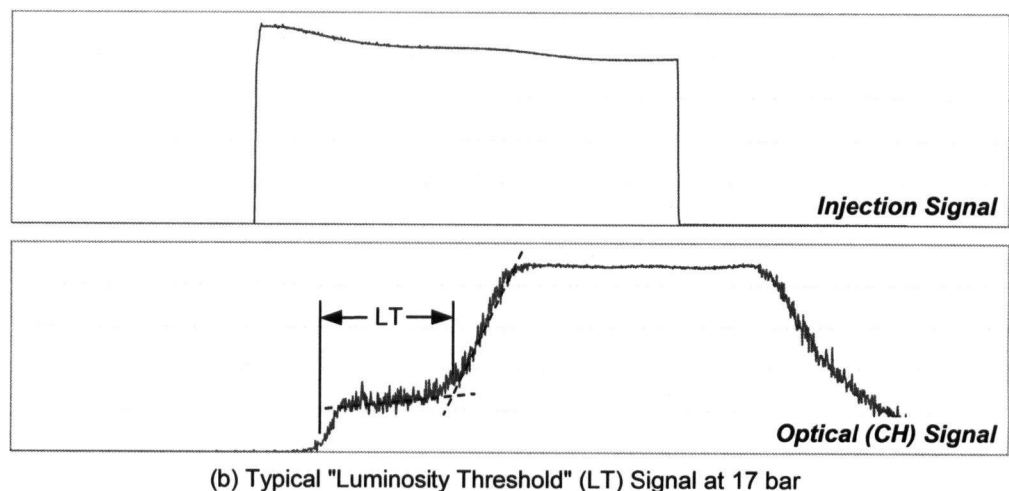
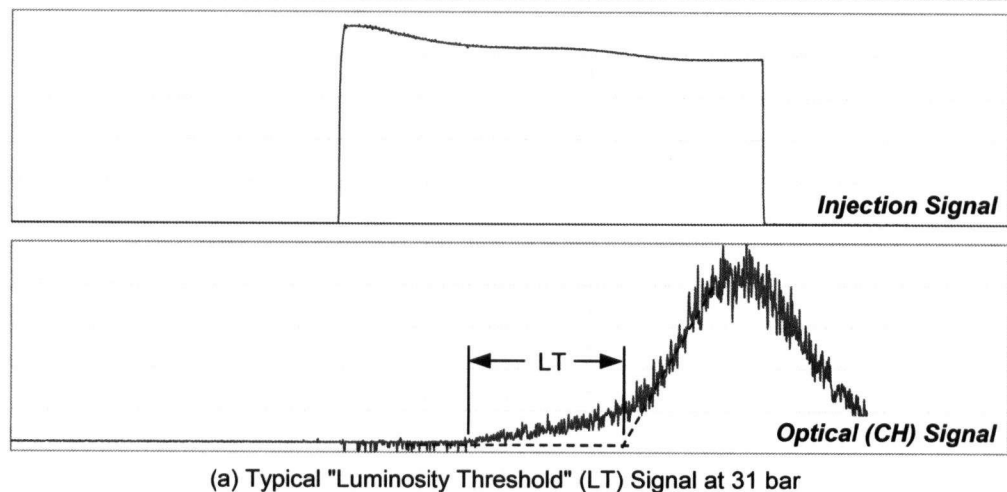
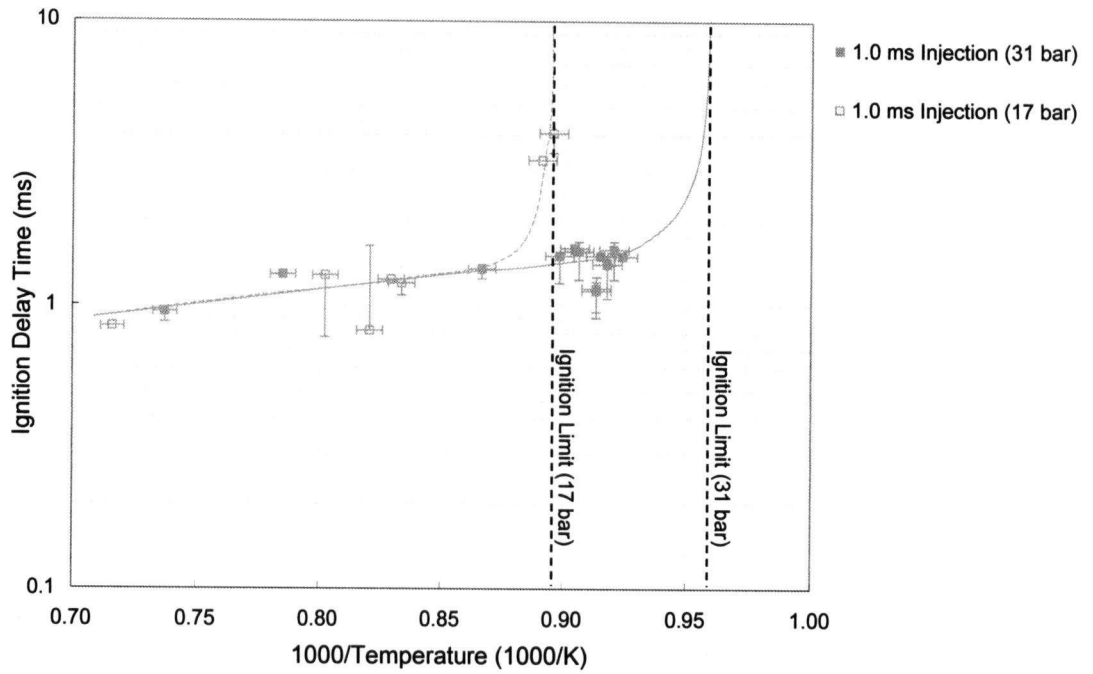
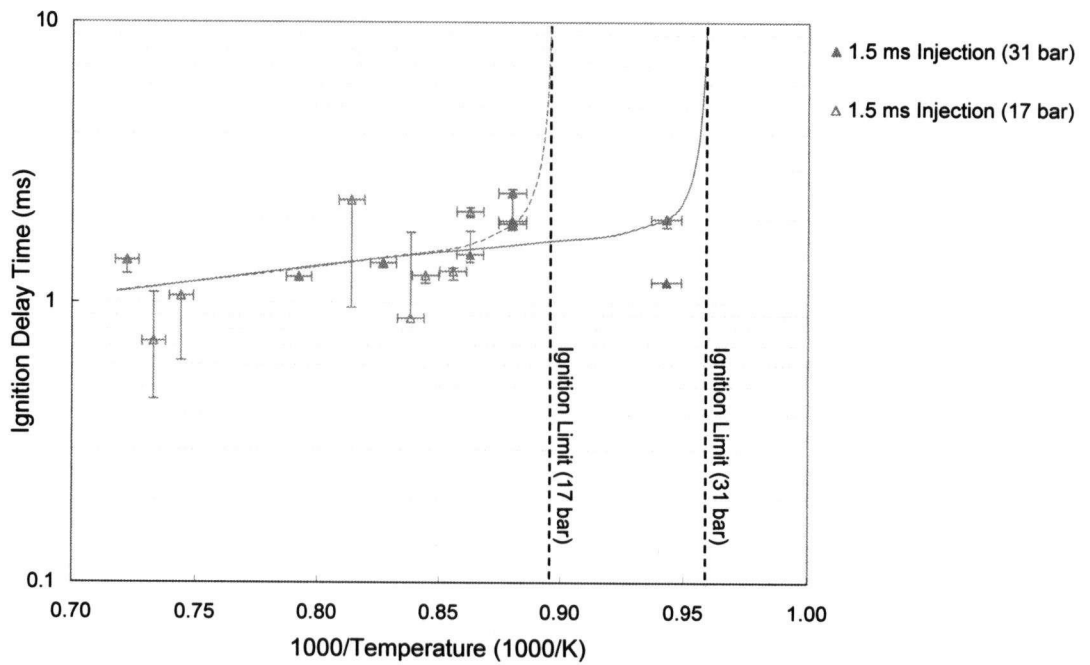


Figure 4.9: Differences in Luminosity Threshold with Pressure

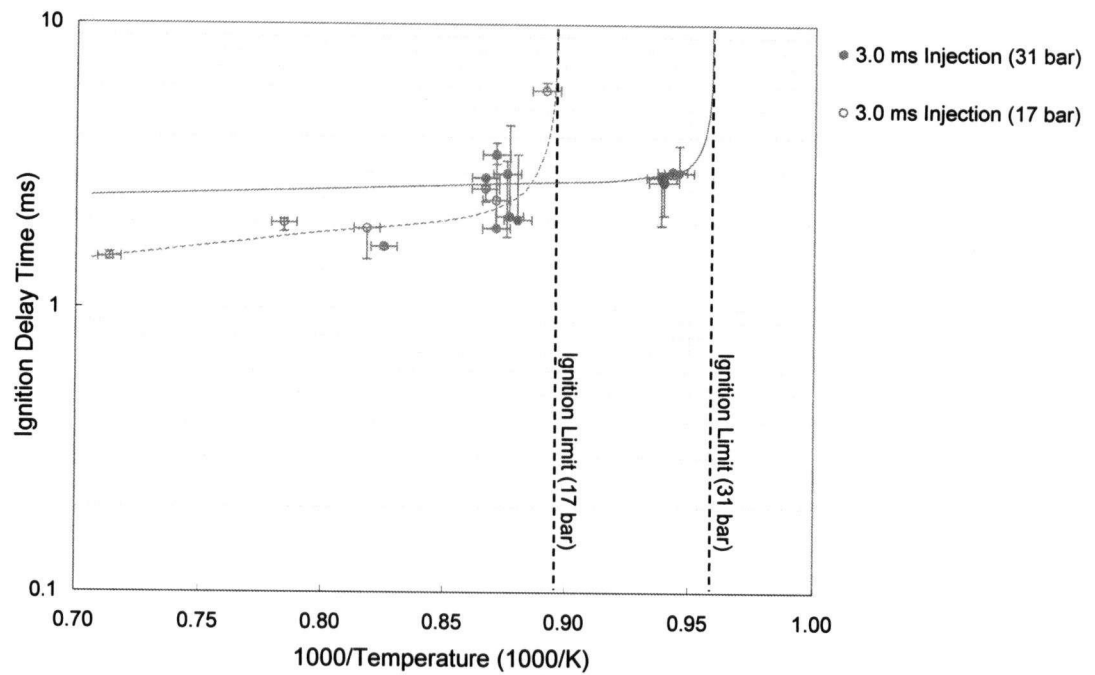


(a) 1.0 ms Injection Duration

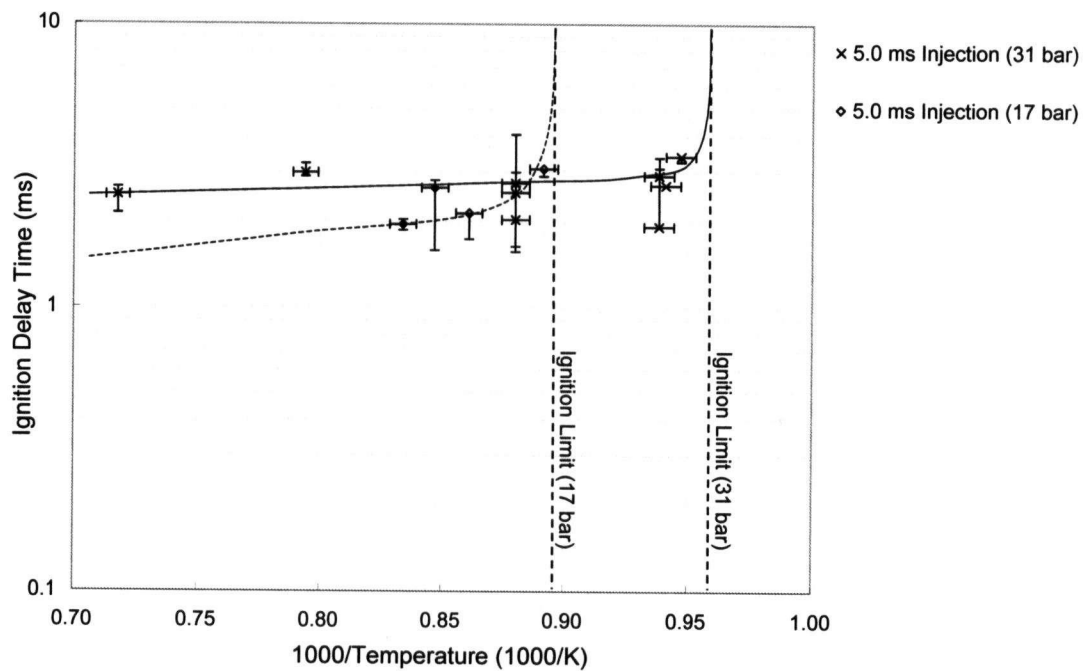


(b) 1.5 ms Injection Duration

Figure 4.10: Autoignition Pressure Sensitivity



(c) 3.0 ms Injection Duration



(d) 5.0 ms Injection Duration

Figure 4.10: Autoignition Pressure Sensitivity cont'd.

4.4.3 Error Analysis

Throughout all current experiments, all error sources previously present in homogeneous autoignition studies were present (Appendix C), with the exception of the error associated with ignition delay measurements and uncertainty in driven gas compositions. Uncertainty in ignition delay times attributable to ambiguous pressure traces in homogeneous ignition delay experiments was replaced by errors associated with ambiguous optical emissions signals, and although uncertainty in the driven gas composition was eliminated since the driven gas was now pure bottled air (eliminating errors in preparing the gas composition manometrically), leakage through the injector yielded uncertainty in the fuel injected.

Ignition Delay Time Error

Ignition delay time errors were primarily associated with the frequent uncertainty in identifying the onset of ignition from light emission signals. Several typical ignition signals are presented in Figure 4.11 to illustrate how upper and lower bounds were defined in such cases.

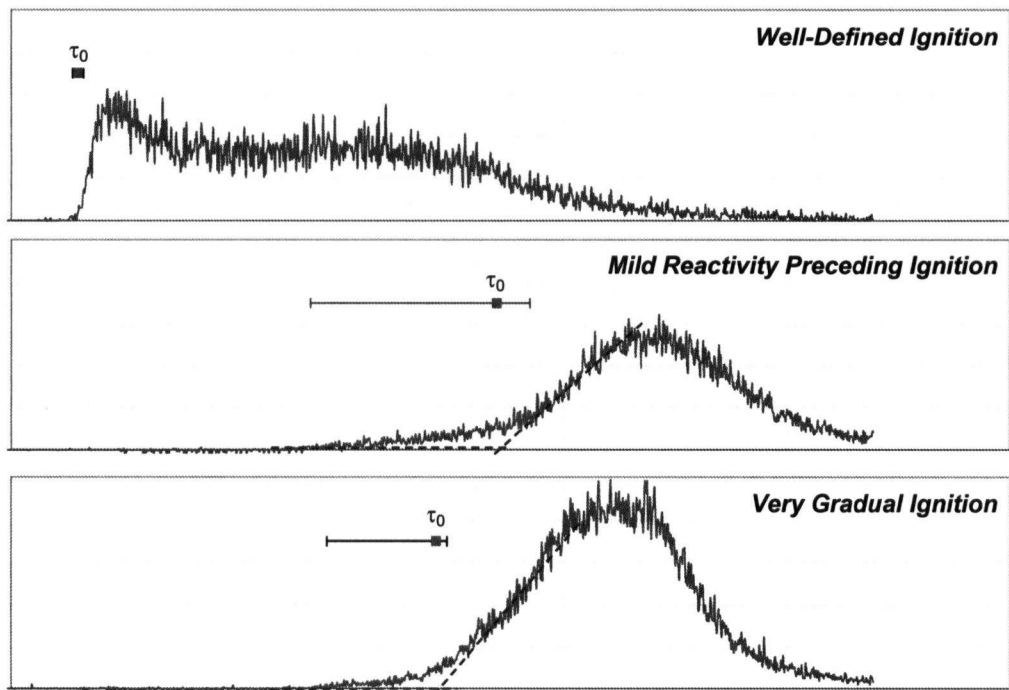


Figure 4.11: Characteristic Optical Emission Signals Over Three Ignition Regimes

In cases where ignition was very well defined and the optical emission signals were strong, minimal errors were introduced, and were on average approximately ± 0.080

ms (Figure 4.11 (a)). When the ignition signal was preceded by weak light emission the lower error bound was defined as the time when the initial weak light emission occurred and upper bounds defined as the time when a slope change was observed in the light emission intensity, signalling a change from mild reactivity to much more rigorous burning (Figure 4.11 (b)). As a result, no quantitative mean error could be defined, since this varied widely from case to case. Finally, when optical emissions signals exhibited a very gradual rise (Figure 4.11 (c)) upper and lower error bounds were defined as shown, with average errors typically in the range of ± 0.100 ms to ± 0.400 ms.

Fuel Mass Flow Error

Uncertainty in the quantity of fuel present (due to leakage) produced no quantifiable effect on measured ignition delay times, but contributed to qualitative uncertainty in analysing the effects of injection durations. Despite previous characterization of the J41 injector used in the present investigation demonstrating a constant fuel mass flux regardless of injection duration ($\pm 10\%$), the effects of any fuel leakage prior to injection are not easily quantified. Though a leakage mitigation system was installed upstream of the fuel injector (Figure 4.1), the injector remained in a charged state for typically 200-800 ms prior to injection. Throughout this time, fuel leakage into the shock tube created a cloud of partially premixed fuel and air in the vicinity of the injector nozzle, which may have had the net effect of promoting ignition. It has been shown by previous researchers⁴³ (and discussed in this investigation) that partially premixing fuel and oxidant promotes ignition by reducing mixture fraction gradients in the flow. The effect of any leakage through the injector would produce precisely such an effect and, while extremely desirable if effective in reducing ignition delay times, this effect introduced an unquantifiable degree of uncertainty throughout all experimental results.

4.4.4 Autoignition Visualization

While identifying the ignition delay time dependence on both kinetic and fluid mechanic parameters of interest, extensive reliance on concepts presented by Bi and Agrawal⁴⁴ and Mastorakos et al.⁴³ was necessary. While the ignition delay data seemed to corroborate those theories, many of the concepts they discussed were unrelated to the ignition delay itself, but rather focussed on the ignition location (fuel lean regions, multiple simultaneous

ignition sites, etc.). So to further explore the present interpretation of theories put forth by previous researchers, autoignition delay experiments were conducted with an optical test section in place to facilitate capturing high-resolution digital images of the ignition event at various stages in the autoignition process. Experiments were conducted at a pressure of 6 bar (nominal), with temperatures between 1250-1400 K (1250 K was determined to be the ignition limit at this pressure), and injection durations between 1.0-5.0 ms. These test conditions are summarized in Table 4.3 with digital images available in Appendix H.

Table 4.3: Experimental Test Matrix (Autoignition Visualization Study)

Experimental Temperature:	1250-1400 K
Experimental Pressure:	6 bar (nominal)
Injection Duration:	1.0-5.0 ms
Injection Pressure Ratio:	4 (nominal)

Apparatus Modifications

To facilitate high-speed digital photography of autoignition events, the experimental apparatus in Figure 4.1 was modified with the addition of an optical test section at the end of the driven section. The optical test section contained three fused quartz windows (for observing ignition events in the shock tube) and one instrumentation window (for mounting a pair of pressure transducers). Figure 4.12 illustrates this modified setup, with detailed drawings of the optical test section itself available in Appendix J. The addition of an optical test section lengthened the driven section by 0.54 m, thus resulting in a total shock tube length of 7.90 m (3.11 m driver section, 4.79 m driven section).

With the addition of the optical test section, light emission signals could no longer be detected from the driven section endplate, since it could no longer accommodate a window and fibreoptic cable. Instead a fibreoptic cable was mounted up against one of the three large quartz windows along the sides of the test section. Although there was initial concern whether such an arrangement was capable of detecting any light emitted downstream of the fibreoptic cables' location, this was not found to be a problem. Additionally, since previous tests had demonstrated excellent agreement between CH and broadband optical emissions, only CH band emissions were used for detecting ignition, as the fibreoptic cable previously used for detecting broadband light was required by the Schlieren imaging system.

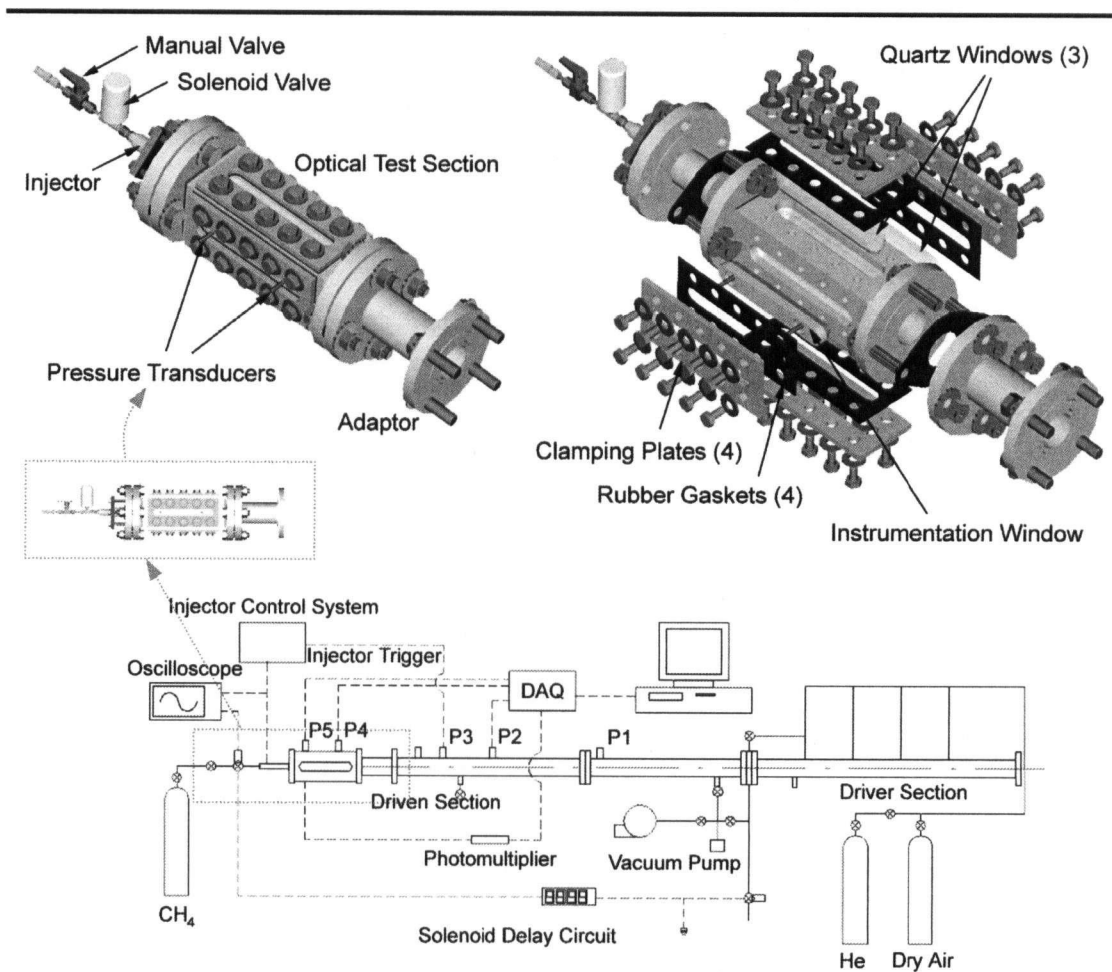


Figure 4.12: Experimental Apparatus (Autoignition Visualization Study)

A Schlieren imaging system was assembled to facilitate visualization of the gaseous jet within the test section. This system was adapted from the one previously used for investigating the jet characteristics of the injector used in the current tests (refer to Chapter 3 for component descriptions). However, space limitations prevented the use of that system in its original configuration, so a modified version was developed to reduce its size (total distance between lenses and mirrors – refer to Figure 4.13). This modified Schlieren system focussed the light from a 200 W mercury arc lamp onto the end of a 0.5 mm diameter fibreoptic cable. This fibreoptic cable replaced a pinhole and allowed both the arc lamp and focussing lens to be located off-axis from the mirrors and lenses used to produce a parallel light beam. The light transmitted through the fibreoptic cable was passed through a 15.24 cm (6 in) diameter double convex lens with a 43.18 cm (17 in) focal length to produce a parallel light beam to pass through the test section's quartz windows. Additionally, to further minimize the

system's total length, rather than having a second converging lens on the opposing side of the test section to focus the parallel light onto a camera, a mirror was used. The mirror reflected the parallel beam back through the test section and through the convex lens, focussing the Schlieren image immediately adjacent to the fibreoptic cable. Although the use of such a fibre optic cable is unconventional for Schlieren systems, passing the parallel light beam through the test section twice and using the same lens to both produce the parallel light and focus the Schlieren image has been previously used successfully by others⁴⁵.

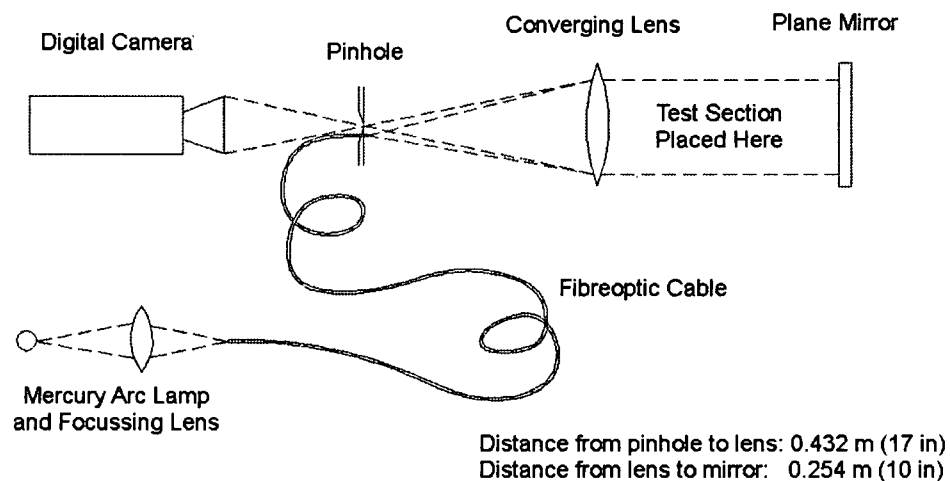


Figure 4.13: Compact Schlieren System Schematic

Finally, since the circular parallel light beam was cropped as it passing through the rectangular quartz windows, the focussed image was correspondingly rectangular, not circular. Therefore, instead of using an aperture to resolve density gradients in all directions (as previously done when testing the injector) or using a single knife edge to resolve density gradients perpendicular to the knife edge (as in conventional Schlieren systems) a rectangular aperture was created. This consisted of four knife edges that could be independently adjusted to "frame" the focussed image, allowing density gradients in two orthogonal directions to be resolved. The resulting image was photographed with a Kodak Megaplus ES 1.0 camera previously described in Chapter 3.

To compensate for any foreign particles on the quartz windows, mirror, and lens, or non-uniformities introduced by the arc lamp, two images were captured during each

experiment; one before and one during ignition. Subsequently the "ignition" image was filtered to compensate for irregularities by using the initial image as a mask. In Figure 4.14 several examples are presented illustrating the initial "baseline" image, the second "ignition" image, and the final filtered image. Finally, to further highlight observed light intensity gradients in the flow, the greyscale intensities were mapped onto a colour scale. It should be emphasized that the colours presented in these figures simply represent a linear colour mapping of the original greyscale intensities and are *not* necessarily representative of any physical parameter.

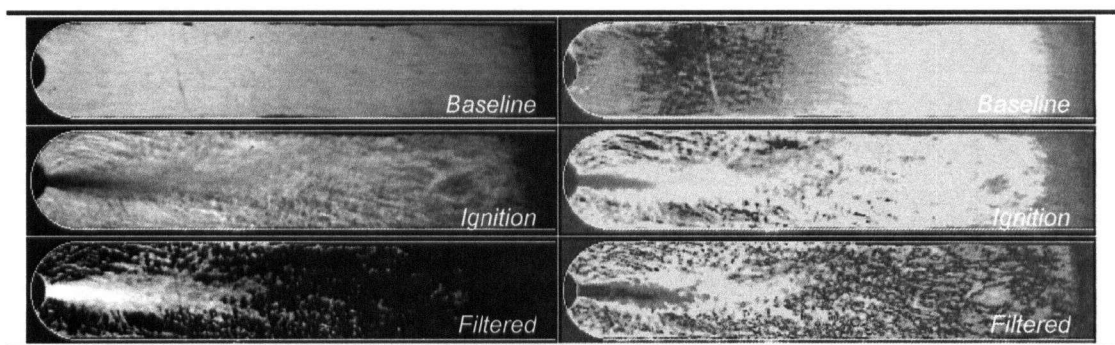


Figure 4.14: Autoignition Visualization Image Post-Processing Examples

Schlieren Photography

Schlieren imaging of the autoignition process did not yield any quantitative results but did provide some further evidence supporting the theories presented throughout the discussion of the autoignition delay time data. In order to interpret these images reacting jets were first compared to equivalent non-reacting jets previously studied in Chapter 3. Several images of the reacting jet *before* the onset of combustion (i.e. before any reaction) indicate close agreement between the reacting jet and the non-reacting jet and are presented in Figure 4.15, which presents the reacting jet before ignition began alongside images of a non-reacting jet of same injection duration and injection pressure ratio. These illustrate that the jet penetration length and length to width ratio were qualitatively identical. In addition, close agreement was observed between the potential core length of the reacting and non-reacting jets, the location of high turbulence regions, the vortex ball location, and other qualitatively features. Interestingly, regions of the non-reacting jet that exhibited high turbulence intensity are nearly indistinguishable in the "reacting" jet images even before ignition. This illustrates the thorough mixing of fuel and oxidant that occurs in these regions.

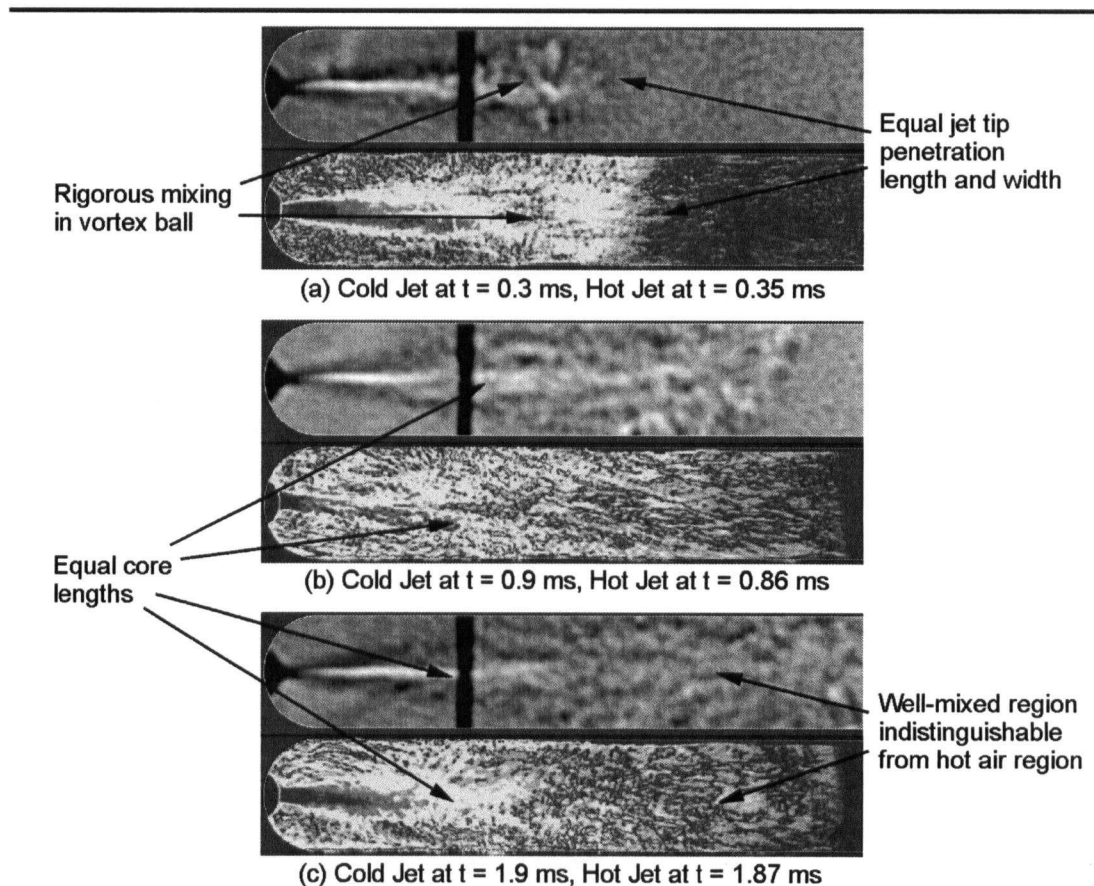


Figure 4.15: Comparison of Hot and Cold Jets

Since the regions in the non-reacting jet where high turbulence intensity and many eddies were observed correspond to regions of the reacting flow that are identical to "hot air" regions, this implies that thorough mixing and/or ignition was occurring in these areas. The images suggest ignition may be occurring in the ball vortex region of the jet that is relatively lean and hot due to extensive mixing and then spreading towards the injector nozzle (as evidenced by decreasing length of the cold jet region in the sequence of images in Figure 4.16). However, when comparing the reacting jet images captured during ignition (Figure 4.16) with those captured prior to ignition (Figure 4.15) little difference is observed in the ball vortex region. As a consequence of the external illumination (necessary to see the jet), it is unclear whether ignition is occurring in the ball vortex or if the hot air and cold fuel are simply very well mixed. Certainly, the two are not unrelated, since mixing is a prerequisite for ignition, but Schlieren images alone cannot conclusively prove that ignition is initiated in the ball vortex region since the external illumination source caused well-mixed regions and reacting regions to appear identical.

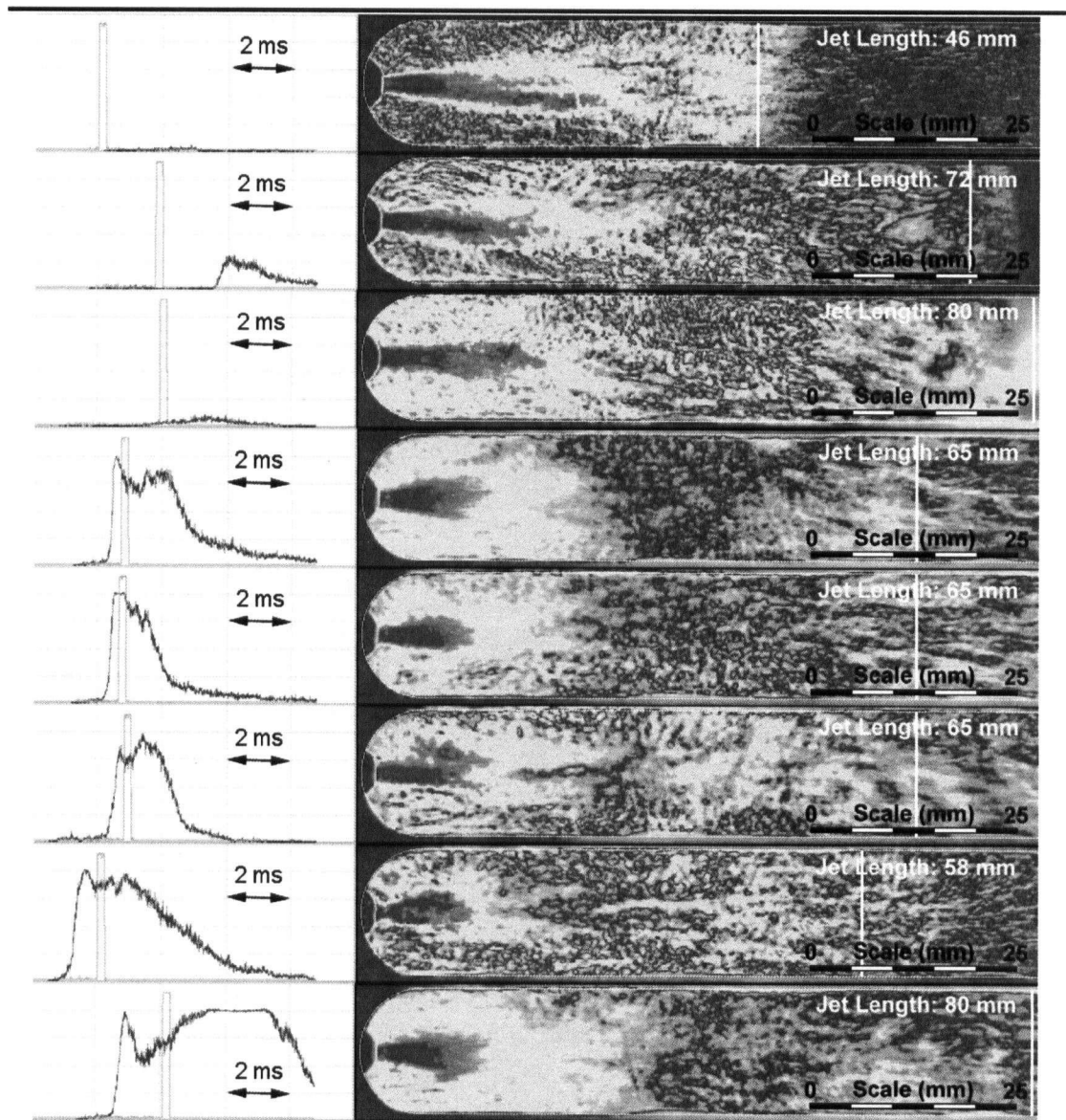


Figure 4.16: Reacting Jet Schlieren Images at Various Ignition Stages

**Note:* CH emissions plotted along the left with a square wave indicating the camera trigger time. Vertical white bar in each image indicates approximate location of jet tip.

Self-Illuminated Photography

Given the difficulties encountered in distinguishing between well-mixed regions and ignition based solely on Schlieren images, additional experiments were conducted without external illumination. In these cases, the jet and other flow phenomena were invisible, and thus the only light detected was that caused by ignition. Several of the captured images are presented in Figure 4.17.

The images in Figure 4.17 conclusively illustrate that autoignition does begin in the ball vortex region of the jet, not near the nozzle, or along the edges of the steady-

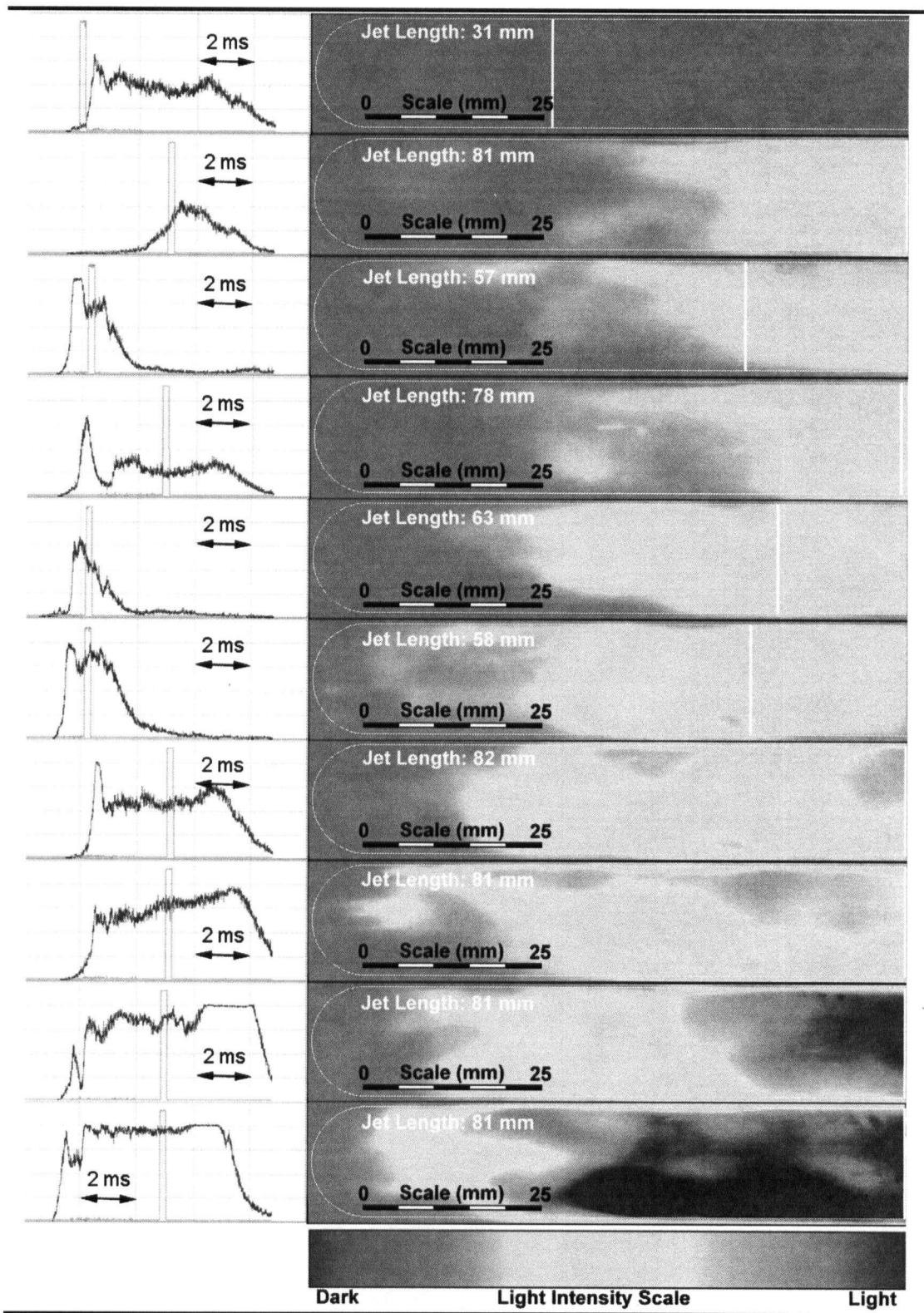


Figure 4.17: Reacting Jet Self-Illuminated Images at Various Ignition Stages

**Note:* CH emissions plotted along the left with a square wave indicating the camera trigger time. Vertical white bar in each image indicates approximate location of jet tip.

state self-similar portion of the jet. Although none of the images captured the start of ignition, the sequence shown clearly suggests ignition preferentially occurs in or around the ball vortex and then gradually spreads towards the injector nozzle. Such an ignition process is corroborated by the numerical simulations of Bi and Agrawal⁴⁴ who indicated autoignition preferentially occurs in the fuel-lean regions of the flow. Additionally, Bi and Agrawal's work suggested several ignition phenomena including the presence of multiple simultaneous ignition sites, the ignition sites moving closer to the nozzle at elevated temperatures, and the ignition originating from hot spots in the free jet that are convected downstream. Similarly, the present experiments seem to indicate similar trends. Several of the images in Figure 4.17 suggest multiple "hot spots" or ignition initiation sites, and collectively the sequence of images definitively shows autoignition occurring around the ball vortex of the jet and then spreading towards the nozzle. Although little more than such qualitative observations can be made from such images, the agreement between the ignition initiation location and growth presently observed and the mechanism described by Bi and Agrawal in their numerical work lends further support to the inferences that were drawn in analysing the autoignition delay time data.

4.5 Conclusions and Recommendations

The present investigation of both the chemical kinetic and fluid mechanic parameters governing the autoignition behaviour of gaseous methane injected into shock-heated air at diesel engine-relevant conditions has led to the following observed dependencies:

1. Autoignition behaviour was found to correspond well with the concept of a kinetic and physical component to ignition delay times. The kinetic component, due to chemical reaction rates, governs the ignition delay time's response to experimental temperature and pressure, while the physical component, due to mixing, dictates the ignition delay time's response to flow parameters including the injection duration, strain rate, and partial premixing.
2. Injection duration and ignition delay times exhibited a linear relationship for injection durations less than 3.0 ms and were independent for longer injections. This behaviour was attributed to the physical component of the ignition delay time as excessive strain in the flow inhibits ignition until the end of injection or until a locally combustible pocket

is convected sufficiently far downstream into a low strain/high temperature region. This suggests use of pulsed injection could yield short ignition delay times when delivering the same quantity of fuel as a single, longer injection as multiple short injections may ignite faster than one long injection.

3. Injection pressure was observed to have a negligible effect on autoignition delay times and was not unexpected since previous numerical research had shown ignition occurs at a "most reactive" mixture fraction where the scalar dissipation rate is lowest. Since increasing the injection pressure has no effect on the conditional mixture fraction and scalar dissipation rate dependence, no increase/decrease in ignition delay times was observed. High injection pressures therefore do not reduce autoignition delay times directly, but may be useful in increasing fuel delivery rates and therefore may indirectly reduce autoignition delay times by reducing required injection durations.
4. Air temperature was found to influence autoignition delay times identically to the way it affected lean homogenous methane/air mixtures. Increasing air temperatures reduced ignition delay times by a magnitude equal to the reduction observed in lean premixed mixtures over the same temperature range. This effect was attributed to the reduction in the kinetic component of the ignition delay time that occurs as the air temperature is increased. Additionally, the close agreement between the ignition limit shift observed between the current results and previous lean homogenous mixtures suggests ignition preferentially occurs in lean regions of the flow.
5. Air pressure had a negligible effect on ignition delay times but dramatically affected the lowest temperature at which ignition was possible, with higher pressures having a lower ignition limit. Also, the magnitude of the ignition limit shift was identical to that observed for lean homogenous mixtures, further supporting the theory that ignition in gaseous jets preferentially occurs in fuel-lean regions.
6. Images of the autoignition process confirmed that ignition initiates in the fuel-lean ball vortex region of the flow. These images illustrated multiple simultaneous ignition sites and provided evidence indicating that ignition occurs along the edges of the ball vortex and then gradually spreads towards the injector nozzle. This finding is significant as it both confirms theories suggested by previous researchers and suggests increasing the mixing rate (reducing the time necessary to form a lean mixture) could effectively reduce ignition delay times.

Conclusions and Recommendations 5

The current three-phase investigation of methane's autoignition behaviour under diesel engine-relevant conditions has included a numerical and experimental study of homogeneous methane autoignition delay times, characterization of a fuel injector for methane injection in non-premixed autoignition studies, and a non-premixed methane autoignition delay time study. Several of the most noteworthy findings from each study are summarized below:

1. The homogeneous methane autoignition delay time study illustrated the importance of using a consistent method for detecting and defining ignition in both experimental and numerical studies. A large portion of the observed discrepancies between previous researchers' results and correlations was attributed to the multitude of different ignition definitions used. In addition, the importance of using a variable activation energy over different experimental temperature regimes was illustrated by the inability of existing correlations to predict a distinct activation energy change observed at a temperature of approximately 1550 K.
2. The injector characterization study quantified the presence of a $180 \pm 20 \mu\text{s}$ delay in the injector driver that must be accounted for to ensure proper injection timing, proposed several numerical models for predicting mass flows and exit conditions at the injector nozzle given only the fuel reservoir state, and verified the injector's ability to operate in a pulsed injection mode. Additionally, Schlieren visualization of the jet produced by the injector under a variety of operating conditions demonstrated the self-similarity of the jet and its close agreement with existing scaling laws. The effects of jet impingement onto objects of various geometries were also illustrated, showing that the penetration length and/or turbulence intensity of the jet could be controlled by varying the distance from the nozzle to the obstruction, and the effects of an enclosure on the transient jet's development were demonstrated to be negligible.
3. The non-premixed methane autoignition delay time study coupled the kinetics studied in the homogeneous autoignition delay time study with the jet fluid mechanics from the

injector characterization study. This led to the finding that kinetic and fluid mechanic parameters influence the autoignition behaviour independently, and thus autoignition delay times can be split into their "kinetic" and "physical" components. Experimental temperatures and pressures affect autoignition delay times through their influence on the kinetic component identically to the manner in which homogeneous ignition times respond to similar temperature/pressure changes. The injection duration affects the physical component of ignition delay times, delaying autoignition until near the end of injection for long injection durations and exhibiting a linear relationship on autoignition times for short injections, with an asymptotic approach to homogeneous autoignition delay times as the injection duration is reduced. Moreover, these experiments agreed well with previous numerical simulations that suggested ignition preferentially occurs in fuel-lean regions of the flow. This was confirmed by capturing images of the ignition process, which clearly illustrated ignition occurring in the fuel-lean ball vortex of the jet.

Following the initial intent of the present investigation, which was to discover potential strategies for reducing methane's prohibitively long autoignition delay time, the following potential ignition delay reduction strategies have emerged and warrant future investigation:

1. High-pressure injection. Although non-premixed autoignition delay time experiments showed no ignition delay reduction with increased injection pressure, the injector characterization study indicated increasing the injection pressure increases the mass flux and thus a shorter injection duration at a high injection pressure could deliver the same quantity of fuel as a longer injection duration at a low pressure. Therefore, this may achieve an ignition delay time reduction by virtue of its reduced injection duration. Additionally, increased injection pressure may be beneficial for pollutant formation processes not investigated in the present study.
2. Partial premixing. Leakage from the injector used in the present study was observed to act as an ignition promoter under certain conditions and numerical simulations have previously indicated that partial premixing of fuel and oxidant is beneficial for ignition promotion through its influence on reducing mixture fraction gradients. Therefore, if the "leakage" can be controlled, partially premixing or stratifying the fuel may reduce autoignition delay times.
3. Pulsed injection. Since effects of injection duration were so pronounced in reducing ignition delay times, using pulsed injection to deliver the desired quantity of fuel over

multiple short injections rather than one long injection may reduce ignition delay times. The injector characterization study showed such a control strategy could be readily implemented using existing hardware and furthermore pulsed injection operation had no adverse impact on the jet's penetration length and width.

4. High-pressure, partially premixed, pulsed direct injection. Finally, given the present understanding of the effects of high-pressure injection at increasing fuel mass fluxes, partial premixing at reducing spatial mixture fraction gradients, and pulsed injection at creating regions of favourable strain, combining all three into a high-pressure, partially premixed, pulsed direct injection system should also be investigated as a potential ignition delay time reduction strategy for diesel engines.

To proceed with implementing the above autoignition delay reduction strategies, the following work remains to be conducted:

1. Replace (or repair) the existing injector to eliminate the large uncertainties currently attributed to leakage. This should be the first priority before conducting any further non-premixed experiments!
2. Repeat the injection duration study (particularly for short injections that exhibited an injection duration dependence) and injection pressure ratio sensitivity experiments with a properly sealing injector to verify that the observed trends are not simply a by-product of leakage effects.
3. Explore pulsed injection by investigating the effects of pulse duration, pulse width, and equal or unequal injection pulse widths on autoignition delay times.
4. Quantify the effects of partial premixing by conducting autoignition experiments with the shock tube's driven section filled with a lean mixture of methane and air (instead of pure air) and comparing autoignition delay times to non-premixed results.
5. Investigate the use of more sophisticated laser-based ignition detection methods since the interpretation of light emission signals was often difficult due to the presence of leakage, multiple ignition/extinction cycles, or luminosity preceding ignition.

References

- ¹ Huang, J., "Experimental Shock Tube Study of Ignition Promotion for Methane Under Engine Relevant Conditions", *MASc Thesis (UBC)*, 2001.
- ² Lifshitz, A. (ed.), "Shock Waves in Chemistry", Marcel Dekker Inc., 1981.
- ³ Seery, D. J., and Bowman, C. T., "An Experimental and Analytical Study of Methane Oxidation Behind Reflected Shock Waves", *Combustion and Flame*, Vol. 14, p. 37, 1970.
- ⁴ Zhou, G., and Karim, G. A., "An Analytical Examination of Various Criteria for Defining Autoignition Within Heated Methane-Air Homogeneous Mixtures", *Journal of Energy Resources Technology*, Vol. 116, p. 175, 1994.
- ⁵ Lifshitz, A., Scheller, K., Burcat, A., and Skinner, G. B., "Shock-Tube Investigation of Ignition in Methane-Oxygen-Argon Mixtures", *Combustion and Flame*, Vol. 16, p. 311, 1971.
- ⁶ Grillo, A. and Slack, M. W., "Shock Tube Study of Ignition Delay Times in Methane-Oxygen-Nitrogen-Argon Mixtures", *Combustion and Flame*, Vol. 27, p. 377, 1976.
- ⁷ Tsuboi, T. and Wagner, H. G., "Homogeneous Thermal Oxidation of Methane in Reflected Shock Waves", *15th Symposium (International) on Combustion, Proceedings*, p. 883, 1974.
- ⁸ Cheng, R. K. and Oppenheim, A. K., "Autoignition in Methane-Hydrogen Mixtures", *Combustion and Flame*, Vol. 58, p. 125, 1984.
- ⁹ Strahle, W. C., "An Introduction to Combustion", Gordon and Breach Science Publishers, 1993.
- ¹⁰ Glassman, I., "Combustion", Third Edition, Academic Press, 1996.
- ¹¹ Ingber, L., "Adaptive Simulated Annealing", <http://www.ingber.com/#ASA> (14 July 2003).
- ¹² Sakata, S., "ASAMIN", <http://www.econ.lsa.umich.edu/~ssakata/software>, (14 July 2003).
- ¹³ Vandenabeele, H., Corbeels, R., and van Tiggelen, A., "Activation Energy and Reaction Order in Methane-Oxygen Flames", *Combustion and Flame*, Vol. 4, p. 253, 1960.

- ¹⁴ Cooke, D. F. and Williams, A., "Shock Tube Studies of Methane and Ethane Oxidation", *Combustion and Flame*, Vol. 24, p. 245, 1975.
- ¹⁵ Dorko, E. A., Bass, D. N., and Crossley, R. W., "Shock Tube Investigation of Ignition in Methane-Oxygen-Nitrogen Dioxide-Argon Mixtures", *Combustion and Flame*, Vol. 24, p. 173, 1975.
- ¹⁶ Ricou, F. P., and Spalding, D. B., "Measurements of Entrainment by Axisymmetrical Turbulent Jets", *Journal of Fluid Mechanics*, Vol. 11, p. 21, 1961.
- ¹⁷ Abdel-Rahman, A. A., Chakroun, W., and Al-Fahed, S. F., "LDA Measurements in the Turbulent Round Jet", *Mechanics Research Communications*, Vol. 24, p. 227, 1997.
- ¹⁸ Malmström, T. G., Kirkpatrick, A. T., Christensen, B., and Knappmiller, K. D., "Centreline Velocity Decay Measurements in Low-Velocity Axisymmetric Jets", *Journal of Fluid Mechanics*, Vol. 246, p. 363, 1997.
- ¹⁹ Hill, P. G., and Ouellette, P., "Transient Turbulent Gaseous Fuel Jets for Diesel Engines", *Journal of Fluids Engineering*, Vol. 121, p. 93, 1999.
- ²⁰ Turner, J. S., "The Starting Plume in Neutral Surroundings", *Journal of Fluid Mechanics*, Vol. 13, p. 356, 1962.
- ²¹ Abramovich, S., and Solan, A., "The Initial Development of a Submerged Laminar Round Jet", *Journal of Fluid Mechanics*, Vol. 59, p. 791, 1973.
- ²² Boyan, X., and Furuyama, M., "Jet Characteristics of CNG Injector with MPI System", *JSAE Review*, Vol. 19, p. 229, 1998.
- ²³ Jenkins, R. M., Foster, W. A. Jr., and Wirth, L. S., "Numerical Analysis of Unsteady Multiple Jet Plume Interactions", *Applied Mathematics and Computation*, Vol. 79, p. 239, 1996.
- ²⁴ Murase, E., Ono, S., Hanada, K., Nakahara, S., Endo, H., and Oppenheim, A. K., "Comparative Study of Pulsed Jet Ignition", *JSAE Review*, Vol. 13, p. 18, 1992.
- ²⁵ Ishii, R., Fujimoto, H., Hatta, N., and Umeda, Y., "Experimental and Numerical Analysis of Circular Pulse Jets", *Journal of Fluid Mechanics*, Vol. 392, p.129, 1999.
- ²⁶ Donaldson, C. P. and Snedeker, R. S., "A Study of Free Jet Impingement. Part 1. Mean Properties of Free and Impinging Jets", *Journal of Fluid Mechanics*, Vol. 45, p. 281, 1971.

- ²⁷ Donaldson, C. D., Snedeker, R. S., and Margolis, D. P., "A Study of Free Jet Impingement. Part 2. Free Jet Turbulent Structure and Impingement Heat Transfer", *Journal of Fluid Mechanics*, Vol. 45, p. 477, 1971.
- ²⁸ Looney, M. K. and Walsh, J. J., "Mean-Flow and Turbulent Characteristics of Free and Impinging Jet Flows", *Journal of Fluid Mechanics*, Vol. 147, p. 397, 1984.
- ²⁹ Krothapalli, A., Rajkuperan, E., Alvi, F., and Lourenco, L., "Flow Field and Noise Characteristics of a Supersonic Impinging Jet", *Journal of Fluid Mechanics*, Vol. 392, p. 155, 1999.
- ³⁰ Fotache, C. G., Kreutz, T. G., and Law, C. K., "Ignition of Counterflowing Methane versus Heated Air under Reduced and Elevated Pressures", *Combustion and Flame*, Vol. 108, p. 442, 1997.
- ³¹ Fotache, C. G., Wang, H., and Law, C. K., "Ignition of Ethane, Propane, and Butane in Counterflow Jets of Cold Fuel versus Hot Air Under Variable Pressures", *Combustion and Flame*, Vol. 117, p. 777, 1999.
- ³² Stårner, S. H., and Bilger, R. W., "Mixture Fraction Imaging in a Lifted Methane Jet Flame", *Combustion and Flame*, Vol. 107, p. 307, 1996.
- ³³ Everest, D. A., Driscoll, J. F., Dahm, W. J. A., and Feikema, D. A., "Images of the Two-Dimensional Field and Temperature Gradients to Quantify Mixing Rates within a Non-Premixed Turbulent Jet Flame", *Combustion and Flame*, Vol. 101, p. 58, 1995.
- ³⁴ Rolon, J. C., Aguerre, F., and Candel, S., "Experiments on the Interaction between a Vortex and a Strained Diffusion Flame", *Combustion and Flame*, Vol. 100, p. 422, 1995.
- ³⁵ Phillips, H., "Ignition in a Transient Turbulent Jet of Hot Inert Gas", *Combustion and Flame*, Vol. 19, p. 187, 1972.
- ³⁶ Peters, N., "Laminar Flamelet Diffusion Models in Non-Premixed Turbulent Combustion", *Progress in Energy and Combustion Science*, Vol. 10, p. 319, 1984.
- ³⁷ Pitsch, H., and Peters, N., "A Consistent Flamelet Formulation for Non-Premixed Combustion Considering Differential Diffusion Effects", *Combustion and Flame*, Vol. 114, p. 26, 1998.
- ³⁸ Chan, S. H., Pan, X. C., and Abou-Elail, M. M., "Flamelet Structure of Radiating CH₄-Air Flames", *Combustion and Flame*, Vol. 102, p. 438, 1995.

- ³⁹ Chan, S. H., Yin, J. Q., and Shi, B. J., "Structure and Extinction of Methane-Air Flamelet with Radiation and Detailed Chemical Kinetic Mechanism", *Combustion and Flame*, Vol. 112, p. 445, 1998.
- ⁴⁰ Yoshida, A., Igarashi, T., and Kotani, Y., "Extinction of Turbulent Diffusion Flames by Kolmogorov Microscale Turbulence", *Combustion and Flame*, Vol. 109, p. 669, 1997.
- ⁴¹ Seshadri, K., and Peters, N., "Asymptotic Structure and Extinction of Methane-Air Diffusion Flames", *Combustion and Flame*, Vol. 73, p. 23, 1988.
- ⁴² Im, H. G. and Chen, J. H., "Chemical Response of Methane/Air Diffusion Flames to Unsteady Strain Rate", *Combustion and Flame*, Vol. 118, p. 204, 1999.
- ⁴³ Mastorakos, E., Baritaud, T. A., and Poinso, T. J., "Numerical Simulations of Autoignition in Turbulent Mixing Flows", *Combustion and Flame*, Vol. 109, p. 198, 1997.
- ⁴⁴ Bi, H., and Agrawal, A. K., "Study of Autoignition of Natural Gas in Diesel Environments Using Computational Fluid Dynamics with Detailed Chemical Kinetics", *Combustion and Flame*, Vol. 113, p. 289, 1998.
- ⁴⁵ Holder, D. W., and North, R. J., "Notes on Applied Science No. 31: Schlieren Methods", Her Majesty's Stationary Office, 1963.

Vacuum Sensor Calibration Data



A.1 Driven Section Pressure Transducer

The Auto Tran 600D-117 vacuum sensor used to measure driven gas pressure was calibrated against an Oakton® Aneroid barometer, yielding extremely repeatable results (as is illustrated in Table A.1). The average slope of all calibrations was -2.997 psi/V with a standard deviation of 0.002 psi/V, agreeing well with the manufacturer's value of -3 psi/V.

Table A.1: Vacuum Sensor Calibration

Atmospheric Pressure			Vacuum Pressure		Regression	
(V)	(bar)	(psi)	(V)	(bar)	(psi/V)	(bar/V)
1.014	1.010	14.649	5.90	0	-2.998	-0.207
1.019	1.014	14.707	5.93	0	-2.995	-0.206
1.019	1.014	14.707	5.93	0	-2.995	-0.206
1.017	1.001	14.518	5.86	0	-2.998	-0.207
1.018	1.001	14.518	5.87	0	-2.992	-0.206
1.018	1.002	14.533	5.87	0	-2.995	-0.207
1.019	1.002	14.533	5.87	0	-2.996	-0.207
1.018	0.995	14.431	5.83	0	-2.999	-0.207
1.019	0.994	14.417	5.83	0	-2.997	-0.207
1.018	0.997	14.460	5.84	0	-2.999	-0.207
1.017	0.995	14.431	5.83	0	-2.998	-0.207
1.015	1.010	14.649	5.90	0	-2.999	-0.207
1.016	1.012	14.678	5.91	0	-2.999	-0.207
1.016	1.015	14.721	5.93	0	-2.999	-0.207
1.016	1.016	14.736	5.93	0	-2.999	-0.207
1.016	1.029	14.924	5.99	0	-3.000	-0.207
1.015	1.000	14.504	5.85	0	-3.000	-0.207
1.016	1.000	14.504	5.85	0	-3.000	-0.207
1.014	0.997	14.460	5.84	0	-2.996	-0.207
1.015	0.991	14.373	5.81	0	-2.998	-0.207
1.015	0.993	14.402	5.82	0	-2.997	-0.207
1.016	0.994	14.417	5.83	0	-2.995	-0.206
1.016	0.997	14.460	5.84	0	-2.998	-0.207
1.015	1.013	14.692	5.92	0	-2.995	-0.207
1.015	1.014	14.707	5.93	0	-2.992	-0.206
1.015	1.015	14.721	5.93	0	-2.995	-0.207

Table A.1: Vacuum Sensor Calibration cont'd.

Atmospheric Pressure			Vacuum Pressure		Regression	
(V)	(bar)	(psi)	(V)	(bar)	(psi/V)	(bar/V)
1.015	1.015	14.721	5.93	0	-2.995	-0.207
1.014	1.004	14.562	5.87	0	-2.999	-0.207
1.015	1.004	14.562	5.87	0	-2.999	-0.207
1.015	1.003	14.547	5.87	0	-2.996	-0.207
1.015	1.003	14.547	5.87	0	-2.996	-0.207
1.015	1.003	14.547	5.87	0	-2.996	-0.207
1.014	1.023	14.837	5.96	0	-3.000	-0.207
1.015	1.018	14.765	5.94	0	-2.998	-0.207
1.015	1.016	14.736	5.93	0	-2.998	-0.207

A.2 Driver Section Pressure Transducer

The Eclipse[®] high-pressure sensor used for measuring driver section gas pressures was not calibrated since it was not used directly in any ignition delay studies (only used for estimating diaphragm burst pressure). However, a discrepancy was discovered between the manufacturer-supplied conversion factor and the one currently used. The manufacturer indicates that the equation for converting measured voltages to pressures is:

$$P \text{ (psi)} = 1250*(V - 0.5)$$

but the equation currently being used is:

$$P \text{ (psi)} = 1200*(V - V_0)$$

where V_0 is determined by measuring the transducer output voltage at atmospheric pressure prior to each experiment (pseudo-calibration) and was found to have an average value of 0.4632 V with a standard deviation of 0.0006 V over the course of the present experimental study. Throughout all experiments, the latter equation using the pseudo-calibration constant was used.

Homogeneous Autoignition Delay Data


Table B.1: Homogeneous Autoignition Delay Data

Y _{Ar}	Y _{O2}	Y _{CH4}	EQR	P Driven (psia)	P Driver (psia)	τ (ms)			P Test (bar)	T Test (K)
						nominal	upper	lower		
0.637	0.242	0.121	0.999	1.109	135.85	0.3	0.426	0.24	6.65	1935
0.609	0.260	0.131	1.002	1.107	30.12				2.414	1103
0.857	0.095	0.048	1.000	1.198	42.13	0.972	1.488	0.882	2.857	1421
0.857	0.095	0.048	1.000	1.199	48.02	1.02	1.104	0.96	3.044	1475
0.962	0.026	0.013	0.980	1.200	58.86	0.582	0.642	0.522	3.415	1813
0.962	0.025	0.013	1.000	1.199	58.83				3.294	1769
0.927	0.049	0.025	1.020	1.199	83.05	0.732	0.792	0.672	3.637	1794
0.727	0.182	0.091	1.004	1.185	73.48	0.504	0.828	0.444	3.865	1491
0.727	0.182	0.091	1.000	1.170	67.52	0.612	1.578	0.552	3.263	1369
0.608	0.262	0.130	0.993	1.529	57.94	0.612	1.248	0.432	3.586	1143
0.608	0.261	0.130	0.998	1.500	41.32	1.386	1.446	1.326	3.26	1102
0.727	0.182	0.091	1.002	1.500	48.10	1.23	1.29	1.17	3.416	1229
0.823	0.118	0.059	1.004	1.470	48.10	1.272	1.472	1.072	3.243	1315
0.790	0.140	0.070	1.000	1.498	36.06				2.589	1120
0.790	0.140	0.070	0.997	1.499	70.77	0.498	1.032	0.438	4.254	1468
0.857	0.096	0.047	0.990	1.499	58.80	1.086	1.146	1.026	3.748	1462
0.926	0.049	0.025	1.000	1.497	67.22	1.146	1.26	0.99	4.022	1658
0.926	0.049	0.025	1.000	1.469	61.26	1.482	1.77	1.422	3.65	1581
0.857	0.095	0.048	1.000	1.018	68.69	0.738	0.876	0.66	3.394	1738
0.608	0.261	0.130	0.998	1.795	60.31	0.96	1.134	0.9	4.152	1135
0.667	0.222	0.111	0.998	1.797	62.72				4.224	1192
0.857	0.095	0.048	1.019	1.198	61.52	0.81	1.23	0.75	3.417	1578
0.608	0.261	0.131	1.002	1.199	58.96	0.63	1.071	0.57	3.536	1281
0.927	0.049	0.024	0.990	1.500	61.36	1.452	1.56	1.116	3.746	1587
0.963	0.025	0.012	1.000	0.989	60.15	0.378	0.438	0.306	3.201	1981
0.667	0.222	0.111	0.998	1.199	34.95	2.412	2.472	2.352	2.58	1141
0.667	0.222	0.111	0.998	1.199	68.55	0.36	0.714	0.3	3.981	1428
0.823	0.118	0.059	1.000	1.500	68.84				1.512	874
0.823	0.118	0.059	0.996	1.499	43.56	1.494	1.614	1.374	3.252	1302
0.824	0.118	0.059	1.000	1.499	90.34	0.01754	0.10754	0.00054	7.787	2212

Homogeneous Autoignition Delay Error Analysis



C.1 Autoignition Delay Time Error

Ignition delay time errors have been discussed in the body of this thesis. These are principally due to ambiguities in the pressure traces that made identifying the point of maximum curvature difficult. Throughout the present study, average errors over each of the three ignition regimes described earlier were:

- High Temperature/Strong Ignition Regime: ± 0.135 ms
- Intermediate Temperature/Two Stage Ignition Regime: ± 0.241 ms
- Low Temperature/Mild Ignition Regime (Well-Defined): ± 0.070 ms
- Low Temperature/Mild Ignition Regime (Ambiguous): ± 0.210 ms

Additional errors were also introduced by the dynamic pressure transducers' response time (3 μ s) and the data acquisition system's sampling frequency (6 μ s) but these were both orders of magnitude smaller than errors introduced by ambiguous pressure traces.

C.2 Driven Gas Composition Error

The driven gas composition was calculated by evacuating the driven section of the shock tube and successively adding individual gases while measuring their partial pressure with the Auto Tran 600D-117 vacuum sensor and Circuit-Test DMR-3600 multimeter. The vacuum sensor was calibrated using a zero and span calibration. At vacuum, the error in the voltage output is ± 0.01 V (maximum multimeter resolution) and at atmospheric pressure the error is ± 0.001 V due to the multimeter and ± 0.001 bar due to the Oakton[®] Aneroid barometer used to calibrate the transducer. When measuring the partial pressure of a gas using the DMR-3600 multimeter, errors of ± 0.001 V translated into errors of ± 0.002 bar (0.028 psi) in all pressure measurements (refer to Figure C.1 to see how errors in calibration and voltage measurements carried forward into errors in measured pressures). Also, the order in which the shock tube was filled (Ar-O₂-

CH₄) introduced variable errors in the pressure measurement and mole fractions of individual gases. These are summarized below:

Argon pressure:

$$P_{Ar} = P_{\text{measured},1} \pm 0.002$$

Oxygen pressure:

$$P_{Ar+O_2} = P_{\text{measured},2} \pm 0.002$$

$$P_{O_2} = P_{Ar+O_2} - P_{Ar}$$

$$P_{O_2} = P_{\text{measured},2} \pm 0.002 - P_{\text{measured},1} \pm 0.002$$

$$\therefore P_{O_2} = P_{\text{measured},2} - P_{\text{measured},1} \pm 0.004$$

Methane pressure:

$$P_{Ar+O_2+CH_4} = P_{\text{measured},3} \pm 0.002$$

$$P_{CH_4} = P_{Ar+O_2+CH_4} - P_{Ar+O_2}$$

$$P_{CH_4} = P_{\text{measured},3} \pm 0.002 - P_{\text{measured},2} \pm 0.002$$

$$\therefore P_{CH_4} = P_{\text{measured},3} - P_{\text{measured},2} \pm 0.004$$

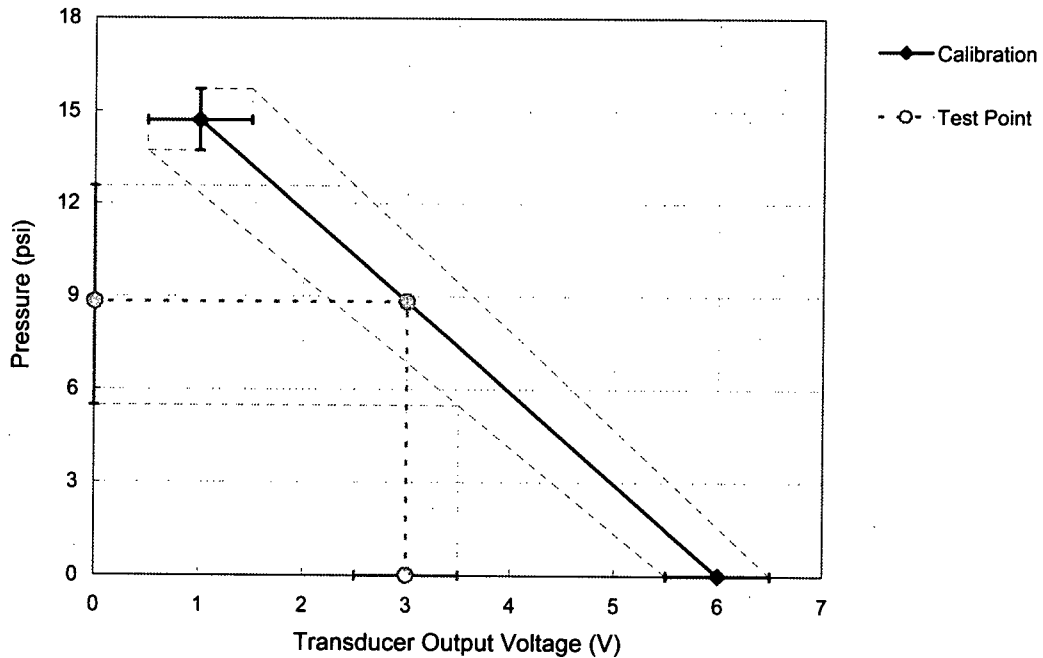


Figure C.1: Illustration of Pressure Measurement Error

**Note: Error bar magnitudes have been greatly exaggerated for illustrative purposes.*

For a given final pressure measurement:

$$P_{\text{total}} = P_{\text{measured,final}} \pm 0.002$$

The errors in the individual mole fractions of the gases are:

$$y_{\text{Ar}} = \frac{P_{\text{Ar}}}{P_{\text{total}}} = \frac{P_{\text{measured,1}} \pm 0.002}{P_{\text{measured,final}} \pm 0.002}$$

$$y_{\text{O}_2} = \frac{P_{\text{O}_2}}{P_{\text{total}}} = \frac{P_{\text{measured,2}} - P_{\text{measured,1}} \pm 0.004}{P_{\text{measured,final}} \pm 0.002}$$

$$y_{\text{CH}_4} = \frac{P_{\text{CH}_4}}{P_{\text{total}}} = \frac{P_{\text{measured,3}} - P_{\text{measured,2}} \pm 0.004}{P_{\text{measured,final}} \pm 0.002}$$

Finally, the error in the equivalence ratio is given by:

$$\text{EQR} = 2 \cdot \frac{y_{\text{CH}_4}}{y_{\text{O}_2}} = \frac{P_{\text{measured,3}} - P_{\text{measured,2}} \pm 0.004}{P_{\text{measured,2}} - P_{\text{measured,1}} \pm 0.004}$$

These produced average errors of 0.7% in the argon mole fraction, 0.8% in the oxygen mole fraction, and 0.7% in the methane mole fraction, with total driven gas pressure error of ~4.5%.

C.3 Experimental Temperature/Pressure Error

Experimental temperature and pressure were found to be proportional to the following:

$$P_{\text{test}} \propto \left(\text{EQR}, \frac{1}{y_{\text{Ar}}}, P_{\text{driven}}, V_i, \frac{1}{T_0} \right) \quad (\text{C.1})$$

$$T_{\text{test}} \propto \left(\frac{1}{\text{EQR}}, y_{\text{Ar}}, V_i, T_0 \right) \quad (\text{C.2})$$

where: *EQR* is the equivalence ratio;
y_{Ar} is the argon mole fraction;
P_{driven} is the initial driven section pressure;
V_i is the measured incident shock velocity; and
T₀ is the initial driven section temperature.

The errors in the gas composition and pressure were discussed above. Errors in the incident shock velocity were minimal as the radius of convergence of the linear fit used to calculate the incident shock from dynamic pressure transducer signal exceeded 0.996 (average = 0.9989, standard deviation = 0.0038). Therefore, the main source of error was in measured distances between transducers and the data acquisition system's sampling rate. Errors in the measured distances were $\pm 0.2\%$ plus the radius of the sensor (0.002 m), therefore the uncertainty in the distance may be expressed as:

$$w_x = 0.002 \cdot X + 0.002$$

The data acquisition system was set to sample data every 6 μs , therefore the error in the time measurement may be expressed as:

$$w_t = 6.0 \times 10^{-6}$$

The uncertainty in the velocity (which is a function of the distance errors and time errors) may be determined from the following formula:

$$w_v = \sqrt{\left(\frac{\partial V}{\partial x}\right)^2 \cdot w_x^2 + \left(\frac{\partial V}{\partial t}\right)^2 \cdot w_t^2}$$

$$w_v = \sqrt{\left(\frac{1}{t}\right)^2 \cdot (0.002 \cdot X + 0.002)^2 + \left(-\frac{X}{t^2}\right)^2 \cdot (6.0 \times 10^{-6})^2}$$

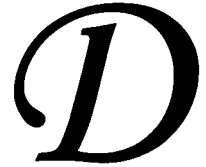
From the configuration of the dynamic pressure transducers along the driven section, $X=3.493$ m and $t=3.003$ - 5.497 ms (based on shock velocities between 635.4-1163 m/s). This leads to an uncertainty in measured velocities of 1.78-2.34 m/s. To account for this uncertainty and that due to shock attenuation, the error in the calculated velocities were considered to be ± 5 m/s.

Using the errors calculated above for the gas composition, initial driven section pressure, initial temperature, and shock velocity, upper and lower error bounds on temperature and pressure were calculated using equations C.1 and C.2. For example, the maximum temperature was calculated as:

$$T_{\max} = T(EQR_{\min}, y_{Ar, \max}, V_{i, \max}, T_{0, \max})$$

These errors cumulatively produced errors in the experimental temperature between 5-164 K and errors in the experimental pressure between 0.2-0.6 bar, with the largest errors at high experimental temperatures due to large uncertainty introduced by the high Ar dilution necessary to produce such temperatures.

Numerical Combustion Equations Derivation



D.1 Thermodynamic Development

Premixed combustion in the shock tube was treated as an adiabatic, constant volume process. With these two assumptions, the first law of thermodynamics for a closed system was simplified by neglected all external heat transfer and work:

$$\begin{aligned}
 \delta q &= du + \delta w \\
 \text{adiabatic} &\Rightarrow \delta q = 0 \\
 \text{const. vol.} &\Rightarrow \delta w = P \cdot dv = 0 \\
 \therefore du &= 0
 \end{aligned}
 \tag{D.1}$$

Transforming the above expression in terms of specific enthalpy:

$$\begin{aligned}
 du &= d(h - P \cdot v) = 0 \\
 \text{const. vol.} &\Rightarrow P \cdot dv = 0 \\
 \therefore dh &= v \cdot dP
 \end{aligned}
 \tag{D.2}$$

Since a solution in time is sought, the above may be restated as:

$$\frac{dh}{dt} = v \cdot \frac{dP}{dt}
 \tag{D.3}$$

To further expand the above equation, an additional assumption that all gases involved in the combustion process behave as ideal gases is made (this is reasonable for the temperatures and pressures in the present investigation). With this final assumption, the enthalpy of the driven gas mixture is expressed as follows:

$$h = \sum_K x_K \cdot h_K
 \tag{D.4}$$

where: x_K is the mass fraction of species K ; and
 h_K is the specific enthalpy of species K , (kJ/kg).

Differentiating equation (D.4) with respect to time, an expression for the LHS of equation (D.3) is obtained:

$$\frac{dh}{dt} = \sum_K \frac{dx_K}{dt} \cdot h_K + \sum_K x_K \cdot \frac{dh_K}{dt} \quad (D.5)$$

The specific enthalpy of species K may be further expressed as (assuming ideal gas):

$$dh_K = c_{P_K} \cdot dT \quad (D.6)$$

Additionally, the rate of change of the mass fraction of species K with time may be restated in terms of molar species production rate by expressing the rate of change of the mass of species K as a function of time and then dividing by the total mass in the driven section (a constant):

$$\begin{aligned} \frac{dm_K}{dt} &= 1000 \cdot \dot{\omega}_K \cdot M_K \cdot V \\ \frac{dx_K}{dt} &= \frac{1000 \cdot \dot{\omega}_K \cdot M_K \cdot V}{m} = \frac{1000 \cdot \dot{\omega}_K \cdot M_K}{\rho} \end{aligned} \quad (D.7)$$

where: m_K is the mass of species K (kg);
 $\dot{\omega}_K$ is the molar production rate of species K (mol/cm³/s);
 M_K is the molecular mass of species K (kg/kmol);
 V is the total mixture volume (m³);
 m is the total mixture mass (kg); and
 ρ is the total mixture density (kg/m³).

Note: The factor of 1000 appearing in equation (D.7) is included to convert the units of the production term from mol/cm³/s to kmol/m³/s for dimensional homogeneity.

Substituting equations (D.6) and (D.7) into (D.5), an expression relating the change in mixture specific enthalpy as a function of the species production rate and the temperature change is obtained:

$$\frac{dh}{dt} = \sum_K \frac{1000 \cdot \dot{\omega}_K \cdot M_K}{\rho} \cdot h_K + \sum_K x_K \cdot c_{P_K} \cdot \frac{dT}{dt} \quad (D.8)$$

This equation forms the LHS of expression (D.3). However, substituting (D.8) into (D.3) yields

an expression containing both the rates of change of temperature and pressure as a function of time. To transform this equation further to a more useful form, the ideal gas law is used to eliminate the pressure term:

$$\begin{aligned}
 P &= \frac{n \cdot R \cdot T}{V} \\
 \frac{dP}{dt} &= \frac{R}{V} \cdot \left(\frac{dn}{dt} \cdot T + n \cdot \frac{dT}{dt} \right) \\
 \frac{dP}{dt} &= \frac{R}{V} \cdot \left(\sum_K 1000 \cdot \dot{\omega}_K \cdot V \cdot T + \frac{P \cdot V}{R \cdot T} \cdot \frac{dT}{dt} \right) \\
 \frac{dP}{dt} &= R \cdot T \cdot \sum_K 1000 \cdot \dot{\omega}_K + \frac{P}{T} \cdot \frac{dT}{dt} \quad (D.9)
 \end{aligned}$$

where: n is the total number of moles in the driven section; and
 R is the universal gas constant (kJ/kmol/K).

Finally, substituting equations (D.9) and (D.8) into (D.3):

$$\frac{dT}{dt} = \frac{\frac{1}{\rho} \cdot \left(\sum_K 1000 \cdot \dot{\omega}_K \cdot M_K \cdot h_K - R \cdot T \cdot \sum_K 1000 \cdot \dot{\omega}_K \right)}{\left(\frac{P}{\rho \cdot T} - \sum_K x_K \cdot c_{P_K} \right)} \quad (D.10)$$

While this equation is complete, it may be more convenient to express all of the terms in molar quantities. This transformation is performed by making the following substitutions:

$$\begin{aligned}
 \frac{1}{\rho} &= \frac{V}{m} = \frac{R \cdot T}{P \cdot M} \quad ; \quad \frac{P}{\rho \cdot T} = \frac{P \cdot V}{m \cdot T} = \frac{R}{M} \\
 x_K &= \frac{y_K \cdot M_K}{M} \quad ; \quad h_K = \frac{\bar{h}_K}{M_K} \quad ; \quad c_{P_K} = \frac{\bar{c}_{P_K}}{M_K}
 \end{aligned}$$

where: y_K is the mole fraction;
 \bar{h}_K is the molar enthalpy (kJ/kmol); and
 \bar{c}_{P_K} is the molar specific heat (kJ/kmol/K).

Thus, the final expression for the rate of change of the system temperature becomes:

$$\frac{dT}{dt} = \frac{\frac{R \cdot T}{P} \cdot \left(\sum_K 1000 \cdot \dot{\omega}_K \cdot \bar{h}_K - R \cdot T \cdot \sum_K 1000 \cdot \dot{\omega}_K \right)}{\left(R - \sum_K y_K \cdot \bar{c}_{P,K} \right)} \quad (\text{D.11})$$

This final expression may be numerically integrated to solve for the mixture temperature, and equation (D.9) may be subsequently used to solve for mixture pressure.

D.2 Chemical Kinetic Development

The above thermodynamic analysis yields an expression for the rate of change of temperature (and subsequently pressure) as a function of time, but this equation depends on an unknown molar species production rate. This production rate may be expressed as follows based upon the reaction stoichiometry:

$$\dot{\omega}_K = \sum_i \left(\nu_K^P - \nu_K^R \right)_i \cdot \left(k_f \cdot \prod_j [X_j]^{\nu_j^R} - k_b \cdot \prod_j [X_j]^{\nu_j^P} \right) \quad (\text{D.12})$$

where: ν^P, ν^R are stoichiometric coefficients of product and reactant species,
 $[X_j]$ is the concentration of species j (mol/cm³); and
 k_f, k_b are the forward and reverse reaction rate coefficients, respectively.

The above production rate is tabulated by summing the production rate of species K in all reactions, i , included in the reaction mechanism. Forward reaction rate coefficients for each reaction are readily available in the literature in a modified Arrhenius form:

$$k_{f_i} = A_i \cdot T^{n_i} \cdot e^{-\frac{E_i}{R \cdot T}} \quad (\text{D.13})$$

where: $A_i, n_i,$ and E_i are experimentally determined coefficients.

The reverse reaction rate coefficient is then calculated from the forward reaction rate and the equilibrium constant using the equation:

$$k_{b_i} = \frac{k_{f_i}}{K_{eq_i}}$$

K_{eq} in the above equation is the equilibrium constant, given by the following relation and

calculated from the JANAF thermochemical data tables:

$$\ln k_{eq_i} = -\frac{\Delta G_i}{R \cdot T}$$

where: ΔG is the change in Gibb's free energy (kJ/kmol).

Injector Hardware Characterization Data *E*

E.1 Injection Delay Experimental Data

The following is the experimental data collected during the injection delay study:

Table E.1: Injection Delay Data

Filename	Injection Duration (ms)	Backpressure (psig)	P1 (ms)	P2 (ms)
inj030	1.45	0	0.157	0.157
inj031	1.45	330	0.179	0.171
inj032	1.49	600	0.186	0.236
inj033	1.49	700	0.200	0.200
inj034	1.49	500	0.186	0.186
inj035	1.49	700	0.200	0.200
inj036	1.49	500	0.214	0.193
inj037	1.46	700	0.200	0.171
inj038	1.45	250	0.171	0.171
inj039	1.50	625	0.200	0.200
inj040	1.50	650	0.186	0.186
inj041	1.45	250	0.214	0.186
inj042	1.48	600	0.179	0.179
inj043	1.45	700	0.150	0.150
inj044	1.46	200	0.186	0.207
inj045	1.49	600	0.200	0.200
inj046	1.47	700	0.164	0.164
inj047	1.41	200	0.243	0.171
inj048	1.48	600	0.186	0.186
inj049	1.48	700	0.193	0.193
inj050	1.45	250	0.157	0.157
inj051	1.46	600	0.171	0.193
inj052	1.44	700	0.229	0.179
inj053	1.44	100	0.164	0.186
inj054	1.45	500	0.171	0.171
inj055	1.47	700	0.179	0.179
inj056	1.39	200	0.164	0.164
inj057	1.46	600	0.157	0.157
inj058	1.44	700	0.186	0.157
inj059	1.49	500	0.214	0.207
inj060	1.47	700	0.179	0.179

Table E.1: Injection Delay Data cont'd.

Filename	Injection Duration (ms)	Backpressure (psig)	P1 (ms)	P2 (ms)
inj061	1.47	300	0.221	0.193
inj062	1.45	600	0.157	0.179
inj063	1.45	700	0.200	0.200
inj064	1.47	600	0.179	0.179
inj065	1.45	600	0.164	0.164
inj066	1.44	700	0.157	0.150
inj067	1.45	200	0.164	0.164
inj068	1.46	600	0.164	0.164
inj069	1.46	700	0.193	0.164
inj070	1.47	250	0.186	0.186
inj071	1.49	600	0.221	0.193
inj072	1.45	700	0.157	0.157
inj073	1.49	200	0.221	0.243
inj074	1.44	500	0.164	0.164
inj075	1.45	700	0.164	0.164
inj076	1.46	200	0.200	0.200
inj077	1.46	500	0.171	0.171
inj078	1.48	700	0.193	0.193
inj079	1.46	150	0.171	0.171
inj080	1.49	500	0.221	0.193
inj081	1.48	700	0.187	0.187
inj082	1.49	400	0.193	0.193
inj083	1.46	600	0.171	0.171
inj084	1.49	500	0.200	0.200
inj085	1.39	150	0.171	0.171
inj086	1.45	500	0.157	0.157
inj087	1.47	700	0.186	0.186
inj088	1.46	150	0.171	0.171
inj089	1.49	500	0.221	0.200
inj090	1.47	650	0.171	0.171
inj091	2.48	200	0.157	0.157
inj092	2.51	300	0.207	0.186
inj093	2.43	600	0.143	0.143
inj094	2.49	0	0.164	0.164
inj095	2.48	0	0.164	0.164
inj096	2.53	600	0.207	0.207
inj097	2.50	0	0.193	0.171
inj098	2.51	500	0.193	0.193
inj099	2.49	400	0.164	0.164
inj100	2.48	300	0.150	0.150
inj101	2.50	700	0.200	0.200
inj102	2.52	0	0.207	0.207
inj103	2.47	500	0.179	0.179
inj104	2.51	200	0.193	0.193

Table E.1: Injection Delay Data cont'd.

Filename	Injection Duration	Backpressure (psig)	P1 (ms)	P2 (ms)
	(ms)			
inj105	2.50	600	0.164	0.164
inj106	2.49	250	0.164	0.164
inj107	2.51	600	0.186	0.186
inj108	2.50	200	0.179	0.179
inj109	2.51	600	0.186	0.186
inj110	2.48	300	0.157	0.157
inj111	3.55	400	0.193	0.186
inj112	3.51	600	0.179	0.150
inj113	3.54	200	0.164	0.164
inj114	3.54	400	0.179	0.179
inj115	3.54	600	0.193	0.193
inj116	3.55	300	0.200	0.193
inj117	3.51	400	0.150	0.157
inj118	3.53	250	0.157	0.157
inj119	3.53	600	0.164	0.164
inj120	3.51	300	0.157	0.157
inj121	3.51	600	0.150	0.150
inj122	3.49	400	0.193	0.193
inj123	3.45	500	0.164	0.164
inj124	3.52	300	0.157	0.157
inj125	3.53	300	0.164	0.164

E.2 Injector Mass Flow Rate Experimental Data

The following is the injector mass flow data:

Table E.2: Injector Mass Flow Rate Data

	CH ₄ Experiments (UBC)				N ₂ Experiments (UBC)				N ₂ Experiments (Westport)				
	Pulse Width (ms)	Injection Pressure (psi)			Pulse Width (ms)	Injection Pressure (psi)			Pulse Width (ms)	Injection Pressure (psi)			
		1000	1500	1820		1000	1500	1850		1000	1500	1850	2500
Final Test Pressure (psig)	0.3	3.6	5.0	6.0	0.3	2.5	3.8	4.2					
	0.4	3.95	6.0	7.0	0.4	2.8	4.2	5.5					
	0.5	4.8	7.0	9.0	0.5	3.6	6.0	6.5					
	0.6	6.2	10.0	12.0	0.6	5.2	7.0	8.5					
	0.7	8.1	12.5	14.5	0.7	6.0	8.5	10.2					
	0.8	9.2	14.0	16.0	0.8	6.8	10.0	12.2					
	1.0	11.9	17.5	20.0	1.0	8.0	12.5	15.0					
	1.25	14.0	21.5	25.5	1.25	10.5	15.0	19.0					
	1.5	17.5	26.0	31.5	1.5	13.0	18.5	23.0					
1.75	20.0	30.5	36.5	1.75	15.0	21.5	27.0						

Table E.2: Injector Mass Flow Rate Data cont'd.

	CH ₄ Experiments (UBC)				N ₂ Experiments (UBC)				N ₂ Experiments (Westport)				
	Pulse Width	Injection Pressure (psi)			Pulse Width	Injection Pressure (psi)			Pulse Width	Injection Pressure (psi)			
	(ms)	1000	1500	1820	(ms)	1000	1500	1850	(ms)	1000	1500	1850	2500
Total Mass Injected (mg)	0.3	3.00	4.17	5.01	0.3	3.64	5.54	6.12	0.3	3.64	4.81	5.97	8.27
	0.4	3.30	5.01	5.84	0.4	4.08	6.12	8.01	0.4	4.39	6.25	7.73	10.40
	0.5	4.00	5.84	7.51	0.5	5.24	8.74	9.47	0.5	6.13	8.87	10.64	14.45
	0.6	5.17	8.34	10.01	0.6	7.58	10.20	12.38	0.6	7.23	10.35	12.54	17.54
	0.7	6.76	10.43	12.10	0.7	8.74	12.38	14.86	0.7	8.31	11.58	14.79	19.86
	0.8	7.68	11.68	13.35	0.8	9.91	14.57	17.77	0.8	9.93	14.24	17.50	23.35
	1.0	9.93	14.60	16.69	1.0	11.65	18.21	21.85	1.0	12.30	17.98	22.05	29.96
	1.25	11.68	17.94	21.27	1.25	15.30	21.85	27.68	1.25	15.55	22.44	27.63	37.45
	1.5	14.60	21.69	26.28	1.5	18.94	26.95	33.51	1.5	18.74	26.88	33.51	45.44
	1.75	16.69	25.45	30.45	1.75	21.85	31.32	39.33	1.75	21.68	31.33	39.02	53.17
Mass Flow Rate (mg/ms)	0.3	10.01	13.90	16.69	0.3	12.14	18.45	20.40	0.3	12.14	16.04	19.90	27.57
	0.4	8.24	12.51	14.60	0.4	10.20	15.30	20.03	0.4	10.98	15.64	19.32	26.01
	0.5	8.01	11.68	15.02	0.5	10.49	17.48	18.94	0.5	12.25	17.73	21.27	28.90
	0.6	8.62	13.90	16.69	0.6	12.63	17.00	20.64	0.6	12.05	17.24	20.90	29.23
	0.7	9.65	14.90	17.28	0.7	12.49	17.69	21.23	0.7	11.88	16.55	21.12	28.38
	0.8	9.59	14.60	16.69	0.8	12.38	18.21	22.22	0.8	12.41	17.80	21.88	29.18
	1.0	9.93	14.60	16.69	1.0	11.65	18.21	21.85	1.0	12.30	17.98	22.05	29.96
	1.25	9.34	14.35	17.02	1.25	12.24	17.48	22.14	1.25	12.44	17.95	22.11	29.96
	1.5	9.73	14.46	17.52	1.5	12.63	17.97	22.34	1.5	12.49	17.92	22.34	30.30
	1.75	9.53	14.54	17.40	1.75	12.49	17.90	22.48	1.75	12.39	17.90	22.29	30.38

E.3 Pulsed Injection System Validation Experimental Data

The following is the data collected when validating the pulsed injection system:

Table E.3: Pulsed Injection System Validation Data

Filename	Pulse Delay (ms)	Pulse Width (ms)	$\Delta P1$ (V)	$\Delta P2$ (V)
multi001	4.0	2.0	0.050	0.040
multi002	4.0	1.0	0.034	0.021
multi003	4.0	3.0	0.088	0.000
multi004	8.0	2.0	0.060	0.045
multi005	8.0	1.0	0.035	0.021
multi006	8.0	3.0	0.085	0.035
multi007	8.0	3.0	0.083	0.037
multi008	3.0	1.0	0.032	0.020
multi009	3.0	2.0	0.058	0.042
multi010	3.0	2.5	0.075	0.015
multi011	1.5	1.0	0.037	0.021
multi012	1.5	0.5	0.020	0.010

Table E.3: Pulsed Injection System Validation Data cont'd.

Filename	Pulse Delay (ms)	Pulse Width (ms)	$\Delta P1$ (V)	$\Delta P2$ (V)
multi013	1.0	0.5	0.021	0.009
multi014	1.0	1.0	0.060	0.000
multi015	1.5	0.5	0.020	0.010
multi016	1.5	1.0	0.035	0.022
multi017	1.5	1.5	0.085	0.000
multi018	2.0	0.5	0.020	0.010
multi019	2.0	1.0	0.033	0.024
multi020	2.0	1.5	0.047	0.036
multi021	2.5	0.5	0.021	0.008
multi022	2.5	1.0	0.033	0.022
multi023	2.5	1.5	0.047	0.036
multi024	2.5	2.0	0.060	0.040
multi025	3.0	0.5	0.021	0.009
multi026	3.0	1.0	0.034	0.022
multi027	3.0	1.5	0.048	0.033
multi028	3.0	2.0	0.059	0.040
multi029	3.0	2.5	0.073	0.015
multi030	4.0	0.2	0.021	0.009
multi031	4.0	1.0	0.033	0.022
multi032	4.0	1.5	0.045	0.035
multi033	4.0	2.0	0.060	0.041
multi034	4.0	2.5	0.070	0.034
multi035	4.0	3.0	0.085	0.000
multi036	4.5	3.0	0.085	0.006
multi037	5.0	3.0	0.085	0.018
multi038	6.0	3.0	0.085	0.029
multi039	7.0	3.0	0.085	0.035
multi040	8.0	3.0	0.085	0.039
multi041	9.0	3.0	0.085	0.040
multi042	10.0	3.0	0.085	0.044
multi043	10.0	2.0	0.058	0.046
multi044	10.0	1.0	0.033	0.022
multi045	12.0	3.0	0.085	0.049
multi046	12.0	2.0	0.058	0.047
multi047	12.0	1.0	0.033	0.022
multi048	15.0	3.0	0.085	0.057
multi049	18.0	3.0	0.085	0.067
multi050	21.0	3.0	0.085	0.070
multi051	21.0	2.0	0.058	0.047
multi052	24.0	3.0	0.085	0.072
multi053	50.0	3.0	0.085	0.072
multi054	50.0	2.0	0.058	0.048
multi055	50.0	1.0	0.034	0.022

Table E.3: Pulsed Injection System Validation Data cont'd.

Filename	Pulse Delay (ms)	Pulse Width (ms)	$\Delta P1$ (V)	$\Delta P2$ (V)
multi056	50.0	3.0	0.085	0.072
multi057	5.0	2.5	0.071	0.035
multi058	6.0	2.5	0.072	0.038
multi059	7.0	2.5	0.072	0.042
multi060	8.0	2.5	0.073	0.045
multi061	9.0	2.5	0.070	0.049
multi062	10.0	2.5	0.071	0.050
multi063	12.0	2.5	0.072	0.052
multi064	15.0	2.5	0.072	0.057
multi065	18.0	2.5	0.073	0.059
multi066	21.0	2.5	0.072	0.061
multi067	24.0	2.5	0.073	0.060
multi068	5.0	1.5	0.046	0.034
multi069	6.0	1.5	0.046	0.034
multi070	7.0	1.5	0.047	0.036
multi071	8.0	1.5	0.047	0.036
multi072	9.0	1.5	0.047	0.036
multi073	10.0	1.5	0.047	0.036
multi074	5.0	2.0	0.059	0.043
multi075	6.0	2.0	0.059	0.045
multi076	7.0	2.0	0.059	0.046
multi077	15.0	2.0	0.059	0.048
multi078	18.0	2.0	0.060	0.048
multi079	50.0	1.5	0.046	0.035
multi080	50.0	2.5	0.072	0.060
multi081	100.0	3.0	0.084	0.072
multi082	100.0	2.5	0.073	0.060
multi083	100.0	2.0	0.059	0.048
multi084	100.0	1.5	0.047	0.036
multi085	100.0	1.0	0.034	0.023

Jet Flow Field Characterization Data *F*

F.1 Single Injection Mode Experimental Data

The following is the data collected during the single injection jet flow field characterization study:

Table F.1: Single Injection Mode Jet Flow Field Data

	Image	Time (ms)	PR = 3				PR = 5			
			Width (pixels)	Length (pixels)	Width (mm)	Length (mm)	Width (pixels)	Length (pixels)	Width (mm)	Length (mm)
0.5 ms Duration		0			1			1		
	1	0.127	20	62	7	21	29	94	10	31
	2	0.327	31	98	10	33	42	130	14	43
	3	0.527	43	115	14	38	44	146	15	49
	4	0.727	41	125	14	42	54	172	18	57
	5	0.927	42	143	14	48	60	180	20	60
	6	1.127	49	139	16	46	69	191	23	64
	7	1.327	60	143	20	48	70	197	23	66
	8	1.527	65	155	22	52	88	190	29	63
	9	1.727	60	167	20	56	82	230	27	77
	10	1.927	48	153	16	51	95	216	32	72
	11	2.127	63	157	21	52	77	232	26	77
	12	2.327	64	185	21	62	75	240	25	80
	13	2.527	59	167	20	56	82	238	27	79
	14	3.127	65	181	22	60	80	242	27	81
	15	3.727	72	196	24	65	121	266	40	89
	16	4.327	72	231	24	77				
17	5.527	111	230	37	77	129	264	43	88	
1.0 ms Duration		0			1			1		
	1	0.127	25	75	8	25	26	88	9	29
	2	0.327	32	103	11	34	37	125	12	42
	3	0.527	39	113	13	38	50	154	17	51
	4	0.727	46	119	15	40	59	184	20	61
	5	0.927	51	142	17	47	62	188	21	63
	6	1.127	60	159	20	53	67	213	22	71
	7	1.327	66	165	22	55	87	234	29	78
	8	1.527	58	173	19	58	71	222	24	74
	9	1.727	55	186	18	62	72	243	24	81

Table F.1: Single Injection Mode Jet Flow Field Data cont'd.

	Image	Time (ms)	PR = 3				PR = 5			
			Width (pixels)	Length (pixels)	Width (mm)	Length (mm)	Width (pixels)	Length (pixels)	Width (mm)	Length (mm)
1.0 ms Duration cont'd.	10	1.927	66	199	22	66	85	263	28	88
	11	2.127	86	180	29	60	87	281	29	94
	12	2.327	79	210	26	70	81	295	27	98
	13	2.527	68	215	23	72	109	294	36	98
	14	2.727	81	205	27	68	106	311	35	104
	15	2.927	74	229	25	76	93	309	31	103
	16	3.527	90	236	30	79	124	309	41	103
	17	4.127	86	266	29	89	140	331	47	110
	18	5.327	103	274	34	91	117	361	39	120
	19	6.527	102	278	34	93	160	360	53	120
1.5 ms Duration		0			1			1		
	1	0.127	25	62	8	21	28	96	9	32
	2	0.327	33	78	11	26	42	132	14	44
	3	0.527	39	121	13	40	59	158	20	53
	4	0.727	48	128	16	43	60	169	20	56
	5	0.927	51	140	17	47	72	190	24	63
	6	1.127	54	144	18	48	73	212	24	71
	7	1.327	63	160	21	53	67	226	22	75
	8	1.527	72	182	24	61	75	240	25	80
	9	1.727	66	184	22	61	89	251	30	84
	10	1.927	79	187	26	62	83	278	28	93
	11	2.127	76	210	25	70	87	281	29	94
	12	2.327	73	208	24	69	116	288	39	96
	13	2.527	95	212	32	71	105	305	35	102
	14	2.727					102	310	34	103
	15	2.927					113	329	38	110
	16	3.127	89	241	30	80	101	334	34	111
	17	3.727	104	258	35	86	127	348	42	116
	18	4.327	120	265	40	88	149	382	50	127
	19	5.527	103	293	34	98	129	389	43	130
20	6.727	120	310	40	103	160	419	53	140	
3.0 ms Duration		0			1			1		
	1	0.127	25	62	8	21	24	97	8	32
	2	0.327	36	93	12	31	40	142	13	47
	3	0.527	37	112	12	37	64	160	21	53
	4	0.727	51	114	17	38	55	183	18	61
	5	0.927	65	136	22	45	73	188	24	63
	6	1.127	58	142	19	47	69	215	23	72
	7	1.327	61	149	20	50	85	222	28	74
	8	1.527	67	183	22	61	89	225	30	75
	9	1.727	76	201	25	67	84	247	28	82
	10	1.927	74	194	25	65	91	266	30	89
11	2.127	78	209	26	70	73	287	24	96	

Table F.1: Single Injection Mode Jet Flow Field Data cont'd.

	Image	Time (ms)	PR = 3				PR = 5			
			Width (pixels)	Length (pixels)	Width (mm)	Length (mm)	Width (pixels)	Length (pixels)	Width (mm)	Length (mm)
3.0 ms Duration cont'd.	12	2.327	85	218	28	73	84	288	28	96
	13	2.527	78	238	26	79	107	298	36	99
	14	2.727	94	240	31	80	103	325	34	108
	15	2.927	96	243	32	81	102	327	34	109
	16	3.127	90	257	30	86	108	328	36	109
	17	3.327	79	267	26	89	136	346	45	115
	18	3.527	86	271	29	90	110	359	37	120
	19	3.727	95	283	32	94	159	319	53	106
	20	3.927	103	281	34	94	114	358	38	119
	21	4.127	94	292	31	97	114	371	38	124
	22	4.327	117	283	39	94	156	390	52	130
	23	4.527	96	309	32	103	164	407	55	136
	24	4.727	93	323	31	108	161	406	54	135
	25	5.327	122	329	41	110	156	422	52	141
	26	5.927	120	345	40	115	160	431	53	144
	27	7.127	136	376	45	125				
	28	8.327	130	385	43	128				
	29	9.527	179	411	60	137				
5.0 ms Duration		0			1			1		
	1	0.127	28	70	9	23	35	94	12	31
	2	0.327	39	96	13	32	37	129	12	43
	3	0.527	35	115	12	38	53	148	18	49
	4	0.727	53	124	18	41	51	178	17	59
	5	0.927	53	150	18	50	62	207	21	69
	6	1.127	49	160	16	53	66	209	22	70
	7	1.327	69	169	23	56	79	228	26	76
	8	1.527	69	173	23	58	95	257	32	86
	9	1.727	67	194	22	65	92	260	31	87
	10	1.927	68	201	23	67	94	273	31	91
	11	2.127	73	212	24	71	86	265	29	88
	12	2.327	99	195	33	65	100	297	33	99
	13	2.527	77	230	26	77	102	300	34	100
	14	2.727	80	236	27	79	121	300	40	100
	15	2.927	96	243	32	81	102	334	34	111
	16	3.127	86	267	29	89	115	330	38	110
	17	3.327	96	265	32	88	120	339	40	113
	18	3.527	87	269	29	90	122	341	41	114
	19	3.727	106	263	35	88	102	386	34	129
	20	3.927	120	271	40	90	145	371	48	124
	21	4.127	89	298	30	99	128	395	43	132
	22	4.327	107	304	36	101	140	390	47	130
	23	4.527	100	295	33	98	115	418	38	139
24	4.727	92	328	31	109	134	394	45	131	

Table F.1: Single Injection Mode Jet Flow Field Data cont'd.

	Image	Time (ms)	PR = 3				PR = 5			
			Width (pixels)	Length (pixels)	Width (mm)	Length (mm)	Width (pixels)	Length (pixels)	Width (mm)	Length (mm)
5.0 ms Duration cont'd.	25	4.927	104	317	35	106	131	434	44	145
	26	5.127	109	308	36	103	153	410	51	137
	27	5.327	114	303	38	101	143	420	48	140
	28	5.527	111	333	37	111	167	404	56	135
	29	5.727	127	325	42	108	184	443	61	148
	30	5.927	126	355	42	118				
	31	6.127	153	331	51	110				
	32	6.827	119	371	40	124				
	33	7.427	121	366	40	122				
	34	8.627	185	372	62	124				
	35	9.827	156	404	52	135				

F.2 Pulsed Injection Mode Experimental Data

The following is data collected during the pulsed injection jet flow field characterization study:

Table F.2: Pulsed Injection Mode Jet Flow Field Data

	Img	Time (ms)	0.5 ms Pulse Delay				1.0 ms Pulse Delay				2.0 ms Pulse Delay			
			Width (pix)	Length (pix)	Width (mm)	Length (mm)	Width (pix)	Length (pix)	Width (mm)	Length (mm)	Width (pix)	Length (pix)	Width (mm)	Length (mm)
0.5 ms Duration		0			1			1					1	
	1	0.127	23	64	8	21	27	58	9	19	25	64	8	21
	2	0.327	33	94	11	31	33	86	11	29	38	92	13	31
	3	0.527	35	121	12	40	41	121	14	40	47	105	16	35
	4	0.727	48	116	16	39	47	131	16	44	49	125	16	42
	5	0.927	47	132	16	44	59	131	20	44	55	135	18	45
	6	1.127	58	137	19	46	54	148	18	49	55	143	18	48
	7	1.327	58	157	19	52	64	145	21	48	49	150	16	50
	8	1.527	60	154	20	51	62	147	21	49	69	141	23	47
	9	1.727	58	175	19	58	67	148	22	49	57	161	19	54
	10	1.927	74	174	25	58	69	159	23	53	63	159	21	53
	11	2.127	66	162	22	54	65	172	22	57	72	171	24	57
	12	2.327	97	162	32	54	77	180	26	60	68	170	23	57
	13	2.527	68	195	23	65	76	167	25	56	83	174	28	58
	14	3.127	74	194	25	65	69	199	23	66	76	188	25	63
	15	3.727	90	209	30	70	69	202	23	67	70	210	23	70
	16	4.327	89	235	30	78	81	207	27	69	74	203	25	68
17	5.527	92	250	31	83	72	236	24	79	100	237	33	79	
1.0 ms		0			1			1					1	
	1	0.127	29	67	10	22	26	65	9	22	30	75	10	25
	2	0.327	35	95	12	32	36	89	12	30	36	97	12	32
	3	0.527	44	114	15	38	44	110	15	37	45	114	15	38

Table F.2: Pulsed Injection Mode Jet Flow Field Data cont'd.

	lmg	Time (ms)	0.5 ms Pulse Delay				1.0 ms Pulse Delay				2.0 ms Pulse Delay				
			Width (pix)	Length (pix)	Width (mm)	Length (mm)	Width (pix)	Length (pix)	Width (mm)	Length (mm)	Width (pix)	Length (pix)	Width (mm)	Length (mm)	
1.0 ms Duration cont'd.	4	0.727	48	130	16	43	50	125	17	42	43	132	14	44	
	5	0.927	46	139	15	46	52	147	17	49	51	142	17	47	
	6	1.127	50	159	17	53	58	154	19	51	59	157	20	52	
	7	1.327	58	178	19	59	60	160	20	53	62	161	21	54	
	8	1.527	69	174	23	58	53	172	18	57	74	177	25	59	
	9	1.727	71	173	24	58	87	177	29	59	68	178	23	59	
	10	1.927	63	208	21	69	68	195	23	65	63	195	21	65	
	11	2.127	63	204	21	68	106	192	35	64	76	203	25	68	
	12	2.327	70	215	23	72	67	209	22	70	80	198	27	66	
	13	2.527	79	217	26	72	92	199	31	66	74	219	25	73	
	14	2.727	97	210	32	70	84	198	28	66	103	218	34	73	
	15	2.927	93	219	31	73	72	223	24	74	87	242	29	81	
	16	3.527	90	240	30	80	74	246	25	82	97	273	32	91	
	17	4.127	97	270	32	90	89	253	30	84	105	268	35	89	
	18	5.327	102	292	34	97	113	298	38	99	89	295	30	98	
	19	6.527	103	324	34	108	122	317	41	106	104	317	35	106	
	1.5 ms Duration	0				1			1				1		
		1	0.127	29	67	10	22	28	69	9	23	29	65	10	22
		2	0.327	34	87	11	29	44	94	15	31	35	100	12	33
3		0.527	44	115	15	38	42	117	14	39	38	104	13	35	
4		0.727	41	131	14	44	45	138	15	46	44	124	15	41	
5		0.927	47	139	16	46	48	141	16	47	52	142	17	47	
6		1.127	74	144	25	48	62	151	21	50	64	148	21	49	
7		1.327	61	165	20	55	55	170	18	57	59	165	20	55	
8		1.527	78	180	26	60	66	180	22	60	79	166	26	55	
9		1.727	71	198	24	66	75	193	25	64	68	183	23	61	
10		1.927	69	205	23	68	69	212	23	71	74	195	25	65	
11		2.127	72	207	24	69	74	216	25	72	74	198	25	66	
12		2.327	76	214	25	71	96	216	32	72	85	220	28	73	
13		2.527	81	217	27	72	81	248	27	83	77	238	26	79	
14		2.727	95	230	32	77	86	239	29	80	93	253	31	84	
15		2.927	88	243	29	81	112	247	37	82	75	260	25	87	
16		3.127	106	260	35	87	99	260	33	87	100	265	33	88	
17		3.727	116	268	39	89	84	293	28	98	92	287	31	96	
18		4.327	120	292	40	97	114	289	38	96	99	292	33	97	
19		5.527	109	333	36	111	95	342	32	114	124	325	41	108	
20	6.727	121	357	40	119	173	332	58	111	111	392	37	131		

F.3 Jet Impingement Experimental Data

The following is experimental data collected when investigating the effects of jet impingement onto circular and rectangular cross-section obstructions:

Table F.3: Jet Impingement Flow Field Data (Circular Obstruction)

	lmg	Time (ms)	0.5 mm Gap				1.0 mm Gap				2.0 mm Gap				
			Width (pix)	Length (pix)	Width (mm)	Length (mm)	Width (pix)	Length (pix)	Width (mm)	Length (mm)	Width (pix)	Length (pix)	Width (mm)	Length (mm)	
1.0 ms Duration		0			1			1					1		
	1	0.127	39	38	14	13	30	35	10	12	33	41	12	14	
	2	0.327	45	51	16	18	42	52	15	18	36	49	13	17	
	3	0.527	54	75	19	26	40	67	14	23	49	74	17	26	
	4	0.727	60	77	21	27	58	72	20	25	58	77	20	27	
	5	0.927	66	87	23	30	65	90	23	31	66	83	23	29	
	6	1.127	72	88	25	31	62	95	22	33	63	88	22	31	
	7	1.327	84	104	29	36	69	98	24	34	71	107	25	37	
	8	1.527	74	110	26	38	116	95	40	33	65	105	23	37	
	9	1.727	77	112	27	39	116	109	40	38	69	112	24	39	
	10	1.927	97	104	34	36	109	98	38	34	105	105	37	37	
	11	2.127	88	121	31	42	112	102	39	36	96	113	33	39	
	12	2.327	94	121	33	42	128	107	45	37	84	125	29	44	
	13	2.527	89	113	31	39	106	131	37	46	119	126	42	44	
	14	2.727	100	138	35	48	131	133	46	46	124	122	43	43	
	15	2.927	139	113	48	39	108	123	38	43	111	142	39	50	
	16	3.527	92	133	32	46	137	133	48	46	101	139	35	48	
	17	4.127	138	133	48	46	94	159	33	55	153	145	53	51	
	18	5.327	172	138	60	48	93	180	32	63	158	160	55	56	
19	6.527	162	180	57	63	148	189	52	66	146	180	51	63		

Table F.4: Jet Impingement Flow Field Data (Rectangular Obstruction)

	lmg	Time (ms)	10 mm Gap				15 mm Gap			
			Width (pix)	Length (pix)	Width (mm)	Length (mm)	Width (pix)	Length (pix)	Width (mm)	Length (mm)
1.0 ms Duration		0			1			1		
	1	0.127	45	38	16	13	42	51	15	18
	2	0.327	57	47	20	16	72	61	25	21
	3	0.527	74	51	26	18	76	68	27	24
	4	0.727	80	58	28	20	85	71	30	25
	5	0.927	103	59	36	21	92	80	32	28
	6	1.127	111	61	39	21	107	81	37	28
	7	1.327	126	58	44	20	117	82	41	29
	8	1.527	138	60	48	21	136	86	47	30
	9	1.727	135	66	47	23	140	94	49	33
	10	1.927	140	63	49	22	140	94	49	33
	11	2.127	149	67	52	23	145	101	51	35
	12	2.327	161	66	56	23	165	91	58	32
	13	2.527	156	71	54	25	158	94	55	33
	14	2.727	165	79	58	28	156	103	54	36
15	2.927	171	64	60	22	164	108	57	38	

Table F.4: Jet Impingement Flow Field Data (Rectangular Obstruction) cont'd.

	Img	Time (ms)	10 mm Gap				15 mm Gap			
			Width (pix)	Length (pix)	Width (mm)	Length (mm)	Width (pix)	Length (pix)	Width (mm)	Length (mm)
cont'd.	16	3.527	175	78	61	27	172	108	60	38
	17	4.127	200	80	70	28	197	99	69	35
	18	5.327	210	102	73	36	205	108	72	38
	19	6.527	202	98	70	34	206	112	72	39

F.4 Jet Enclosure Experimental Data

The following is data collected when investigating the effects of an enclosure:

Table F.5: Jet Enclosure Flow Field Data

	Img	Time (ms)	12 mm Walls				23 mm Walls				50 mm Walls			
			Width (pix)	Length (pix)	Width (mm)	Length (mm)	Width (pix)	Length (pix)	Width (mm)	Length (mm)	Width (pix)	Length (pix)	Width (mm)	Length (mm)
1.0 ms Duration		0			1			1					1	
	1	0.127	17	78	6	27	29	76	10	27	28	75	10	26
	2	0.327	28	104	10	36	32	110	11	38	35	106	12	37
	3	0.527	34	114	12	40	47	124	16	43	50	130	17	45
	4	0.727	34	142	12	50	46	138	16	48	48	142	17	50
	5	0.927	34	147	12	51	49	154	17	54	51	149	18	52
	6	1.127	34	162	12	57	53	166	18	58	66	160	23	56
	7	1.327	34	174	12	61	57	180	20	63	53	183	18	64
	8	1.527	34	192	12	67	65	196	23	68	64	185	22	65
	9	1.727	34	197	12	69	65	197	23	69	70	215	24	75
	10	1.927	34	199	12	69	65	212	23	74	70	207	24	72
	11	2.127	34	205	12	72	65	203	23	71	80	231	28	81
	12	2.327	34	232	12	81	65	238	23	83	65	235	23	82
	13	2.527	34	232	12	81	65	215	23	75	86	232	30	81
	14	2.727	34	225	12	78	65	210	23	73	92	245	32	85
	15	2.927	34	234	12	82	65	246	23	86	89	260	31	91
	16	3.527	34	242	12	84	65	253	23	88	96	286	33	100
	17	4.127	34	244	12	85	65	271	23	95	108	281	38	98
	18	5.327	34	272	12	95	65	293	23	102	108	301	38	105
19	6.527	34	278	12	97	65	294	23	103	121	310	42	108	

Non-Premixed Autoignition Delay Data



G.1 Experimental Data

The following is experimental data collected during the non-premixed autoignition experiments:

Table G.1: Non-Premixed Autoignition Delay Data

Pulse Width (ms)	Inj. Press. (psig)	P Driven (psia)	P Driver (psia)	τ CH (ms)			τ BB (ms)			P Test (bar)	T Test (K)
				nominal	upper	lower	nominal	upper	lower		
0.5	1550	11.163	624.23							31.706	1142
0.5	1550	11.163	622.92							31.706	1142
0.5	1550	11.161	623.51							31.821	1144
0.5	1530	11.164	622.98							30.780	1125
0.5	1550	11.160	623.04							32.017	1148
0.5	1550	13.359	665.02							32.381	1056
0.5	1525	13.360	665.61							33.655	1076
1	1500	11.164	623.64	1.50	1.50	1.20	1.38	1.38	0.88	30.110	1113
1	1550	11.165	624.23	1.56	1.68	1.24	1.55	1.70	1.19	29.593	1103
1	1500	11.163	623.03	1.58	1.68	1.24	1.44	1.58	1.15	28.671	1086
1	1500	11.163	622.32	1.13	1.26	0.91	1.11	1.23	0.89	29.127	1095
1	1480	11.160	622.90	1.49	1.49	1.46	1.38	1.56	1.11	28.448	1082
1	1520	11.162	622.90	1.40	1.46	1.06	1.24	1.33	0.94	28.841	1090
1	1500	11.151	623.54	1.15	1.21	0.95	1.06	1.21	0.98	29.096	1095
1	1500	11.160	622.98	1.60	1.60	1.53	1.47	1.53	1.31	29.693	1105
1	1500	11.163	622.99	1.50	1.55	1.45	1.43	1.55	1.31	29.016	1093
1	1550	11.164	623.06	1.35	1.38	1.24	1.28	1.41	1.23	32.348	1154
1	1525	11.163	623.54							31.513	1139
1	1480	8.619	609.35	1.28	1.28	1.28	1.08	1.08	0.95	30.285	1273
1	1480	7.497	614.16	0.95	0.95	0.87	1.21	1.21	0.94	29.680	1356
1	1480	13.150	594.97							29.644	1020
1.5	1550	11.164	623.05	1.48	1.80	1.39	1.48	1.58	1.31	32.674	1159
1.5	1580	11.165	623.01							31.398	1136
1.5	1575	11.159	622.99							31.695	1142
1.5	1550	11.165	624.14							31.518	1139
1.5	1530	11.153	622.98							31.366	1136
1.5	1550	11.160	623.04	1.96	1.96	1.88	1.97	1.97	1.85	31.386	1136
1.5	1550	13.362	665.03	1.18	1.18	1.18	1.24	1.24	1.24	32.699	1061
1.5	1530	13.361	665.02	1.99	1.99	1.86	1.89	1.89	1.81	32.699	1061
1.5	1550	13.357	665.02							32.374	1056

Table G.1: Non-Premixed Autoignition Delay Data cont'd.

Pulse Width (ms)	Inj. Press. (psig)	P Driven (psia)	P Driver (psia)	τ CH (ms)			τ BB (ms)			P Test (bar)	T Test (K)
				nominal	upper	lower	nominal	upper	lower		
1.5	1525	13.360	665.01							32.818	1063
1.5	1475	7.501	613.86	1.41	1.41	1.26	1.31	1.31	1.14	30.864	1385
1.5	1475	8.626	608.47	1.23	1.23	1.23	1.23	1.23	1.23	29.801	1262
1.5	1475	9.288	606.08	1.38	1.38	1.33	1.46	1.46	1.06	29.545	1210
3	1525	11.159	623.00	2.98	3.30	1.79	3.02	3.09	1.86	31.696	1142
3	1525	11.163	623.01	2.88	2.88	2.62	2.83	2.83	2.53	32.346	1154
3	1525	11.164	623.60	3.47	3.82	3.21	3.51	4.60	3.21	32.028	1148
3	1525	11.160	623.05	1.91	3.38	1.91	1.93	4.15	1.93	32.017	1148
3	1520	11.160	623.05	2.11	4.40	2.11	2.14	3.74	2.14	31.625	1141
3	1520	11.159	623.05	2.05	3.47	2.05	2.41	3.49	2.41	31.381	1136
3	1515	13.356	665.05	3.02	3.75	3.02	3.16	4.03	3.16	32.493	1058
3	1510	13.361	665.70							33.659	1076
3	1510	13.374	665.10	2.79	2.94	2.14	3.09	3.09	2.09	32.972	1065
3	1510	13.360	665.11	3.05	3.05	3.05	2.81	3.38	2.30	32.696	1061
3	1510	13.359	665.11	2.91	2.91	1.96	2.99	2.99	1.96	33.009	1066
5	1500	13.359	665.14	2.68	2.68	2.68	2.74	2.74	2.74	32.816	1063
5	1500	13.360	665.14	3.41	3.41	3.26	3.38	3.38	3.29	32.383	1056
5	1500	13.362	665.13	2.91	3.09	2.91	2.95	2.99	2.95	33.016	1066
5	1500	13.358	666.92	1.92	3.37	1.92	1.72	2.19	1.72	33.007	1066
5	1500	11.163	623.11	2.03	4.06	1.57	2.47	4.63	1.79	31.393	1136
5	1500	11.160	623.16	2.73	2.99	2.68	2.87	3.38	2.87	31.384	1136
5	1500	11.162	623.16	2.53	2.53	1.64	2.55	2.55	1.65	31.389	1136
5	1490	8.620	609.45	2.98	3.20	2.89	3.14	3.19	2.64	29.662	1260
5	1480	7.500	614.26	2.48	2.64	2.14	2.46	2.79	2.17	31.219	1393
5	1480	14.553	590.27							29.921	976
5	1480	13.146	594.46							29.464	1017
0.5	1380	5.748	355.62	1.78	2.10	1.78	1.78	2.10	1.78	16.961	1164
0.5	1380	5.750	355.47	8.70	8.70	8.70	8.64	8.64	8.64	15.758	1122
0.5	1375	5.744	355.25	3.79	3.79	3.79	3.74	3.74	3.49	15.586	1116
1	1390	5.748	355.63	1.23	1.23	1.23	1.23	1.23	1.23	18.170	1206
1	1380	5.750	355.61	3.27	3.27	3.27	3.12	3.12	3.06	15.759	1122
1	1375	5.749	355.30	4.06	4.06	3.46	3.96	3.96	3.37	15.600	1116
1	1370	4.928	357.86	1.20	1.20	1.09	1.05	1.05	1.05	15.419	1199
1	1350	4.286	361.40	0.84	0.84	0.84	0.78	0.78	0.78	17.919	1397
1	1350	4.578	359.01	1.28	1.28	0.77	1.13	1.13	0.67	15.427	1246
1	720	5.310	356.61							17.419	1229
1	680	5.310	356.71	0.81	1.63	0.81	0.73	1.09	0.73	17.130	1218
1.5	1390	5.750	354.44	1.25	1.25	1.17	1.20	1.20	1.12	17.559	1185
1.5	1370	5.744	355.50	1.29	1.33	1.20	1.32	1.40	1.27	17.085	1169
1.5	1380	5.747	355.46	0.88	1.78	0.88	0.81	1.63	0.76	17.801	1193
1.5	1370	5.301	357.25	2.12	2.19	2.02	2.21	2.21	1.75	15.515	1159
1.5	1350	4.435	360.21	0.73	1.08	0.45	0.49	1.05	0.38	17.748	1364
1.5	1350	4.435	360.18	1.06	1.06	0.62	0.99	0.99	0.76	17.257	1344
1.5	725	5.310	357.30	2.32	2.32	0.96	2.15	2.15	0.94	17.418	1229

Table G.1: Non-Premixed Autoignition Delay Data cont'd.

Pulse Width (ms)	Inj. Press. (psig)	P Driven (psia)	P Driver (psia)	τ CH (ms)			τ BB (ms)			P Test (bar)	T Test (K)
				nominal	upper	lower	nominal	upper	lower		
3	1390	5.744	354.43	5.82	6.20	5.82	5.85	6.38	5.85	15.742	1122
3	1370	5.752	359.10	1.65	1.68	1.61	1.65	1.69	1.48	18.370	1212
3	1390	5.749	355.45							15.448	1111
3	1370	4.287	361.45	1.51	1.56	1.46	1.30	1.35	1.15	18.042	1402
3	1350	4.436	360.81	1.99	2.05	1.86	1.93	2.05	1.93	15.620	1275
3	1350	5.937	354.20	2.63	2.72	2.37	2.73	2.73	2.53	17.204	1154
3	700	5.939	354.80	2.40	2.40	2.40	2.34	2.34	2.34	17.037	1148
3	770	5.310	357.20	1.91	1.91	1.49	1.88	3.02	1.78	17.241	1222
5	1390	5.746	354.43	2.63	2.80	1.59	2.55	2.74	1.37	17.439	1181
5	1380	5.747	355.47							15.750	1122
5	1380	5.750	355.47	1.96	2.04	1.86	2.01	2.20	1.52	17.992	1199
5	1380	5.749	355.26	3.07	3.07	2.89	3.11	3.17	2.02	15.754	1122
5	1370	5.308	356.64	2.14	2.14	1.73	2.24	2.45	1.11	15.594	1162
5	700	5.309	356.71							17.305	1225

Autoignition Visualization Images *H*

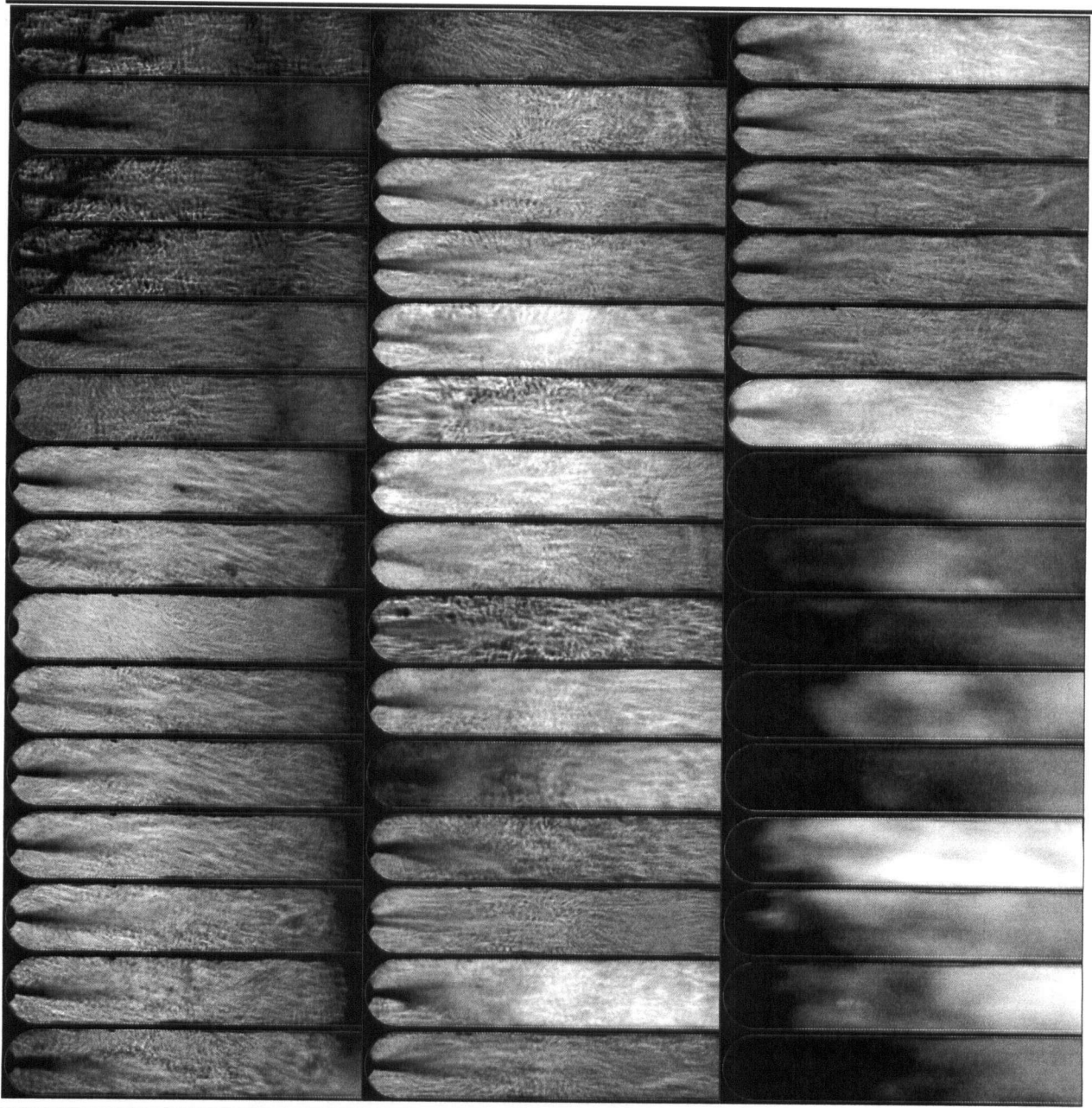


Figure H.1: Autoignition Visualization Images

Shock Tube Optical Test Section Design Calculations

I

I.1 Design Variables

In the design of the optical test section several key parameters were optimized to ensure that both the material strength and fatigue limits were not exceeded during “normal” operation.

These parameters included:

1. Test section width;
2. Viewing window profile; and
3. Viewing window offset from test section endplate.

I.1.1 Test Section Width

Increasing the test section width increases the overall strength and stiffness of the test section, but the increased width also requires increasing the width of the viewing window keyway to maintain the field of view. There are also limitations imposed on how wide the test section can be made by the fact that it must be mounted to a standard flange and must be smaller than the flange’s bolt circle diameter.

I.1.2 Viewing Window Profile

The viewing window profile consists of a narrow window, which is flush-mounted to the inner walls of the test section, and a much wider keyway, which is used for applying clamping force onto the window. Of these two, the keyway design offers the most flexibility. The keyway’s width is fixed by the requirement to maintain a full field of view within the test section and is therefore purely a function of the test section width. Its minimum thickness is set by the strength of the fused quartz window and is calculated using the following empirical formula:

$$p_{\max} = 2.28 \cdot \sigma_{\max} \cdot \frac{t^2}{w^2} \Rightarrow t_{\min} = \sqrt{\frac{p_{\max}}{2.28 \cdot \sigma_{\max}}} \cdot w$$

where: p_{\max} is the maximum design pressure differential across the quartz window;
 σ_{\max} is the maximum stress (1000 psi (70 bar) for quartz with a S.F. of 7);
 t is the quartz window thickness; and
 w is the unsupported quartz window width.

Thus the only parameter available for optimization is the shape of the transition from the narrow inner window to the wider keyway. Previous tests with a small 10 mm diameter fused quartz window had shown that the only acceptable transition between the two was a smooth taper (i.e. no sharp corners or o-ring grooves) and so the design was set by these constraints.

I.1.3 Viewing Window End Offset

Increasing the viewing window offset from the test section endplate increases both the strength and stiffness of the test section as well as reducing stresses on both the viewing window's inner radius (the point of maximum stress concentration) and the welds holding the test section to the endplate flange. However, the tip of the fuel injector must be flush with the end of the viewing window in order to see the entire gas jet during experiments, and so the injector dimensions (length) constrain the maximum end offset.

I.2 Stress Analysis (Static Loading)

Given the three identified design variables, seven possible designs were analysed using finite element methods. For this preliminary comparison between the various options, static analysis was performed since only a relative comparison between options was desired, and static analysis is much less CPU-time intensive than dynamic analysis. In all cases the test pressure was 100 bar, and two sets of boundary conditions, "fully-constrained" and "free" were tested (since the actual constraints fall somewhere between these two). The design variations considered are summarized below, with results in Table I.1 and Table I.2:

Baseline: Original design (J. Huang) but with a width of 4.5 in and a chamfered keyway.

Opt 1: Baseline + increased viewing window end offset from 1.2 in to 1.5 in.

Opt 2: Baseline + increased viewing window end offset from 1.2 in to 2.0 in.

Opt 3: Baseline + increased viewing window end offset from 1.2 in to 3.0 in.

Opt 4: Opt 3 + increased test section width from 4.5 in to 5.0 in.

Opt 5: Opt 4 + increased viewing window end offset from 3.0 in to 4.0 in.

Opt 6: Opt 5 + increased test section width from 5.0 in to 6.0 in.

Table I.1: Maximum Stress and Deflection for Fully Constrained B.C.

	Baseline	Opt 1	Opt 2	Opt 3	Opt 4	Opt 5	Opt 6
Stress psi [Mpa]	54241 [374]	50823 [350]	54277 [374]	53123 [366]	49548 [342]	48671 [336]	N/A
Deflection in [mm]	0.00409 [0.104]	0.00414 [0.105]	0.00404 [0.103]	0.00390 [0.099]	0.00294 [0.075]	0.00287 [0.073]	N/A

Table I.2: Maximum Stress and Deflection for Free B.C.

	Baseline	Opt 1	Opt 2	Opt 3	Opt 4	Opt 5	Opt 6
Stress psi [Mpa]	N/A	91232 [629]	75723 [522]	57806 [399]	56650 [391]	50043 [345]	34684 [239]
Deflection in [mm]	N/A	0.00650 [0.165]	0.00514 [0.131]	0.00408 [0.104]	0.00319 [0.081]	0.00292 [0.074]	0.00169 [0.042]

Among the options analysed, the optimal design is somewhere between Opt 2 and Opt 3. While Opt 4 – 6 exhibited improved performance, their increased test section width was too large for mounting into standard flanges without interfering with the flange bolts. Additionally, the viewing window end offset of Opt 3 was longer than the available injector mounting length, so this had to be reduced.

I.3 Stress Analysis (Dynamic Loading)

Some preliminary stress analysis with dynamically applied pressure indicated that the common convention of treating dynamic loads as equivalent to static loads of double the magnitude was reasonably accurate. Window deflections using both statically and dynamically applied loads are plotted in Figure I.1. This shows that the maximum deflection at 100 bar is 0.090 mm under static loading and 0.180 mm under dynamic loading, while at 40 bar the maximum deflections are 0.036 mm and 0.071 mm under static and dynamic loading, respectively. The dynamic deflections are approximately double their static equivalents, mimicking the trend observed in maximum stresses. Additionally, when materials are subjected to dynamic loads for very short durations (~ milliseconds) material properties are greatly strengthened and catastrophic failure is therefore not a concern. From the limited stress analysis conducted, it was concluded that failure of the test section itself is not a concern.

I.4 Fatigue Analysis

Given the location of the maximum stresses along the inner radius of the optical window slot, fatigue analysis was performed assuming this would be the location of failure.

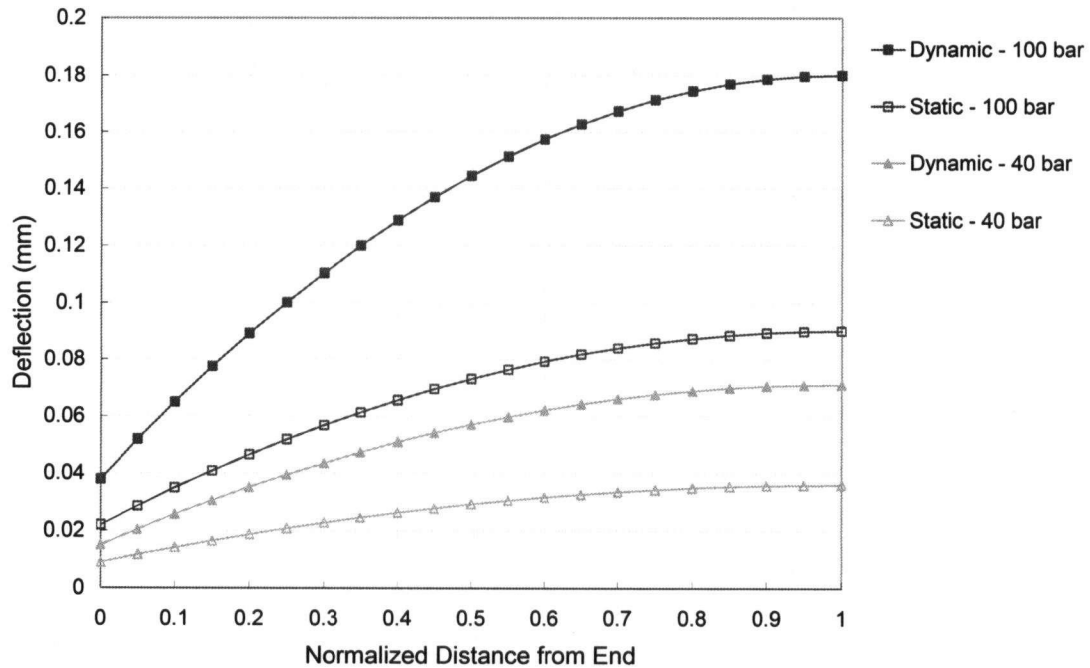


Figure I.1: Maximum Window Deflection Under Dynamic Loading

Properties of Stainless Steel used in fatigue analysis:

304 SS Annealed Ultimate Tensile Strength, $S_{ut} = 82.4 \text{ kpsi}$

Endurance Limit:

This is the endurance limit of the raw material for a polished rotating beam specimen undergoing fully reversed loading:

$$S'_e = 0.504 \cdot S_{ut} = 0.504 \cdot 82.4 = 41.5 \text{ kpsi}$$

Endurance Limit Modifying Factors:

Surface Factor, k_a :

Corrects for surface finish, with rough surfaces providing many crack initiation sites and thus resulting in smaller endurance limit. The constants (2.70, -0.265) were empirically derived for a "Machined or cold-drawn" surface finish:

$$k_a = 2.70 \cdot S_{ut}^{-0.265} = 2.70 \cdot 82.4^{-0.265} = 0.839$$

Size Factor, K_b :

Corrects for the size of the component, with larger components having a smaller endurance limit:

$$k_b = \left(\frac{d}{0.3} \right)^{-0.1133}$$

where d is the effective diameter found by equating the area of the specimen stressed at and above 95% of the maximum stress to the equivalent area in a round specimen:

$$A_{95\%,rect} = 0.05 \cdot h \cdot b = 0.05 \cdot 0.306 \cdot 1.043 = 0.01596 \text{ in}^2$$

$$A_{95\%,circ} = \frac{\pi}{4} [d^2 - (0.95 \cdot d^2)] = 0.0766 \cdot d^2$$

$$0.01596 = 0.0766 \cdot d^2 \Rightarrow d = 0.456 \text{ in}$$

$$k_b = \left(\frac{0.456}{0.3} \right)^{-0.1133} = 0.954$$

Load Factor, k_c :

Corrects for the type of loading (axial, bending, torsion, shear). The location of maximum stress on the test section is primarily in bending, so the correction factor for bending is used:

$$k_c = 1$$

Temperature Factor, k_d :

Corrects for increased likelihood of brittle failure during low temperature operation or yielding at high temperatures. Since the test section is only exposed to high temperatures for a few milliseconds, the nominal operating temperature is assumed to be room temperature and no correction is applied:

$$k_d = \frac{S_T}{S_{RT}} = 1$$

Miscellaneous Effects Factor, k_e :

Corrects for corrosion, cyclic frequencies, stress concentrations, etc. Since stress analysis of the test section has already provided the maximum stress at the inner window radius (rather than the nominal) and all analysis has been performed based on this maximum

stress, the effects of stress concentration have already been implicitly accounted for. The only other potentially relevant factor is corrosion:

$$k_e = 0.8 (?)$$

Using the above endurance limit modifying factors, the endurance limit is:

$$S_e = k_a \cdot k_b \cdot k_c \cdot k_d \cdot k_e \cdot S'_e = 0.839 \cdot 0.954 \cdot 0.8 \cdot 41.5 = 26.6 \text{ kpsi}$$

Additionally, to calculate the expected lifetime if the test section is subjected to a given loading, the following equation may be used:

$$N = \left(\frac{\sigma}{a} \right)^{\frac{1}{b}}$$

where:

$$a = \frac{(0.9 \cdot S_{ut})^2}{S_e} = \frac{(0.9 \cdot 82.4)^2}{26.6} = 207$$

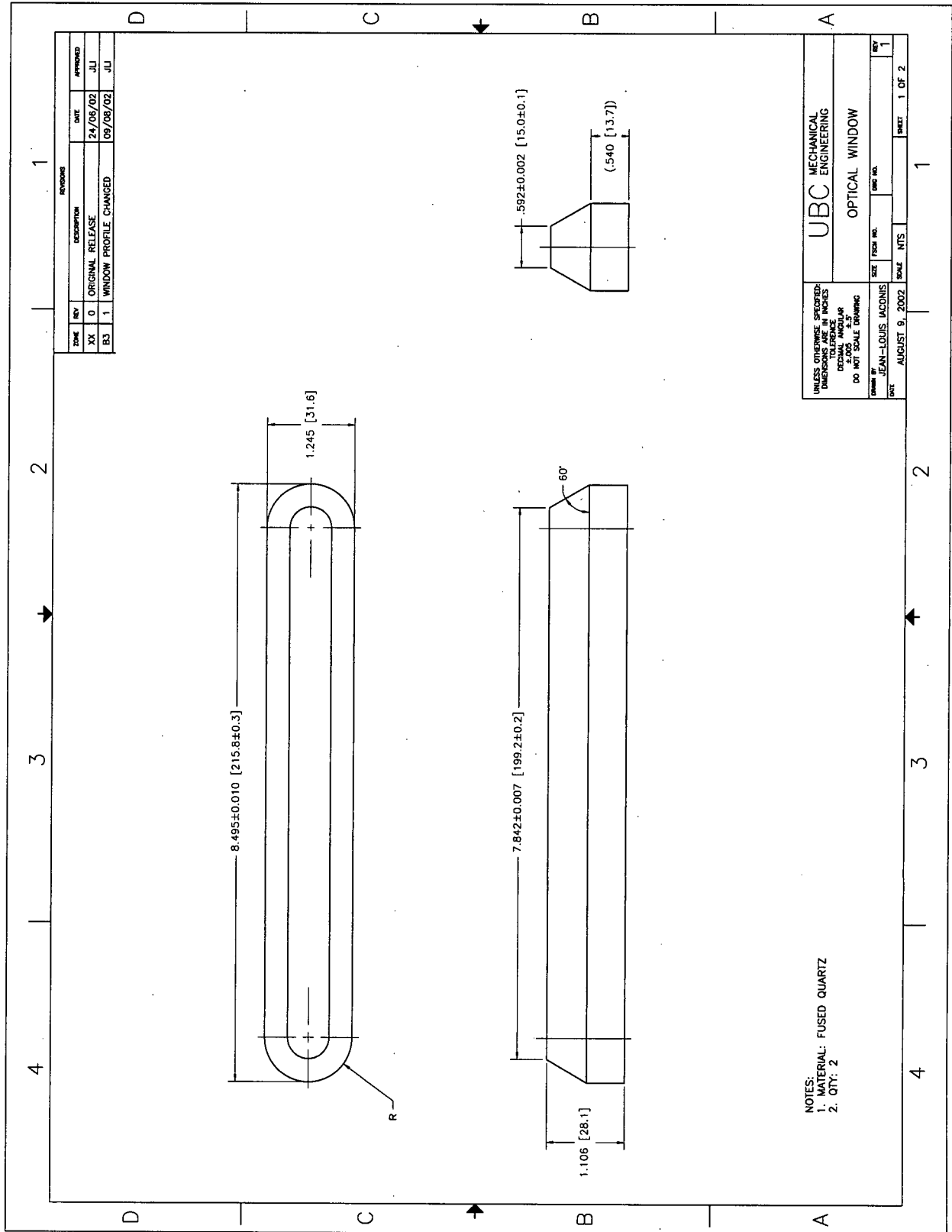
$$b = -\frac{1}{3} \log \frac{0.9 \cdot S_{ut}}{S_e} = -\frac{1}{3} \log \frac{0.9 \cdot 82.4}{26.6} = -0.088$$

$$N = \left(\frac{\sigma}{a} \right)^{\frac{1}{b}} = \left(\frac{\sigma}{207} \right)^{-11.326}$$

Since the calculated endurance limit is greater than the maximum stresses experienced at 40 bar, the test section has infinite life at this operating pressure. Using the above equation, the greatest stress that the test section may be subjected to while maintaining infinite life (1,000,000 cycles) is 61.1 kpsi. This is just slightly greater than the maximum stresses if the test section is operated continuously at 100 bar.

***Shock Tube Optical
Test Section Drawings***

J

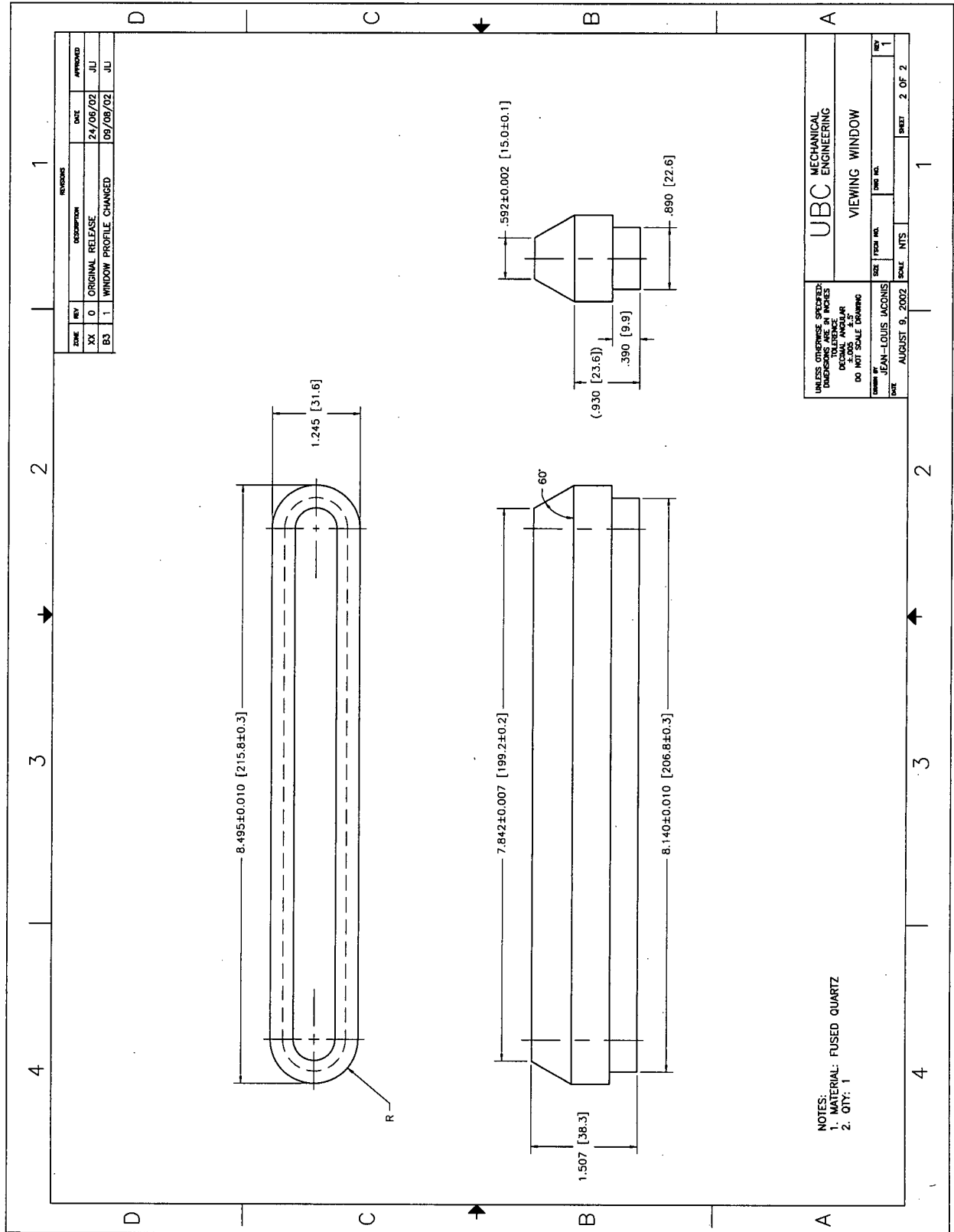


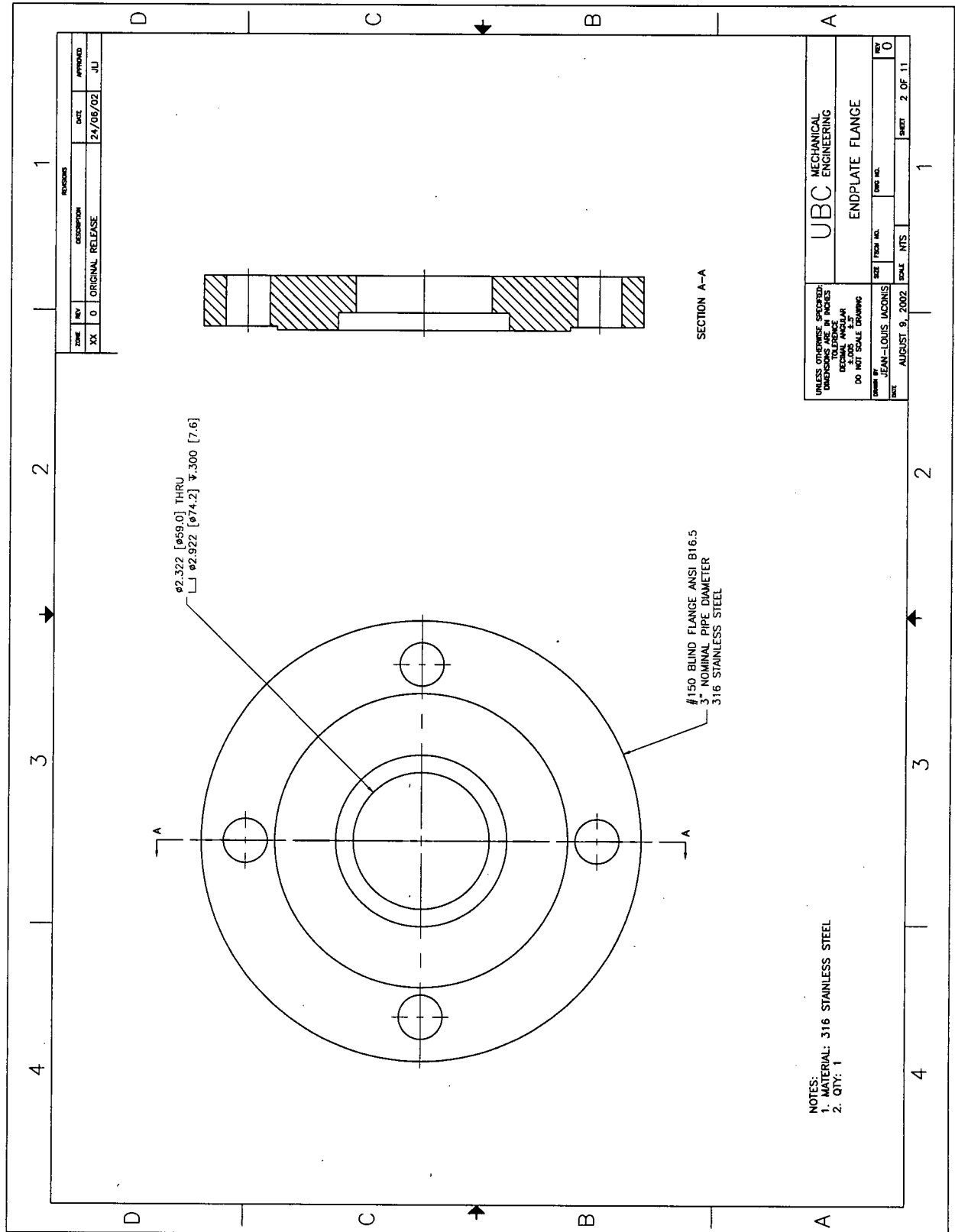
REV		DESCRIPTION	DATE	APPROVED
XX	0	ORIGINAL RELEASE	24/06/02	JLI
B3	1	WINDOW PROFILE CHANGED	09/08/02	JLI

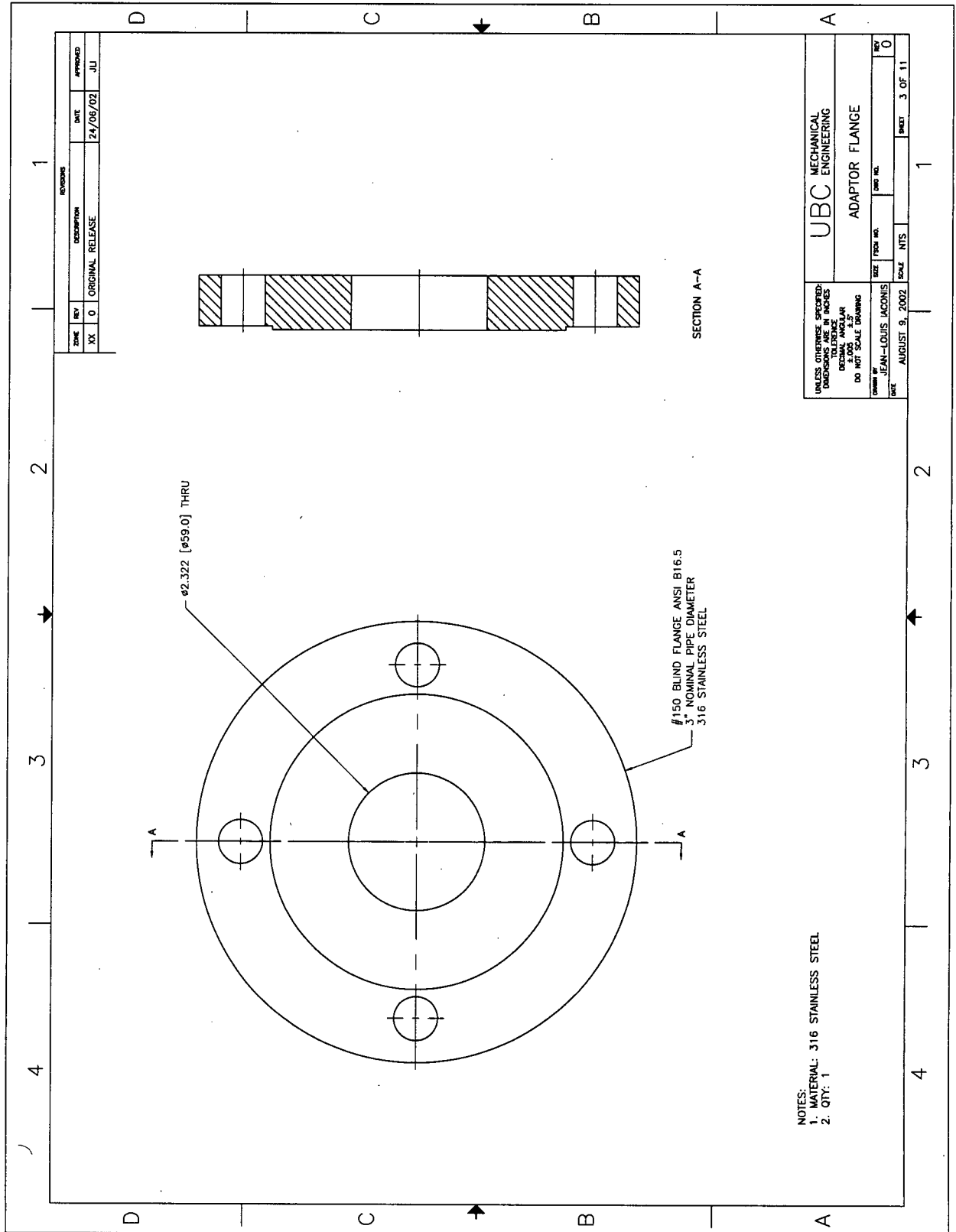
UNLESS OTHERWISE SPECIFIED:
 DIMENSIONS ARE IN INCHES
 TOLERANCES ARE:
 DECIMAL FRACTIONS
 .005 .010 .015
 DO NOT SCALE DRAWING

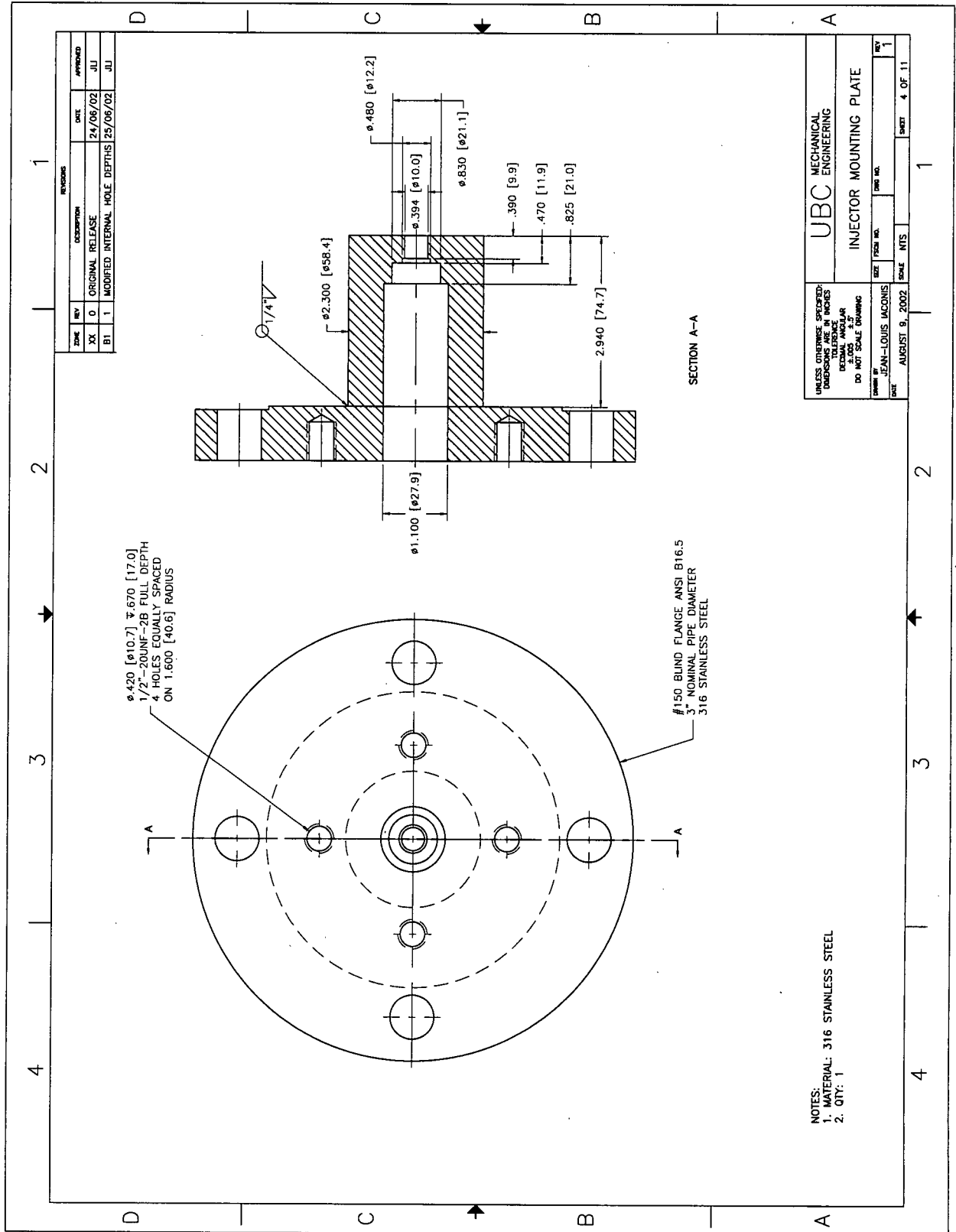
OWNER BY		JEAN-LOUIS IACONIS	DATE	AUGUST 9, 2002
SIZE	SHEET NO.	SCALE	NTS	SHEET 1 OF 2
UBC MECHANICAL ENGINEERING		OPTICAL WINDOW		

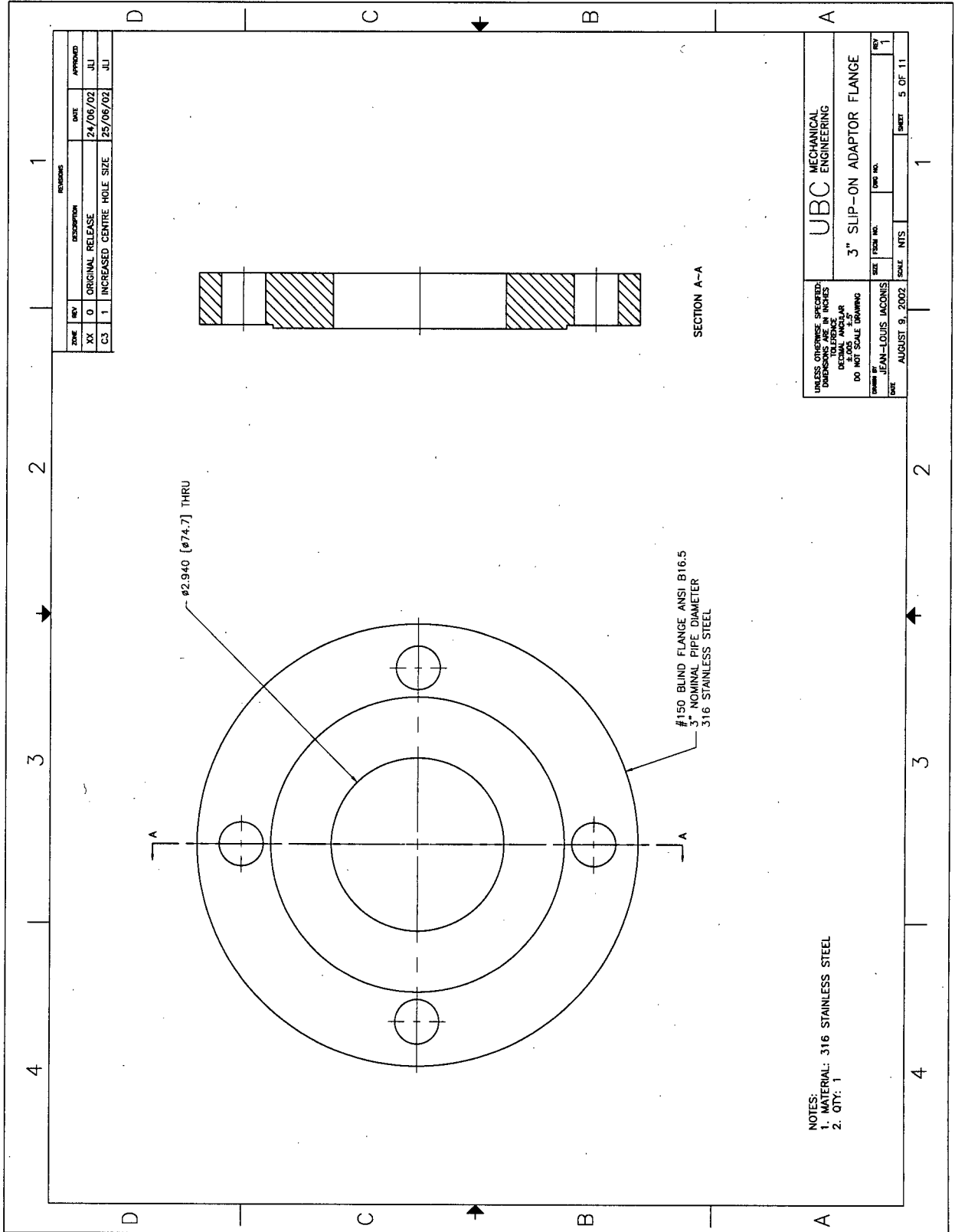
- NOTES:
 1. MATERIAL: FUSED QUARTZ
 2. QTY: 2







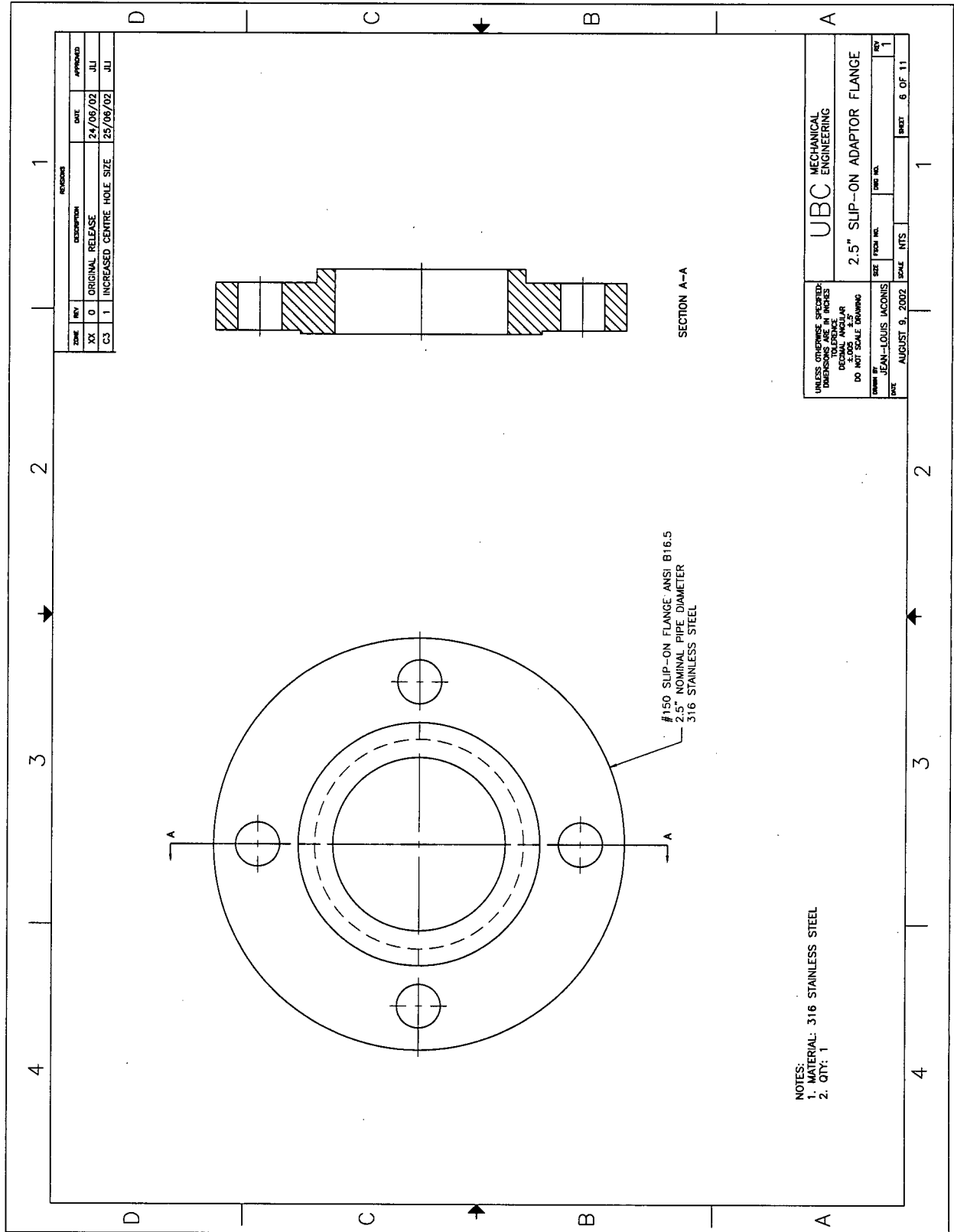




REVISIONS		DATE	APPROVED
ZONE	REV	DESCRIPTION	DATE
XX	0	ORIGINAL RELEASE	24/06/02
C3	1	INCREASED CENTRE HOLE SIZE	25/06/02

UNLESS OTHERWISE SPECIFIED: DIMENSIONS ARE IN INCHES TOLERANCES ARE: FRACTIONS DECIMALS ±.005 ±.005 ±.005 DO NOT SCALE DRAWING		UBC MECHANICAL ENGINEERING	
DRAWN BY: JEAN-LOUIS IACONIS		SIZE: 11x17	DATE: AUGUST 9, 2002
DATE: AUGUST 9, 2002		SCALE: NTS	SHEET: 5 OF 11

- NOTES:
1. MATERIAL: 316 STAINLESS STEEL
2. QTY: 1



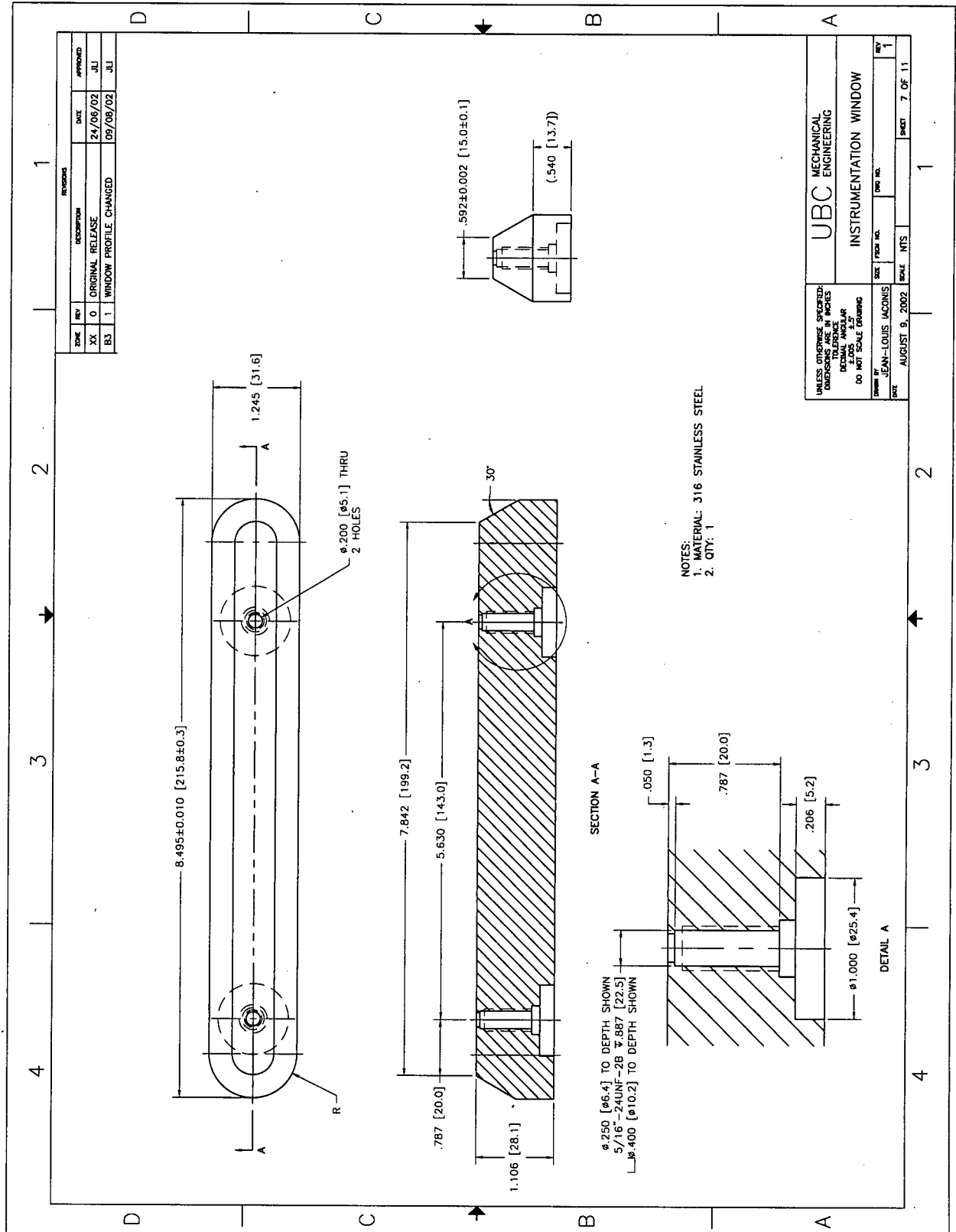
ZONE	REV	DESCRIPTION	DATE	APPROVED
XX	0	ORIGINAL RELEASE	24/06/02	JLI
C3	1	INCREASED CENTRE HOLE SIZE	25/06/02	JLI

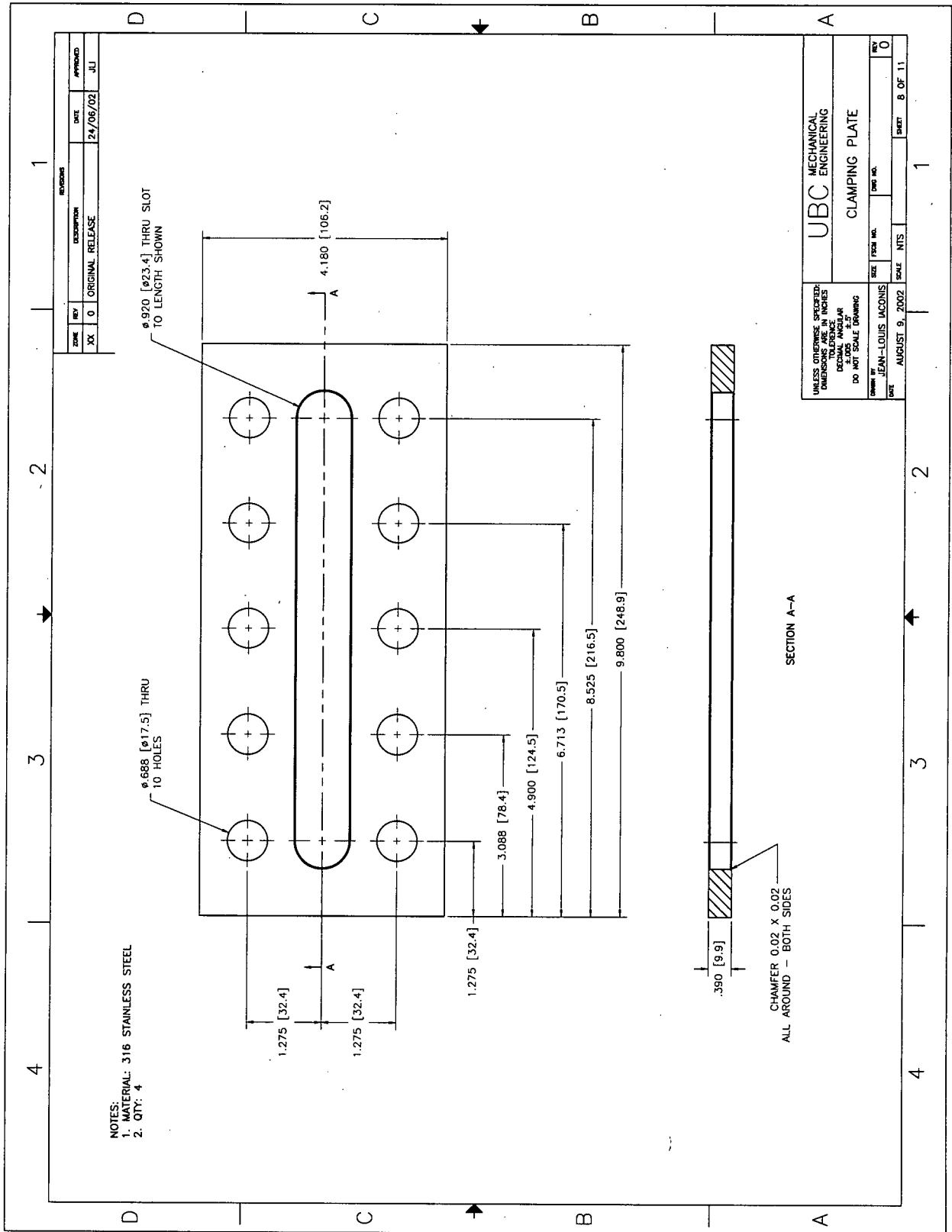
NOTES:
 1. MATERIAL: 316 STAINLESS STEEL
 2. QTY: 1

UNLESS OTHERWISE SPECIFIED, DIMENSIONS ARE IN INCHES		UBC MECHANICAL ENGINEERING	
TOLERANCE	±.005	SIZE	FRENCH NO.
DO NOT SCALE DRAWING	±.005	SCALE	NTS
DATE	AUGUST 9, 2002	DRAWN BY	JEAN-LOUIS INCONIS
DATE	AUGUST 9, 2002	DATE	AUGUST 9, 2002
REV	1	SHEET	6 OF 11

#150 SLIP-ON FLANGE, ANSI B16.5
 2.5" NOMINAL PIPE DIAMETER
 316 STAINLESS STEEL

SECTION A-A

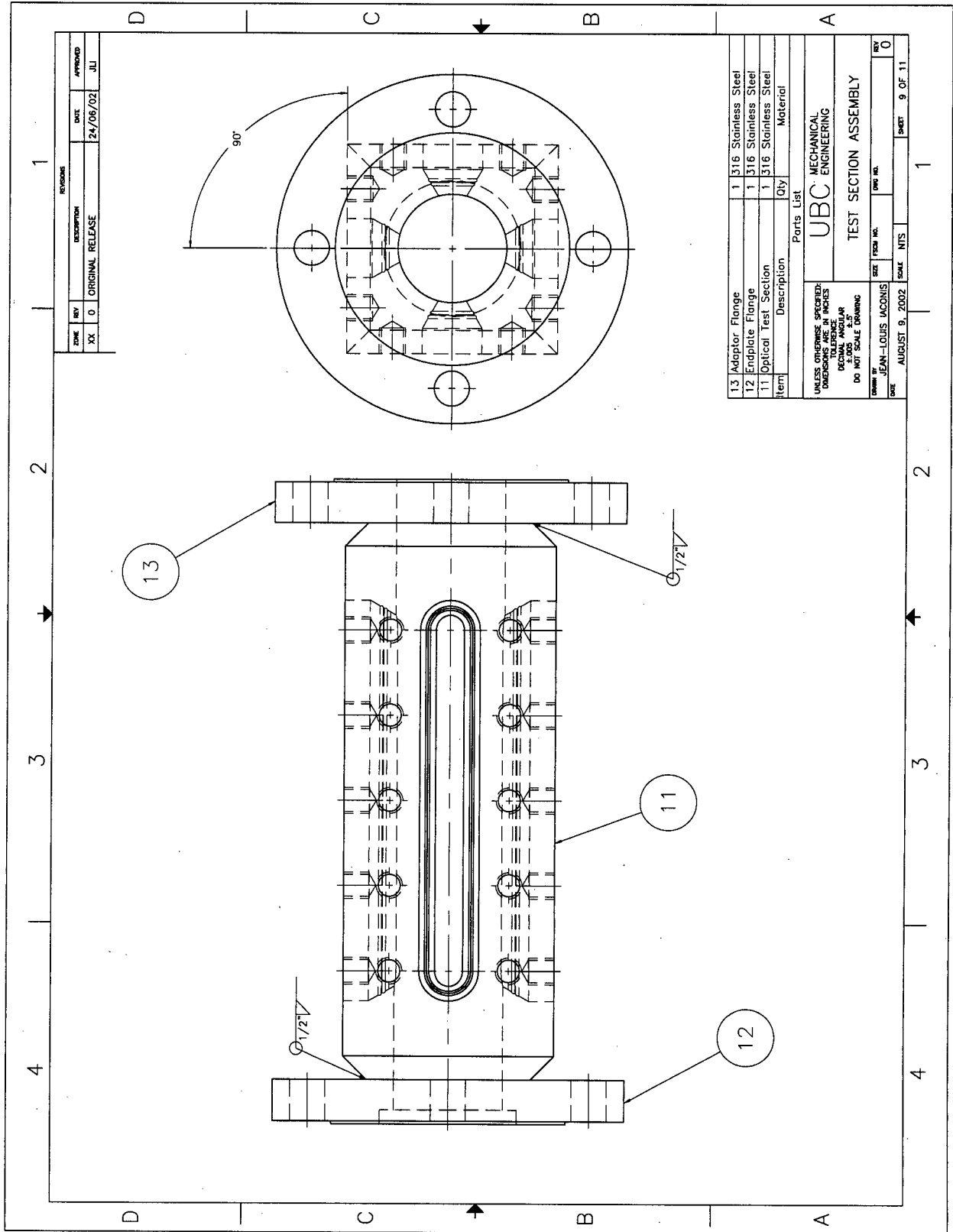




NOTES:
 1. MATERIAL: 316 STAINLESS STEEL
 2. QTY: 4

DATE	REV	DESCRIPTION	DATE	APPROVED
XX	0	ORIGINAL RELEASE	24/06/02	JLI

UBC MECHANICAL ENGINEERING	
CLAMPING PLATE	
UNLESS OTHERWISE SPECIFIED: DIMENSIONS ARE IN INCHES TOLERANCES ARE AS SHOWN FINISH AS SHOWN DO NOT SCALE DRAWING	SIZE FIG. NO. SHEET NO.
DRAWN BY JEAN-LOUIS IACONIS	SCALE NTS
DATE AUGUST 9, 2002	SHEET 8 OF 11



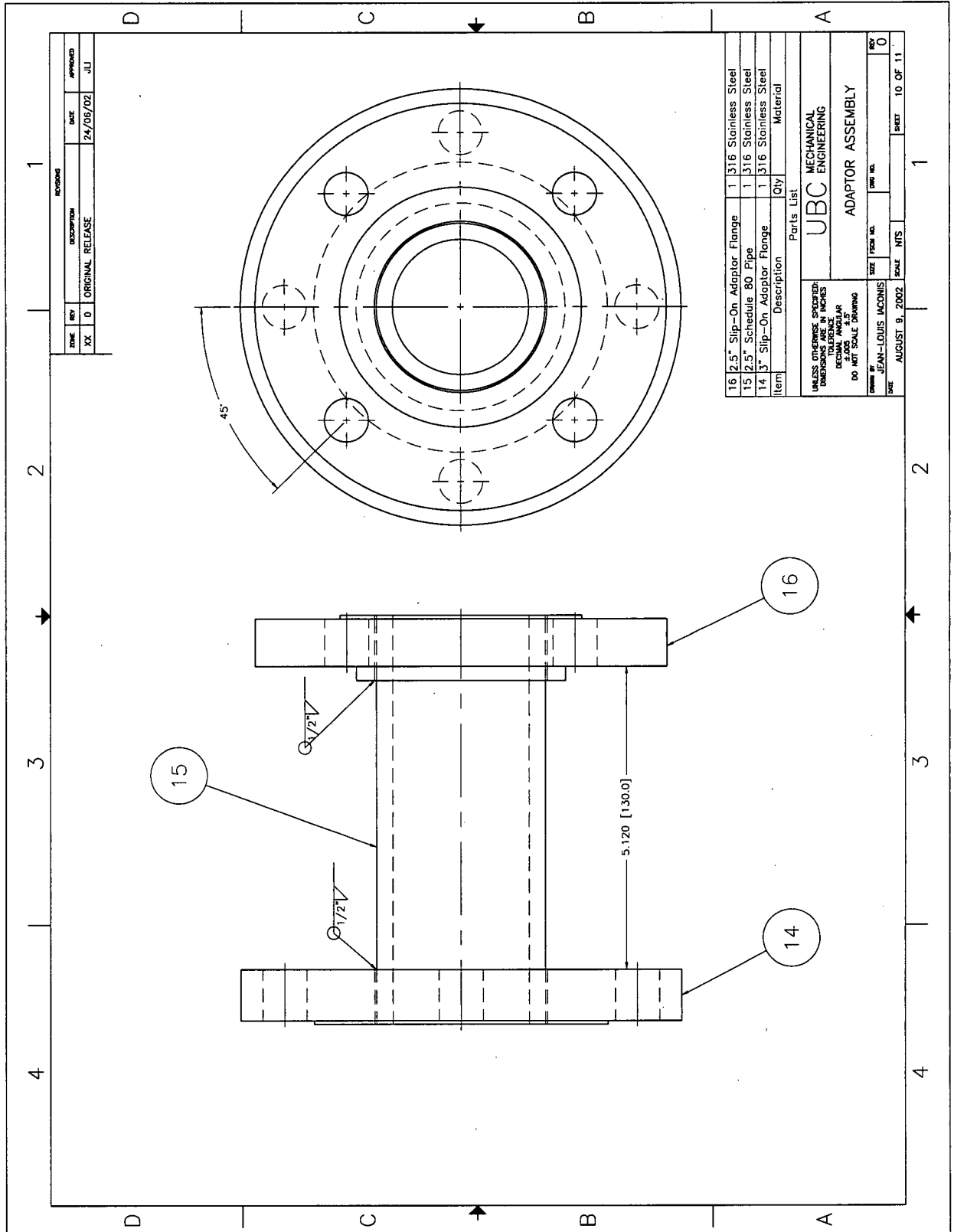
REVISED		DATE	APPROVED
ZONE	REV	DESCRIPTION	
XX	0	ORIGINAL RELEASE	24/06/02 JLI

Item	Description	Qty	Material
13	Adaptor Flange	1	316 Stainless Steel
12	Endplate Flange	1	316 Stainless Steel
11	Optical Test Section	1	316 Stainless Steel

Parts List

UNLESS OTHERWISE SPECIFIED: DIMENSIONS ARE IN INCHES TOLERANCES ARE AS SHOWN DECIMALS ARE IN 10'S DO NOT SCALE DRAWING	
DESIGNED BY	JEAN-LOUIS LACONIS
DATE	AUGUST 9, 2002
SCALE	N.T.S.
SHEET	9 OF 11

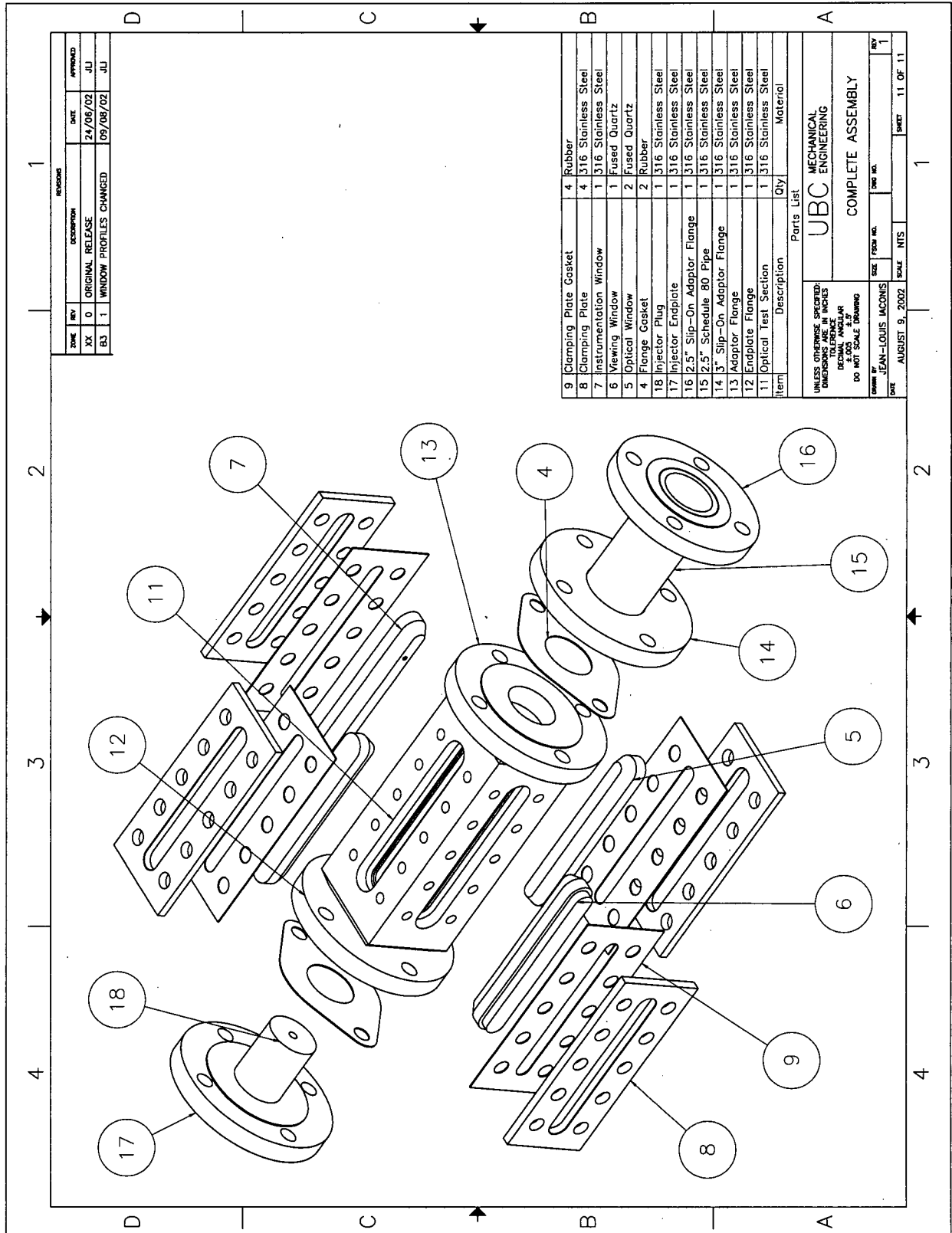
UBC MECHANICAL ENGINEERING
TEST SECTION ASSEMBLY



REVISIONS			
ZONE	REV	DESCRIPTION	DATE
XX	0	ORIGINAL RELEASE	24/06/02
			JLI

Item	Description	Qty	Material
16	2.5" Slip-On Adaptor Flange	1	316 Stainless Steel
15	2.5" Schedule 80 Pipe	1	316 Stainless Steel
14	3" Slip-On Adaptor Flange	1	316 Stainless Steel

Parts List			
UNLESS OTHERWISE SPECIFIED: DIMENSIONS ARE IN INCHES DECIMAL ANGULAR DIMENSIONS ARE IN DEGREES DO NOT SCALE DRAWING			
DESIGNED BY	JEAN-LOUIS LACONIS	SIZE	FROM NO.
DATE	AUGUST 9, 2002	SCALE	NTS
		SHEET	10 OF 11
		REV	0



ZONE	REV	DESCRIPTION	DATE	APPROVED
XX	0	ORIGINAL RELEASE	24/06/02	JU
BB	1	WINDOW PROFILES CHANGED	09/08/02	JU

Item	Description	Qty	Material
9	Clamping Plate Gasket	4	Rubber
8	Clamping Plate	4	316 Stainless Steel
7	Instrumentation Window	1	316 Stainless Steel
6	Viewing Window	1	Fused Quartz
5	Optical Window	2	Fused Quartz
4	Flange Gasket	2	Rubber
18	Injector Plug	1	316 Stainless Steel
17	Injector Endplate	1	316 Stainless Steel
16	2.5" Slip-On Adaptor Flange	1	316 Stainless Steel
15	2.5" Schedule 80 Pipe	1	316 Stainless Steel
14	3" Slip-On Adaptor Flange	1	316 Stainless Steel
13	Adaptor Flange	1	316 Stainless Steel
12	Endplate Flange	1	316 Stainless Steel
11	Optical Test Section	1	316 Stainless Steel

UNLESS OTHERWISE SPECIFIED:
 DIMENSIONS ARE IN INCHES
 TOLERANCES ARE:
 DECIMALS AND .01"
 DO NOT SCALE DRAWING

DESIGNED BY: JEAN-LOUIS LACOMIS
 DATE: AUGUST 9, 2002
 SCALE: NTS
 SHEET: 11 OF 11

UBC MECHANICAL ENGINEERING
 COMPLETE ASSEMBLY